



Politecnico di Bari

Repository Istituzionale dei Prodotti della Ricerca del Politecnico di Bari

Smartphone and low-cost sensors systems for geospatial data acquisition in terrestrial and water scenarios and processing methods

This is a PhD Thesis

Original Citation:

Smartphone and low-cost sensors systems for geospatial data acquisition in terrestrial and water scenarios and processing methods / Vozza, Gabriele. - ELETTRONICO. - (2024). [10.60576/poliba/iris/vozza-gabriele_phd2024]

Availability:

This version is available at <http://hdl.handle.net/11589/266940> since: 2024-03-07

Published version

DOI:10.60576/poliba/iris/vozza-gabriele_phd2024

Publisher: Politecnico di Bari

Terms of use:

(Article begins on next page)



POLITECNICO DI BARI

17

2023

DICATECh

D.R.R.S.

2023

Doctor of Philosophy in Risk and Environmental, Territorial and Building Development

Gabriele Vozza

Coordinator: Prof. Michele Mossa

XXXV CYCLE
ICAR/06 Topography and cartography

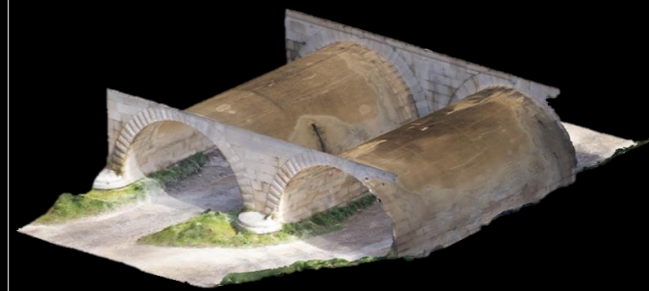
DICATECh
Department of Civil, Environmental, Land, Building Engineering and Chemistry

Gabriele Vozza

Smartphone and low-cost sensors systems for geospatial data acquisition in terrestrial and water scenarios and processing methods

Smartphone and low-cost sensors systems for geospatial data acquisition in terrestrial and water scenarios and processing methods

Prof. Eufemia Tarantino – Prof. Domenica Costantino
DICATECh - Department of Civil, Environmental, Land, Building Engineering and Chemistry, Polytechnic University of Bari
Prof. Sorin Herban
CCTFC – Department of Overland Communication Ways, Foundation and Cadastral Survey, Politehnica University of Timisoara
Prof. Massimiliano Pepe
InGeo - Department of Engineering and Geology, "G. d'Annunzio" University of Chieti - Pescara



Cover image: 3D mesh model textured of the bridge arcades.

Abstract
Geospatial data support the definition of policies, programmes and projects dedicated to sustainable development by providing information for planning, assessment, monitoring and forecasting. Sadly, the collection of geospatial data on a local scale in situ is often an expensive operation due to the instruments to be used, the specialised staff employed in the survey operations and the logistics involved.
Based on these observations, a research project dedicated to the study of smartphones, tablets and low-cost external sensors (which can be interfaced with mobile devices) for cost-effective geospatial data acquisition in terrestrial and water environments was realised for the thesis work.
The research project consisted of four parts.
In the first part of the research project, through a statistical analysis method potentially applicable to all Android devices with an integrated GNSS receiver, the quality of GNSS positioning in post-processing with only pseudorange measurements of Android smartphones was evaluated.
In the second part of the research project, the performances of the depth sensors of Android and Apple mobile devices were evaluated by analysing the point clouds produced by them using both visual methods (analysis of point cloud sections) and mathematical descriptors (eigenfeatures: planarity, omnivariance and surface variation).
In the third part of the research project, a sonar system consisting of low-cost sensors called GNSS > Sonar > Phone System (G > S > P Sys) able to collect bathymetric data in shallow water was implemented, and a method for 3D modelling of the collected data based on mapping via a machine learning approach was developed.
In the fourth part of the research project, GNSS-aided photogrammetry via video was studied for the production of automatically scaled and georeferenced point clouds and 3D mesh models. GNSS-aided photogrammetry was implemented using the smartphone and various low-cost sensors considering two systems and three different approaches.
Observing the results obtained, it can be deduced that the use of smartphones and tablets for the acquisition of good and high quality geospatial data is possible only by finding the most appropriate method for the positioning the devices.

17



Politecnico
di Bari

LIBERATORIA PER L'ARCHIVIAZIONE DELLA TESI DI DOTTORATO

Al Magnifico Rettore
del Politecnico di Bari

Il sottoscritto VOZZA GABRIELE nato a TARANTO (TA) il 01/03/1986 residente a TARANTO (TA) in via UMBRIA n.192 e-mail gabriele.vozza@poliba.it iscritto al 3° anno di Corso di Dottorato di Ricerca in RISCHIO, SVILUPPO AMBIENTALE, TERRITORIALE ED EDILIZIO ciclo 35° ed essendo stato ammesso a sostenere l'esame finale con la prevista discussione della tesi dal titolo:

"Smartphone and low-cost sensors systems for geospatial data acquisition in terrestrial and water scenarios and processing methods".

DICHIARA

- 1) di essere consapevole che, ai sensi del D.P.R. n. 445 del 28.12.2000, le dichiarazioni mendaci, la falsità negli atti e l'uso di atti falsi sono puniti ai sensi del codice penale e delle Leggi speciali in materia, e che nel caso ricorressero dette ipotesi, decade fin dall'inizio e senza necessità di nessuna formalità dai benefici conseguenti al provvedimento emanato sulla base di tali dichiarazioni;
- 2) di essere iscritto al Corso di Dottorato di ricerca RISCHIO, SVILUPPO AMBIENTALE, TERRITORIALE ED EDILIZIO ciclo 35°, corso attivato ai sensi del "Regolamento dei Corsi di Dottorato di ricerca del Politecnico di Bari", emanato con D.R. n.286 del 01.07.2013;
- 3) di essere pienamente a conoscenza delle disposizioni contenute nel predetto Regolamento in merito alla procedura di deposito, pubblicazione e autoarchiviazione della tesi di dottorato nell'Archivio Istituzionale ad accesso aperto alla letteratura scientifica;
- 4) di essere consapevole che attraverso l'autoarchiviazione delle tesi nell'Archivio Istituzionale ad accesso aperto alla letteratura scientifica del Politecnico di Bari (IRIS-POLIBA), l'Ateneo archiverà e renderà consultabile in rete (nel rispetto della Policy di Ateneo di cui al D.R. 642 del 13.11.2015) il testo completo della tesi di dottorato, fatta salva la possibilità di sottoscrizione di apposite licenze per le relative condizioni di utilizzo (di cui al sito <http://www.creativecommons.it/Licenze>), e fatte salve, altresì, le eventuali esigenze di "embargo", legate a strette considerazioni sulla tutelabilità e sfruttamento industriale/commerciale dei contenuti della tesi, da rappresentarsi mediante compilazione e sottoscrizione del modulo in calce (Richiesta di embargo);
- 5) che la tesi da depositare in IRIS-POLIBA, in formato digitale (PDF/A) sarà del tutto identica a quelle **consegnate**/inviolate/da inviarsi ai componenti della commissione per l'esame finale e a qualsiasi altra copia depositata presso gli Uffici del Politecnico di Bari in forma cartacea o digitale, ovvero a quella da discutere in sede di esame finale, a quella da depositare, a cura dell'Ateneo, presso le Biblioteche Nazionali Centrali di Roma e Firenze e presso tutti gli Uffici competenti per legge al momento del deposito stesso, e che di conseguenza va esclusa

qualsiasi responsabilità del Politecnico di Bari per quanto riguarda eventuali errori, imprecisioni o omissioni nei contenuti della tesi;

- 6) che il contenuto e l'organizzazione della tesi è opera originale realizzata dal sottoscritto e non compromette in alcun modo i diritti di terzi, ivi compresi quelli relativi alla sicurezza dei dati personali; che pertanto il Politecnico di Bari ed i suoi funzionari sono in ogni caso esenti da responsabilità di qualsivoglia natura: civile, amministrativa e penale e saranno dal sottoscritto tenuti indenni da qualsiasi richiesta o rivendicazione da parte di terzi;
- 7) che il contenuto della tesi non infrange in alcun modo il diritto d'Autore né gli obblighi connessi alla salvaguardia di diritti morali ed economici di altri autori o di altri aventi diritto, sia per testi, immagini, foto, tabelle, o altre parti di cui la tesi è composta.

Luogo e data Taranto, 26/02/2024

Firma



Il sottoscritto, con l'autoarchiviazione della propria tesi di dottorato nell'Archivio Istituzionale ad accesso aperto del Politecnico di Bari (POLIBA-IRIS), pur mantenendo su di essa tutti i diritti d'autore, morali ed economici, ai sensi della normativa vigente (Legge 633/1941 e ss.mm.ii.),

CONCEDE

- al Politecnico di Bari il permesso di trasferire l'opera su qualsiasi supporto e di convertirla in qualsiasi formato al fine di una corretta conservazione nel tempo. Il Politecnico di Bari garantisce che non verrà effettuata alcuna modifica al contenuto e alla struttura dell'opera.
- al Politecnico di Bari la possibilità di riprodurre l'opera in più di una copia per fini di sicurezza, back-up e conservazione.

Luogo e data Taranto, 26/02/2024

Firma





POLITECNICO DI BARI

D.R.R.S.

17

Doctor of Philosophy in Risk and Environmental, Territorial and Building Development

2023

Coordinator: Prof. Michele Mossa

XXXV CYCLE

ICAR/06 Topography and cartography

DICATECh

Department of Civil, Environmental, Land, Building Engineering and Chemistry

Smartphone and low-cost sensors systems for geospatial data acquisition in terrestrial and water scenarios and processing methods

Prof. Eufemia Tarantino – Prof. Domenica Costantino
DICATECh - Department of Civil, Environmental, Land, Building Engineering and Chemistry, Polytechnic University of Bari

Prof. Sorin Herban
CCTFC – Department of Overland Communication Ways, Foundation and Cadastral Survey, Politehnica University of Timisoara
Prof. Massimiliano Pepe
InGeo - Department of Engineering and Geology, “G. d’Annunzio” University of Chieti - Pescara

Gabriele Vozza



POLITECNICO DI BARI

D.R.R.S.

17

Dottorato di Ricerca in Rischio, Sviluppo Ambientale, Territoriale ed Edilizio

2023

Coordinatore: Prof. Michele Mossa

XXXV CICLO

ICAR/06 Topografia e cartografia

DICATECh

Dipartimento di Ingegneria Civile, Ambientale, del Territorio, Edile e di Chimica

Smartphone e sistemi di sensori low-cost per l'acquisizione di dati geospaziali in scenari terrestri e acquatici e metodi di elaborazione

Prof. Eufemia Tarantino – Prof. Domenica Costantino
DICATECh - Dipartimento di Ingegneria Civile, Ambientale, del Territorio, Edile e di Chimica, Politecnico di Bari

Prof. Sorin Herban
CCTFC – Department of Overland Communication Ways, Foundation and Cadastral Survey, Politehnica University of Timisoara
Prof. Massimiliano Pepe
InGeo – Dipartimento di Ingegneria e Geologia, Università degli Studi "G. d'Annunzio" Chieti - Pescara

Gabriele Vozza

EXTENDED ABSTRACT (ENG)

The outcome document “The future we want” and the 2030 Agenda for Sustainable Development recognise the importance of geospatial data as an supporting elements for achieving the sustainable development. Geospatial data support the definition of policies, programmes and projects dedicated to sustainable development by providing information for planning, assessment, monitoring and forecasting. Sadly, the collection of geospatial data on a local scale in situ is often an expensive operation due to the instruments to be used, the specialised staff employed in the survey operations and the logistics involved. The economic side can be a problem for the most vulnerable nations, that on the one hand need data on a local scale to support their sustainable development projects, but on the other hand have problems of data scarcity and a “digital divide” compared to more developed nations. Furthermore, the economic side can be an obstacle for the creation of citizen science projects useful for the achievement of sustainable development according to the principles of inclusiveness, transparency and participation.

Based on these observations, a research project dedicated to the study of smartphones, tablets and low-cost external sensors (which can be interfaced with mobile devices) for cost-effective geospatial data acquisition in terrestrial and water environments was realised for the thesis work. The research project consisted of four parts, the principal aims of which were: evaluation of smartphones Global Navigation Satellite System (GNSS) positioning; evaluation of depth sensors integrated on mobile devices; implementation of a low-cost sonar system based on smartphones for collecting bathymetric data and development of a modelling method for the subsequent 3D reconstruction of the collected data; and finally, study of GNSS-aided photogrammetry via smartphones and low-cost sensors.

In particular, in the first part of the research project, through a statistical analysis method potentially applicable to all Android devices with an integrated GNSS receiver,

the quality of GNSS positioning in post-processing with only pseudorange measurements of Android smartphones was evaluated.

In the second part of the research project, the performances of the depth sensors of Android and Apple mobile devices were evaluated by analysing the point clouds produced by them using both visual methods (analysis of point cloud sections) and mathematical descriptors (eigenfeatures: planarity, omnivariance and surface variation).

In the third part of the research project, a sonar system consisting of low-cost sensors called GNSS > Sonar > Phone System (G > S > P Sys) able to collect bathymetric data in shallow water was implemented, and a method for 3D modelling of the collected data based on mapping via a machine learning approach was developed.

In the fourth part of the research project, GNSS-aided photogrammetry via video was studied for the production of automatically scaled and georeferenced point clouds and 3D mesh models. GNSS-aided photogrammetry was implemented using the smartphone and various low-cost sensors considering two systems and three different approaches.

Finally, observing the results obtained, it can be deduced that the use of smartphones and tablets for the acquisition of good and high quality geospatial data is possible only by finding the most appropriate method for the positioning the devices. Based on the applications experimented in the research project, the problem of mobile device positioning was solved using a low-cost external GNSS receiver for smartphones. However, this does not exclude the possibility of exploring other positioning methods in future research.

Keywords: *Smartphone; Low-cost sensors systems; Global Navigation Satellite System; Time-of-flight detection system; Sound navigation and ranging; Photogrammetry; Point cloud; 3D model; Sustainable development*

EXTENDED ABSTRACT (ITA)

Il documento finale “The future we want” e l’Agenda 2030 per lo Sviluppo Sostenibile riconoscono l’importanza dei dati geospaziali in quanto elementi di supporto per il raggiungimento dello sviluppo sostenibile. I dati geospaziali supportano la definizione di politiche, programmi e progetti dedicati allo sviluppo sostenibile fornendo informazioni per la pianificazione, la valutazione, il monitoraggio e la previsione. Purtroppo, la raccolta di dati geospaziali su scala locale in situ è un’operazione spesso costosa a causa della strumentazione da utilizzare, del personale specializzato impiegato nelle operazioni di rilievo e della logistica coinvolta. L’aspetto economico può rappresentare un problema per i Paesi più vulnerabili che da una parte hanno necessità di dati su scala locale per sostenere i propri progetti di sviluppo sostenibile ma dall’altra hanno un problema di scarsità di dati e di “digitale divide” rispetto ai paesi più sviluppati. Inoltre, il fattore economico può rappresentare un ostacolo anche alla creazione di progetti di citizen science utili per il raggiungimento dello sviluppo sostenibile secondo i principi dell’inclusività, della trasparenza e della partecipazione.

Sulla base di queste osservazioni, per il lavoro di tesi, è stato realizzato un progetto di ricerca dedicato allo studio di smartphone, tablet e sensori low-cost esterni (interfaciabili con dispositivi mobili) per l’acquisizione di dati geospaziali a basso costo in ambienti terrestri e acquatici. Il progetto di ricerca si è composto di quattro parti i cui obiettivi principali sono stati: valutazione del posizionamento tramite Global Navigation Satellite System (GNSS) con smartphones; valutazione dei sensori di profondità integrati sui dispositivi mobili; implementazione di un sistema sonar low-cost basato sugli smartphones per la raccolta di dati batimetrici e sviluppo di un metodo di modellazione per la successiva ricostruzione 3D dei dati raccolti; infine studio della GNSS-aided photogrammetry implementata attraverso smartphones e sensori low-cost.

In particolare, nella prima parte del progetto di ricerca, attraverso un metodo di analisi statistica potenzialmente applicabile a tutti i dispositivi Android dotati di un ricevitore

GNSS integrato, è stata valutata la qualità del posizionamento GNSS in post-processing con sole misure di pseudorange degli smartphone Android.

Nella seconda parte del progetto di ricerca, sono state valutate le performance dei sensori di profondità dei dispositivi mobili Android e Apple attraverso l'analisi delle nuvole di punti da essi prodotte usando sia metodi visivi (analisi delle sezioni della nuvola di punti) che descrittori matematici (eigenfeatures: planarity, omnivariance e surface variation).

Nella terza parte del progetto di ricerca, è stato implementato un sistema sonar formato da sensori low-cost chiamato GNSS > Sonar > Phone System (G > S > P Sys) capace di raccogliere dati batimetrici in acque poco profonde ed è stato sviluppato un metodo per la modellazione 3D dei dati batimetrici raccolti basato sulla mappatura attraverso un metodo di machine learning.

Nella quarta parte del progetto di ricerca, è stata studiata la GNSS-aided photogrammetry attraverso video per la produzione di nuvole di punti e modelli 3D mesh automaticamente scalati e georeferenziati. La GNSS-aided photogrammetry è stata implementata utilizzando lo smartphone e alcuni sensori low-cost considerando due sistemi e tre approcci diversi.

Infine, osservando i risultati ottenuti si può dedurre che l'uso di smartphone e tablet per l'acquisizione di dati geospaziali di buona e alta qualità è possibile solo individuando il metodo più idoneo per il posizionamento dei dispositivi. In base alle applicazioni sperimentate nel progetto di ricerca, il problema del posizionamento dei dispositivi mobili è stato risolto tramite un ricevitore GNSS esterno low-cost per smartphone. Ciò non esclude la possibilità di altri metodi di posizionamento da esplorare in ricerche future.

Parole chiave: *Smartphone; Sistemi di sensori a basso costo; Sistemi Globali di Navigazione Satellitare; Sistemi di rilevamento a Tempo di Volo; Suono navigazione e misurazione; Fotogrammetria; nuvola di punti; modello 3D; Sviluppo sostenibile.*

INDEX

<i>INTRODUCTION</i>	7
<i>CHAPTER 1. BASIC THEORETICAL CONCEPTS</i>	14
<i>CHAPTER 2. SMARTPHONE GNSS POSITIONING EVALUATION</i>	39
<i>CHAPTER 3. SMARTPHONE DEPTH SENSORS EVALUATION</i>	61
<i>CHAPTER 4. GNSS > SONAR > PHONE SYSTEM AND 3D MODELLING</i>	84
<i>CHAPTER 5. GNSS-AIDED PHOTOGRAMMETRY VIA VIDEO BY SMARTPHONE AND LOW-COST SENSORS SYSTEMS</i>	123
<i>CONCLUSIONS</i>	166
<i>ACKNOWLEDGEMENTS</i>	171
<i>REFERENCES</i>	172
<i>ANNEXES</i>	192
<i>CURRICULUM VITAE</i>	206

INTRODUCTION

Geospatial data is a type of data capable of generating geospatial information to describe objects, events and phenomena located or occurring on the surface of the Earth through the combination of position data, characteristics and in some cases even temporal data (Stock and Guesgen, 2016; *What is geospatial data?* | IBM, accessed: 20 October 2023). Some examples of geospatial data are: vectors and attributes, point clouds, raster and satellite images, Computer-Aided Design (CAD) images, census data, telephone data and social media data (*What is geospatial data?* | IBM, accessed: 20 October 2023).

Geospatial information and sustainable development are related topics. In “The future we want”, outcome document of the United Nations Conference on Sustainable Development, geospatial information is explicitly referred to in points 187 and 274. Point 187 states:

“We recognize the importance of early warning systems as part of effective disaster risk reduction at all levels in order to reduce economic and social damages, including the loss of human life, and in this regard encourage States to integrate such systems into their national disaster risk reduction strategies and plans. We encourage donors and the international community to enhance international cooperation in support of disaster risk reduction in developing countries, as appropriate, through technical assistance, technology transfer as mutually agreed, capacity-building and training programmes. We further recognize the importance of comprehensive hazard and risk assessments, and knowledge- and information-sharing, including reliable geospatial information. We commit to undertake and strengthen in a timely manner risk assessment and disaster risk reduction instruments” (United Nations, 2012).

And point 274 states:

“We recognize the importance of space-technology-based data, in situ monitoring and reliable geospatial information for sustainable development policymaking, programming and project operations. In this context, we note the relevance of global mapping, and recognize the efforts in developing global environmental observing systems, including by the Eye on Earth network and through the Global Earth Observation System of Systems. We recognize the need to support developing countries in their efforts to collect environmental data” (United Nations, 2012).

Later, in “Transforming our world: the 2030 Agenda for Sustainable Development”, geospatial information is mentioned in point 76 which asserts:

“We will support developing countries, particularly African countries, least developed countries, small island developing States and land-locked developing countries, in strengthening the capacity of national statistical offices and data systems to ensure access to high quality, timely, reliable and disaggregated data. We will promote transparent and accountable scaling-up of appropriate public-private cooperation to exploit the contribution to be made by a wide range of data, including earth observation and geospatial information, while ensuring national ownership in supporting and tracking progress” (United Nations, 2015).

Points 187 and 274 of “The future we want” recognise the importance of geospatial information both for disaster risk reduction and for the definition of policies, programmes and projects dedicated to achieving sustainable development, and the 2030 Agenda for Sustainable Development recognises the need for high quality data, including geospatial data, to achieve the Sustainable Development Goals (SDGs) and

promotes the use of geospatial data to support the SDGs (Scott and Rajabifard, 2017).

Geospatial data and geospatial analysis techniques support and assist the achievement of the SDGs by providing information and tools for planning, assessment, monitoring and forecasting (Scott and Rajabifard, 2017; Avtar *et al.*, 2019; Das *et al.*, 2022).

Geospatial data can be acquired on a global scale through the use of satellite remote sensing techniques, and on a local scale via monitoring and surveying using various sensors systems directly in situ (Avtar *et al.*, 2019; Das *et al.*, 2022).

In the thesis work, integrated sensors systems on smartphones (and tablets) and low-cost external sensors systems that can be connected to smartphones were studied for local scale geospatial data acquisition in terrestrial and water/marine operative scenarios. The performance of the sensors systems investigated was evaluated and methods for connecting and synchronising smartphones with external sensors and for processing the acquired data were studied and implemented. The study and implementation of connection, synchronisation and processing methods are important elements to consider working with low-cost sensors, as these sensors and their acquired raw data may require appropriate processing to generate the desired output products. The geospatial data produced by the methods studied (mainly point clouds and 3D mesh models georeferenced) can describe objects and portions of territory based on position, shape and geometric dimensions.

Research project motivations

The sensors systems studied have the potential to provide geospatial data at a low cost and with medium to high quality. In addition to the obvious economic benefits extended to all possible users, the sensors studied, due to their affordability, can help solve the problem of data scarcity in the most vulnerable countries and fill the “digital divide” (Scott and Rajabifard, 2017). Also, the possibility of implementing external sensors systems via smartphones or directly using the sensors already integrated in smartphones offers the opportunity to involve local communities in citizen

science projects and achieve the SDGs in an inclusive, transparent and participatory way (Romano, 2015; Andrachuk *et al.*, 2019; Avtar *et al.*, 2019).

Considering the type of geospatial data, tests and case studies explored in the researches conducted, it is believed that the geospatial information that can be generated can be useful to support SDGs 9, 11 and 14. Furthermore, considering the technological aspect of the research project, it is believed that the studies conducted can also have a positive influence with respect to the specific targets 9.a, 11.c, and 14.a. Table (Tab.) 1 and 2 describe SDGs 9, 11 and 14 and targets 9.a, 11.c, and 14.a.

Tab. 1 - SDGs description (data source: United Nations, 2015).

SDGs	Description
9	<i>“Build resilient infrastructure, promote inclusive and sustainable industrialization and foster innovation.”</i>
11	<i>“Make cities and human settlements inclusive, safe, resilient and sustainable.”</i>
14	<i>“Conserve and sustainably use the oceans, seas and marine resources for sustainable development.”</i>

Tab. 2 - Targets description (data source: United Nations, 2015).

Targets	Description
9.a	<i>“Facilitate sustainable and resilient infrastructure development in developing countries through enhanced financial, technological and technical support to African countries, least developed countries, landlocked developing countries and small island developing States.”</i>
11.c	<i>“Support least developed countries, including through financial and technical assistance, in building sustainable and resilient buildings utilizing local materials.”</i>
14.a	<i>“Increase scientific knowledge, develop research capacity and transfer marine technology, taking into account the Intergovernmental Oceanographic Commission Criteria and Guidelines on the Transfer of Marine Technology, in order to improve ocean health and to enhance the contribution of marine biodiversity to the development of developing countries, in particular small island developing States and least developed countries.”</i>

Research project structure

The research project consisted of four interconnected parts, each corresponding to a research with specific topics of investigation. In general, the first and second

research investigated sensors systems already integrated in smartphones and tablets. The third and fourth research (considering the results of the first two researches) investigated low-cost external sensors systems connectable to smartphones that allow mobile devices to expand the number of sensors available to them and improve the quality and type of geospatial data that can be acquired.

The first research assessed the performance of built-in Global Navigation Satellite System (GNSS) receivers in Android mobile devices for post-processing GNSS positioning using pseudorange measurements. Data were collected statically under controlled conditions and the post-processing was performed employing two methods: Differential Global Navigation Satellite System (DGNSS) and Single Point Positioning (SPP) with both rapid and final ephemerides. The statistical analysis method used in the experimentation, relying solely on pseudorange measurements, could be applied to all Android mobile devices. However, the smartphone GNSS positioning results did not meet the requirements for subsequent parts of the research project.

The second research evaluated the performance of smartphone and tablet depth sensors, including Time-of-Flight (ToF) cameras for Android and LiDAR scanners for iOS, as well as the quality of point clouds generated by these sensors. The experiment involved using mobile devices to survey and create point clouds of various objects, including 10 different building materials, a statue, the interior of a room, and the remains of a Doric column at an archaeological site. Point cloud analysis was conducted through visual methods (examining sections) and using three mathematical descriptors (eigenfeatures): planarity, omnivariance, and surface variation. This part of the research project identified several issues in the point clouds produced by built-in depth sensors on smartphones and tablets.

The third research introduced a cost-effective sensors system named GNSS > Sonar > Phone System (G > S > P Sys) and developed a method for 3D mesh modelling of bathymetric data. This system combines a Single Beam Echo Sounder (SBES), an external GNSS receiver connectable to mobile devices, and a smartphone for system synchronization. The choice to use an external GNSS receiver was based on findings

from the first research. The G > S > P Sys's primary function is to gather bathymetric data in shallow waters.

In testing, the performance of the G > S > P Sys and SBESs was evaluated, focusing on GNSS positioning in static and kinematic modes and the accuracy and precision of water depth measurements. The 3D mesh modelling method employed is data driven, utilizing Machine Learning (ML) for mapping. This method was used to reconstruct a swimming pool with a variable bottom and a section of the seabed. Therefore, it can be applied to model both artificial underwater structures and natural seabed.

Finally, in the fourth research (based on the critical aspects found in the first and second part and the experience accumulated with the external sensors systems from the third part of the research project) GNSS-aided terrestrial photogrammetry via video was investigated for the production of point clouds and 3D mesh models automatic scaled and georeferenced. The GNSS-aided photogrammetry was implemented through two low-cost sensors systems. The first system consisted of a smartphone, a rear camera built-in the smartphone and an external GNSS receiver for smartphones. The second system consisted of a smartphone, 360° action camera and external GNSS receiver for smartphones. Three different approaches to GNSS-aided photogrammetry were tested in the research, two approaches were static and the third was kinematic. A specific pipeline for processing geospatial photogrammetric data was used to produce the point clouds and 3D mesh models. The performances of the tested GNSS-aided photogrammetry systems and approaches were evaluated through a GNSS positioning test, two survey tests under controlled conditions and two field case studies under realistic conditions.

Regarding operational scenarios, the first, second and fourth researches were dedicated to geospatial data acquisition in terrestrial scenarios, while the third research was specifically dedicated to geospatial data acquisition in water/marine scenarios.

Aims of the research project

Based on the previous paragraph, the research aims can be summarised in four main points:

1. evaluation of GNSS positioning with the receiver built-in to mobile devices through pseudorange measurements;
2. evaluation of depth sensors built-in to mobile devices;
3. implementation via smartphone of a low-cost sensors system and development of a 3D modelling method for surveying, mapping and reconstruction of water scenarios;
4. study of systems and approaches to GNSS-aided photogrammetry via video and smartphone for the production of point clouds and 3D mesh models.

Thesis organisation

The thesis presented consists of five chapters with conclusions. In the first chapter, the basic theoretical knowledge for understanding the functioning of sensors and sensors systems that were used in the research was provided. In the second chapter, the first research concerning the evaluation of GNSS positioning with pseudorange measurements of mobile devices was presented. The third chapter presented the second research where the depth sensors built-in to mobile devices and the point clouds produced were evaluated. In the fourth chapter, the third research was presented devoted to the implementation of the G > S > P Sys and the development of the 3D mesh modelling method for bathymetric data. Chapter five presented the fourth research concerning the production of point clouds and 3D mesh models using GNSS-aided photogrammetry via video and smartphone. Finally, the summary of the results achieved and the final reflections were reported in the conclusions.

Some of the researches presented in the chapters of the thesis were previously published in the form of a scientific paper; the bibliographical data of the published papers were reported at the beginning of each chapter containing a published material.

CHAPTER 1. BASIC THEORETICAL CONCEPTS

This chapter provides the theoretical basic knowledge about the different types of sensors systems that were used, studied and tested during the research activities conducted in the thesis work. For each system (or part of the system most interesting for the treatment), the functional principles, block diagrams of the functional architecture and the fundamental mathematical equations were explained. Focusing on aspects considered useful for a better understanding of the topics discussed in the following chapters, this chapter does not claim to be exhaustive, and reference is made to the authors cited for further details.

1.1. The Global Navigation Satellite Systems

1.1.1. The functional composition of the Global Navigation Satellite System and receiver

A Global Navigation Satellite System (GNSS) can be defined as a system consisting of a constellation of artificial satellites in Earth orbit, whose task is to transmit data used primarily for geolocalisation of the users of the system, equipped with specific receiving devices (Hofmann-Wellenhof, Lichtenegger and Wasle, 2007; Langley, Teunissen and Montenbruck, 2017). Currently the operational GNSSs are: the Global Positioning System (GPS) of the United States of America (USA), the GLObal'naya NAVigatsionnaya Sputnikovaya System (GLONASS) of Russia, the Galileo of the European Union (EU) and the BeiDou Navigation System (BDS) of China (Hofmann-Wellenhof, Lichtenegger and Wasle, 2007; Langley, Teunissen and Montenbruck, 2017; Hein, 2020). In addition to GNSSs, there are also briefly mentioned the Regional Navigation Satellite Systems (RNSS), such as the Quasi-Zenith Satellite System (QZSS) of Japan and the Indian Regional Navigation Satellite System (IRNSS) of India, and the Satellite-Based Augmentation Systems (SBAS) (Hofmann-Wellenhof, Lichtenegger and Wasle, 2007; Langley, Teunissen and Montenbruck, 2017; Hein, 2020).

The GNSSs consist of three elements: the space segment, the control segment and the user segment (Hofmann-Wellenhof, Lichtenegger and Wasle, 2007; Langley, Teunissen and Montenbruck, 2017).

The space segment consists of the satellites constellation orbiting the Earth (Hofmann-Wellenhof, Lichtenegger and Wasle, 2007; Langley, Teunissen and Montenbruck, 2017). Satellites are equipped with a payload consisting of: atomic clocks, radio transmitters, antennas, navigation systems, attitude and orbit control systems, tracking, telemetry and command systems, solar panels and power systems (Hofmann-Wellenhof, Lichtenegger and Wasle, 2007). The number of satellites constituting a constellation is chosen to (virtually) ensure the visibility of at least four satellites in every part of the world, to this number is also added a certain number of spare satellites (in case of maintenance or decommissioning) in order to prevent the system from easily going down (Hofmann-Wellenhof, Lichtenegger and Wasle, 2007; *GPS.gov: Space Segment*, accessed: 20 October 2023). The GNSS satellites occupy the Medium Earth Orbits (MEO) while the RNSSs occupy the Inclined GeoSynchronous Orbits (IGSO) and Geostationary Orbits (GEO), furthermore, the satellites are placed in different orbital planes in order to improve the Geometric Dilution Of Precision (GDOP) parameter (Hofmann-Wellenhof, Lichtenegger and Wasle, 2007; Langley, Teunissen and Montenbruck, 2017). Initially, the satellites in each constellation transmitted signals for GNSS positioning on at least two frequencies, but over the years, due to improved and modernised systems (e.g. GPS), the number of available frequencies has increased (Langley, Teunissen and Montenbruck, 2017). In Tab. 3, some data about the spatial segment of GNSSs are summarised.

Tab. 3 - Data on GNSS spatial segments (data sources: Langley, Teunissen and Montenbruck, 2017; GPS (Global Positioning System), United States, accessed: 20 October 2023; GPS.gov: Space Segment, accessed: 20 October 2023; GLONASS (Global Navigation Satellite System), Russia, accessed: 20 October 2023; About GLONASS, accessed: 20 October 2023; Galileo (European Union), accessed: 20 October 2023; System | European GNSS Service Centre, accessed: 20 October 2023; BeiDou Navigation Satellite System (China), accessed: 20 October 2023; System, accessed: 20 October 2023).

GNSS	GPS	GLONASS	GALILEO	BeiDou
Origin	USA	Russia	EU	China
Operational Satellites (no.)	31	24	24	29; 11; 4
Datum	World Geodetic System 1984 (WGS84)	Parametry Zemli 1990 (PZ-90)	Galileo Terrestrial Reference Frame (GTRF)	China Geodetic Coordinate System 2000 (CGCS2000)
Orbit altitude (km)	MEO 20,200	MEO 19,100	MEO 23,222	MEO; IGSO; GEO 21,528; 35,787; 35,787
Orbital planes (no.)	6	3	3	3; -; -
Orbit inclination (°)	55	64.8	56	55; 55; -
Frequency (MHz)	L1; L2; L5 1575.42; 1227.60; 1176.45	L1; L2; L3OC 1598.0625– 1609.3125; 1242.9375– 1251.6875; 1202.025	E1 A/B/C; E5a I/Q; E5b I/Q; Alt- BOC; E6 A/B/C 1575.42; 1176.45; 1207.14; 1191.795; 1278.75	B1I, B2I, B3I; B1C; B2a; B2b 1561.098; 1207.14; 1268.52; 1575.42; 1176.45; 1207.14

The control segment is a part of the GNSS located on the Earth and consists of a master control station, a network of monitoring stations distributed across the Earth and antennas for communicating with satellites (Hofmann-Wellenhof, Lichtenegger and Wasle, 2007; Langley, Teunissen and Montenbruck, 2017). The control segment manages the system and monitors the satellites (Hofmann-Wellenhof, Lichtenegger

and Wasle, 2007; Langley, Teunissen and Montenbruck, 2017). The main tasks of the control segment are therefore: checking and forecasting satellite orbits, sending data for the alignment of clocks, checking atmospheric parameters, checking the attitude of satellites and monitoring the signals transmitted by satellites (Hofmann-Wellenhof, Lichtenegger and Wasle, 2007).

Finally, the user segment consists of both civil and military users equipped with a GNSS receiver (Langley, Teunissen and Montenbruck, 2017). According to Hofmann-Wellenhof, Lichtenegger and Wasle (2007), GNSS receivers can be schematically subdivided according to: the GNSS measurements performed (e.g. pseudorange and/or carrier-phase), the number of frequencies received, and the number and type of GNSS used for geolocation. The main tasks performed by a GNSS receiver involve determining the satellites in view, processing satellite signals, geolocation of the user, determining velocity and time and recording of raw data for post-processing (Hofmann-Wellenhof, Lichtenegger and Wasle, 2007).

Concerning the architecture of the GNSS receiver, a typical GNSS receiver can be divided into an analogue section and a digital section (Eissfeller and Won, 2017).

The analogue section consists mainly of two functional blocks: the antenna and the Radio Frequency (RF) front-end (Hofmann-Wellenhof, Lichtenegger and Wasle, 2007; Eissfeller and Won, 2017).

The function of the antenna is receiving the satellite signal, converting the electromagnetic waves into electronic signals, sending the electronic signals to the RF front-end and reducing interference (Hofmann-Wellenhof, Lichtenegger and Wasle, 2007; Eissfeller and Won, 2017). The antennas can be divided into passive antennas and active antennas; active antennas integrate a preamplifier inside them to set the noise figure (Hofmann-Wellenhof, Lichtenegger and Wasle, 2007; Eissfeller and Won, 2017). Omnidirectional antennas with a uniform gain pattern are used for GNSS receivers, and depending to the application (e.g. terrestrial) the gain can be limited to the upper hemisphere in order to limit the arrival of signals below the horizon (Hofmann-Wellenhof, Lichtenegger and Wasle, 2007). Among the possible antenna designs are helical antennas and planar microstrip antennas. Helical antennas can be

spiral helical or quadrifilar helical, they have sufficient bandwidth to receive signals up to 30-50 MHz but have problems with phase centre stability (Eissfeller and Won, 2017). Due to their small size, planar microstrip antennas are the preferred solution adopted in the smartphone environment, the main problem with planar microstrip antennas is the narrow bandwidth of approximately 3 - 5 MHz (Eissfeller and Won, 2017).

The signals are then processed in the RF front-end. This block can be subdivided into two further blocks: the reference Local Oscillator (LO) and the radio section, consisting of the preamplifier (in case a passive antenna is used), the Band-Pass Filters (BPF), the frequency mixer, the Automatic Gain Control (AGC) and the Analog-to-Digital (A/D) converter (Hofmann-Wellenhof, Lichtenegger and Wasle, 2007; Eissfeller and Won, 2017). The local oscillator generates a local signal (with fundamental frequency) and allows the GNSS receiver to track the code and carrier phase of the satellite signal (Eissfeller and Won, 2017). Regarding the radio section, the signal is processed by the preamplifier, filtered by the first BPF and downconverted to Intermediate Frequency (IF) by the mixer (Hofmann-Wellenhof, Lichtenegger and Wasle, 2007). The downconversion process consists of mixing together the satellite signal centred on a frequency f with a pure harmonic signal of frequency F generated locally by the oscillator (Wells *et al.*, 1986; Hofmann-Wellenhof, Lichtenegger and Wasle, 2007). At the end of the process, there is a band of signals centred on the frequency $f + F$ (up-conversion) and a band of signals centred on the frequency $f - F$ (downconversion), but the two bands are overlapping (Wells *et al.*, 1986; Hofmann-Wellenhof, Lichtenegger and Wasle, 2007). Subsequently, a second BPF selects the signal band $f - F$ corresponding to the IF (Wells *et al.*, 1986; Hofmann-Wellenhof, Lichtenegger and Wasle, 2007). The power level of the signal output from the second BPF is normalised in the AGC so that the A/D can transform the signal from analogue to digital with time discretization (sampling) and amplitude discretization (quantisation) (Hofmann-Wellenhof, Lichtenegger and Wasle, 2007; Eissfeller and Won, 2017). As reported in Dorsey *et al.* (2006) and subsequently resumed in Hofmann-Wellenhof, Lichtenegger and Wasle (2007) realistic sampling values are between 2 and 20 times

the chipping rate of the Pseudo-Random Noise (PRN) code, and again in Hofmann-Wellenhof, Lichtenegger and Wasle (2007) quantization values between 1 and 2 or 4 bits are reported.

The converted signal is sent to the digital section of the receiver. The main electronic components that compose the digital section are: the Digital Signal Processor (DSP), the microprocessor (μ P), the Read Only Memory (ROM), the Random-Access Memory (RAM) and the input/output interface (Eissfeller and Won, 2017). The digital section can be divided into two functional blocks: the DSP and the navigation processor (Hofmann-Wellenhof, Lichtenegger and Wasle, 2007; Eissfeller and Won, 2017). The main function of the DSP is to find the maximum correlation between the incoming satellite signal and a locally produced signal replica (Hofmann-Wellenhof, Lichtenegger and Wasle, 2007). However, the input signal is the result of the superposition of several satellite signals, noise, interference, multipath signals etc.; the first operation to be performed is therefore the identification of the satellite signal of interest by auto-correlation, cross-correlation and de-spread processes (Hofmann-Wellenhof, Lichtenegger and Wasle, 2007). The maximum correlation between the identified satellite signal and the local signal is researched. The local signal is characterised by a certain coding delay and frequency offset, and in the correlation operation the DSP bi-dimensionally searches for all possible combinations of frequency offset and coding delay between the signals (Hofmann-Wellenhof, Lichtenegger and Wasle, 2007). The main output products of the DSP are observables (code, carrier phase and doppler frequencies), time data and navigation data (Hofmann-Wellenhof, Lichtenegger and Wasle, 2007). Finally, the navigation processor, through data demodulation, decodes the navigation message, obtaining ephemeris, almanacs, times and satellite positions, and using code, carrier phase and doppler measurements, it calculates time, velocity and receiver position (Hofmann-Wellenhof, Lichtenegger and Wasle, 2007). A functional block diagram of the GNSS receiver is shown in figure (Fig.) 1.

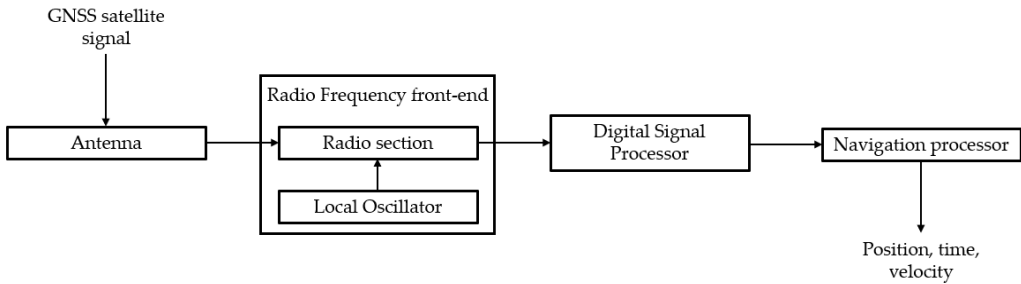


Fig. 1 - Functional diagram of GNSS receiver (image adapted from: Hofmann-Wellenhof, Lichtenegger and Wasle, 2007; Eissfeller and Won, 2017).

Currently, thanks to the development of chip technology and Systems-on-a-Chip (SoC), the elements composing the RF front-end and the digital section can be integrated on chips (Eissfeller and Won, 2017). As will be seen in chapters 2, 4 and 5, this has allowed the installation of GNSS receivers on smartphones (chapter 2), in other electronic devices such as single beam echo sounders (chapter 4) and on small electronic boards and hardware platforms (chapters 4 and 5).

1.1.2. The Global Navigation Satellite Systems positioning

Trilateration is the principle that makes GNSS positioning possible (Blewitt, 1997), indeed, theoretically hypothesising perfect synchronisation between the clock of the receiver and the GNSS time (e.g. GPS Time), three simultaneous measurements of the distance (range) between the receiver and three satellites of known positions are needed to determine the three unknown coordinates that determine the position of the receiver (Langley, Teunissen and Montenbruck, 2017). Unfortunately, the assumption of perfect synchronisation of the clock of the receiver cannot be satisfied for physical and technological reasons, so a fourth unknown corresponding to the synchronicity error of the clock with the GNSS time is introduced to solve the problem (Langley, Teunissen and Montenbruck, 2017). Therefore, by performing four simultaneous pseudo-distance measurements (called pseudorange measurements) with respect to four satellites of known positions, it will be possible to solve four equations in four unknowns and determine the three coordinates of the receiver position and the clock error (Langley, Teunissen and

Montenbruck, 2017). Furthermore, the satellite clocks also have a certain synchronisation error with GNSS time (of the millisecond), fortunately the synchronisation errors of the satellite clocks and the position of the satellites are derived from the navigation message transmitted to the receiver (Blewitt, 1997; Langley, Teunissen and Montenbruck, 2017).

A GNSS receiver can perform two types of measurements (observable) fundamental for positioning: pseudorange measurement and carrier-phase measurement (Hofmann-Wellenhof, Lichtenegger and Wasle, 2007; Shen *et al.*, 2019).

A range measurement affected by temporal misalignment errors is called a pseudorange measurement (Langley, Teunissen and Montenbruck, 2017). In a pseudorange measurement, the receiver computes the time delay with respect to the transmission of the satellite signal through the correlation between the code transmitted by the satellite and a replica of the code generated by the receiver (Hofmann-Wellenhof, Lichtenegger and Wasle, 2007). The equation underlying a pseudorange measurement is as follows (Langley, Teunissen and Montenbruck, 2017; Shen *et al.*, 2019):

$$P_r^s = \rho_r^s + c(dt_r - dt^s) + T_r^s + I_r^s + E_r^s \quad (1)$$

where ρ_r^s is the geometric distance between receiver r and satellite s, equal to:

$$\rho_r^s = \sqrt{(x_r - x^s)^2 + (y_r - y^s)^2 + (z_r - z^s)^2} \quad (2)$$

c is the speed of light, dt_r and dt^s are the synchronisation errors of the receiver and satellite clock (respectively) with respect to GNSS time, T_r^s is the tropospheric delay (modellable), I_r^s is the ionospheric delay (that can be corrected by the parameters transmitted in the navigation message or by two simultaneous measurements on two transmission frequencies) and E_r^s is a non-modellable error that computes together receiver electronic noise, the multipath effect and other minor errors.

Instead, in a carrier-phase measurement, the receiver, through alignment between carriers, measures the fractional phase difference (shift) between the carrier signal received by the satellite and a replica of the carrier at the same frequency produced

internally (Hofmann-Wellenhof, Lichtenegger and Wasle, 2007; Hauschild, 2017). The receiver can also count the number of integer phase cycles, when there is a change in the relative distance between the receiver and satellite greater than one cycle, the receiver, based on the integer cycles counted, returns the continuous phase measurement (Hauschild, 2017). The equation underlying a carrier-phase measurement in units of length is (Hauschild, 2017; Langley, Teunissen and Montenbruck, 2017; Shen *et al.*, 2019):

$$\Phi_r^s = \rho_r^s + c(dt_r - dt^s) + T_r^s - I_r^s + \varepsilon_r^s + \lambda N_r^s \quad (3)$$

where, in addition to the previous terms already defined, λ is the wavelength of the carrier, N_r^s is the ambiguity and represents an unknown integer number of carrier-phase cycles and ε_r^s is a non-modelable phase error that computes receiver electronic noise, the multipath effect and other minor errors.

On the basis of the measurements just described, two macro types of positioning can be performed: Single Point Positioning (SPP) and relative positioning.

Single Point Positioning is also called Point Positioning and Absolute Point Positioning (Hofmann-Wellenhof, Lichtenegger and Wasle, 2007).

SPP is the simplest and most direct positioning mode possible, in SPP a single receiver, based on pseudorange measurements (as described above), defines its position (Odijk, 2017). Positioning errors in SPP can be several metres (up to 10 m), so SPP is mainly used in navigation (Langley, Teunissen and Montenbruck, 2017; Odijk, 2017).

Another standalone positioning mode is Precise Point Positioning (PPP), that can be viewed as an advanced version of SPP (Langley, Teunissen and Montenbruck, 2017). Compared to the SPP, the PPP utilises phase measurements as the primary data and pseudorange measurements as the secondary data, and in order to obtain centimetre-order positionings, it tries to minimise the magnitude of errors in the equations (Langley, Teunissen and Montenbruck, 2017). Therefore, in the PPP, in addition to modelling and correcting for tropospheric and ionospheric effects, precise orbits and satellite clock errors derived from services such as the International GNSS Service (IGS)

are used in the equations (Langley, Teunissen and Montenbruck, 2017). PPP can be performed in static or kinematic mode (independent epoch-by-epoch position fixed), PPP static achieves accuracy in the order of a few centimetres (depending on observation time) and PPP kinematic achieves accuracy in the order of 10 centimetres (Langley, Teunissen and Montenbruck, 2017).

Regarding the relative positioning, Hofmann-Wellenhof, Lichtenegger and Wasle (2007) highlight that the terms “relative positioning” and “differential positioning” are often used as synonymous. In the opinion of Hofmann-Wellenhof, Lichtenegger and Wasle (2007), although there is no universal agreement on the use of these terms, there should at least be a theoretical difference, since differential positioning focuses more on the concept of measurement correction, whereas relative positioning focuses more on the combination of measures. Finally, Hofmann-Wellenhof, Lichtenegger and Wasle (2007) report how historically the term “differential” was associated more with code pseudorange measurements, whereas the term “relative” was associated more with carrier-phase measurements.

The Differential Global Navigation Satellite System (DGNSS) positioning is a positioning method using at least two receivers, the first receiver is fixed on a point of known coordinates and assumes the role of base station (or reference station), while the second receiver of unknown coordinates (to be determined), fixed or mobile, assumes the role of rover, base and rover can be connected to each other via radio (Hofmann-Wellenhof, Lichtenegger and Wasle, 2007; Langley, Teunissen and Montenbruck, 2017). The base receiver tracks the GNSS data of the satellites in view and, based on its own information, computes differential pseudorange corrections, then the rover receiver, that performs GNSS positioning close to the base, uses the base corrections to correct its own pseudorange measurements, improving GNSS positioning (Hofmann-Wellenhof, Lichtenegger and Wasle, 2007; Odijk and Wanninger, 2017). Pseudorange corrections mainly correct satellite orbit and clock errors and atmospheric effects (Langley, Teunissen and Montenbruck, 2017). The DGNSS positioning errors increase with increasing base-to-rover distance with typical values of 1

- 3 m, a rule of thumb says to add an error of 1 m per 100 km (Langley, Teunissen and Montenbruck, 2017).

In relative positioning, the position of a receiver of unknown coordinates is computed in relation to another receiver of known coordinates, determining the vector between the receivers (vector baseline or baseline), through the combination of the measurements of the two receivers (Hofmann-Wellenhof, Lichtenegger and Wasle, 2007; Langley, Teunissen and Montenbruck, 2017). The receiver measurements to be combined must be simultaneous and, in practice, mainly carrier-phase measurements are used in order to achieve more accurate positioning (Hofmann-Wellenhof, Lichtenegger and Wasle, 2007; Langley, Teunissen and Montenbruck, 2017). Therefore, considering two receivers r and m performing simultaneous observations with respect to two satellites s and t , the measurements can be combined into: single, double and triple differences (Hofmann-Wellenhof, Lichtenegger and Wasle, 2007). The single differences are obtained by differentiating the measurements made by receivers r and m with respect to satellite s , in the process the satellite clock error is eliminated and the equation can be written as follows (Hofmann-Wellenhof, Lichtenegger and Wasle, 2007; Langley, Teunissen and Montenbruck, 2017):

$$\Phi_{rm}^s = \rho_{rm}^s + cdt_{rm} + T_{rm}^s - I_{rm}^s + \varepsilon_{rm}^s + \lambda N_{rm}^s \quad (4)$$

where:

$$\Phi_{rm}^s = \Phi_m^s - \Phi_r^s \quad (5)$$

and with a similar generic notation for the other “n” terms in the equation:

$$(n)_{rm}^s = (n)_m^s - (n)_r^s \quad (6)$$

If the satellite t is then also considered and the single differences of the receivers r and m with respect to the satellites s and t are differentiated from each other, the double differences are obtained and the error of the clocks of the receivers is elimi-

nated in the process, the equation then assumes the form (Hofmann-Wellenhof, Lichtenegger and Wasle, 2007; Langley, Teunissen and Montenbruck, 2017):

$$\Phi_{rm}^{st} = \rho_{rm}^{st} + T_{rm}^{st} - I_{rm}^{st} + \varepsilon_{rm}^{st} + \lambda N_{rm}^{st} \quad (7)$$

where:

$$\Phi_{rm}^{st} = \Phi_{rm}^t - \Phi_{rm}^s. \quad (8)$$

Finally, if in addition to receivers r and m and satellites s and t, two epochs of observation t_1 and t_2 are also considered, and double differences are differentiated between them, triple differences are obtained and the initial ambiguity is removed, the equation assumes the form (Hofmann-Wellenhof, Lichtenegger and Wasle, 2007):

$$\Phi_{rm}^{st}(t_{12}) = \rho_{rm}^{st}(t_{12}) + T_{rm}^{st}(t_{12}) - I_{rm}^{st}(t_{12}) + \varepsilon_{rm}^{st}(t_{12}) \quad (9)$$

where:

$$\Phi_{rm}^{st}(t_{12}) = \Phi_{rm}^{st}(t_2) - \Phi_{rm}^{st}(t_1). \quad (10)$$

The relative positioning can be performed in static mode, Post-Processed Kinematic (PPK) and Real-Time Kinematic (RTK).

In the static mode, assuming a pair of receivers is used, the first receiver with base station function is placed on a point of known coordinates while the second receiver is placed on a point of coordinates to be determined, during the survey the receivers remain stationary (Rizos, 2017). In static mode, observation sessions have times of at least one hour (up to several days) with a horizontal accuracy of about 5 mm + 0.5 ppm for baseline up to about 20 km (with a deterioration by a factor of 1.5 - 2 in height) (Hofmann-Wellenhof, Lichtenegger and Wasle, 2007; Rizos, 2017). A variant of the static mode is the rapid-static mode, where observation session times are significantly reduced from a few minutes to over 30 minutes (Rizos, 2017). In rapid-static mode, by limiting the baselines to approximately 20 km, accuracy values of the

sub-centimetric order can be achieved (Hofmann-Wellenhof, Lichtenegger and Wasle, 2007).

In the PPK, one receiver assumes the role of a base station on a point of known coordinates, while the second receiver assumes the role of rover and moves and performs GNSS positioning (Rizos, 2017). There are two types of PPK, “stop-&-go” and “continuous”. In stop-&-go mode, the receiver interrupts movement to acquire points (stop) and then resumes movement (go), instead in continuous mode the receiver acquires points based on a continuous sampling (e.g. 1 per second), generating points trajectories (Hofmann-Wellenhof, Lichtenegger and Wasle, 2007; Rizos, 2017). For baselines of approximately 20 km, horizontal accuracy values in the order of 50 mm + 5 ppm (with a degradation of a factor of 1.5 - 2 in height) can be achieved approximately (Hofmann-Wellenhof, Lichtenegger and Wasle, 2007).

In the RTK positioning method, carrier-phase measurements are transmitted from the base receiver to the rover receiver and combined in real time to determine the position of the rover during the survey (Hofmann-Wellenhof, Lichtenegger and Wasle, 2007). The two receivers are connected to each other via a wireless data link, for example a data link via radio modem or mobile internet (Rizos, 2017).

A variation of RTK is the Network Real-Time Kinematic (NRTK). In NRTK, a single personal receiver with rover function (a more economical choice) and a network of Continuously Operating Reference Stations (CORS) installed on the territory that the rover connects during the survey (often after subscription), are used to perform the real-time positioning (Rizos, 2017). In addition to the economic aspects, the advantage of NRTK is that the network of CORSs maps the spatially related biases and errors mitigating their effects on the user’s positioning, this also allows operation with distances between receiver and CORSs of 50 - 70 km (Rizos, 2017). Finally, the CORSs services also allow the raw data downloading of CORSs observations, enabling the positioning modes described before, that requires post-processing of the data.

1.2. Time-of-flight detection systems without scanning mechanisms

As mentioned in the introduction and reported subsequently in chapter 3, recently, “depth sensors” promoted as “Time-of-Flight (ToF) depth cameras” for Android or “Light Detection and Ranging (LiDAR) scanners” for iOS are integrated in smartphones and tablets.

Independent of the name under that depth sensors are presented, the detection systems for determining depth, or better distance, work on the basis of the Time-of-Flight principle, so the distance between the detection system and a target object can be calculated by measuring (directly or indirectly) the time that a light wave needs to be emitted by the system, hit the target and return (Hansard *et al.*, 2012; Piatti, Remondino and Stoppa, 2013; Horaud *et al.*, 2016). The ToF principle is also the basis for the functioning of classic LiDAR scanners (e.g. Terrestrial LiDAR Scanner - TLS, Airborne LiDAR Scanner - ALS and Mobile LiDAR Scanner - MLS), that also integrate fast scanning mechanisms such as rotating mirror systems into their design (Piatti, Remondino and Stoppa, 2013; Horaud *et al.*, 2016). However, conventional scanning mechanisms are not compatible with the size of smartphones and tablets, so these devices are instead equipped with ToF detection systems scannerless (in this case, the term “scannerless” refers to the lack of scanning mechanisms such as rotating mirror systems, so the term “LiDAR scanner” for iOS devices remains a valid term since the sensor still performs “scanning”) (Piatti, Remondino and Stoppa, 2013; Horaud *et al.*, 2016; Padmanabhan, Zhang and Charbon, 2019; Gyongy, Dutton and Henderson, 2022). A typical ToF detection system scannerless consists of the following functional blocks: an emitter to generate the light (usually in the infrared spectrum - IR); an optical diffuser that diffuses the emitted light to illuminate the entire scene; a lens to collect the light reflected from the target object that is to be surveyed; a solid-state ToF range sensor consisting of a two-dimensional array of photodetectors, with the function of measuring (directly or indirectly) the time required for the light to hit the target object and return; and finally, a controller to power the system, support data processing and connect to an external processor (Hansard *et al.*, 2012; Piatti,

Remondino and Stoppa, 2013; Horaud *et al.*, 2016). In Fig. 2, the functional diagram of a typical ToF detection system scannerless is shown.

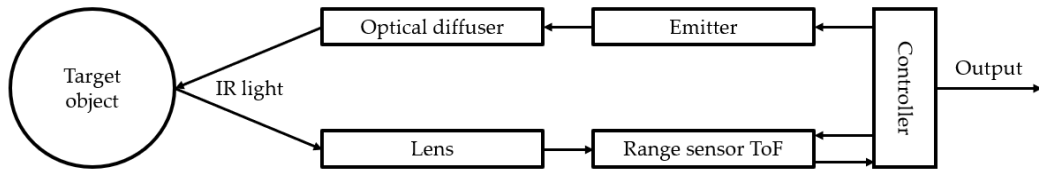


Fig. 2 - Functional diagram of a ToF detection system scannerless (image adapted from: Hansard *et al.*, 2012; Piatti, Remondino and Stoppa, 2013; Horaud *et al.*, 2016).

Based on this general diagram, ToF detection systems scannerless can be divided into pulsed-light and Continuous-Wave (CW). In a ToF detection system scannerless implemented by pulsed-light technology (ToF detection system scannerless pulsed-light), the emitter generates light pulses via a laser or laser diode, the ToF range sensor photodetectors are based on Single-Photon Avalanche Diodes (SPAD) and are integrated with Time-to-Digital Converters (TDC) or time-to-amplitude circuitry (Horaud *et al.*, 2016). Instead, in a ToF detection system scannerless implemented with CW technology (ToF detection system scannerless CW), the emitter generates a sinusoidally modulated continuous light wave via an LED or light-emitting diode, and the ToF range sensor photodetectors independently demodulate the emitted signal (Horaud *et al.*, 2016).

Regarding the measurement of the light ToF, ToF detection systems scannerless can perform direct or indirect measurements.

The Direct Time-of-Flight (DToF) measurement is performed by a high precision stopwatch, synchronised with the emitter and the range sensor ToF of the system, that starts at the moment the light is emitted and stops at the moment it is received, the measured time corresponds to the ToF of the light (Charbon *et al.*, 2013; Piatti, Remondino and Stoppa, 2013). The DToF measurement is applied by ToF detection systems scannerless pulsed-light (Horaud *et al.*, 2016), the equation for computing the distance D , between the detection system and the target object, assumes the form (Charbon *et al.*, 2013; Piatti, Remondino and Stoppa, 2013):

$$D = \frac{1}{2} \cdot c \cdot \tau_{ToF} \quad (11)$$

where, c is the speed of light and τ_{ToF} is the measure of the time required for light to travel.

In Indirect Time-of-Flight (IToF) measurement, the ToF of light is determined indirectly by measuring the phase difference between the continuous signal of the emitted sinusoidal light wave and the received signal (Charbon *et al.*, 2013; Piatti, Remondino and Stoppa, 2013). In an IToF measurement, the stopwatch is replaced by time gated photons counters or charge integrators (Piatti, Remondino and Stoppa, 2013). The ToF detection systems scannerless CW apply IToF measurements (Horaud *et al.*, 2016); assuming now a detection system with four photon counters, the equation for computing the distance D assumes the form (Charbon *et al.*, 2013; Piatti, Remondino and Stoppa, 2013; Horaud *et al.*, 2016):

$$D = \frac{c}{4\pi f} \cdot \phi_{ToF} = \frac{c}{4\pi f} \cdot \arctan\left(\frac{C_3 - C_1}{C_0 - C_2}\right) \quad (12)$$

where, in addition to terms already defined, f is the modulation frequency, ϕ_{ToF} is the phase shift measurement and (C_0, C_1, C_2, C_3) correspond to the counted photons.

The outputs of a ToF detection system scannerless are primarily depth maps (3D images where each pixel is associated with a depth value) and, through rendering in a 3D space, depth maps can be transformed into classic 3D point clouds (Li, 2014; Horaud *et al.*, 2016).

Concerning the Android ToF cameras and the iOS LiDAR scanners integrated into mobile devices, as reported in (Bookhahn *et al.*, 2021), the Android devices integrate ToF detection systems scannerless CW that perform IToF measurements, whereas the iOS devices integrate ToF detection systems scannerless pulsed-light that perform DToF measurements.

In general, the accuracy of the depth measurement of ToF detection systems depends on several factors, such as the nature of the surfaces, and can range from a few centimetres to several metres (Horaud *et al.*, 2016). Therefore, the performances of

depth sensors for smartphones and tablets were specifically evaluated in chapters 3 and 5 of the thesis.

1.3. The single beam echo sounders

Regarding the possibility of surveying in operative water scenarios, the set of sensors integrated on smartphones and tablets can be expanded through Single Beam Echo Sounders (SBES) that can be connected to mobile devices.

The SBES is a type of Active SOund NAVigation and Ranging (sonar) system (Kuperman and Roux, 2014). A main application of SBES is the mapping of underwater bottoms by the serial determination of the distance (depth) between the water surface and the bottom (Kuperman and Roux, 2014). In particular, SBES computes the water depth by measuring the time required for a sound wave to hit the underwater bottom and travel back in the form of an echo (International Hydrographic Organization, 2011; Kuperman and Roux, 2014).

The SBES (descendants of military sonars) were the first echo sounding instruments produced, and despite their simplicity and the existence of newer, more advanced instruments (e.g. Multibeam echo sounders and Side-Scan Sonars), they still represent the traditional devices for surveying the underwater bottom (International Hydrographic Organization, 2011; Kuperman and Roux, 2014).

The fundamental functional blocks of an SBES are: the transmitter (equipped with an electrical signal generator and an amplifier) that generates the electrical impulse; the first transducer that converts the electrical impulse into an acoustic impulse and emits it towards the water bottom; the second transducer that receives the echo of the acoustic impulse reflected by the bottom and converts it into an electrical impulse; the receiver whose main tasks are the amplification of the received electrical impulse in function of time (Time Varying Gain-TVG) and the conversion of the electrical impulse into a digital signal; and finally the microprocessor that processes the digital signal to determine the depth and produce the output (Medwin and Clay, 1997; International Hydrographic Organization, 2011). Fig. 3 shows the functional diagram of an SBES. The transmission-receive cycle is initialised by a sonar system clock (Medwin and Clay, 1997).

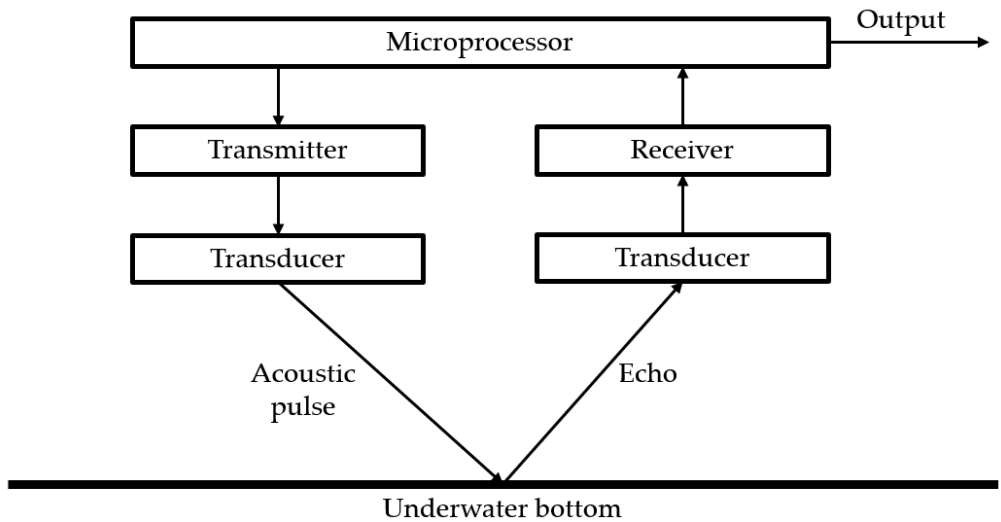


Fig. 3 - Functional diagram of a SBES (image adapted from: Medwin and Clay, 1997; International Hydrographic Organization, 2011).

The proposed functional diagram uses two transducers (one for transmission and one for receive), however, it must be remembered that many echo sounders can also use a single transducer, with an automatic transmit/receive switch, that allows the transducer to perform both transmit and receive functions (Medwin and Clay, 1997). Based on the functioning principle and components, transducers can be of three types: piezoelectric, magnetostrictive and electrostrictive (International Hydrographic Organization, 2011). The piezoelectric transducers consist of two plates with a layer of quartz crystals in between; due to the piezoelectric effect, the application and alteration of an electrical potential between the plates produces a vibration of the quartz crystals, and vice versa if the crystals are compressed mechanically, an electrical potential difference is generated (International Hydrographic Organization, 2011). The magnetostrictive transducers consist of an iron shaft and a nickel coil; the flux of an electric current generates a magnetic field in the coil, which contracts and expands, generating a vibration (International Hydrographic Organization, 2011). Finally, electrostrictive transducers also work by piezoelectric effect, but are built with ceramic or polymer materials that are polarised during the production phase (International Hy-

drographic Organization, 2011). As reported by the International Hydrographic Organization (2011) most of the transducers used today are electrostrictive transducers. In a SBES, the equation for determining the water depth Z assumes the form (Jones, 1999; International Hydrographic Organization, 2011):

$$Z = \frac{1}{2} \cdot \bar{v}_{sound} \cdot \tau_{SBES} \quad (13)$$

where, τ_{SBES} is equal to the time interval between transmission of the sound wave and reception of the echo and \bar{v}_{sound} is the mean vertical velocity of sound in water. The speed of sound in water is a function of temperature, salinity and pressure, which in turn is a function of depth (Kuperman and Roux, 2014). The speed of sound v_{sound} can be determined with empirical formulae such as that given by (Medwin, 1975):

$$v_{sound} = 1449.2 + 4.6T - 0.055T^2 + 0.00029T^3 + (1.34 - 0.010T) \cdot (S - 35) + 0.016Z \quad (14)$$

where, v_{sound} is expressed in m/s (with an accuracy of 0.1 m/s), T is the temperature in the range $0 \leq T \leq 35$ °C, S is the salinity in the range $0 \leq S \leq 45$ ‰ and Z is the depth in the interval $0 \leq Z \leq 1000$ m. For near-surface waters, the velocity of sound can vary from 1400 m/s to 1525 m/s, with mean values for the velocity of sound in salt water of 1500 m/s (Morang, Larson and Gorman, 1997; Jones, 1999).

As reported in (Medwin and Clay, 1997), the possibility of processing signals digitally has allowed the realisation of small, inexpensive and sophisticated fishing sonars equipped with pre-programmed processors. As stated at the beginning of this paragraph, some SBES models for fishing can also be connected to smartphones and tablets. As anticipated in the introduction, the performances of these sonars, interactions with mobile devices and the processing of output data were specifically studied and evaluated in chapter 4 of the thesis.

1.4. The photogrammetry and image sensor

Photogrammetry can be defined as the science and technique of measuring, locating, detecting and reconstructing 3D objects and environments using light rays captured from several photographs (or images) of the same scene, acquired at different positions and with a certain overlapping percentage (Yilmaz, Yakar and Yildiz, 2008; Schindler and Förstner, 2014; Tannant, 2015; Förstner and Wrobel, 2016; Granshaw, 2020).

The main product of modern digital photogrammetry, supported by the well-known Structure from Motion and Multi-View Stereo (SfM-MVS) algorithms, is the 3D point cloud (Tannant, 2015). Thus, photogrammetry has several practical applications, such as territory mapping, surveying of artefacts and structures, and metrology (Schindler and Förstner, 2014; Förstner and Wrobel, 2016).

A specific photogrammetry method called “GNSS-aided terrestrial photogrammetry” or “GNSS-assisted terrestrial photogrammetry” was used in the research project (the term “GNSS-aided photogrammetry” will be used in the following). As reported in Forlani *et al.* (2014), in GNSS-aided photogrammetry, by combining a camera with a GNSS receiver, the coordinates of the camera projection centre are determined by the GNSS receiver during the photogrammetric survey photo acquisition phase. Thus, using geolocalised photos, this method can produce automatically scaled and georeferenced 3D point clouds without the use of Ground Control Points (GCPs). GNSS-aided photogrammetry saves time both during survey operations and during the restitution phase and is particularly interesting in those situations where, for whatever reason, the surveyed site is inaccessible (e.g. security) (Jaud *et al.*, 2020).

3D measurements in photogrammetry are based on the mathematical model of central projection, the reference camera model is the pinhole camera, that can also model classic modern digital “frame” cameras (Hassan and Fritsch, 2019). The fundamental equations of photogrammetry are the collinearity equations that express the collinearity condition so that the object point P , image point p and camera projection centre O are aligned (Luhmann *et al.*, 2023). The collinearity equations allow the connection between object space and image space through the transformation between the ob-

ject coordinate system and the camera coordinate system (Hassan and Fritsch, 2019; Luhmann *et al.*, 2023). The collinearity equations assume the form (Hassan and Fritsch, 2019; Luhmann *et al.*, 2023):

$$x_p = x_o - c \cdot \frac{r_{11} \cdot (X_P - X_o) + r_{21} \cdot (Y_P - Y_o) + r_{31} \cdot (Z_P - Z_o)}{r_{13} \cdot (X_P - X_o) + r_{23} \cdot (Y_P - Y_o) + r_{33} \cdot (Z_P - Z_o)} \quad (15)$$

$$y_p = y_o - c \cdot \frac{r_{12} \cdot (X_P - X_o) + r_{22} \cdot (Y_P - Y_o) + r_{32} \cdot (Z_P - Z_o)}{r_{13} \cdot (X_P - X_o) + r_{23} \cdot (Y_P - Y_o) + r_{33} \cdot (Z_P - Z_o)} \quad (16)$$

where,

x_p, y_p : coordinates of image point p;

X_P, Y_P, Z_P : coordinates of object point P;

x_o, y_o : coordinates of the principal point;

X_o, Y_o, Z_o : coordinates of the camera projection centre O in the object coordinates system;

c: camera constant;

r_{ij} : elements of the 3D rotation matrix R.

The 3D rotation matrix R is equal to (Luhmann *et al.*, 2023):

$$R = \begin{bmatrix} r_{11} & r_{12} & r_{13} \\ r_{21} & r_{22} & r_{23} \\ r_{31} & r_{32} & r_{33} \end{bmatrix} \quad (17)$$

where:

$$r_{11} = \cos \varphi \cdot \cos \kappa \quad (18)$$

$$r_{12} = -\cos \varphi \cdot \sin \kappa \quad (19)$$

$$r_{13} = \sin \varphi \quad (20)$$

$$r_{21} = \cos \omega \cdot \sin \kappa + \sin \omega \cdot \sin \varphi \cdot \cos \kappa \quad (21)$$

$$r_{22} = \cos \omega \cdot \cos \kappa - \sin \omega \cdot \sin \varphi \cdot \sin \kappa \quad (22)$$

$$r_{23} = -\sin \omega \cdot \cos \varphi \quad (23)$$

$$r_{31} = \sin \omega \cdot \sin \kappa - \cos \omega \cdot \sin \varphi \cdot \cos \kappa \quad (24)$$

$$r_{32} = \sin \omega \cdot \cos \kappa + \cos \omega \cdot \sin \varphi \cdot \sin \kappa \quad (25)$$

$$r_{33} = \cos \omega \cdot \cos \varphi \quad (26)$$

where, (ω, ϕ, κ) are the angles of rotation of the image with respect to the (X, Y, Z) axes of the object space coordinate system.

In order to reconstruct a 3D scene by measuring the image points of coordinates (x_p, y_p) in 2D photos, the collinearity equations (15) and (16) must be solved with respect to the 3D coordinates of the object point (Luhmann *et al.*, 2023):

$$X_P = X_o + (Z_P - Z_o) \cdot \frac{r_{11} \cdot (x_p - x_o) + r_{12} \cdot (y_p - y_o) - r_{13} \cdot c}{r_{31} \cdot (x_p - x_o) + r_{32} \cdot (y_p - y_o) - r_{33} \cdot c} \quad (27)$$

$$Y_P = Y_o + (Z_P - Z_o) \cdot \frac{r_{21} \cdot (x_p - x_o) + r_{22} \cdot (y_p - y_o) - r_{23} \cdot c}{r_{31} \cdot (x_p - x_o) + r_{32} \cdot (y_p - y_o) - r_{33} \cdot c} \quad (28)$$

Furthermore, since the GNSS-aided photogrammetry method was used in the experimentation, an additional equation expressing the relationship between the GNSS antenna phase centre and the camera projection centre O must be added to equations (27) and (28) (Forlani *et al.*, 2014). Based on the mechanical frames used to join the camera and GNSS receiver and the operational conditions (see chapter 5), the equation is expressed considering (Jaud *et al.*, 2020), in the following form:

$$\begin{bmatrix} X_o \\ Y_o \\ Z_o \end{bmatrix} = \begin{bmatrix} X_{GNSS} \\ Y_{GNSS} \\ Z_{GNSS} \end{bmatrix} - \begin{bmatrix} X_{offset} \\ Y_{offset} \\ Z_{offset} \end{bmatrix} \quad (29)$$

where, in addition to the terms previously defined, $(X_{GNSS}, Y_{GNSS}, Z_{GNSS})$ are the position of the GNSS antenna phase centre and $(X_{offset}, Y_{offset}, Z_{offset})$ are the offset between the GNSS antenna phase centre and the camera projection centre O.

Observing the collinearity equations (27) and (28), it can be seen that the Z coordinate of the object points cannot be calculated with a single photograph, as each image point would correspond to infinite object points (Luhmann *et al.*, 2023). In order to calculate the Z coordinate of the object point, at least two photographs observing

the same scene, acquired from different positions and capturing the same object point, are required (Luhmann *et al.*, 2023).

Concerning the other elements appearing in the collinearity equations (15), (16), (27) and (28), (x_0, y_0, c) are the interior orientation parameters of the camera, they describe the internal geometry of the camera, and can be declared by the manufacturer or can be calculated through camera calibration processes (Luhmann *et al.*, 2023). The elements of the equations (X_0, Y_0, Z_0) and (ω, ϕ, κ) are the exterior orientation parameters of the camera and describe the position and orientation of the camera at the moment of image acquisition (Luhmann *et al.*, 2023). In the GNSS-aided photogrammetry method, the parameters (X_0, Y_0, Z_0) are determined by equation (29) via the knowledge of the GNSS position and the offset between the GNSS antenna phase centre and the camera projection centre O, instead, the parameters (ω, ϕ, κ) are determined in the data post-processing phase during the photogrammetric alignment process via the image Tie Points (Forlani *et al.*, 2014).

In photogrammetry applications where “spherical” digital cameras (also called 360° cameras) and spherical images are used in an equirectangular projection, the collinearity equations can be expressed in the following form (Fangi and Nardinocchi, 2013; Fangi, 2018):

$$\theta = \theta_0 + \vartheta = \theta_0 + \frac{x_p}{r} = \theta_0 + \arctan\left(\frac{(X_P - X_0) + d\alpha_y \cdot (Z_P - Z_0)}{(Y_P - Y_0) - d\alpha_x \cdot (Z_P - Z_0)}\right) \quad (30)$$

$$\varphi = \frac{y_p}{r} = \arccos\left(\frac{-d\alpha_y \cdot (X_P - X_0) + d\alpha_x \cdot (Y_P - Y_0) + (Z_P - Z_0)}{\sqrt{(X_P - X_0)^2 + (Y_P - Y_0)^2 + (Z_P - Z_0)^2}}\right) \quad (31)$$

where,

x_p, y_p : coordinates of image point p;

X_P, Y_P, Z_P : coordinates of object point P;

X_0, Y_0, Z_0 : coordinates of the centre O of the spherical image;

r: radius of the spherical image;

ϑ, ϕ : longitude and latitude of the point on the spherical image;

θ_0 : spherical orientation angle (zero bearing);

α_x, α_y : correction angles.

As mentioned in the introduction and as will be seen in chapter 5, a smartphone digital camera and a spherical digital camera (a 360° action camera) were used in the research project; furthermore, based on the observations of (Previtali *et al.*, 2023), some particular approaches to GNSS-aided photogrammetry based on video acquisition were applied and investigated.

A camera can be intended as a system for capturing and memorising an image, and if in traditional silver halide cameras the photographic film performs both the task of capturing and memorising images, in modern digital cameras the task of capturing images is performed by the image sensor and the function of memorising images is performed by a specific digital storage device (Toyoda, 2006). Thus, a digital photographic system can be diagrammed through three basic functional blocks: a lens to convey the photons onto the image sensor and form the optical image, the image sensor that captures the image and a digital storage device to memorize the data (Nakamura, 2006; Toyoda, 2006). Fig. 4 shows the functional diagram of digital photographic system.

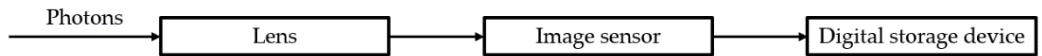


Fig. 4 - Functional diagram of a digital photographic system (image adapted from: Nakamura, 2006; Toyoda, 2006).

Observing the functional diagram, it can be seen that the image sensor is the core of a digital camera. An image sensor is a semiconductor device consisting of a set of photodetectors arranged in orderly rows and columns to form an array (Nakamura, 2006; Zhang *et al.*, 2009). An image sensor “captures images” by converting light into signal charge (electrons or holes), the signal charge is then converted into voltage, which is finally converted into a digital signal through an A/D converter (Nakamura, 2006; Mehta, Patel and Mehta, 2015). The conversion of light to signal charge occurs when a photon flux with an E_{photon} energy level greater than the band gap energy E_{gap} of

the semiconductor enters into the semiconductor, thus respecting the following condition (Nakamura, 2006):

$$E_{\text{photon}} = h \cdot f = \frac{h \cdot c}{\lambda} \geq E_{\text{gap}} \quad (32)$$

where, h is Plank's constant, c is the speed of light, f is the frequency of light and λ represents the wavelength of light. The band gap energy of silicon is 1.1 eV so only light with a wavelength inferior to 1100 nm can be absorbed by the semiconductor and produce the conversion of photons into signal charge (Nakamura, 2006).

Image sensors can be principally of two types: Charge Coupled Device (CCD) and Complementary Metal Oxide Semiconductor (CMOS). Several authors (to which please refer) have studied and compared CCD and CMOS sensors to highlight their differences, performance, advantages and disadvantages (Zhang *et al.*, 2009; Mehta, Patel and Mehta, 2015; RadhaKrishna, Govindh and Veni, 2021). However, currently the CMOS sensor appears to be a high speed signal readout, low power consumption, easy to manufacture and inexpensive, these characteristics have resulted in the CMOS sensor being used, for example, in smartphones and consumer cameras (Mehta, Patel and Mehta, 2015; RadhaKrishna, Govindh and Veni, 2021). In the research project, the cameras used for experimentations are all based on CMOS sensors.

CHAPTER 2. SMARTPHONE GNSS POSITIONING EVALUATION

For your knowledge, the material and research reported in this chapter were previously published in:

Pepe, M., Costantino, D., **Voza, G.** and Alfio, V.S. (2021) '**Comparison of Two Approaches to GNSS Positioning Using Code Pseudoranges Generated by Smartphone Device**', Applied Sciences, 11(11), p. 4787. Available at: <https://doi.org/10.3390/app11114787>.

In 2016, Google enabled smartphones and tablets with Android 7.0 to access GNSS raw measurements. According to the European GNSS Agency (2017), this access has facilitated numerous studies aimed at enhancing the performances of commercial GNSS devices in smartphones and tablets. These improvements primarily involve post-processing measurement techniques.

In their 2020 study, Dabove, Di Pietra and Piras (2020) demonstrated the versatility of raw smartphone measurements in sectors where precise positioning is not essential. They outlined various applications, such as commercial product detection, public protection search and rescue, intelligent transportation systems, healthcare, and environmental monitoring.

Gioia and Borio (2020) highlighted the emerging opportunities in developing navigation algorithms and post-processing methods using raw data from GNSS mobile devices, steering research in this area. They noted that approximately 1900 papers have been published recently, focusing on algorithm development for enhanced positioning (both static and kinematic) and on resolving initial carrier-phase ambiguities to refine positioning precision and accuracy.

2.1. Literature review of the first part of the research project

Zhang *et al.* (2018) proposed an algorithm to enhance GNSS kinematic positioning using a time difference filter. The process involves multiple stages. Initially, GNSS measurement error is estimated using Signal-to-Noise Ratio (SNR) values. This

is followed by the application of a Single Point Positioning (SPP) algorithm and a Single-Point Velocity determination (SPV) algorithm, combined with a Time-Differentiated Phase measurement technique (TDCP), to accurately estimate the velocity of the GNSS system. The final stage involves determining the receiver's position using the Kalman filter.

In 2019, Zhang *et al.* (2019) and Liu *et al.* (2019) aimed to enhance the pedestrian positioning algorithm, proposing a new method. Their findings in kinematic positioning revealed a Root Mean Square (RMS) accuracy of 3 meters horizontally and approximately 5 meters vertically. They noted that these accuracies are achievable with commercial Android devices capable of acquiring continuous and reliable positioning solutions.

Zhang *et al.* (2019) developed the Smart-RTK algorithm for kinematic positioning, incorporating a Doppler-Smoothed-Code (DSC) filter to minimize code measurement noise from smart devices. They also employed a stochastic SNR model to assign weights to observations. The Kalman filter, integrated with a Constant Acceleration (CA) model, was used to estimate kinematic states. In horizontal positioning, the Root Mean Square Error (RMSE) achieved varied according to conditions: 0.3 to 0.6 meters in stationary settings, 0.4 to 0.7 meters for pedestrian movement, and 0.85 meters for walking scenarios.

Guo *et al.* (2020) introduced a temporal differential filter algorithm utilizing the dual-frequency GNSS receiver of the Xiaomi Mi 8. This algorithm resulted in different levels of accuracy depending on the environment. In urban settings under kinematic mode, the Root Mean Square Error (RMSE) was 1.22 meters horizontally and 1.94 meters vertically. In challenging environments like Urban Canyons, the RMSE increased to 1.61 meters for horizontal and 2.16 meters for vertical positioning. In static conditions, the algorithm achieved an RMSE of 1 meter horizontally and 1.5 meters vertically.

Realini *et al.* (2017) conducted a significant study focusing on correcting initial ambiguities to enhance positioning accuracy and precision. They showed that using smart devices like the Nexus 9, decimetre level positioning accuracy can be achieved

through 15 minute rapid-static surveys over a baseline of approximately 8 km, even without resolving the carrier-phase observation ambiguities.

Dabove *et al.* (2019) conducted a comparative study of the Huawei P10+ and the Ublox NEO M8T. The research involved collecting measurements at two different sites and across three observation durations: 10, 30, and 60 minutes. They examined static, kinematic, and Single Point Positioning modes. All results were derived by resolving ambiguities using the “Fix and Hold” method.

Wanninger and Heßelbarth (2020) analysed the positioning quality using a Huawei P30, conducting several GNSS static survey sessions totalling about 80 hours, each lasting 6–12 hours. The experiments were carried out in obstruction-free environments, such as a roof and an open field, to avoid multipath effects. The Huawei P30 could only correct phase ambiguities for GPS L1 carrier-phase observations. The authors divided the data into 280 shorter sessions of 5 minutes or 23 sessions of 60 minutes each. Post-correction, the three-dimensional positioning errors (standard deviation) were approximately 0.04 meters for 5 minute sessions and 0.02 meters for 60 minute sessions. For observations lasting only a few minutes, ambiguity correction was unsuccessful due to poor signal quality.

Gogoi *et al.* (2019) conducted comparative experiments on various smart devices, both outdoors and in an anechoic chamber. They demonstrated that the GNSS measurements of Android devices could be enhanced by stabilizing the C/N0 signal-to-noise ratio and reducing pseudorange measurement noise. Additionally, they highlighted the impact of low-cost hardware components on the positioning errors of smartphone GNSS systems.

Li and Geng (2019) discovered that the C/N0 value of a smart device’s GNSS receiver was 10 dB-Hz lower compared to a low-cost geodetic receiver, particularly at high altitudes where rapid changes occur. They attributed this difference to the smartphone’s GNSS receiver antenna’s inability to reduce multipath effects and its non-uniform gain pattern. This was confirmed by substituting the device’s antenna with an external one. Thus, the embedded antenna in smartphones remains a hurdle in achieving high-accuracy positioning.

Elmezayen and El-Rabbany (2019) researched the capabilities of Precise Point Positioning (PPP) using a dual-frequency smartphone, specifically the Xiaomi Mi 8. They gathered data from the smartphone and a Trimble R9, a geodetic-quality GNSS receiver, in both post-processing and real-time static and kinematic modes. Their findings showed that the Xiaomi Mi 8 could attain decimetric-level accuracy in both post-processing and real-time modes, and metric accuracy in kinematic mode.

Paziewski *et al.* (2021) carried out comprehensive research using data from various devices: two Xiaomi Mi 8s, two Xiaomi Mi 9s, two Huawei P30 Pros, a Huawei P Smart, a Huawei P20, and two geodetic receivers (Topcon NetG5 and Trimble Alloy). They noted a lower C/N0 ratio in smartphones compared to geodetic receivers. Furthermore, they observed that the disparity in C/N0 between smartphones and geodetic receivers widened as the elevation of the tracked satellite increased.

Robustelli, Paziewski and Pugliano (2021) examined the observation quality and assessed the positioning performance of three smartphones—Huawei P30 Pro, Xiaomi Mi 8, and Xiaomi Mi 9—in Single Point Positioning using Code Pseudoranges. They found that the Huawei P30 Pro achieved the most precise positioning in mono frequency (L1/E1/B1/G1) with a horizontal RMS of 3.24 meters. The Xiaomi Mi 8 and Xiaomi Mi 9 recorded RMS errors of 4.14 meters and 4.90 meters, respectively.

2.2. Aims of the first part of the research project


Paziewski *et al.* (2021) and Robustelli, Paziewski and Pugliano (2021) noted that only a limited number of smartphones are capable of producing GNSS raw data with carrier-phase measurements, whereas most enabled devices can generate GNSS raw data with code pseudorange measurements. Accordingly, the first part of the research project focused on exploring the capabilities of smartphone GNSS positioning using only code pseudorange measurements. This initial study conducted a statistical analysis to compare and evaluate two GNSS positioning methods: Differential Global Navigation Satellite System (DGNSS) and Single Point Positioning (SPP), with potential applicability to other Android mobile devices.

2.3. Materials and methods of the first part of the research project

2.3.1. Mobile devices, apps and tools

During the experiment, three smartphones were utilized: Xiaomi Mi 10 (Xiaomi Inc., Beijing, China), Oppo Reno4 z 5G (Guangdong Oppo Mobile Telecommunications Corp. Ltd, Dongguan, China), and Huawei P20 Lite (Huawei Technologies Co. Ltd., Shenzhen, China). The primary analysis focused on the Xiaomi Mi 10, detailed in the chapter, while the Oppo Reno4 z 5G and Huawei P20 Lite were used for comparative purposes in the “Evaluations and discussions of the first part of the research project” paragraph. Key features of the Xiaomi Mi 10 are summarized in Tab. 4, and those of the Oppo Reno4 z 5G and Huawei P20 Lite are presented in Tab. A1 in the Annexes.

Tab. 4 - Xiaomi Mi 10 key features.

Device	Xiaomi Mi 10
Image	
Chipset	Snapdragon 865 Qualcomm SDM865
RAM [GB]	8
Original operative system	Android 10 MIUI11
GNSS constellation	GPS, GLONASS, BeiDou, Galileo, QZSS
Frequency	L1/L5
Observations	Code, carrier-phase
Weight [g]	208
Dimensions [mm]	162.58 × 74.8 × 8.96

The GEO++ Rinex Logger app (Geo++ GmbH, Garbsen, Germany) was utilized for collecting GNSS raw data. This app captures smartphone or tablet GNSS measurements and stores them in RINEX (Receiver INdependent EXchange) format. It is compatible with GPS, GLONASS, GALILEO, BeiDou, and QZSS satellite data across L1,

L5, E1B, E1C, E5A frequencies. The output file includes carrier-phase and pseudorange measurements, delta intervals, doppler frequencies, and noise values. Files generated by Geo++ Rinex Logger are readily usable in post-processing software, including open-source options, without additional processing steps (Wübbena *et al.*, 2018).

Regarding the tools used for post-processing the GNSS raw data, in the experimentation, two tools were used: RTKLIB ver. 2.4.2 and CSRS-PPP.

RTKLIB, an open-source software suite for GNSS positioning, was developed by T. Takasu and A. Yasuda. It includes a portable program library and various Application Programs (APs) (Takasu and Yasuda, 2009; Takasu, 2013). This library facilitates essential navigation functions and features algorithms for relative positioning using carrier-phase measurement and ambiguity resolution via LAMBDA (Teunissen, 2006). RTKLIB comprises several applications, as detailed in (RTKLIB: An Open Source Program Package for GNSS Positioning, accessed: 22 October 2023):

1. AP Launcher - RTKLAUNCH;
2. Real-Time Positioning - RTKNAVI;
3. Communication Server - STRSVR;
4. Post-Processing Analysis - RTKPOST;
5. RINEX Converter - RTKCONV;
6. Plot Solutions and Observation Data - RTKPLOT;
7. Downloader of GNSS Data - RTKGET;
8. NTRIP Browser - SRCTBLBROWS.

RTKPOST, a key component of RTKLIB, was predominantly employed for GNSS data post-processing. This tool allows users to upload RINEX files containing observation and navigation data. By inputting observation data in RINEX format along with navigation message files from systems like GPS, GLONASS, Galileo, QZSS, and SBAS, RTKPOST can calculate positioning solutions in several modes. These include Single, DGPS/DGNSS, Kinematic, Static, Moving-Base, Fixed, PPP Kinematic, PPP Static, and PPP Fixed.

CSRS-PPP (Canada, 2013), a web service initiated in October 2003, is provided by the Canadian Geodetic Survey of Natural Resources Canada (NRCan) (Tétreault *et al.*, 2005).

The CSRS-PPP application enables global users to conduct Precise Point Positioning by uploading their RINEX files from single or dual-frequency receivers. Its user-friendly graphical interface allows selection of the processing mode (static or kinematic), the reference frame for output coordinates (NAD83 or ITRF14), and the insertion of an Ocean Tidal Loading (OTL) file. Once processed, the results are delivered directly to the users via email. For data processing, CSRS-PPP utilizes the most accurate ephemerides available at the time:

1. Ultra-fast (± 15 cm) - 90 min;
2. Rapid (± 5 cm) - 24 h;
3. Finals (± 2 cm) - 15 days.

The third version of CSRS-PPP is capable of reaching millimetre-level accuracy for extended observations (over 24 hours) in static mode. For shorter observation periods, such as 1 hour, it typically attains accuracies within a few centimetres (Banville, accessed: 21 December 2020).

2.3.2. First research methodology

The first research was divided into two phases.

The first phase involved multiple observation sessions to gather the necessary GNSS data for assessing smartphone performances. In the second stage, this data was analysed using a static analysis method to evaluate the performances in question. These two phases, “Smartphone GNSS data collection” and “Smartphone GNSS data elaboration”, are detailed in the subsequent two paragraphs.

2.3.2.1. Smartphone GNSS data collection

Data collection occurred in static mode over multiple days atop the Politecnico di Bari’s building in Taranto, Italy. The rooftop location provided open sky conditions for observations. The smartphone was placed on the historical vertex of a permanent GNSS network known as FATA (Galeandro *et al.*, 2005) for this purpose. The

FATA point, characterized by known coordinates and devoid of external electromagnetic disturbances, has been monitored for several years.

The GNSS permanent station TARA, used as the base for static DGNSS, is within the HxGN SmartNet (Hexagon AB, Stockholm, Sweden) CORS network (Alkan, Ozulu and İlçi, 2017; Pepe, 2018). During experimentation, TARA had a LEICA GR30 receiver and LEIAS10 antenna, enabling multi-frequency, multi-constellation observations including GPS, GLONASS, Galileo, and BeiDou.

The smartphone was positioned for optimal satellite signal reception, guided by data on its antenna's location. The GNSS permanent station TARA's antenna was about 22 meters away from FATA, where the smartphone was located. Fig. 5 illustrates the positioning of the Xiaomi Mi 10 smartphone and TARA's antenna during data collection. For comparison, other smartphones, Oppo Reno4 z 5G and Huawei P20 Lite, were placed similarly at the same location. The coordinates of TARA and FATA are given in the Annexes, Tab A4.

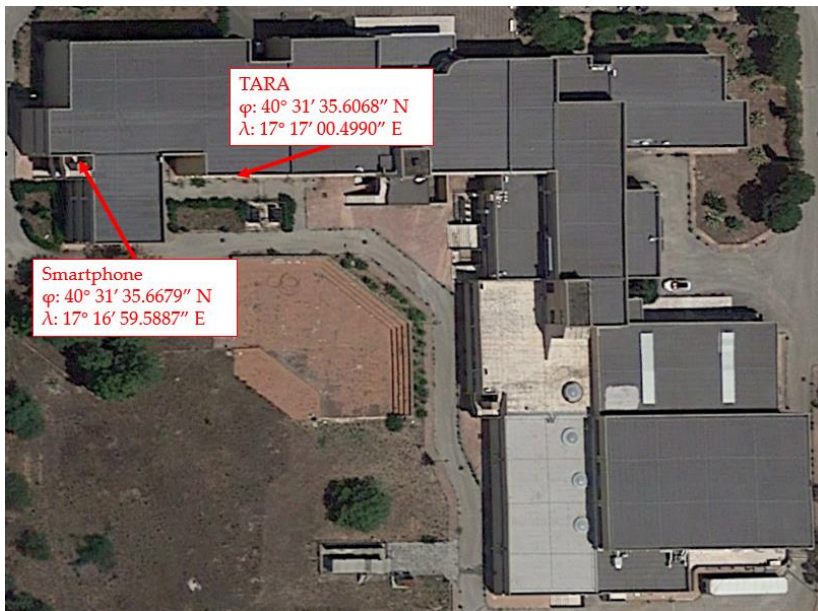


Fig. 5 - Smartphones and the GNSS permanent station TARA position on the roof of the Politecnico di Bari, Taranto, Italy.

2.3.2.2. Smartphone GNSS data elaboration

Data collection occurred on various days to capture different satellite configurations. The first dataset included observations from the initial 5 minutes of each observation hour; the second from the first 10 minutes; the third from 15 minutes; the fourth from 30 minutes; and the fifth spanned a full 60 minutes. RTKPOST and CSRS-PPP processed each observation. RTKPOST used static differential positioning with pseudorange measurements, referencing the TARA GNSS station as the base. CSRS-PPP executed Single Point Positioning on single-frequency code observations, primarily using a rapid ephemeris and switching to a final ephemeris when available. After processing, each observation yielded the Xiaomi Mi 10's positioning coordinates in East ($\bar{E}_{Xiaomi MI10,i}$) and North ($\bar{N}_{Xiaomi MI10,i}$) in the WGS84-UTM system, along with the ellipsoidal height ($\bar{U}_{Xiaomi MI10,i}$) and their respective standard deviations ($\overline{SDE}_{Xiaomi MI10,i}$, $\overline{SDN}_{Xiaomi MI10,i}$, $\overline{SDU}_{Xiaomi MI10,i}$). The results for the sub-datasets of 5, 10, 15, 30, and 60 minutes are then presented:

$$E = \{\bar{E}_{Xiaomi MI10,1}, \dots, \bar{E}_{Xiaomi MI10,n}\} \quad (33)$$

$$N = \{\bar{N}_{Xiaomi MI10,1}, \dots, \bar{N}_{Xiaomi MI10,n}\} \quad (34)$$

$$U = \{\bar{U}_{Xiaomi MI10,1}, \dots, \bar{U}_{Xiaomi MI10,n}\} \quad (35)$$

$$SDE = \{\overline{SDE}_{Xiaomi MI10,1}, \dots, \overline{SDE}_{Xiaomi MI10,n}\} \quad (36)$$

$$SDN = \{\overline{SDN}_{Xiaomi MI10,1}, \dots, \overline{SDN}_{Xiaomi MI10,n}\} \quad (37)$$

$$SDU = \{\overline{SDU}_{Xiaomi MI10,1}, \dots, \overline{SDU}_{Xiaomi MI10,n}\} \quad (38)$$

Using the FATA coordinates (E_{FATA} , N_{FATA} , and U_{FATA}), as a reference, the Xiaomi Mi 10's positioning errors (ΔE_i , ΔN_i , ΔU_i) were calculated using these formulas:

$$\Delta E_i = |\bar{E}_{Xiaomi MI10,i} - E_{FATA}| \quad (39)$$

$$\Delta N_i = |\bar{N}_{Xiaomi MI10,i} - N_{FATA}| \quad (40)$$

$$\Delta U_i = |\bar{U}_{Xiaomi MI10,i} - U_{FATA}| \quad (41)$$

The sub-datasets formed (ΔE , ΔN , ΔU) are structured as follows:

$$\Delta E = \{\Delta E_1, \dots, \Delta E_n\} \quad (42)$$

$$\Delta N = \{\Delta N_1, \dots, \Delta N_n\} \quad (43)$$

$$\Delta U = \{\Delta U_1, \dots, \Delta U_n\} \quad (44)$$

where:

$i = 1, \dots, n$;

the number of observations, n , varies with each dataset's duration: 9 for the 5, 10, and 15-minute datasets, and 7 for the 30 and 60-minute datasets. Thus, for each observation time in DGNS and SPP, ten datasets comprising sub-datasets (E, N, U), (SDE, SDN, SDU), and (ΔE , ΔN , ΔU) can be created:

$$Xiaomi MI 10_{Method, Time} = \{E, N, U, SDE, SDN, SDU, \Delta E, \Delta N, \Delta U\} \quad (45)$$

For sub-dataset (ΔE , ΔN , ΔU), a Shapiro–Wilk normality test can be applied using this formula (Shapiro and Wilk, 1965):

$$W = \frac{(\sum_{i=1}^n a_i x_{(i)})^2}{\sum_{i=1}^n (x_i - \bar{x})^2} \quad (46)$$

where:

$x_{(i)}$ represents the smallest value ($\Delta E_{(i)}$, $\Delta N_{(i)}$, $\Delta U_{(i)}$) in the sub-dataset (ΔE , ΔN , ΔU);
 \bar{x} is the arithmetic mean of the values (ΔE_i , ΔN_i , ΔU_i) in the sub-dataset (ΔE , ΔN , ΔU);
 a_i is defined as:

$$a_i = (a_1, \dots, a_n) = \frac{m' V^{-1}}{(m' V^{-1} V^{-1} m)^{\frac{1}{2}}} \quad (47)$$

where:

$$m' = m_1, \dots, m_n \quad (48)$$

where, m_1, \dots, m_n represent the expected ranks of a standardized random number, and V is the covariance matrix of these ranks.

Using RStudio software (Posit Software, PBC formerly RStudio, PBC, Boston, Massachusetts, USA), the Shapiro–Wilk test can be conducted, providing W and p values. This test assesses the following hypotheses:

- H_0 : the dataset's distribution is normal;
- H_1 : the dataset's distribution is not normal;

Setting a threshold value at 0.05 leads to the following:

- if the p -value > 0.05 , the null hypothesis H_0 is accepted;
- if the p -value < 0.05 , the null hypothesis H_0 is rejected.

The Shapiro–Wilks tests indicate that the sub-datasets of $(\Delta E, \Delta N, \Delta U)$ which conform to normality, follow Gauss's normal distribution:

$$f(x) = \frac{1}{SD\sqrt{2\pi}} e^{-\frac{(x - \bar{x})^2}{2SD^2}} \quad (49)$$

Next, the arithmetic means of the sub-datasets $(\Delta E, \Delta N, \Delta U)$ were determined. This involved calculating the average of all x_i values $(\Delta E_i, \Delta N_i, \Delta U_i)$ within these datasets, using this formula:

$$\bar{x} = \frac{1}{n} \sum_{i=1}^n x_i \quad (50)$$

To detect potential outliers in the sub-datasets, two approaches were used. The first method identified and removed x_i outliers in the sub-datasets $(\Delta E, \Delta N, \Delta U)$ using the Tukey method (Tukey, 1977; Hoaglin, Iglewicz and Tukey, 1986; Kannan, Manoj and Arumugam, 2015).

The method involves identifying two boundaries, a lower fence and an upper fence:

$$\text{Lower Fence} = Q_1 - (1.5 \cdot IQR) \quad (51)$$

$$\text{Upper Fence} = Q_3 + (1.5 \cdot IQR) \quad (52)$$

where:

Q_1 : first quartile;

Q_3 : third quartile;

IQR (interquartile range):

$$IQR = Q_3 - Q_1 \quad (53)$$

This method allows for the removal of x_i values that fall below or above the two fences. As a result, three new sub-datasets (ΔE_{Mm} , ΔN_{Mm} , ΔU_{Mm}) are created. Normality tests were then conducted using equations (46) and (50).

The second method identifies potential outliers x_i using the K-means unsupervised classification algorithm, based on distance-related exclusion criteria (Barai and Dey, 2017). It labels values farthest from the cluster centres as outliers. The K-means algorithm application involves these steps (Yadav and Sharma, 2013; Barai and Dey, 2017):

1. select the number of classes K ($K = 2$);
2. establish a mean cluster centre C_i ($i = 1, 2$) for elements x_i in classes K ;
3. allocate elements x_i to one of the two classes C_i based on the following condition:

$$|x_i - C_i| = \min \quad (54)$$

4. calculate the new cluster centres:

$$C_i = \frac{1}{n} \sum_{i=1}^n x_i \quad (55)$$

5. end the process if clustering remains the same for two consecutive steps. If not, restart from step 2.

Following clustering, three exclusion criteria are applied to the elements x_i of the sub-datasets (ΔE , ΔN , ΔU):

1. if a cluster contains more than two elements ($x_i > 2$), remove the element furthest from the cluster centre, following this condition:

$$|x_i - C_i| = \max \quad (56)$$

2. if a cluster has exactly two elements, neither is removed as they are equidistant from C_i ;
3. if a cluster has only one element, that single element is removed from the sub-dataset.

For sub-datasets with few values, simple exclusion rules are sufficient, but larger datasets require more complex rules (Barai and Dey, 2017). Using the described method, outlier elements x_i are removed, forming three new sub-datasets (ΔE_{km} , ΔN_{km} , ΔU_{km}). Normality tests were then conducted on each using equations (46) and (50). Mean values of all sub-datasets (ΔE , ΔN , ΔU), (ΔE_{Mm} , ΔN_{Mm} , ΔU_{Mm}) and (ΔE_{km} , ΔN_{km} , ΔU_{km}) were compiled, analysed, and compared to assess normal distributions, standard deviations, and positioning errors. Linear regressions were used to explore potential correlations between mean values and observation times. Results from these analyses are presented in paragraph 2.4, with further evaluations and discussions in paragraph 2.5.

2.4. Results of the first part of the research project

2.4.1. Normality test data

This paragraph presents the p-values and tables for sub-datasets tested in the normality assessment.

Tab. 5 shows the results of the normality test for sub-datasets (ΔE , ΔN , ΔU), (ΔE_{Mm} , ΔN_{Mm} , ΔU_{Mm}) and (ΔE_{km} , ΔN_{km} , ΔU_{km}) in DGNSS positioning across five observation times. Using a threshold of 0.05, the sub-datasets that did not meet the normality criteria are ΔE for 5 and 15 minutes, ΔU for 15 minutes, ΔE_{Mm} for 5 minutes, and ΔE_{km} for 5 and 15 minutes.

Tab. 5 - Normality test of DGNSS Positioning Error.

DGNSS sub-dataset normality test, threshold value: 0.05									
Normality Test	ΔE	ΔN	ΔU	ΔE_{Mm}	ΔN_{Mm}	ΔU_{Mm}	ΔE_{Km}	ΔN_{Km}	ΔU_{Km}
p-value 5 min	0.03 NO	0.16 YES	0.42 YES	0.03 NO	0.16 YES	0.30 YES	0.03 NO	0.14 YES	0.14 YES
p-value 10 min	0.37 YES	0.44 YES	0.96 YES	0.56 YES	0.44 YES	0.96 YES	0.16 YES	0.12 YES	0.53 YES
p-value 15 min	0.04 NO	0.59 YES	0.01 NO	0.08 YES	0.59 YES	0.82 YES	0.03 NO	0.61 YES	0.82 YES
p-value 30 min	0.14 YES	0.35 YES	0.24 YES	0.14 YES	0.35 YES	0.24 YES	0.06 YES	0.27 YES	0.05 YES
p-value 60 min	0.31 YES	0.35 YES	0.18 YES	0.31 YES	0.35 YES	0.18 YES	0.09 YES	0.26 YES	0.15 YES

Table 6 details the normality test results for SPP sub-datasets over five observation periods. Using a 0.05 threshold, the sub-datasets failing the test are ΔE for 30 minutes, ΔN for 15 minutes, ΔE_{Km} for 5 minutes, ΔN_{Km} and ΔU_{Km} for 10 and 15 minutes.

Tab. 6 - Normality test of SPP error.

SPP sub-dataset normality test, threshold value: 0.05									
Normality Test	ΔE	ΔN	ΔU	ΔE_{Mm}	ΔN_{Mm}	ΔU_{Mm}	ΔE_{Km}	ΔN_{Km}	ΔU_{Km}
p-value 5 min	0.06 YES	0.35 YES	0.66 YES	0.06 YES	0.56 YES	0.66 YES	0.03 NO	0.42 YES	0.21 YES
p-value 10 min	0.05 YES	0.34 YES	0.32 YES	0.05 YES	0.34 YES	0.78 YES	0.07 YES	0.02 NO	0.02 NO
p-value 15 min	0.25 YES	0.01 NO	0.13 YES	0.77 YES	0.47 YES	0.45 YES	0.54 YES	0.001 NO	0.01 NO
p-value 30 min	0.02 NO	0.36 YES	0.39 YES	0.21 YES	0.90 YES	0.39 YES	0.11 YES	0.09 YES	0.11 YES
p-value 60 min	0.06 YES	0.13 YES	0.51 YES	0.19 YES	0.74 YES	0.24 YES	0.05 YES	0.74 YES	0.24 YES

2.4.2. DGNSS and SPP standard deviations

This paragraph discusses the standard deviations of the sub-dataset (ΔE , ΔN , ΔU) across various observation times and includes linear regression analyses between these standard deviations and the observation durations.

Tab. 7 outlines the standard deviations corresponding to different lengths of DGNSS sessions. Fig. 6 illustrates the trend of standard deviation over time for the (ΔE , ΔN , ΔU) sub-dataset in DGNSS positioning, along with R^2 values for these sub-datasets. The notation “NTNV” in the tables stands for “Normality Test Not Verified”, indicating that values are omitted where the normality test was not validated.

Tab. 7 - Standard deviation metrics for DGNSS sub-datasets: (ΔE , ΔN , ΔU).

Standard deviations DGNSS			
Session Length [min]	ΔE [m]	ΔN [m]	ΔU [m]
5	NTNV	2.87	2.95
10	2.05	1.27	2.83
15	NTNV	2.27	NTNV
30	2.30	1.10	4.08
60	0.76	1.85	3.65

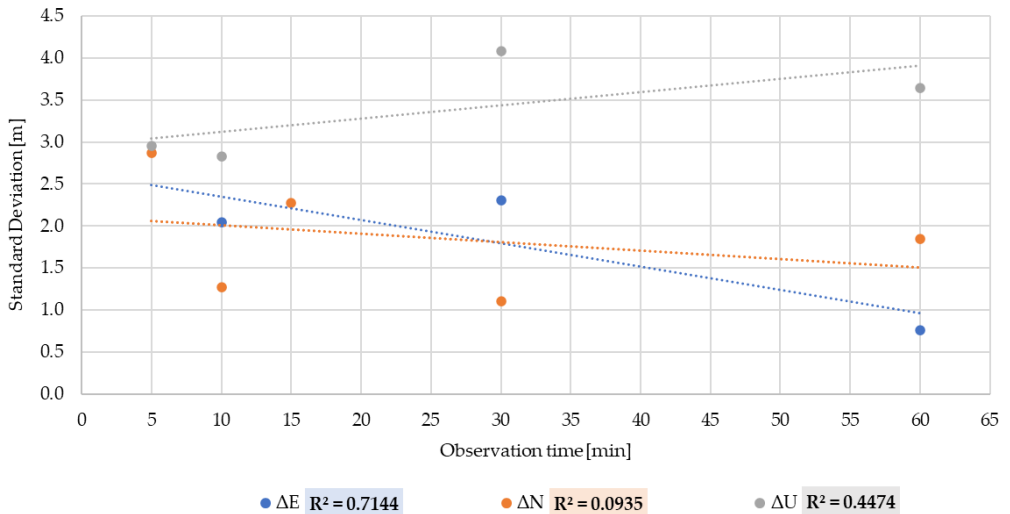


Fig. 6 - Linear regression analysis of DGNSS standard deviations relative to observation time.

Tab. 8 presents the standard deviations for all SPP observations. Fig. 7 depicts the trend of standard deviation over time for the (ΔE , ΔN , ΔU) sub-dataset in Single Point Positioning and includes the R^2 values for these sub-datasets.

Tab. 8 - Standard deviation metrics for SPP sub-datasets: (ΔE , ΔN , ΔU).

Standard deviations SPP			
Session Length [min]	ΔE [m]	ΔN [m]	ΔU [m]
5	1.67	2.16	6.02
10	1.39	1.90	4.92
15	1.29	NTNV	5.39
30	NTNV	1.82	1.43
60	0.79	1.55	1.90

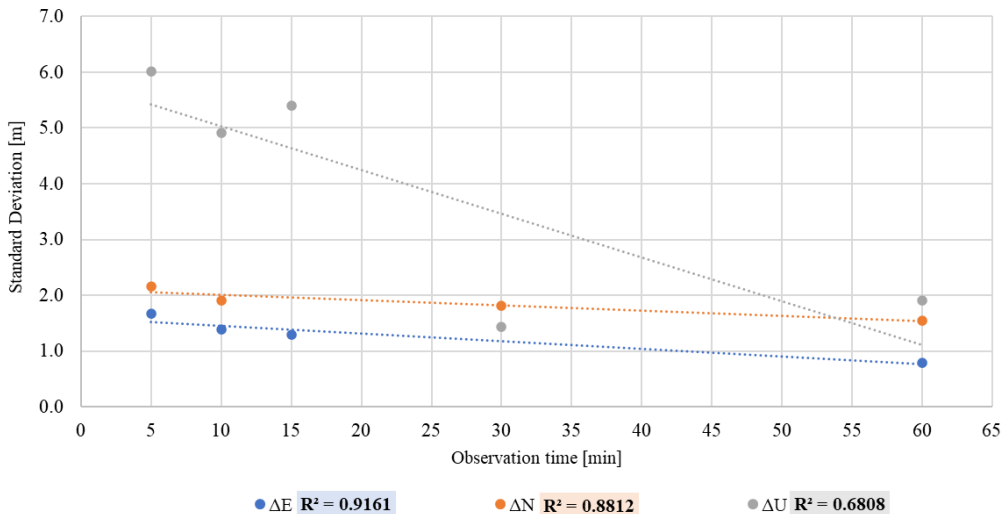


Fig. 7 - Linear regression analysis of SPP standard deviations relative to observation time.

2.4.3. DGNSS positioning and SPP errors

This paragraph details the analyses of GNSS positioning error sub-datasets derived from code pseudorange measurements.

Tabs. 9, 10, and 11 display the means DGNSS positioning errors in East, North, and Up. These means relate to the sub-datasets (ΔE , ΔN , ΔU), (ΔE_{Mm} , ΔN_{Mm} , ΔU_{Mm}) and

(ΔE_{Km} , ΔN_{Km} , ΔU_{Km}). Mean values were omitted in cases where the normality test was not confirmed.

Tab. 9 – Mean East, North, and Up errors in DGNSS Positioning for: (ΔE , ΔN , ΔU).

Mean of East, North and Up positioning errors			
Session Length [min]	ΔE [m]	ΔN [m]	ΔU [m]
5	NTNV	3.150	4.429
10	2.244	2.016	4.468
15	NTNV	2.912	NTNV
30	2.361	2.513	4.880
60	1.875	2.489	3.579

Tab. 10 - Mean East, North, and Up errors in DGNSS Positioning for: (ΔE_{Mm} , ΔN_{Mm} , ΔU_{Mm}).

Mean of East, North and Up positioning errors			
Session Length [min]	ΔE_{Mm} [m]	ΔN_{Mm} [m]	ΔU_{Mm} [m]
5	NTNV	3.150	3.591
10	1.759	2.016	4.468
15	1.471	2.912	3.087
30	2.361	2.513	4.880
60	1.875	2.489	3.579

Tab. 11 - Mean East, North, and Up errors in DGNSS Positioning for: (ΔE_{Km} , ΔN_{Km} , ΔU_{Km}).

Mean of East, North and Up positioning errors			
Session Length [min]	ΔE_{Km} [m]	ΔN_{Km} [m]	ΔU_{Km} [m]
5	NTNV	2.369	4.225
10	2.155	2.070	4.054
15	NTNV	2.700	3.087
30	1.808	2.372	4.651
60	1.698	2.105	3.572

Tab. 12 displays the R^2 values from linear regressions conducted between the means of all DGNSS positioning error sub-datasets and their observation times. Meanwhile, Fig. 8 exemplifies the linear regression between ΔE , ΔN , and ΔU DGNSS positioning errors and observation time.

Tab. 12 – R^2 values from linear regression analysis between mean values of all DGNSS positioning error sub-datasets and observation time.

Linear regression: DGNSS error positioning - observation time									
	ΔE	ΔN	ΔU	ΔE_{Mm}	ΔN_{Mm}	ΔU_{Mm}	ΔE_{Km}	ΔN_{Km}	ΔU_{Km}
R^2	0.6424	0.0616	0.4564	0.1109	0.0616	0.0001	0.8451	0.1352	0.0241

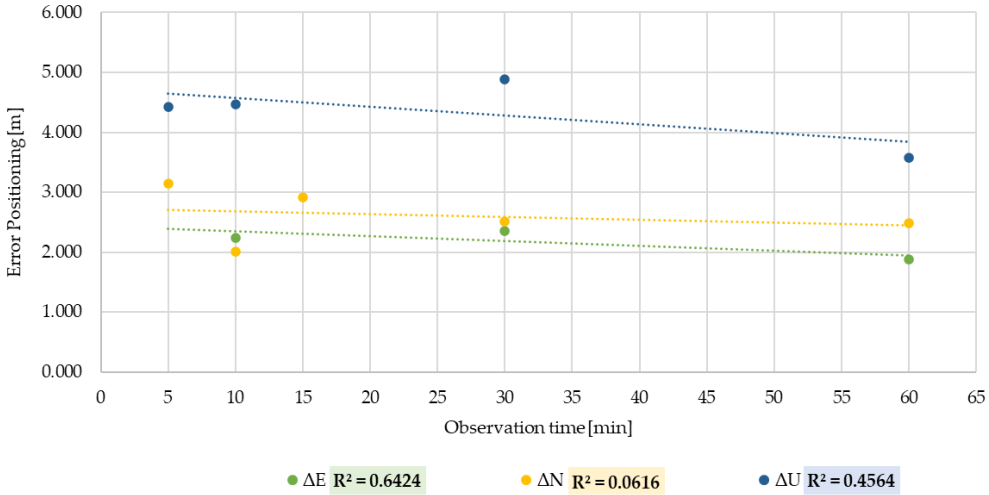


Fig. 8 - Linear regression analysis of ΔE , ΔN , and ΔU DGNSS positioning errors relative to observation time.

The analysis of Single Point Positioning in East, North, and Up is summarized in Tabs. 13, 14, and 15. These tables specifically list the mean values for the sub-datasets (ΔE , ΔN , ΔU), (ΔE_{Mm} , ΔN_{Mm} , ΔU_{Mm}) and (ΔE_{Km} , ΔN_{Km} , ΔU_{Km}). Here too, mean values were omitted when the normality test results were not confirmed.

Tab. 13 - Mean East, North, and Up errors in SPP for: (ΔE , ΔN , ΔU).

Mean of East, North and Up positioning errors			
Session Length [min]	ΔE [m]	ΔN [m]	ΔU [m]
5	1.727	3.795	8.599
10	1.958	3.522	8.862
15	1.644	NTNV	7.512
30	NTNV	2.313	7.111
60	0.700	2.509	5.346

Tab. 14 - Mean East, North, and Up errors in SPP for: (ΔE_{Mm} , ΔN_{Mm} , ΔU_{Mm}).

Mean of East, North and Up positioning errors			
Session Length [min]	ΔE_{Mm} [m]	ΔN_{Mm} [m]	ΔU_{Mm} [m]
5	1.727	3.289	8.599
10	1.958	3.522	8.586
15	1.305	2.577	5.986
30	0.988	1.718	7.111
60	0.439	1.984	5.916

Tab. 15 - Mean East, North, and Up errors in SPP for: (ΔE_{Km} , ΔN_{Km} , ΔU_{Km}).

Mean of East, North and Up positioning errors			
Session Length [min]	ΔE_{Km} [m]	ΔN_{Km} [m]	ΔU_{Km} [m]
5	NTNV	4.106	9.674
10	1.616	NTNV	NTNV
15	1.467	NTNV	NTNV
30	1.004	2.675	7.462
60	0.706	1.984	5.916

Lastly, Tab. 16 presents the R^2 values from linear regressions conducted between the mean values of all SPP error sub-datasets and their observation times. Additionally, Fig. 9 illustrates an example of the linear regression analysis for the sub-datasets ΔE , ΔN , and ΔU in SPP.

Tab. 16 – R^2 values from linear regression analysis between mean values of all SPP error sub-datasets and observation time.

Linear regression: SPP error - observation time									
	ΔE	ΔN	ΔU	ΔE_{Mm}	ΔN_{Mm}	ΔU_{Mm}	ΔE_{Km}	ΔN_{Km}	ΔU_{Km}
R^2	0.9370	0.6576	0.9298	0.8820	0.5806	0.4855	0.9215	0.9383	0.9764

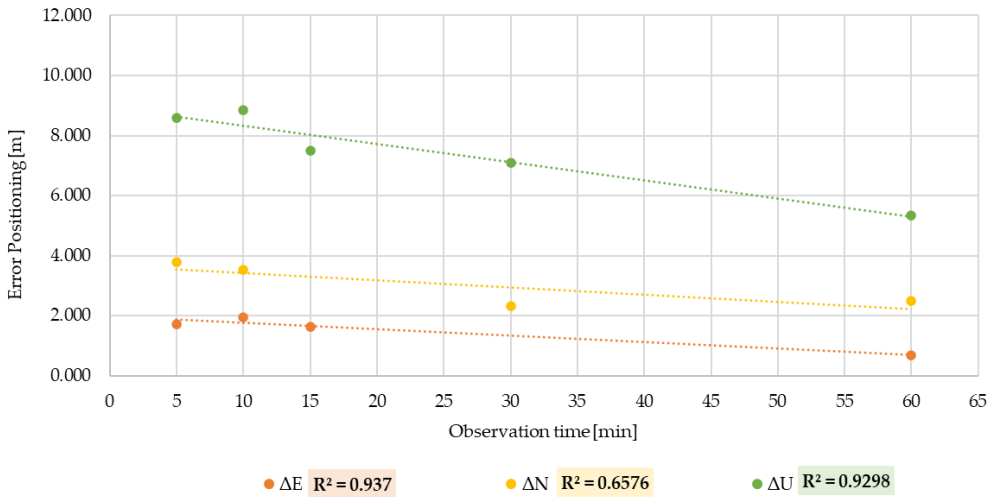


Fig. 9 - Linear regression analysis of ΔE , ΔN , and ΔU SPP errors relative to observation time.

2.5. Evaluations and discussions of the first part of the research project

Reviewing Tabs. 5 and 6, it appears that there is no discernible correlation between the duration of observation time and the success of the normality test for DGNSS positioning and SPP.

Tab. 7 and Fig. 6 show a significant linear relationship between the standard deviation of DGNSS and observation time for ΔE ($R^2 = 0.7144$) (Moore, Notz and Fligner, 2015). Additionally, Annexes (Figs. A1, A2, A3) visually display the relationship between standard deviations and observation times for DGNSS using normal distributions. For SPP, as seen in Tab. 8 and Fig. 7, there is a linear correlation between standard deviations and observation times across all three sub-datasets. ΔE and ΔN exhibit strong correlations ($R^2 = 0.9161$ for ΔE and $R^2 = 0.8812$ for ΔN), while ΔU shows a moderate correlation ($R^2 = 0.6808$) (Moore, Notz and Fligner, 2015). The standard deviation and observation time relationships for SPP are further illustrated in Annexes (Figs. A4, A5, A6).

The study of Tabs. 9, 10, and 11 allows the assessment of the DGNSS mean positioning error. Specifically, the smallest East error ($\Delta E_{Mm} = 1.471$ m) occurred at 15 minutes for the ΔE_{Mm} sub-dataset. This indicates that ΔE_{Mm} 's error does not depend on observation duration; an error of 1.875 m was noted for a 60 minute acquisition.

For the East coordinate at 60 minutes, the highest errors were recorded for ΔE and ΔE_{Mm} , with the smallest being 1.698 m for ΔE_{Km} . In North positioning, the minimum error of 2.016 m occurred at 10 minutes for ΔN and ΔN_{Mm} subsets. However, even with a 60 minute acquisition, the error did not reduce, remaining at 2.489 m for ΔN and ΔN_{Mm} . The smallest up coordinate positioning error, 3.087 m, occurred at 15 minutes for ΔU_{Mm} and ΔU_{Km} . At 60 minutes, ΔU_{Km} 's error was 3.572 m, the least among the three sub-datasets. The largest error at 60 minutes was 3.579 m, observed in both ΔU_{Mm} and ΔU . The study of linear regressions between the DGNS positioning errors of all sub-datasets and observation times (Tab. 12 and Fig. 8) reveals a generally weak relationship, with R^2 values below 0.5 for most sub-datasets. Only ΔE and ΔE_{Km} sub-datasets demonstrate a linear relationship, with R^2 values of 0.6424 (moderate for ΔE) and 0.8451 (strong for ΔE_{Km}).

Tabs. 13, 14, and 15 provide data on the mean error in SPP. For the East coordinate at 60 minutes, the largest error is 0.706 m in the ΔE_{Km} sub-dataset, and the smallest is 0.439 m in ΔE_{Mm} . In North positioning at 60 minutes, the largest error, 2.509 m, occurs in the ΔN sub-dataset. The smallest North error is 1.984 m, found in both ΔN_{Mm} and ΔN_{Km} . At 60 minutes, the largest Up positioning error, 5.916 m, is observed in the ΔU_{Mm} and ΔU_{Km} . The smallest error, 5.346 m, occurs in the ΔU . Analysis of R^2 values (Tab. 16 and Fig. 9) shows the correlation between SPP errors in each sub-dataset and observation time. In contrast to DGNS positioning, SPP generally exhibits a linear relationship between observation time and positioning errors, ranging from moderate to strong. The ΔE , ΔE_{Mm} , and ΔE_{Km} , exhibit the strongest linear relationship between variables, with R^2 values of 0.9370, 0.8820, and 0.9215 respectively. In North positioning, the ΔN_{Km} shows a strong relationship between variables with an R^2 value of 0.9383. However, ΔN and ΔN_{Mm} exhibit a moderate relationship with R^2 values of 0.6576 (ΔN) and 0.5806 (ΔN_{Mm}). The Up sub-dataset ΔU_{Km} shows the better R^2 value at 0.9764, while ΔU also has a notable R^2 value of 0.9298. However, the lowest R^2 value in Up positioning is found in ΔU_{Mm} at 0.4855. This suggests that, at most, a moderate linear relationship exists between variables in Up positioning.

When comparing 60 minute positioning errors, Single Point Positioning is more effective than DGNSS for the East coordinate, while DGNSS outperforms SPP in Up positioning. Additionally, the Annexes (Fig. A7) provide a visual representation of the spatial distribution of errors for both SPP and DGNSS.

The analysis of linear regressions indicates that SPP performance improves with longer observation times.

In this first research, very short baselines (under 1 km) were used to evaluate the fixed error component, ignoring error variation due to distance. However, using a different permanent GNSS station with about 50 km baseline (AVTR, coordinates in Annexes, Tab. A4), it was confirmed that DGNSS positioning errors remain relatively stable with code pseudorange measurements.

The tests with three smartphones—Xiaomi Mi 10, Huawei P20 Lite and OPPO Reno4 Z 5G—revealed similar performance. Positioning errors for these devices were analysed over one, five, and ten minutes. Errors in the range of meters were noted at one minute, which decreased as observation time increased to five and ten minutes. Both SPP and DGNSS solutions were compared.

In conclusion, while smartphone GNSS positioning has significant potential for applications not requiring high accuracy, the results of this initial research indicate that the performance of built-in GNSS receivers in smartphones was inadequate for the applications developed in the continuation of research project. Therefore, chapters 4 and 5 will focus on applications using an external low-cost GNSS receiver and specific smartphone apps for positioning.

CHAPTER 3. SMARTPHONE DEPTH SENSORS EVALUATION

For your knowledge, the material and research reported in this chapter were previously published in:

Costantino, D., **Vozza, G.**, Pepe, M. and Alfio, V.S. (2022) '**Smartphone LiDAR Technologies for Surveying and Reality Modelling in Urban Scenarios: Evaluation Methods, Performance and Challenges**', *Applied System Innovation*, 5(4), p. 63. Available at: <https://doi.org/10.3390/asi5040063>.

Recently, depth-sensing smartphones and tablets entered the market. These devices feature "Light Detection and Ranging (LiDAR) scanners" for iOS and "Time-of-Flight depth cameras" for Android. Initially enhancing photo quality and supporting Augmented Reality (AR) apps, these sensors have also found scientific applications, as indicated in studies by e.g. Mikita *et al.* (2020), Gollob *et al.* (2021), and Luetzenburg, Kroon and Bjørk (2021).

Android smartphones were early adopters of depth sensors and augmented reality technology. The Lenovo Phab 2 Pro, released in 2016, was the first in the market with a ToF camera and AR features. This was followed by releases like the ASUS Zenfone AR in 2017 and the Oppo RX17 Pro and Honor View 20 in 2018. Google's Tango Project, aimed at enhancing AR on Android devices, consisted of depth sensing, motion mapping, and area learning. It used an RGB-D sensor for depth estimation, inertial sensors for motion tracking, and simultaneous localization and mapping (SLAM) technology for precise positioning (Durrant-Whyte and Bailey, 2006; Engelhard *et al.*, 2011; Mikita *et al.*, 2020).

Google discontinued the project in March 2018, likely due to the sensors' limited appeal to general users and their high battery consumption (Mikita *et al.*, 2020).

Also in 2018, Google introduced ARCore. ARCore detects environmental depth without active sensors and is now the primary augmented reality technology on most Android devices.

In 2020, Apple launched the iPad Pro 2020 and iPhone 12 Pro, the first devices with LiDAR scanners. These innovations facilitated research, particularly in scanning and modelling indoor and outdoor environments, as detailed in subsequent literature reviews.

3.1. Literature review of the second part of the research project

Diakit  and Zlatanova (2016) explored the use of the Google Tango Tablet, a developer-focused device, for scanning and modelling building interiors to aid indoor navigation. While the resulting 3D models lacked detail for advanced navigation, basic semantic and topological information could be added through simple data processing. Tomařt k *et al.* (2017) utilized Google Tango technology for forest inventory, employing the Lenovo Phab 2 Pro to scan three distinct tree test areas with a radius of 12.62 m, varying in age and species composition. The scans produced point clouds of tree stems, demonstrating a Root Mean Square Error (RMSE) in Diameter at Breast Height (DBH) below 0.02 m.

Hyypp  *et al.*, (2018) conducted a study measuring tree stem diameters using the Lenovo Phab 2 Pro. They compared the diameters of 121 tree stems measured traditionally with those obtained from the Lenovo device's point clouds. The results from the Lenovo Phab 2 Pro aligned closely with traditional methods, showing an RMSE of 0.0073 m and a mean bias of 0.003 m.

Mikita *et al.* (2020) utilized a Xiaomi Mi 8 with ARCore to survey and model two boulders in the Treb tcko Nature Park. The models they generated were closely accurate, with discrepancies from reference models (created by Terrestrial Laser Scanning) under 6 cubic meters for volume and 2 square meters for area.

Tsoukalos, Drosos and Tsohis (2021) experimented with using ARCore and EasyAR, a commercial augmented reality application, to detect a 12 square meter room. The results did not meet their expectations, leading them to suggest enhancements for better 3D models. These improvements included adopting a depth recognition API, like the DepthAPI recently introduced on some Android devices, and the integration of LiDAR sensors.

Vogt, Rips and Emmelmann (2021) explored the ability of Apple devices, particularly the iPad Pro with its LiDAR scanner and TrueDepth technology, to scan small objects like variously shaped LEGO bricks. They compared these scans with those from an industrial 3D scanner, the Artec Space Spider. Their findings indicated that while the industrial scanner outperformed in accuracy, the smartphone's scanning capabilities could be adequate for certain applications.

Spreafico *et al.* (2021) conducted research on the large-scale 3D mapping capabilities of the iPad Pro's LiDAR sensor, with a focus on architectural survey applications. They scanned an outdoor emergency staircase attached to a historic building. The point cloud obtained from the iPad Pro demonstrated a precision of 0.02 meters and an accuracy of 0.04 meters, proving suitable for architectural mapping at a 1:200 scale.

Riquelme *et al.* (2021) utilized an iPhone 12 Pro to scan a 26 meter cretaceous marlstone and limestone rock face, mechanically excavated, and extracted rock discontinuities from the resulting point cloud. Their research found that the optimal scanning distance for rocks with the iPhone 12 Pro is under 3 meters. Based on these findings, they underscored the device's significant potential in detecting rocky slopes.

Luetzenburg, Kroon and Bjørk (2021) examined the precision of the iPad Pro 2020 and iPhone 12 Pro LiDAR scanners in mapping large natural structures, assessing their utility in geosciences. They conducted a 3D survey and reconstruction of the Roneklint cliff in Denmark, a 130 meter long cliff with an average height of 10 meters. The 3D model created using the iPad Pro 2020 and iPhone 12 Pro LiDAR scanners achieved an accuracy of 0.1 meters.

Gollob *et al.* (2021) employed the iPad Pro LiDAR scanner for forest inventory tasks. They reported a data acquisition time of about 7.51 minutes for each sample plot with a radius of 7 meters. The study achieved a 97.3% detection rate for trees with a DBH under 10 cm, and the most accurate DBH measurement had a RMSE of 0.0313 meters.

Tavani *et al.* (2022) evaluated the iPhone 12 Pro's suitability for geoscience applications as an alternative to traditional geological tools. They assessed the device's

GNSS, IMU, magnetometer, cameras, and LiDAR scanner. Their findings indicated that the LiDAR scanner is particularly effective for less demanding tasks, including geoheritage documentation and the creation of educational materials.

3.2. Aims of the second part of the research project

Literature review shows that research on smartphone depth sensors typically concentrates on one device type. There's a distinct separation between studies on Android and Apple depth sensors, with a notable absence of comparative research between the two platforms. Additionally, recent years have seen a decline in research on Android ToF cameras, despite the development of new applications utilizing ToF technology.




The ToF cameras on Android devices and LiDARs on iOS show promise as effective sensors systems for data collection, surveying, and 3D reconstruction of objects and environments. In light of this, the second research evaluated the performance of depth sensors on both Android and iOS devices. This part also established a method for examining point clouds generated in various urban environment case studies.

3.3. Materials and methods of the second part of the research project

3.3.1. Smartphones, tablet and apps for 3D scanning

The experiment involved: the Huawei P30 Pro (Huawei Technologies Co. Ltd., Shenzhen, China), iPhone 12 Pro, and iPad 2021 Pro (both from Apple Inc., Cupertino, California, USA). These devices were chosen to represent the most advanced depth sensor solutions for Android and iOS operating systems at the time of the study. Tab. 17 details the technical specifications of these three devices.

Tab. 17 – Key technical specifications of the smartphones and tablet utilized in the experiment.

Device	Huawei P30 Pro	iPhone 12 Pro	iPad 2021 Pro
Image			
Chipset	Huawei HiSilicon Kirin 980	Apple A14 Bionic	Apple M1
RAM [GB]	8	6	8
Original operative system	Android 9 EMUI 9.1 Pie	iOS 14	iOS 14
Digital camera [MP]	40 + 20 + 8	12 + 12 + 12	12 + 10
Aperture Size	F 1.6 + F 2.2 + F 3.4	F 1.6 + F 2.4 + F 2	F 1.8 + F 2.4
Depth sensor	Sony IMX316 (ToF)	Sony IMX590	Sony IMX590
GNSS Constellation	GPS, GLONASS, BeiDou, Galileo, QZSS	GPS, GLONASS, BeiDou, Galileo, QZSS	GPS, GLONASS, BeiDou, Galileo, QZSS
Frequency	L1/L5	L1/L5	L1/L5
Inertial sensors	Accelerometer, gyroscope, magnetometer	Accelerometer, gyroscope, magnetometer	Accelerometer, gyroscope, magnetometer
Weight [g]	191	189	466
Dimensions [mm]	158 × 73 × 8	146.7 × 71.5 × 7.4	247.6 × 178.5 × 5.9

The 3D Live Scanner Pro app (Lubos Vonasek Programmierung) was employed for scanning with the Huawei P30 Pro. This app facilitates both indoor and outdoor scanning on Android devices equipped with augmented reality. Smartphones with a depth sensor capture finer details, accurately calculate depth, and produce precise 3D scans with well-defined contours. The app's maximum point cloud resolution is 2 centimetres.

The 3D Scanner App™ (Laan Labs) was utilized for 3D scanning with the iPhone 12 Pro and iPad 2021 Pro. This application creates 3D models using iOS LiDAR data and

photographs. It offers two scanning resolutions: low resolution (approximately 1.5 cm) and high resolution (1 cm).

3.3.2. *Second research methodology*

The methodology for this second experiment comprised two primary stages: conducting 3D surveys using smartphones and tablets, and analysing the resulting point clouds.

The first phase of this experiment involved conducting 3D surveys to acquire point clouds of selected objects. To assess the quality of these point clouds across different objects, four case studies were examined. Scans were carried out using the three mobile devices and the applications outlined in section 3.3.1. The Huawei P30 Pro scans were executed at a 2 cm resolution, whereas the iPhone 12 Pro and iPad 2021 Pro scans were performed at resolutions of 1.5 cm and 1 cm, respectively.

The second phase involved segmenting the point clouds to isolate the scanned objects. These point clouds were then analysed using mathematical descriptors to determine the quality of the 3D models. Additionally, visual analysis was conducted to detect anomalies in the point clouds. CloudCompare software (DF R&D/TELECOM ParisTech ENST-TSI, Paris, France) (Girardeau-Montaut, 2016) was employed for this data analysis.

The subsequent paragraphs (3.3.2.1 and 3.3.2.2) will provide detailed descriptions of both phases

3.3.2.1. *3D survey by smartphones and tablet*

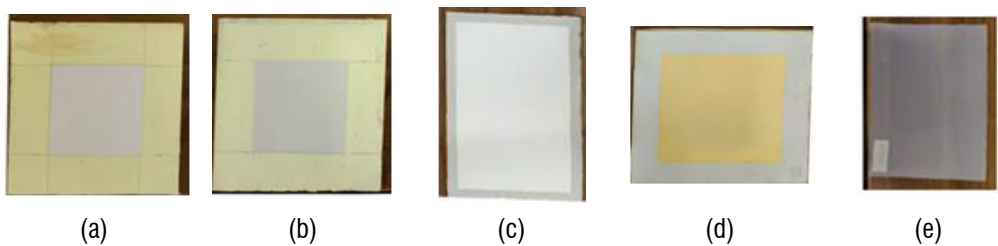
The first phase involved conducting 3D surveys of various elements in both indoor and outdoor scenarios. Specifically, four test/case studies were studied.

The initial case study concentrated on scanning building material samples. This test aimed to assess the performance of depth sensors in controlled laboratory conditions with minimal sensor movement. It was conducted at the Geomatics Laboratory of the Politecnico di Bari, located in Taranto, Italy. Various building material samples were selected for 3D acquisition. In this test, albedo was the key parameter characterizing the materials. The measurement of albedo is detailed in the study by Costantino, Pepe

and Angelini (2021). For the experimentation, mobile devices were positioned directly on top the samples for scanning, with minimal movement. Scans occurred at 0.5 m and 1.5 m distances, using 2 cm resolution on Android, and 1.5 cm and 1 cm on iOS. This process created 6 unique point clouds per sample by varying distances and resolutions. With 10 samples, the dataset included 60 point clouds, each differing in distance, resolution, and material type. Tab. 18 details each sample's dimensions, area, material, and albedo. Fig. 10 provides a visual summary of the samples scanned.

Tab. 18 – Characteristics of the material samples

Sample Material	Dimensions [m]	Area [sqm]	Albedo
Smooth cement plaster	$0.4 \times 0.45 \times 0.05$	0.180	0.514
Raw cement plaster	$0.4 \times 0.45 \times 0.05$	0.180	0.524
White lime plaster	$0.505 \times 0.365 \times 0.01$	0.184	0.518
Coloured lime plaster	$0.525 \times 0.47 \times 0.01$	0.247	0.510
Tetrafluoroethylene (TFE)	$0.245 \times 0.19 \times 0.001$	0.046	0.455
Methacrylate (PMMA)	$0.305 \times 0.12 \times 0.005$	0.037	0.433
High-density polyethylene (HDPE)	$0.23 \times 0.22 \times 0.002$	0.051	0.623
Frosted glass	$0.3 \times 0.3 \times 0.005$	0.090	0.517
Steel	$0.205 \times 0.3 \times 0.008$	0.061	0.606
Brass	$0.105 \times 0.303 \times 0.009$	0.032	0.661



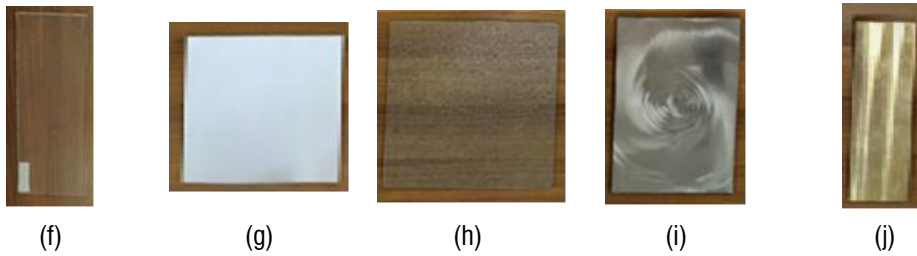


Fig. 10 - Collection of building samples: (a) smooth cement plaster; (b) raw cement plaster; (c) white lime plaster; (d) coloured lime plaster; (e) tetrafluoroethylene (TFE); (f) methacrylate (PMMA); (g) high-density polyethylene (HDPE); (h) frosted glass; (i) steel; (j) brass.

For the second test, a public garden statue was scanned to examine the impact of sensor movement on 3D acquisition quality. This test took place in Villa Peripato's public gardens in Taranto, Italy (coordinates - ϕ : 40° 28' 20" N; λ : 17° 14' 80" E). A statue depicting an animal was the focus of the scan (see Fig. 11a). Scans were conducted in concentric circles around the statue at 2 m and 3 m distances. The mobile devices used were kept parallel to the statue, operating at 2 cm resolution on Android and 1.5 cm on iOS. The test produced a dataset of four point clouds, each varying in acquisition distance and resolution.

The third test involved scanning a room in the geomatics laboratory (Herban *et al.*, 2022 - see Fig. 11b) to assess depth sensor performance in interior object scanning. The room, a simple rectangular box, measures $4.85 \times 4.15 \times 2.95$ m and contains three cabinets and an air conditioner. For the test, windows were covered with paper sheets. Surveys included walls, floor, and ceiling, using resolutions of 2 cm on Android, and 1.5 cm and 1 cm on iOS. This process resulted in a dataset of three point clouds.

In the fourth test, Doric column bases at an archaeological site were scanned to evaluate sensor performance on complex free-form objects. The site, located in Taranto, Italy's historic centre (coordinates - ϕ : 40° 28' 26" N; λ : 17° 13' 59" E), features two complete Doric columns and a third's remains, including a base and three column drums, dating back to the 6th century BC (see Fig. 11d). The test focused on scanning the third column's remains (Fig. 11c), using concentric circles around the column at various distances. The aim was to capture detailed 3D scans using mobile

devices at resolutions of 2 cm on Android, and 1.5 cm and 1 cm on iOS. This method produced a dataset of three point clouds.



(a)



(b)



(c)



(d)

Fig. 11 – Elements scanned for second, third and fourth test - case study: (a) statue representing an animal; (b) room scanned; (c) remains of the Doric column; (d) overview of the Doric columns of Taranto.

3.3.2.2. Depth sensors point clouds analysis and elaboration

During the second phase, the point clouds underwent segmentation to isolate the experimental object. Post-segmentation, the point clouds were examined using mathematical descriptors. The geometric characteristics of a point cloud are ascer-

tainable by applying Principal Component Analysis (PCA) to the covariance matrix C of the neighbourhood p_{i_j} of a point \bar{p} of a set of points N_p . This covariance matrix C , defined in equation 57, acts as a three-dimensional tensor that contains the geometric data of the point set N_p in the neighbourhood p_{i_j} (Pauly, Gross and Kobbelt, 2002; Farella, Torresani and Remondino, 2019):

$$C = \begin{bmatrix} p_{i_1} & -\bar{p} \\ \dots & \dots \\ p_{i_k} & -\bar{p} \end{bmatrix}^T \cdot \begin{bmatrix} p_{i_1} & -\bar{p} \\ \dots & \dots \\ p_{i_k} & -\bar{p} \end{bmatrix}, i_j \in N_p \quad (57)$$

where,

\bar{p} : centroid of a neighbourhood p_{i_j} , of a set of points N_p (Fig. 12).

Considering an eigenvector problem, it can be written:

$$C \cdot v_l = \lambda_l \cdot v_l, l \in \{1, 2, 3\} \quad (58)$$

The covariance matrix C is symmetric and positive semidefinite. Through Principal Component Analysis, three eigenvalues $\lambda_1, \lambda_2, \lambda_3$ can be extracted from this matrix (Jolliffe, 1990). These eigenvalues provide a local description of the 3D structure of the point set N_p and measure its variation along the directions of the corresponding eigenvectors v_1, v_2, v_3 (refer to Fig. 12).

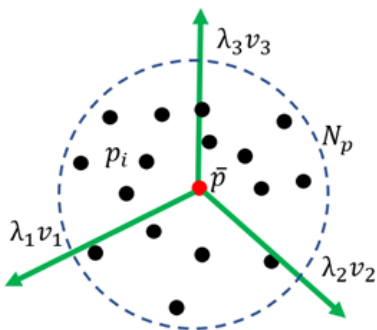


Fig. 12 – Neighbourhood and covariance analysis (image adapted from: Pauly, Gross and Kobbelt, 2002).

Mathematical operations involving the three eigenvalues enable the calculation of specific mathematical descriptors known as covariance-features or eigenfeatures. These descriptors effectively represent certain geometric aspects of the point cloud. Examples from existing literature include linearity, planarity, anisotropy, omnivariance, eigentropy, surface variation, and sphericity (Pauly, Gross and Kobbelt, 2002; Hackel, Wegner and Schindler, 2016; Farella, Torresani and Remondino, 2019). In the experimentation, the eigenfeatures of planarity, omnivariance, and surface variation were selected for analysing point clouds based on their shape (the so called eigenfeature analysis). The equations for these three descriptors are:

$$\text{Planarity } P_\lambda = \frac{\lambda_2 - \lambda_3}{\lambda_1} \quad (59)$$

$$\text{Omnivariance } O_\lambda = (\lambda_1 \cdot \lambda_2 \cdot \lambda_3)^{\frac{1}{3}} \quad (60)$$

$$\text{Surface Variation } SV_\lambda = \frac{\lambda_3}{\lambda_1 + \lambda_2 + \lambda_3} \quad (61)$$

Planarity measures how much a point cloud aligns with plane surfaces. It is useful for characterizing point clouds of planar objects or those comprising multiple planes. Consequently, planarity served as a key descriptor for analysing the 10 samples in the first test and the room in the third test.

Omnivariance assesses the point cloud's inhomogeneity across three dimensions. This descriptor is suitable for analysing freeform objects' point clouds. In this research's second part, omnivariance was applied to the statue in the second test and the column remains in the fourth test.

Surface variation quantifies changes perpendicular to a point cloud's surface. As Pauly, Gross and Kobbelt (2002) demonstrated, it helps identify adjacent, overlapping point clouds at a certain distance (see Fig. 13a). Figure 13b illustrates the descriptor on two flat, adjacent point clouds with overlapping corners (the orange ellipse highlights the overlapping areas identified by surface variation). Therefore, surface variation was employed in all four case studies to detect and attempt to quantify the phenomenon of smartphone point cloud surface splitting.

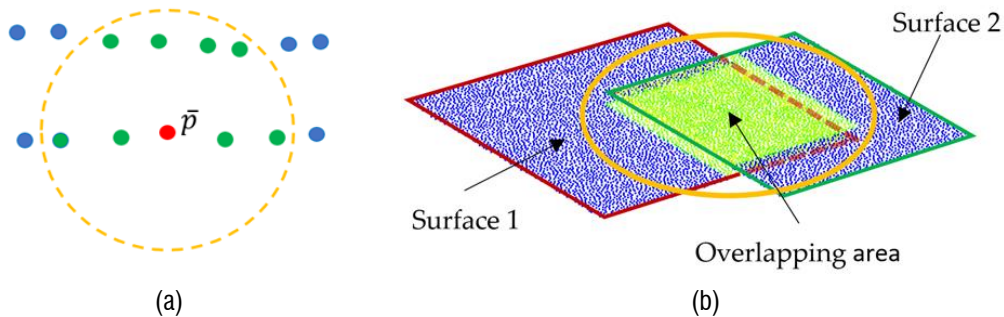


Fig. 13 – Surface variation descriptor: (a) surface variation functioning (image adapted from: Pauly, Gross and Kobbelt, 2002); (b) example of surface variation application in a generic case.

A visual examination of the point clouds was conducted to validate and visually emphasize anomalies and issues in the scans. This analysis involved slicing the point clouds at critical areas identified by the scalar field from the prior eigenfeature analysis, simplifying and enhancing the visual evaluation.

3.4. Results of the second part of the research project

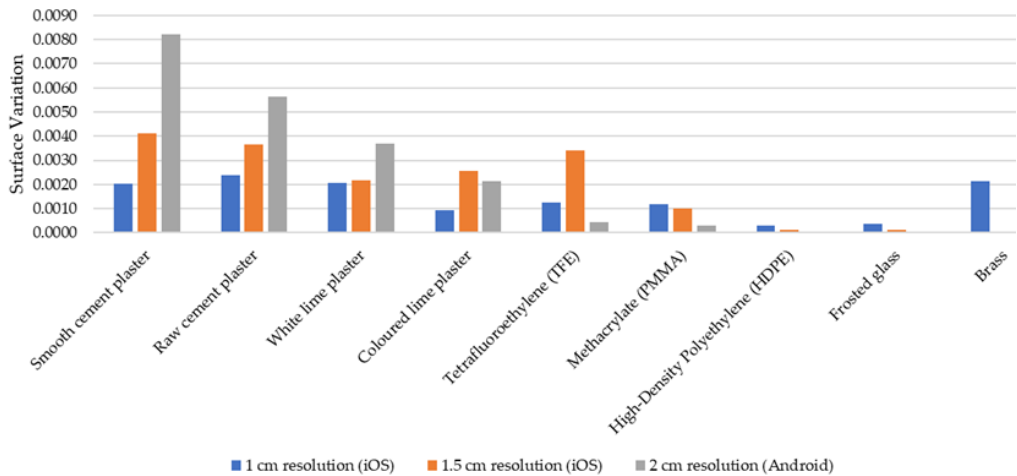
This paragraph presents the results from analysing data in the four case studies. The next section, 3.5, will cover the evaluation and discussion of these results. The findings are further divided into two sub-sections: one focuses on laboratory tests, and the other on field tests conducted under real conditions. As the LiDAR depth sensor in iOS devices (iPhone 12 Pro and iPad 2021 Pro) is identical (see Tab. 17), the discussion will centre on the most notable point clouds from these two devices.

3.4.1. Laboratory testing of depth sensors

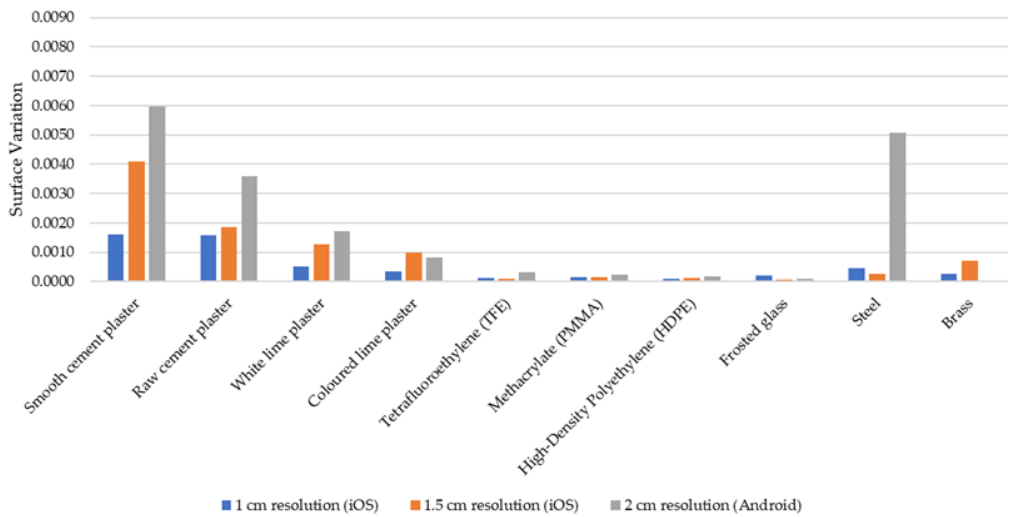
In the first test, 10 building material samples were scanned. Selected point clouds captured at 1 cm resolution and 0.5 m distance are included in the Annexes (see Fig. A8).

The mean surface variation and planarity values were computed for the 60 point clouds derived from these scans. Tables displaying these values are located in the Annexes (Tabs. A2 and A3). For easier review and analysis, the data are also presented graphically below. Fig. 14 illustrates the calculated surface variation values for

most samples scanned at distances of 0.5 m (Fig. 14a) and 1.5 m (Fig. 14b). The cases of steel and brass will be examined in section 3.5.



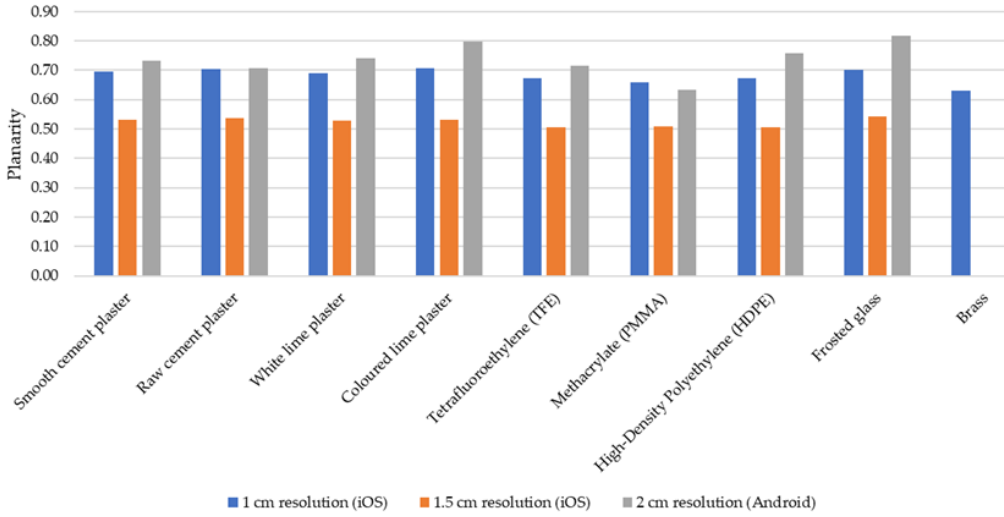
(a)



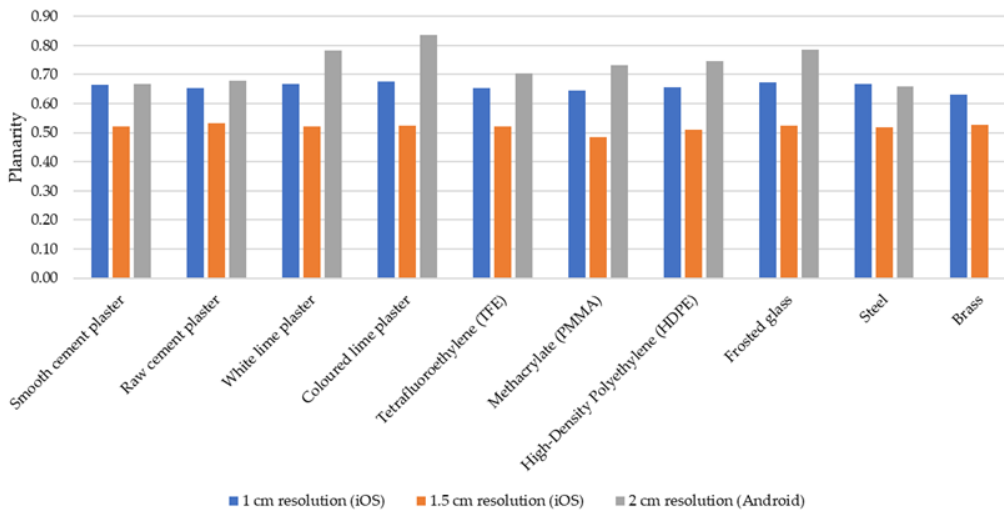
(b)

Fig. 14 –Surface variation values for building samples, distance of acquisition: (a) 0.5 m; (b) 1.5 m.

Fig. 15 displays the planarity values for samples acquired from distances of 0.5 m (Fig. 15a) and 1.5 m (Fig. 15b).



(a)



(b)

Fig. 15 – Planarity values for building samples, distance of acquisition: (a) 0.5 m; (b) 1.5 m.

Finally, the potential linear correlation between the materials' albedo and surface variation values was explored. The R^2 values derived from this investigation are presented in Tab. 19.

Tab. 19 – Linear regression analysis of albedo respect surface variation values.

Resolution	R^2 - scanning distance:	
	0.5 m	1.5 m
1 cm (iOS)	0.54	0.68
1.5 cm (iOS)	0.53	0.40
2 cm (Android)	0.27	0.20

3.4.2. Depth sensors tests under real conditions

This paragraph details the point clouds analysis from field tests conducted under real and dynamic conditions in the second, third, and fourth case studies. 3D point clouds of the statue, laboratory room, and Doric column remains are included in the Annexes (Fig. A9).

In the second case study's analysis phase, the statue's shaft was the primary interest. The point cloud was therefore sectioned in the middle of the shaft for this analysis. The analysis made it clear that there was a drift issue with the iOS device during scanning at 3 m distance. Fig. 16a demonstrates the drift's extension using a metric bar. This problem was not present in iOS and Android scans at 2 m, and sections of these scans are shown in the Annexes (Fig. A10a,b). Tab. 20 lists the surface variation and omnivariance values from the scans. Notably, the Android device's 3 m scan failed to acquire any points, suggesting its range is less than 3 m. Figs.16b and 16c provide additional views of the point cloud affected by drift, with Fig.16b depicting a section (C-C) in the scan closure area and Fig. 16c showing a top view of the statue.

Tab. 20 – Values of surface variation and omnivariance for the statue in the second case study.

Object scanned	Scan distance: 2 m		Scan distance: 3 m	
	SV_{λ} 1.5 cm	SV_{λ} 2 cm	SV_{λ} 1.5 cm	SV_{λ} 2 cm
Statue	0.0071	0.0103	0.0417	No data
	O_{λ} 1.5 cm	O_{λ} 2 cm	O_{λ} 1.5 cm	O_{λ} 2 cm
	0.0012	0.0013	0.0017	No data

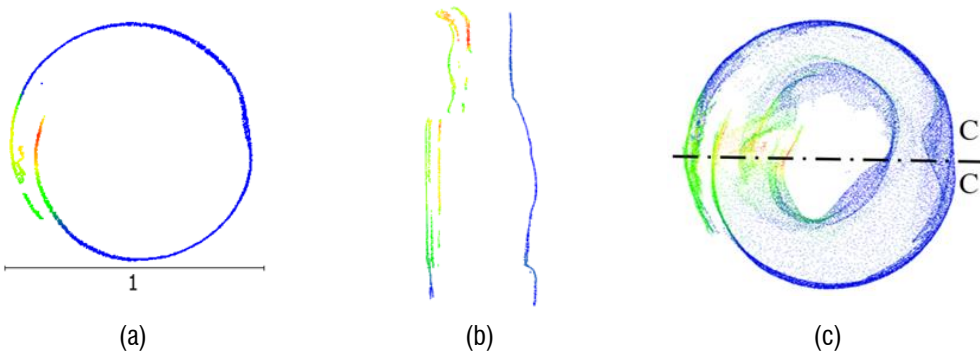


Fig. 16 – Sections of the statue’s point clouds, acquired from a distance of 3 meters, displaying the scalar field indicative of surface variation values: (a) section of stem of statue; (b) vertical section C-C of the statue in the scan closure zone; (c) top view of the statue and indication of the vertical section C-C.

Tab. 21 presents the values of surface variation and planarity for the laboratory room (third case study). Fig. 17 depicts the room’s planimetry, derived by slicing the point clouds at around 1.50 m height, with the scalar field illustrating the planarity values.

Tab. 21 – Values of surface variation and planarity for the laboratory room’s point cloud in the third case study.

Object scanned	Scan distance: adaptive		
	SV _λ 1 cm	SV _λ 1.5 cm	SV _λ 2 cm
Laboratory room	0.0119	0.0109	0.0234
	P _λ 1 cm	P _λ 1.5 cm	P _λ 2 cm
	0.8607	0.8940	0.7849

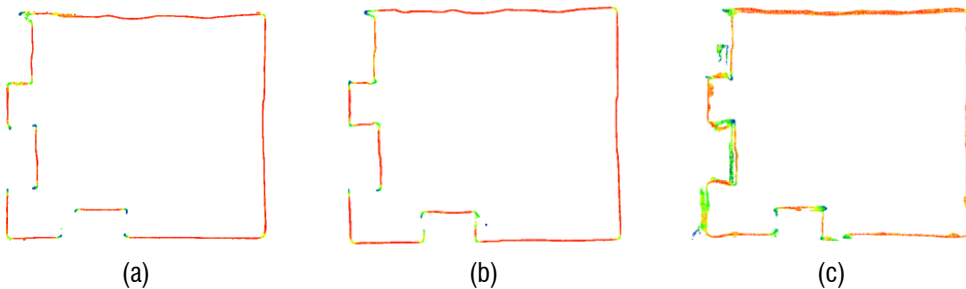


Fig. 17 – Laboratory room’s point clouds sections, with the scalar field indicating planarity values (a) 1 cm resolution scan; (b) 1.5 cm resolution scan; (c) 2 cm resolution scan.

The fourth case study focused on scanning the remains of a Doric column in Taranto. Scans were conducted using 1 cm and 1.5 cm resolutions on iOS devices, and 2 cm on an Android device. Tab. 22 lists the surface variation and omnivariance values from these three scans.

Tab. 22 – Values of surface variation and omnivariance for the point cloud of the Doric column remains in the fourth case study.

Object scanned	Scan distance: adaptative		
	SV _λ 1 cm	SV _λ 1.5 cm	SV _λ 2 cm
Doric column remains	0.0400	0.0682	0.0309
	O_λ 1 cm	O_λ 1.5 cm	O_λ 2 cm
	0.0019	0.0022	0.0018

To detect potential drifts and surface splitting, vertical section A-A and horizontal section B-B (on the third column drum) of the point cloud were analysed in the scan closing areas (see Fig. 18).

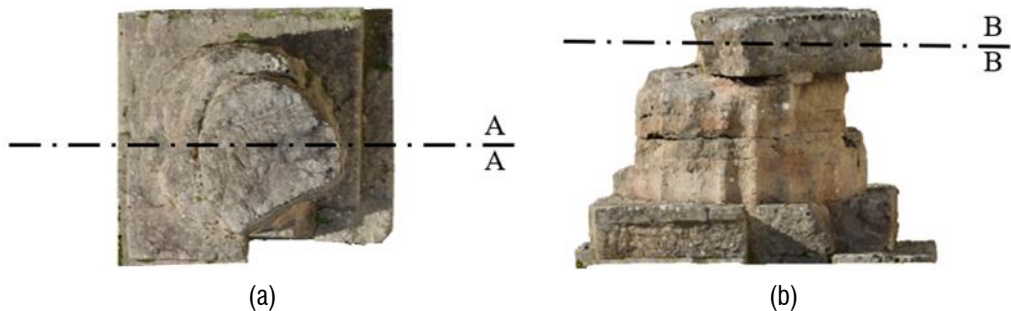


Fig. 18 – Sections A-A and B-B: (a) section at the closure of the scan of the lateral surface; (b) section at the vertical closure of the scan on the third column drum.

Fig. 19 displays the A-A and B-B sections performed on the columns point clouds. Specifically, Figs. 19a and 19d depict the sections from the 1 cm resolution 3D acquisition, Figs. 19b and 19e show the sections from the 1.5 cm resolution 3D acquisition, and Figs. 19c and 19f present the sections from the 2 cm resolution 3D acquisition.

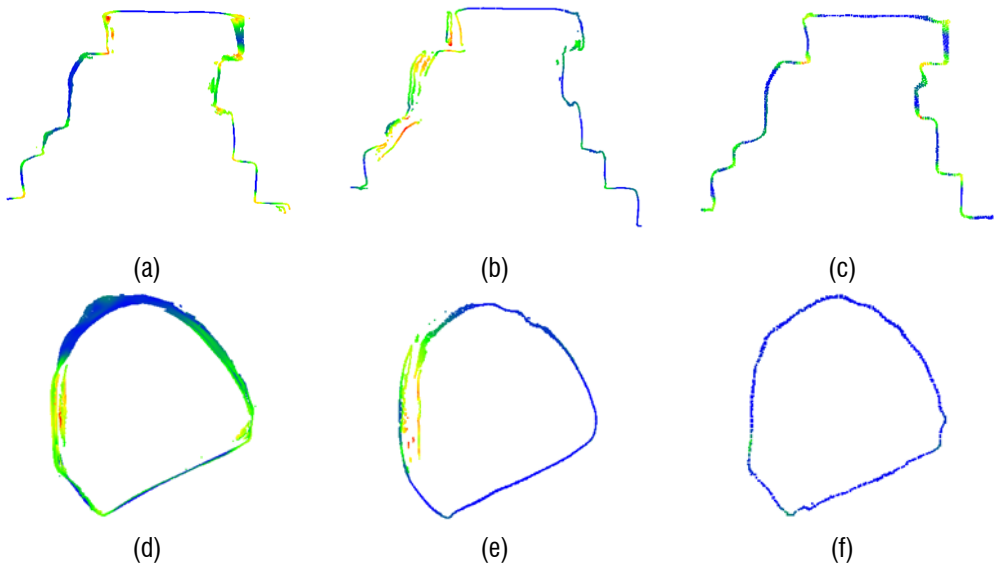


Fig. 19 – Sections of the point cloud: (a) section A-A resolution 1 cm; (b) section A-A resolution 1.5 cm; (c) section A-A resolution 2 cm; (d) section B-B resolution 1 cm; (e) section B-B resolution 1.5 cm; (f) section B-B resolution 2 cm.

Furthermore, to evaluate the accuracy and precision of the point clouds from the third and fourth case studies, the Cloud-to-Cloud (C2C) distance was calculated against a point cloud surveyed using Terrestrial Laser Scanning and photogrammetry.

In the third test, a HDS3000 Terrestrial Laser Scanner, boasting a positional accuracy of 6mm at 50m, was used to obtain the 3D point cloud.

In the fourth test, a photogrammetric survey was conducted using a Digital Single Lens Reflex camera and a Structure from Motion-Multi View Stereo (SfM-MVS) approach (Koutsoudis *et al.*, 2020). Specifically, a Nikon D3300 equipped with a Nikkor 20 mm f/2.8D fixed focal lens was employed for the 3D survey (Alfio *et al.*, 2022). The point cloud was generated within an Agisoft Metashape environment, achieving a RMSE of 0.001 m (metric assessed on six Ground Control Points).

Tab. 23 presents the C2C distance mean (μ) and Standard Deviation (SD) for the third and fourth case studies. Additionally, the corresponding histograms are provided in the Annexes (see Fig. A11).

Tab. 23 – C2C distance values for the third and fourth tests.

Object Scanned	Resolution: 1 cm		Resolution: 1.5 cm		Resolution: 2 cm	
	μ 3D [m]	SD3D [m]	μ 3D [m]	SD3D [m]	μ 3D [m]	SD3D [m]
Laboratory room	0.0334	0.0264	0.0224	0.0449	0.0518	0.0580
Doric column remains	0.0153	0.0132	0.0383	0.0238	0.0127	0.0107

3.5. Evaluations and discussions of the second part of the research project

When analysing planar samples (the building material samples), the structure of point clouds created by smartphone apps was interesting. Fig. 20 demonstrates that iOS devices scanning at 1 cm resolution produced an organized point cloud (Fig. 20a), while at approximately 1.5 cm resolution, the result was a more disordered cloud (Fig. 20b). The Android point cloud, as displayed in Fig. 20c, was as orderly as the iOS's 1 cm resolution cloud but with a distinct resolution.

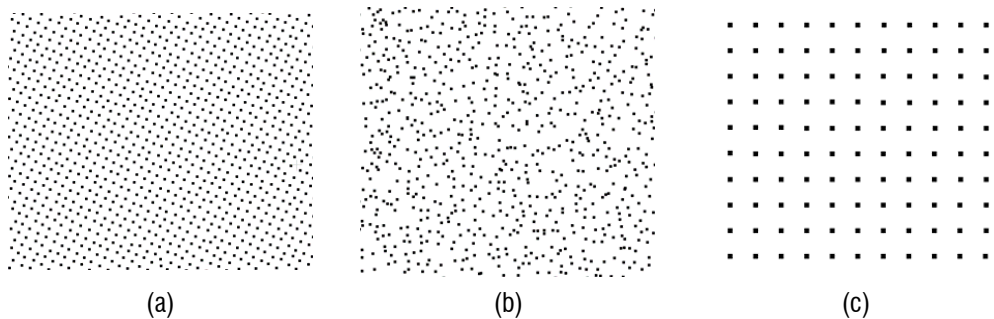


Fig. 20 – Structure of 3D scans: (a) iOS resolution point cloud 1 cm; (b) iOS resolution point cloud ~1.5 cm; (c) Android resolution point cloud 2 cm (c).

In the tests under controlled laboratory conditions, materials like plasters, plastics, and frosted glass exhibited generally very good SV_λ and P_λ values (refer to Figs. 14 and 15). Notably, the obtained SV_λ values were below 0.33, the theoretical maximum for surface variation (Pauly, Gross and Kobbelt, 2002). The planarity analysis also

showed values near unity, indicating the point clouds' alignment with planar surfaces. This is advantageous, considering smartphone depth sensors may need to scan various material surfaces in a single environment (for example urban scenarios). A closer look at the SV_λ results reveals a slight distinction between the “plasters” group and the “plastics and frosted glass” group, the latter having lower values. However, the difference is minimal, suggesting that scanning multiple materials concurrently should not pose significant issues.

Steel and brass samples scanned from 0.5 m away at 1 cm and 1.5 cm resolutions exhibited significant noise, rendering them unanalysable. However, scanning these materials at a 2 cm resolution resulted in a surface variation value of 0.1672 and revealed a split and deformed surface, as illustrated in Fig. 21a.

When scanned from a distance of 1.5 m, steel and brass samples generally exhibited improved surface variation values compared to those scanned from a closer distance of 0.5 m. The brass scanned at 1 cm resolution showed favourable results. However, the 1.5 cm and 2 cm resolution scans of brass resulted in surface variation values of 0.1455 and 0.1000, respectively, due to some splitting and deformation, as seen in Figs. 21b and 21c. Issues in scanning metallic materials might stem from their surface properties. Easier scanning of metallic materials can be achieved by increasing the laser beam's acquisition distance and angle (Costantino, Pepe and Angelini, 2021).

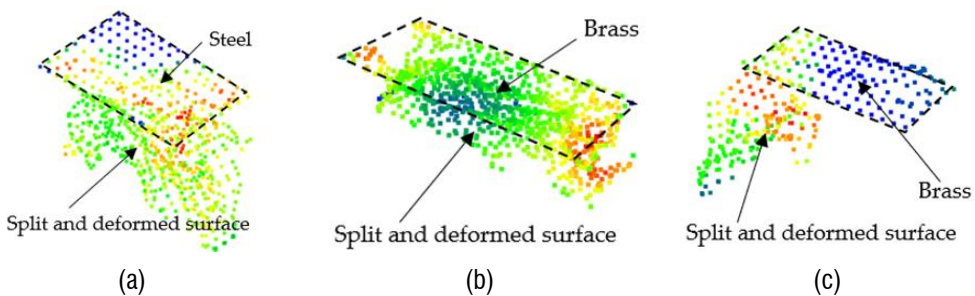


Fig. 21 – Point clouds aberrations, scalar field is the surface variation value: (a) steel resolution point cloud 2 cm, (b) brass resolution point cloud 1.5 cm, (c) brass resolution point cloud 2 cm.

Investigations into a linear correlation between albedo and surface variation (Tab. 19) revealed a moderate to very weak association (Moore, Notz and Fligner, 2015). This finding is encouraging, as it suggests that the material's nature does not significantly influence scan quality.

Tab. 20 reveals that the highest SV_λ value corresponds to the scan experiencing drift issues. Furthermore, by examining the omnivariance value, an increase in the point cloud's inhomogeneity is noticeable alongside a rise in the SV_λ value.

Reviewing the planarity values in Tab. 21 and referencing Fig. 17, it is evident that the Android device yielded unsatisfactory results for geomatics applications. In contrast, the iOS device delivered promising outcomes for scans at both 1 cm and 1.5 cm resolutions.

Analysing the data in Tab. 22, the 1.5 cm resolution scan on iOS emerged as the least effective. Further examination of the sections in Figs. 18 and 19 reveals that this scan, particularly at 1.5 cm resolution (Figs. 19b and 19e), suffered the most from surface splitting due to drift issues. This splitting occurred horizontally during side surface scanning and vertically while scanning the column drum at the top to complete the scan. The 1 cm resolution scan (Figs. 19a and 19d) exhibited less surface splitting on the third column drum compared to the 1.5 cm resolution. Meanwhile, the 2 cm resolution scan (Figs. 19c and 19f) appeared to be the most successful of the three, with only minor issues at the junctions between column drums.

Dynamic condition tests highlighted issues associated with moving scans. Two primary problems were identified: surface splitting and scan closure inaccuracies due to Inertial Navigation System (INS) drift. Drift issues arise from the calculation of the mobile device's position, which is determined instantaneously based on its previously estimated position by inertial sensors. Small INS inaccuracies can amplify, leading to significant positioning errors during the scanning of large objects or areas (Kelly and Sukhatme, 2011; Tavani *et al.*, 2022). Additionally, drift problems often caused surface splitting and overlapping in scan closure zones, indicating a correlation between these two issues.

From the second case study, it's evident that increasing the scanning distance heightens the likelihood of encountering drift problems. This is particularly noticeable in scans conducted along a circular path around an object. Additionally, changes in scanning distance, possibly due to obstacles, further raise the risk of drift effects. This phenomenon is also observable in scans of two structures conducted for documentation purposes, using an iPad Pro 2021 at a 1.5 cm resolution, as depicted in Fig. 22.

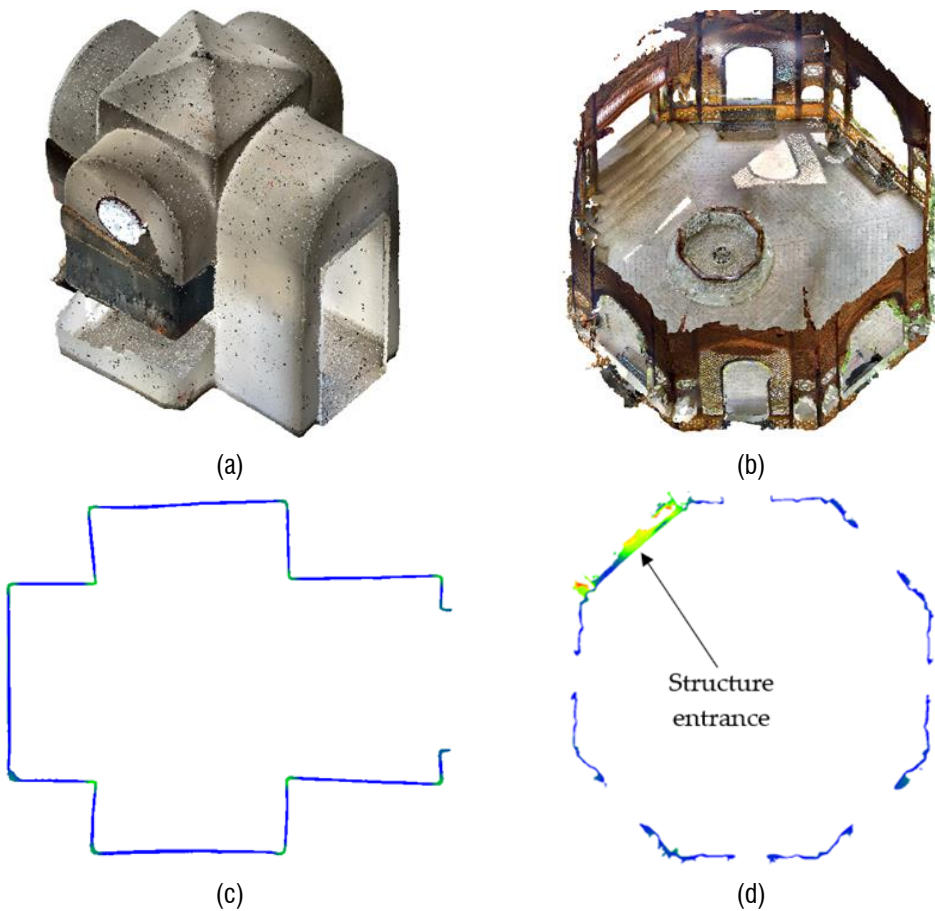


Fig. 22 – Scans of two structures compiled for documentation, with the scalar field indicating surface variation values: (a) first structure; (b) second structure; (c) section of first structure; (d) section of second structure.

For the first structure (Fig. 22a), limited space required the operator to scan by standing still and rotating in the structure's centre. Conversely, for the second structure (Fig. 22b), the operator moved around actively to capture every detail. While the scans of both structures are generally of good quality, a closer look at their sections reveals that the first structure's section (Fig. 22c) exhibits fewer or no surface splitting issues, unlike the second (Fig. 22d), which shows surface splitting at the entrance where the scan concluded. This highlights how movement during scanning can lead to drift problems, manifesting as surface splitting or more broadly, in challenges with surface reconstruction.

The third and fourth case studies demonstrate that typical scanning accuracies range from 1–3 cm. However, issues like surface splitting can significantly worsen these values, potentially doubling them (refer to Tab. 23). Consequently, monitoring such issues in scans conducted with smartphone and tablet depth sensors (Android ToF cameras and iOS LiDARs) is crucial.

In light of the issues encountered in this second research phase, chapter 5 (fourth research) will explore systems and methods related to a specific photogrammetric technique known as GNSS-aided photogrammetry via video (refer to the Introduction for details). This approach promises to offer a quick surveying experience similar to that of smartphone depth sensors while potentially addressing issues in surface reconstruction and point cloud creation observed during these experiments.

CHAPTER 4. GNSS > SONAR > PHONE SYSTEM AND 3D MODELLING

For your knowledge, the material and research reported in this chapter were previously published in:

Vozza, G., Costantino, D., Pepe, M. and Alfio, V.S. (2023) ‘**Smart Sensors System Based on Smartphones and Methodology for 3D Modelling in Shallow Water Scenarios**’, *Applied System Innovation*, 6(1), p. 28. Available at: <https://doi.org/10.3390/asi6010028>.

Besides the points discussed in the Introduction about geospatial data, SDG 14 and target 14.a. The United Nations declared 2021–2030 as the “Decade of Ocean Science for Sustainable Development”. A key social outcome targeted is “Data Transparency and Accessibility”, aiming to ensure open access to ocean data, information, and technologies for nations, stakeholders, and citizens (Ryabinin *et al.*, 2019).

Gathering data from underwater environments using proprietary instruments is often challenging, especially compared to terrestrial settings. Specifically, acquiring bathymetric data is costly regarding the required equipment, specialized staff, logistics, time, and execution methods (Monteys *et al.*, 2015; Helminen *et al.*, 2019; Tonion *et al.*, 2020; Bio *et al.*, 2022). These factors could hinder the achievement of SDG 14 and the objectives of the Decade of Ocean Science for Sustainable Development. Nonetheless, the rise of new smart and Internet of Things (IoT) technologies in the consumer market for mapping aquatic and marine environments presents an opportunity. It offers a way to distribute low-cost tools for research, democratize data access in remote and developing regions, and engage the public in citizen science projects.

Thus, the third part of the research project aims to explore the Single Beam Echo Sounders (SBES) sonar (Sound Navigation And Ranging) developed by Deeper UAB. These devices, known as Deeper Smart Sonar, are cost-effective, portable, and user-friendly, even for those without expert knowledge. They can be attached to Unmanned

Aerial Vehicles (UAVs) or Unmanned Surface Vehicles (USVs). As highlighted in the literature review, these SBES have garnered interest for scientific applications.

4.1. Literature review of the third part of the research project

In their study on Deeper Smart Sonar, Bandini *et al.* (2018) utilized the Deeper Smart Sonar Pro+ attached to a UAV via a winch to map three Danish inland water bodies: Lake Furesø, Marrebæk Kanal, and Åmose Å. They found that the built-in GNSS receiver of the Deeper Smart Sonar Pro+ had an accuracy of up to 30 meters and, by comparing with depth measurements, identified a sonar error rate of 3.8%. Bandini *et al.* (2018) developed a method to correct the SBES's horizontal positioning using nadiral images from a UAV equipped with GNSS, Inertial Measurement Unit (IMU), and RADAR sensor systems. Depth accuracy was improved through linear regression with ground truth data collected during the survey. These adjustments led to a horizontal positioning accuracy of approximately 20 cm and a depth error rate of about 2.1% for depths up to 30 meters.

Alvarez *et al.* (2018) combined UAV imagery, sonar data from the Deeper Smart Sonar Pro+, and adaptive sampling to survey a small reservoir at the Kessler Atmospheric and Ecological Field Station (KAEFS) near Purcell, Oklahoma, USA. They attached the SBES to a UAV using a cable and used a small vessel equipped with an Android tablet to gather bathymetric data. Comparing direct measurements with echosounder readings, Alvarez *et al.* (2018) reported a Root Mean Square Error of 0.0147 and a correlation coefficient of 0.987.

Giambastiani *et al.* (2020) employed the Deeper Smart Sonar Pro+, linked to a bait boat, for depth measurement in small-to-medium-sized water bodies (ranging from 50,000 to 2000 square meters) in Tuscany. They characterized the sonar's internal GNSS as "highly accurate". Analysing the collected data, they calculated the volumes of 204 water bodies and discovered a strong correlation ($R^2 = 94$) between these calculated volumes and the actual volumes of 55 sampled water bodies.

Bogoyavlensky *et al.* (2020) utilized a combination of UAVs, georadar, and two sonars, including a Deeper Smart Sonar Pro+, to survey the Seyakha C11 crater in Siberia, creating a Digital Elevation Model (DEM) of the area. The Deeper Smart Sonar

Pro+ used its internal GNSS for geolocation, with the authors noting a positioning accuracy of up to 3 meters.

Kellerer-Pirklbauer *et al.* (2021) utilized the Deeper Smart Sonar CHIRP+ alongside other sensor systems to investigate the recession of the Pasterze glacier in Austria. While using the CHIRP+, they noted an absence of reference studies on its accuracy for depth measurements. Nonetheless, they estimated the device's accuracy to be less than 0.1 m in shallow waters (<5 m) with flat bottoms, and around 0.5 m in deeper, sloping waters.

Broere *et al.* (2021) employed the Deeper Smart Sonar CHIRP+ to identify suspended macro-plastics in rivers. Their research showed that this low-cost sonar could effectively detect suspended macro-plastics, with different plastic objects producing distinct reflections.

Ruffell, Lally and Rocke (2021) evaluated a system named "Dronar" designed for forensic applications. This system integrated a Deeper Smart Sonar (Pro+ or CHIRP+ 2) connected to a UAV via a wire. They demonstrated Dronar's potential in identifying submerged objects, offering preliminary data for in-depth investigations, and indicating possible hazards to the navigation of boats and divers.

Sanjou *et al.* (2022) designed a floating UAV system to measure natural river discharge. This system included a UAV with a floating ring, a GPS-Real-Time Kinematic (GPS-RTK) receiver (the DG-PRO1RWS), a smartphone for data recording, and a Deeper Smart Sonar Pro+. By using the GPS-RTK receiver to gauge river velocity and the sonar for cross-sectional measurements, they successfully calculated the river's discharge.

Koutalakis and Zaimis (2022) developed a UAV and sonar system to calculate a river's velocity and discharge. They utilized images captured by the UAV (IV-UAV) and bathymetry data gathered with the Deeper Smart Sonar Pro+.

In a subsequent experiment, Bandini *et al.* (2023) examined the use of Ground Penetrating Radar (GPR) and Unmanned Aerial Systems (UAS) for mapping inland water bodies. They explored the potential of enhancing the Deeper Smart Sonar's CHIRP+ geolocation accuracy through GNSS Post-Processed Kinematic (PPK) corrections.

They recorded sonar data in NMEA0183 format and GNSS raw data from a ZED-F9P receiver separately on a single-board computer during the bathymetric survey. In post-processing, the researchers synchronized the sonar data with the GNSS positioning data, processed in PPK, based on Coordinated Universal Time (UTC) timestamps, to recalibrate the sonar's position.

4.2. Aims of the third part of the research project

The review of current literature shows varying and different values concerning the accuracy achievable by sensor systems used for bathymetry. This inconsistency in data complicates the categorization of surveys in broader contexts and the determination of application ranges with geomatic sensitivity. Given these factors, this third research aims to analyse the following aspects:

1. conduct tests to assess the accuracy and precision of shallow-water depth measurements and planimetric positioning using Deeper Smart Sonar models (specifically CHIRP+ and Pro+ 2). Develop and evaluate a system that synchronizes Deeper Smart Sonars with an external GNSS receiver via smartphone, aimed at enhancing GNSS Single Point Positioning (SPP) in real-time. Additionally, devise a method to refine the GNSS positioning of the Deeper Smart Sonar in Post-Processed Kinematic (PPK), utilizing a space-time approach and GPS Time (GPST) to further improve positioning accuracy;
2. create 3D models of the water environments surveyed.

To align with globally recognized benchmarks, the data gathered during tests and the outcomes of the experiments were first evaluated against the standardized uncertainty values of the International Hydrographic Organization (2020) (IHO). Subsequently, potential applications in scientific and engineering domains were considered.

4.3. Materials and methods of the third part of the research project

4.3.1. Third research methodology

The third research was segmented into three distinct phases. In the initial phase, an system named GNSS > Sonar > Phone System (G > S > P Sys) was developed to synchronize the Deeper Smart Sonar (CHIRP+ or Pro+ 2)

with an external GNSS receiver via a smartphone. The purpose of the G > S > P Sys was to establish a data exchange network, utilizing the smartphone as a hub for managing input and output data between the GNSS receiver and the sonar. The system's primary goal was to transmit real-time Single Point Positioning (SPP) data from the external GNSS receiver to the Deeper Smart Sonar, enhancing sonar geolocation during bathymetric surveys. It also simultaneously captured raw data from the GNSS receiver for PPK elaboration, further refining sonar GNSS positioning. This real-time correction of sonar geolocation was enabled by the "mock location" feature in Android Operative System (OS), allowing an app connected to an external GNSS receiver to adjust the geolocation of other apps on the device.

During the second phase, specific tests were conducted to compile datasets for assessing the performance of the Deeper Smart Sonar and the G > S > P Sys. An initial test evaluated the static GNSS positioning capabilities of both the Deeper Smart Sonar (CHIRP+ and Pro+ 2) and the G > S > P Sys. This was followed by two dynamic tests to examine their performance in kinematic positioning. To determine the accuracy and precision of the Deeper Smart Sonars in depth measurement, controlled tests in a swimming pool and real-world tests in the sea were carried out.

To implement the PPK correction method for sonar geolocation and assess the 3D modelling process using data from the G > S > P Sys, comprehensive surveys of a swimming pool and a section of the seabed were conducted. From the pool survey, a dataset was generated to evaluate 3D modelling of artificial structures. Similarly, the sea survey produced a dataset for 3D modelling of natural surfaces. Moreover, the sea survey aimed to examine the devices under actual operating conditions. Both surveys utilized the Deeper Smart Sonar CHIRP+.

In the final phase, a pipeline was established for 3D modelling of both natural surfaces and artificial structures. The employed method for 3D modelling falls into the broader category of data-driven modelling (Costantino *et al.*, 2021).

The pipeline for modelling natural surfaces involves three stages: synchronization, interpolation, and 3D modelling.

In the synchronization phase, GNSS positions logged by the external receiver and corrected using PPK were aligned with the depth measurements from the sonar. This spatio-temporal method, involving the alignment of data from the system based on latitude and longitude coordinates, followed by synchronization with GPS Time (GPST). This process is feasible because the real-time electronic synchronization via smartphone enabled the external GNSS receiver to transmit its coordinates to the sonar. This approach achieves synchronization precision to a millisecond (1/1000 second).

During the interpolation phase, discrete data points were converted into continuous grid format data. This step involved employing a novel interpolation technique based on Machine Learning (ML). Specifically, the Forest-based Classification and Regression algorithm available in ArcGIS PRO software (ESRI, Redlands, California, USA) was utilized. This algorithm, rooted in the Random Forest supervised ML method developed by Leo Breiman and Adele Cutler, is a robust tool for classification and regression tasks.

In its fundamental form, as proposed by Leo Breiman (2001), a Random Forest for regression creates trees based on a random vector Θ . The tree predictor, represented as $h(x, \Theta)$, yields numerical values, assuming that the training set is independently drawn from the random vector Y, X . The mean-squared generalization error for any predictor $h(x)$ is determined by this methodology:

$$E_{X,Y}(Y - h(X))^2 \tag{62}$$

To solely utilize the captured bathymetric data without relying on external sources, a grid created by the Inverse Distance Weight (IDW) method was employed to establish the initial training features for the algorithm (Pereira, Valente, de Queiroz, *et al.*, 2022; Pereira, Valente, Queiroz, *et al.*, 2022).

The formula for the IDW interpolation, as outlined e.g. by Ferreira *et al.* (2017) and Parente and Vallario (2019), was used in this process:

$$V_g = \frac{\sum_{i=1}^n \frac{v_i}{d_i^P}}{\sum_{i=1}^n \frac{1}{d_i^P}} \quad (63)$$

where,

V_g represents the value estimated at the x and y coordinates of the grid;

v_i is the value of the i-th observed point;

n denotes the number of points near the point being interpolated;

d_i refers to the distance of the i-th point from the point being interpolated;

P indicates the power (positive parameter).

The IDW grid was then converted into a 3D model for use in the results analysis phase for comparative evaluation.

To facilitate future comparisons with the 3D model created using the grid from the Forest-based Classification and Regression, an additional grid was generated in ArcGIS Pro, employing the Ordinary Kriging interpolation method, represented by the following mathematical model (Matheron, 1962; Posa and De Iaco, 2009):

$$\hat{\gamma}(d) = \frac{1}{2|N(d)|} \sum_{N(d)} [V(u_i) - V(u_j)]^2 \quad (64)$$

where,

$N(d)$ refers to the set of pairs of measured points;

$|N(d)|$ indicates the number of distinct pairs within $N(d)$;

d is the vector representing the separation between points;

$|d|$ is the difference between u_i and u_j ;

$V(u_i)$ denotes the value of the random variable describing potential outcomes of the measured quantity V at the spatial location u_i ;

$V(u_j)$ represents the value of the random variable for possible outcomes of the quantity V at the spatial location u_j .

As demonstrated e.g. by Alcaras, Carnevale and Parente (2020), Ordinary Kriging is particularly suitable for the interpolation of bathymetric data.

In the 3D modelling phase, the three bathymetric grids were converted into 3D triangular mesh models. This transformation process interprets the bathymetric grids as digital values in a matrix, converting them first into point clouds and then into 3D models. The 3D mesh modelling utilized the Poisson surface reconstruction method. The method, given a set S of points p from a solid model M with surface ∂M , reconstructs the 3D surface by solving a classical Poisson problem (Kazhdan, Bolitho and Hoppe, 2006; Kazhdan and Hoppe, 2013):

$$\Delta \tilde{X} = \nabla \cdot \vec{V} \quad (65)$$

where \vec{V} is a vector field, the gradient of M 's smoothed indicator function equals the vector field derived from smoothing the normal field to the surface:

$$\nabla(X_M * \tilde{F})(q_0) = \int_{\partial M} \tilde{F}_p(q_0) \vec{N}_{\partial M}(p) dp \quad (66)$$

where,

$\vec{N}_{\partial M}$: normal to the surface at point p ;

\tilde{F} : smoothing filter.

The integral cannot be directly computed because the surface of the solid intended for modelling is unknown. To address this issue, the surface is segmented into numerous patches using the set of points p , and the integral over each patch is approximated as the value at the point, adjusted by the patch's area:

$$\begin{aligned} \nabla(X_M * \tilde{F})(q) &= \sum_{s \in S} \int_{P_s} \tilde{F}_p(q) \vec{N}_{\partial M}(p) dp \approx \sum_{s \in S} |P_s| \tilde{F}_{s,p}(q) s \cdot \vec{N} \\ &\equiv \vec{V}(q) \end{aligned} \quad (67)$$

Modelling artificial structures is considered a specific case of natural surface modelling. Detailed information and a description of the implementation of this pipeline can be found in paragraph 4.3.4.4, which is devoted to the artificial structures.

4.3.2. GNSS > Sonar > Phone System assembly

4.3.2.1. Sonars, electronic devices and smartphone apps

The G > S > P Sys is composed of both hardware and software components. The hardware elements of the G > S > P Sys include the Deeper Smart Sonar Pro+ 2 and CHIRP+ (both from Deeper UAB, Vilnius, Lithuania), the SimpleRTK2B (ArduSimple, Principality of Andorra), and the Huawei P30 Pro (Huawei Technologies Co., Ltd., Shenzhen, China).

The Deeper Smart Sonar Pro+ 2 and CHIRP+ are Single Beam Echo Sounders (Jones, 1999; Lurton, 2002) operating at 100 kHz, 240 kHz, and 675 kHz frequencies, featuring scan cones of 47°, 20°, and 7°. These devices conduct approximately 15 scans per second, scanning depths from a minimum of 0.15 m to a maximum of 100 m.



These Sonars include an internal GNSS receiver for geolocation, with the alternative option of using the smartphone's GNSS receiver. They connect to smartphones via Wi-Fi and are managed through the Fish Deeper—Fishing App. This setup enables the Sonars to send scan data to the smartphone (as shown in Fig. 23).

The Sonars generate 2D maps containing bathymetric data acquired from scanning the bottom. Users can immediately access georeferenced sonar scans of the bottom and 2D bathymetric maps in real-time on their smartphones, with the data also accessible post-survey on the Deeper UAB web platform. The raw data, downloadable as a text file (*.csv) from both the smartphone and web platform, include latitude and longitude of the points collected, depth measurements from the scans (in meters), water temperature (in °C), and the time of sonar scans (in UNIX format).

The primary distinction between the Deeper Smart Sonar CHIRP+ and the Pro+ 2 is the inclusion of CHIRP technology in the former. CHIRP, short for “Compressed High Intensity Radar Pulse”, differs from classic sonar by emitting multiple pulses simultaneously for scanning. This results in more detailed information, producing more precise scans, better bottom detection, and improved target separation.

Tab. 24 details the technical specifications of the Deeper Smart Sonar Pro+ 2 and the Deeper Smart Sonar CHIRP+.


Tab. 24 – Specifications of the Deeper Smart Sonar Pro+ 2 and the Deeper Smart Sonar CHIRP+.

Device	Deeper Smart Sonar Pro+ 2	Deeper Smart Sonar CHIRP+
Image		
Beam cone [°]	47-20-7	47-20-7
Frequency [kHz]	100-240-675	100-240-675
GNSS constellation	GPS, GLONASS, Galileo, BeiDou, QZSS	GPS, GLONASS, Galileo, BeiDou, QZSS
Wi-Fi connection range [m]	100	100
Sonar scan rate [x/s]	15	15
Depth range min/max [m]	0.15-100	0.15-100
Weight [g]	90	90
Dimensions [mm]	Ø 65	Ø 65
Operating temperature [°C]	-20/40	-20/40

The SimpleRTK2B, an external GNSS receiver, is built around the ZED-F9P GNSS module from U-Blox (U-Blox, Thalwil, canton of Zürich, Switzerland). This receiver can be connected to various devices, including smartphones, enhancing geolocation precision (Semler *et al.*, 2019). It supports observation of GPS, GLONASS, Galileo, and BeiDou constellations and receives L1C/A, L2C, L10F, L20F, E1-B/C, E5b, B1I, and B2I frequencies. For this third experiment, the receiver was equipped with a Bluetooth data transmission module (AS-XBEE-BT-2.4-INT-00) and a Helical multiband GNSS antenna (IP67). Using U-Center software for U-Blox GNSS management, the receiver was set to send real-time positions in Single Point Positioning (GNSS-SPP data Real-time in Fig. 23) via Bluetooth and GNSS raw data in *.ubx format (GNSS-Raw data in Fig. 23) through a USB On-The-Go (USB OTG) connection. Two files were generated from the raw data (*.ubx format): the first, produced via U-center in *.csv format, contained coordinates of latitude, longitude, ellipsoid height, and GPS Time from real-time SPP positioning; the second, created using RTKLIB: demo5_b34f.1 (version of RTKLIB, developed by rtklibexplorer (rtklibexplorer, accessed: 8 January 2023b) for working with the ZED-F9P and downloadable from

(rtklibexplorer, accessed: 8 January 2023a)) resulted in a RINEX file of observables for post-processing, primarily including latitude, longitude, ellipsoidal height, and GPS Time. Tab. 25 displays the technical specifications of the SimpleRTK2B.

Tab. 25 – Specifications of the SimpleRTK2B.

Device	SimpleRTK2B
Image	
GNSS Module	ZED-F9P
GNSS Constellation	GPS, GLONASS, Galileo, BeiDou
Frequency [kHz]	L1C/A L2C, L10F L20F, E1-B/C E5b, B1I B2I
Bluetooth connection module	AS-XBEE-BT-2.4-INT-00
Antenna	Lightweight helical for multiband GNSS (IP67)
Weight [g]	20
Dimensions [mm]	69 × 53

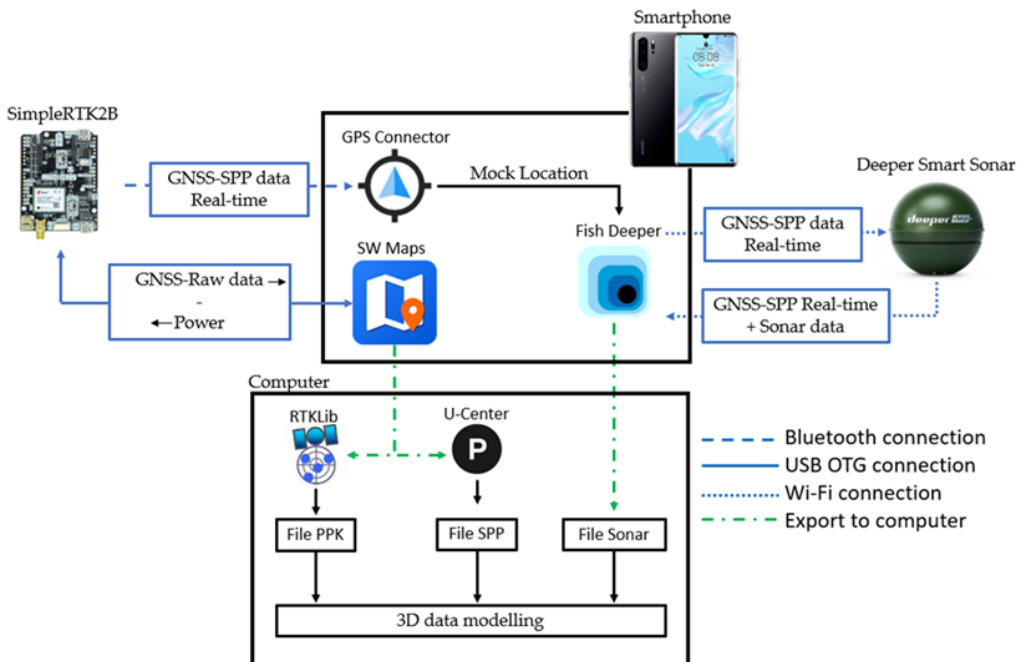


Fig. 23 – G > S > P Sys composition and data exchange

The Huawei P30 Pro smartphone was utilized for synchronizing the Deeper Smart Sonars with the SimpleRTK2B in the G > S > P Sys setup. While the specific smartphone model is not critical for the system's implementation, certain features are essential. These include a robust chipset and consistent RAM for simultaneous background app management, an Android OS, the capability to enable "mock location", and USB OTG connection compatibility.

The software components of the system included: GPS Connector v1.0.1.7 (PilaBlu - Apps, Stuttgart, Germany), SW Maps GIS & Data Collector v2.9.1.1 (Softwel Pvt. Ltd., Kathmandu, Nepal), and Fish Deeper—Fishing App v1.22.0.3259 (Deeper UAB, Vilnius, Lithuania).

GPS Connector enables the connection of an external GNSS receiver to a smartphone via Bluetooth or USB. It supplies external GNSS position data to other navigation apps on the smartphone through the "mock location" feature, thereby enhancing the GNSS positioning accuracy of these apps. This app was utilized to refine the real-time Single Point Positioning (SPP) of the Fish Deeper—Fishing App and, by extension, the sonar. SW Maps offers various GIS (Geographic Information System) functions and connects an external GNSS receiver to a smartphone via Bluetooth or USB. It was employed to capture data from the external GNSS receiver in *.ubx format for later post-processing.

Fish Deeper—Fishing App connects Deeper Smart Sonars to the smartphone via Wi-Fi. It enables users to configure sonar scanning, view mapped data and download raw data (Jivthesh *et al.*, 2022).

4.3.2.2. Connection management and apps data transfer

To effectively manage and synchronise the devices described, it is essential to organise the connections between devices and the transmission of data between apps properly.

The external GNSS receiver (SimpleRTK2B) was linked to the smartphone through a USB OTG connection, drawing power from the smartphone and sending GNSS-Raw data to the SW Maps app for recording and post-processing (illustrated as GNSS-Raw data—Power in Fig. 23). Concurrently, the receiver was Bluetooth-connected to

the smartphone to relay real-time GNSS SPP positioning data (shown as GNSS-SPP data Real-time in Fig. 23) to the GPS Connector app. This app then forwarded the real-time GNSS-SPP data to the Fish Deeper—Fishing App using the smartphone’s “mock location” feature. The Deeper Smart Sonar, connected to the smartphone via Wi-Fi, received the real-time GNSS-SPP data from the Fish Deeper—Fishing App and transmitted both the GNSS-SPP data and Sonar data back to the app (depicted as GNSS-SPP Real-time + Sonar data in Fig. 23).

To enable GPS Connector to distribute external GNSS positioning data to other applications, the “mock location” feature, found in the developer options and settings within the app itself need to be activated. This action is crucial as it facilitates real-time synchronization between the external GNSS receiver and the sonar, and subsequent synchronization in PPK.

For the sonar to utilize GNSS data from the smartphone within the Fish Deeper—Fishing App for geolocation, the “Boat” option should be selected as the fishing mode. Additionally, to enhance the connection between the smartphone and sonar, Deeper UAB suggests turning off mobile data and settings that automatically switch between Wi-Fi and mobile data. Consequently, internet access is not available during surveys. During tests with the Huawei P30 Pro, it was observed that to avoid GNSS positioning interference from nearby mobile and Wi-Fi networks, it is advisable to disable the “Google Location Accuracy—Improve Location Accuracy” function. Whether this issue affects other smartphones is not confirmed.

4.3.3. Construction of tests and datasets

The subsequent paragraphs detail the tests conducted and the datasets created to evaluate the performance of the devices under study.

In these tests, sonar scans were executed at 675 kHz with a 7° cone, selected for its accuracy in the test environments (Bandini *et al.*, 2023). For relative GNSS positioning in post-processing, the HxGN SmartNet (Hexagon AB, Stockholm, Sweden) CORS network was utilized, with the nearest station being TARA, situated atop the Politecnico di Bari, Taranto, Italy. RTKLIB: demo5_b34f.1 was the primary software for static

and kinematic post-processing, while Precise Point Positioning (PPP) post-processing was carried out using CSRS-PPP (Tétreault *et al.*, 2005).

4.3.3.1. Sonars and G > S > P Sys static datasets

The performances of the Deeper Smart Sonar Pro+ 2, CHIRP+, and G > S > P Sys in static GNSS positioning was evaluated under open sky conditions at the Politecnico di Bari’s Geomatics Laboratory in Taranto, Italy. This initial test utilized the FATA vertex of a permanent GNSS network, previously employed in early experiments (see chapter 2). The site’s coordinates were re-confirmed using a professional Trimble R10 GNSS receiver for enhanced precision. The Deeper Smart Sonars were activated and positioned on the observation vertex in a water-filled cylinder, 0.25 meters in height, with an opening matching the sonars’ diameter. The G > S > P Sys was set up with a Helical antenna mounted on a stand at the survey point. Each unit performed 8 hours of static observation, generating five datasets. Tab. 26 details the static datasets composition, with “Deeper GNSS CHIRP+” and “Deeper GNSS Pro+ 2” indicating the internal GNSS receivers of the respective sonar units.

Tab. 26 – Sonars and G > S > P Sys static datasets.

Device	Positioning	Obs. time [s]	Data sample (no.)	Main data
Deeper GNSS CHIRP+	SPP	28,800	28,800	Latitude, longitude
Deeper GNSS Pro+ 2	SPP	28,800	28,800	Latitude, longitude
	SPP	28,800	28,800	Latitude, longitude, ellipsoid height
G > S > P Sys	Post-Processing Static	28,800	28,800	Latitude, longitude, ellipsoid height
	PPP	28,800	28,800	Latitude, longitude, ellipsoid height

4.3.3.2. Sonars and G > S > P Sys dynamic datasets

To assess the kinematic positioning capabilities of the Deeper Smart Sonar Pro+ 2, CHIRP+, and G > S > P Sys, two experiments were conducted: a sea test in Mar Grande, Taranto, Italy (coordinates ϕ : 40° 25' 23.32" N; λ : 17° 12' 53.01" E), and a pool test. The sea test aimed to evaluate the horizontal positioning of the devices, involving their movement along a straight 11.50 meter path from point A to B, marked by stakes and a corridor for guidance. This path was also surveyed using traditional methods and GNSS for comparison.

The pool test, illustrated in Fig. 24a, focused on the G > S > P Sys, presumed more precise than the Deeper Smart Sonars from initial tests. It involved surveying the perimeter of a rectangular pool (8.95 m x 4.47 m, approximately 40.01 sqm) using the pool's edges as guides. This was compared against traditional survey methods and a static GNSS survey.

Both tests utilized a prototype floating platform (Fig. 24b) equipped with a high-density foam base for buoyancy, a waterproof container for instrumentation control, mounts for the G > S > P Sys antenna and smartphone, and a flexible arm mount for consistent sonar-water contact (the "flexible arm mount 2.0" by Deeper UAB). Tabs. 27 and 28 detail the composition of the dynamic datasets from the sea and pool tests, respectively.

Tab. 27 – Sonars and G > S > P Sys dynamic datasets in the sea test.

Path length [m]	Device	Positioning	Data sample (no.)	Main data
~11.50 linear	Deeper GNSS CHIRP+	SPP	150	Latitude, longitude
	Deeper GNSS Pro+ 2	SPP	150	Latitude, longitude
		SPP	150	Latitude, longitude
	G > S > P Sys	PPP-kinematic	150	Latitude, longitude
		PPK	150	Latitude, longitude

Tab. 28 – G > S > P Sys dynamic datasets in the pool test.

Path length [m]	Device	Positioning	Data sample (no.)	Main data
~26.84 rectangular	G > S > P Sys	SPP	1000	Latitude, longitude, ellipsoidal height
		PPP-kinematic	1000	Latitude, longitude, ellipsoidal height
		PPK	1000	Latitude, longitude, ellipsoidal height



(a)



(b)

Fig. 24 – (a) Pool test; (b) G > S > P Sys on the floating platform.

4.3.3.3. Sonars depth dataset

Two tests were conducted to assess the Deeper Smart Sonar CHIRP+ and Pro+ 2's effectiveness in depth measurement. The first test, in a swimming pool, aimed to determine sonar accuracy in fresh, clear, and still water. The second test, conducted in the sea, evaluated sonar performance in saltwater and natural conditions, at locations specified in paragraph 4.3.3.2. In both environments, sonar was used to measure depths at two points: 0.9 m and 1.52 m, representing the pool's shallow and deep ends. Depth measurements at these points were also taken using traditional tools, such as a rigid meter, graduated pole, and weighted metric roll, for validation against the sonar readings (Alvarez *et al.*, 2018; Bandini *et al.*, 2018). Ef-

forts were made to maintain consistent water temperatures across both tests. The mean salinity at the Mar Grande in Taranto, the sea test site, is approximately 37.8‰ (Di Leo *et al.*, 2014; Cardellicchio *et al.*, 2016). The “flexible arm mount 2.0” by Deeper UAB was employed in both tests to ensure the sonar’s stable immersion in water. Tab. 29 presents the data composition for these water depth measurements.

Tab. 29 – Sonars depth dataset.

Device	Real depth [m]	Water	Temperature [°C]	Data sample (no.)	Main data
Deeper Smart Sonar CHIRP+	0.9	Fresh	22.27	3700	Depth
		Salt ~ 37.8‰	20.90	3700	Depth
	1.52	Fresh	22.27	3700	Depth
		Salt ~ 37.8‰	20.90	3700	Depth
Deeper Smart Sonar Pro+ 2	0.9	Fresh	22.27	3700	Depth
		Salt ~ 37.8‰	20.90	3700	Depth
	1.52	Fresh	22.27	3700	Depth
		Salt ~ 37.8‰	20.90	3700	Depth

4.3.3.4. G > S > P Sys 3D modelling datasets

Surveys for creating 3D modelling datasets were carried out using the Deeper Smart Sonar CHIRP+ integrated into the G > S > P Sys, as depicted in Fig. 23. The dataset aimed at modelling artificial structures, specifically a swimming pool with varying bottom depths, was generated through surveys in the pool mentioned in paragraph 4.3.3.2. A separate dataset for 3D modelling of natural surfaces was created through seabed surveys at the site indicated in the same paragraph. This survey encompassed an area of approximately 3 hectares, extending to a maximum distance of 240 meters from the coast, as illustrated in Fig. 25a.

The seabed survey involved executing 16 orthogonal transects and one parallel to the coastline, collecting a total of 1659 points. It was conducted semi-automatically, with real-time mapping facilitated by the Fish Deeper—Fishing App, guiding the completion of transects in specific map areas. This method is suitable for cost-efficient science and citizen science projects.

The G > S > P Sys was mounted on a Stand Up Paddle (SUP) board, connected to a new floating platform (prototype 3, shown in Fig. 25b,c). This low-cost platform featured a trimaran structure for enhanced navigational stability. An “F” bracket was installed at the stern to align the external GNSS antenna planimetrically with the Sonar, as indicated in Fig. 25b, d (green circle).

For clarity in paragraph 4.3.4, which discusses 3D modelling, specific naming conventions were adopted for different data files. The file from the Deeper Smart Sonar CHIRP+ was named “File Sonar”. The file with real-time positioning data in SPP from the SimpleRTK2B was designated as “File SPP”. Lastly, the file containing post-processed positioning data in PPK from the SimpleRTK2B was labelled “File PPK”.

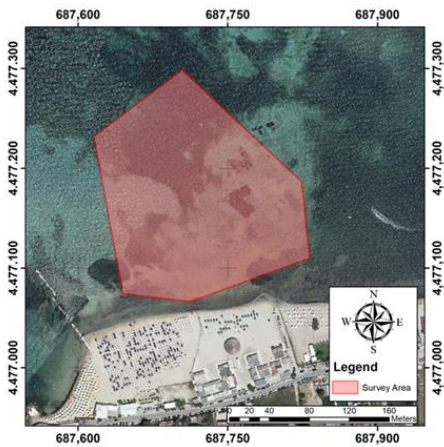
Tab. 30 details the dataset components for 3D seabed modelling (natural surface), while Tab. 31 outlines the dataset composition for 3D modelling of the swimming pool (artificial structure).

Tab. 30 – Dataset for natural surface modelling (sea survey).

Area Surveyed [sqm]	Transects (no.)	Device	File produced	Positioning	Points Surveyed (no.)	Main data
~30,000	16 + 1	Deeper Smart Sonar CHIRP+	File Sonar	SPP	1659	Latitude, longitude, depth
		SimpleRTK2B	File SPP	SPP	6098	Latitude, longitude, ellipsoidal height, GPST
		SimpleRTK2B	File PPK	PPK	6098	Latitude, longitude, ellipsoidal height, GPST

Tab. 31 – Dataset for artificial structure modelling (pool survey).

Area Surveyed [sqm]	Transects (no.)	Device	File produced	Positioning	Points Surveyed (no.)	Main data
~40.01	2 + 2	Deeper Smart Sonar CHIRP+	File Sonar	SPP	111	Latitude, longitude, depth
		SimpleRTK2B	File SPP	SPP	982	Latitude, longitude, ellipsoidal height, GPST
			File PPK	PPK	982	Latitude, longitude, ellipsoidal height, GPST



(a)



(b)



(c)



(d)



(e)



(f)

Fig. 25 –(a) Sea survey area; (b) instruments setup; (c) deployment of the floating platform; (d) SUP setup; (e) floating platform - SUP final setup; (f) execution of survey operations at sea.

4.3.4. Technical notes on bathymetric data 3D modelling

The paragraph details the pipeline used to create 3D models from the datasets reported in paragraph 4.3.3.4. The process models the seabed as an example of natural surfaces and the swimming pool as an example of an artificial structure. As outlined in paragraph 4.3.1, the modelling process involves three stages: synchronization, interpolation, and 3D modelling. Fig. 26 illustrates the comprehensive pipeline for 3D modelling, including the primary software utilized for implementation.

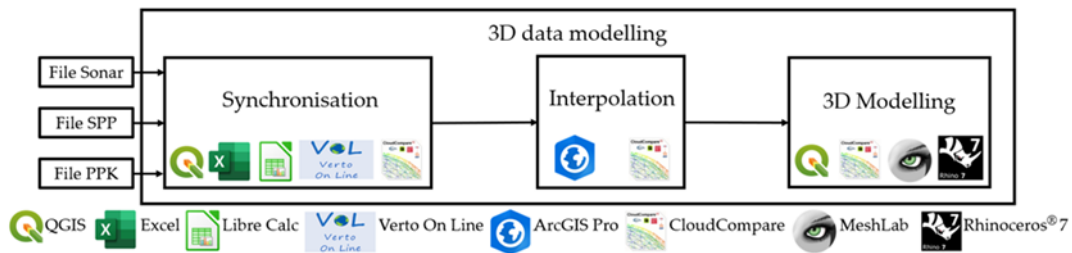
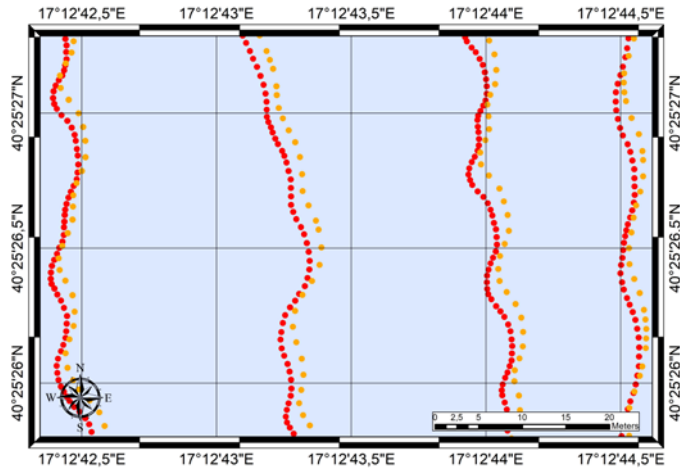


Fig. 26 – G > S > P Sys pipeline for 3D modelling of bathymetric data.

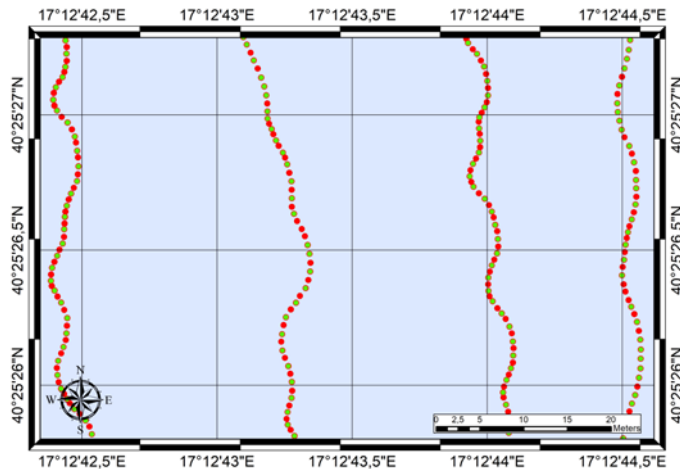
4.3.4.1. Synchronisation of Sonar and GNSS data

Synchronization was executed in the software QGIS (QGIS Development Team), utilizing the ‘native:joinattributetable’ geoprocessing algorithm for joining attributes between fields. Additional data processing tasks were carried out using spreadsheet applications, specifically Excel and Libre Calc. The synchronization process entailed the following steps:

1. the File Sonar was aligned with File SPP using latitude and longitude fields, resulting in a combined file termed “File Sonar + SPP”. This process linked the File Sonar with the GPS Time value from the system;
2. File Sonar + SPP was then synchronized with File PPK through the shared GPS Time field. Fig. 27a illustrates the pre-synchronization File Sonar + SPP in orange and File PPK in red. The resultant file, “File Sonar + SPP + PPK”, incorporated latitude, longitude, and ellipsoid height data adjusted to PPK, along with water depth and point acquisition time. Fig. 27b presents a comparative view of File Sonar + SPP + PPK in green against File PPK in red.



(a)



(b)

Fig. 27 – (a) Comparative representation of File Sonar + SPP (depicted in orange) and File PPK (show in red); (b) Comparative representation of File Sonar + SPP + PPK (represented in green) and File PPK (illustrated in red).

Following synchronization, the File Sonar + SPP + PPK typically undergoes these processing steps:

1. adjustment for the spatial discrepancy between the GNSS antenna and the sonar transducer;

2. correction for the difference in position between the sonar transducer and the keel line;
3. selection of an appropriate vertical reference system, such as Mean Sea Level (MSL), Lowest Astronomical Tide (LAT), a physical geoid model, or a reference ellipsoid (International Hydrographic Organization, 2020);
4. adjustment for water level fluctuations.

In this particular instance, the horizontal offset between the GNSS antenna and the sonar transducer was effectively neutralized by the design of the floating platform. For vertical referencing, the Taranto tide gauge from the National Mareographic Network was employed, situated a few kilometres from the survey site in Mar Grande. Corrections for water level variations were derived from this tide gauge data. To facilitate subsequent processing in CloudCompare, the GNSS coordinates of the survey points were converted to the WGS84/UTM33N system.

A random sample of 1,000 points, approximately 60% of the surveyed points, was selected for 3D modelling. The remaining 40% were reserved for use in the model validation phase.

4.3.4.2. Interpolation for bathymetric grid creation

As indicated in paragraph 4.3.1, the primary interpolation utilized ArcGIS Pro, employing the Forest-based Classification and Regression algorithm. The steps for data interpolation involved:

1. establishing parameters and generating an initial bathymetric grid using the IDW interpolation, as depicted in Fig. 28c;
2. identifying training features for the Forest-based Classification and Regression technique;
3. conducting training, executing the algorithm, and creating the conclusive bathymetric grid using the Forest-based Classification and Regression approach (referred to as grid FCR).

During the second stage, the surveyed bathymetric points were utilized as input training features. The depth functioned as the variable to predict, and the IDW bathymetric grid served as the explanatory training variable.

Fig. 28a displays the grid FCR, generated using the Forest-based Classification and Regression algorithm with 1×1 m cells. Figs. 28b and 28c illustrate additional grids for analytical comparison. Specifically, Fig. 28b features the bathymetric grid derived from the Ordinary Kriging interpolation (grid OK), and Fig. 28c presents the grid created using the IDW interpolation (grid IDW). The data in Figure 28 represent depth values in meters relative to the water level.

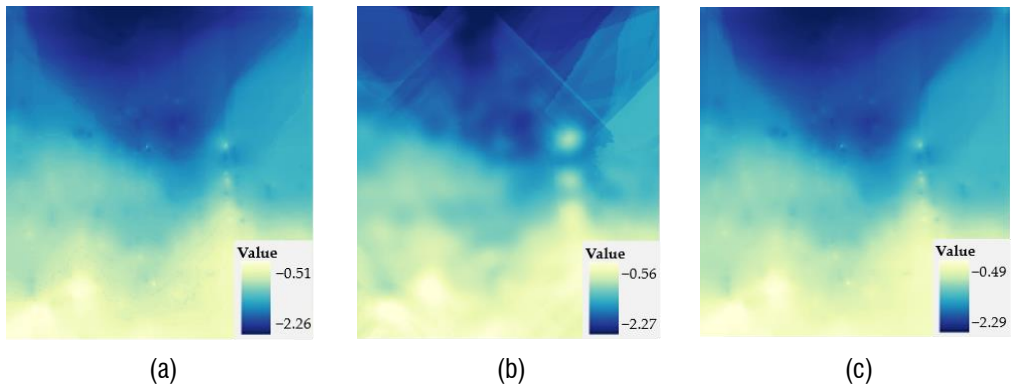


Fig. 28 – Interpolated bathymetric models: (a) grid FCR; (b) grid OK; (c) grid IDW.

4.3.4.3. Natural surface bathymetric 3D modelling

3D modelling was conducted using QGIS, CloudCompare, and Meshlab (Visual Computing Lab-ISTI-CNR, Pisa, Italy) (Cignoni *et al.*, 2008). The bathymetric grids from paragraph 4.3.4.2 (grid FCR, grid OK, and grid IDW) were imported into QGIS and converted into point shapefiles. Each point was assigned a depth value from the cell and coordinates in the WGS84/UTM33N system (using ID algorithms ‘native:pixelstopoints’ and ‘native:addxyfields’). The layers were then exported as text files (*.csv), with the option to add information for creating 3D models that emphasize depth, suitable for visualizing large surfaces with minimal height variations (examples in Fig. 29). These files were transformed into the Polygon File Format (*.ply) through CloudCompare to generate point clouds (Fig. 29a, 29b, 29c). Subsequently, Meshlab was used for 3D modelling. Within Meshlab, normals for the point cloud were generated, and the Poisson surface reconstruction method was applied to create tri-mesh 3D models (Fig. 29d, 29e, 29f). Textures from the bathymetric grids were

added in Meshlab to enhance model readability (Fig. 29g, 29h, 29i). For clarity, the 3D model using grid FCR was named 3D model FCR, that using grid OK as 3D model OK, and the one from grid IDW as 3D model IDW.

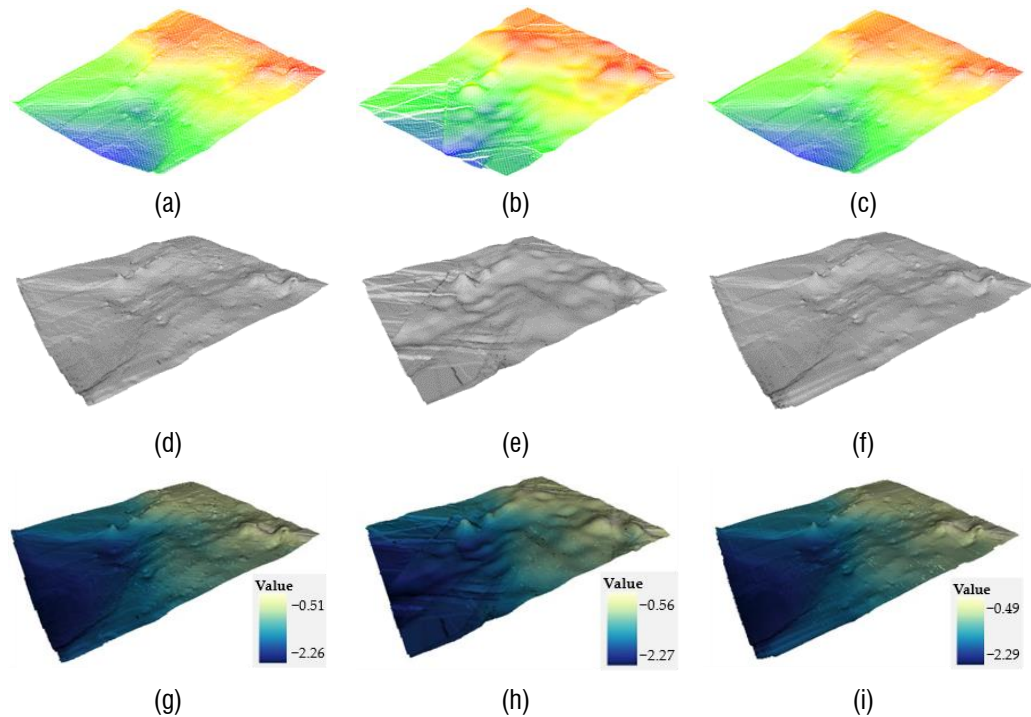


Fig. 29 – Modelling illustrations include: (a) point cloud FCR; (b) point cloud OK; (c) point cloud IDW; (d) 3D model FCR; (e) 3D model OK; (f) 3D model IDW; (g) textured 3D model FCR; (h) textured 3D model OK; (i) textured 3D model IDW.

4.3.4.4. Artificial structure bathymetric 3D modelling

In the 3D modelling of artificial structures, CloudCompare and Rhinoceros® 7 software (Robert McNeel & Associates, Seattle, Washington, USA) were utilized. For the swimming pool's modelling, GNSS and sonar data synchronization followed the procedure outlined in paragraph 4.3.4.1. Due to the use of the initial prototype floating platform in the survey, an horizontal adjustment was necessary between the GNSS antenna and the sonar. The pool's overflow edge served as the vertical reference. During the interpolation phase, given the small reconstruction area, the bottom point

cloud was created through linear interpolation of the nearest non-empty neighbouring cells.

Fig. 30a illustrates the point cloud post-synchronization and correction, with emerged edges from GNSS data and the bottom from $G > S > P$ Sys data. Red circles highlight unmeasured sections, such as pool ladders. Fig. 30b displays the interpolated pool bottom, a crucial step for providing longitudinal continuity to the sonar data for slicing operations. Fig. 30c presents the 3D model of the pool, surveyed using traditional techniques and considered as the ground truth in the analysis phase.

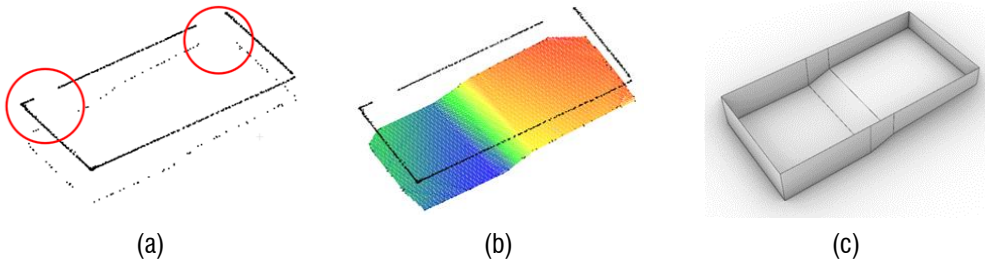


Fig. 30 – (a) Point cloud post synchronization and correction; (b) Interpolated bottom of the pool; (c) 3D model of the pool, surveyed through conventional methods.

In CloudCompare, using the Cross Section tool, contour lines for primitive creation were generated by extracting sections of the pool edge and bottom. To regularize the contour line of the pool edge, a mesh plane technique, as detailed in Costantino *et al.* (2021), was employed (see Fig. 31).

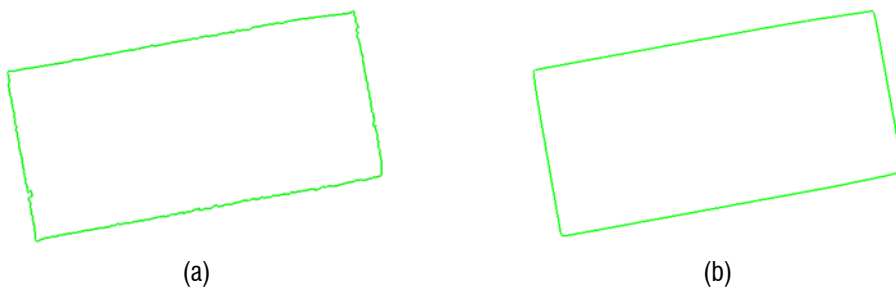


Fig. 31 – Pool edge regularization (a) before; (b) after.

Contour lines were imported into Rhino 7 for primitive creation and final 3D modelling. Primitives for pool walls and bottom were auto-generated using the ExtrudeCrv and

ExtendSrf commands (see Fig. 32a). The 3D model was then constructed using the Intersect, Meshpolyline, and Loft commands (refer to Fig. 32b).

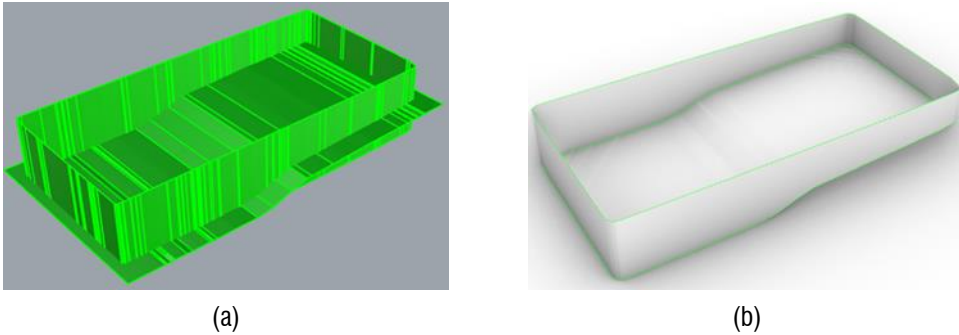


Fig. 32 – (a) Walls and bottom primitives; (b) 3D model of the pool.

4.4. Results of the third part of the research project

This paragraph summarizes the outcomes of tests analysing static and kinematic GNSS positioning, depth measurement accuracy and precision, and the 3D models' quality. It includes calculations of Total Horizontal Uncertainty (THU) and Total Vertical Uncertainty (TVU) at a 95% confidence level, based on the sixth edition of the IHO Standards for Hydrographic Surveys (International Hydrographic Organization, 2020), by:

$$TVU = 1.96 \cdot SDV \quad (68)$$

$$THU = 2.45 \cdot SD2D \quad (69)$$

the formulas defines SDV as the vertical Standard Deviation, applicable in depth measurements, and SD2D as the horizontal Standard Deviation, relevant in planimetric GNSS positioning. When positioning data are presented in North and East coordinates (SDN for North and SDE for East), the larger of the two Standard Deviation values is used. This approach aligns with the standard that represents THU with a single value. Evaluations and discussions of the results are reported in paragraph 4.5.

4.4.1. Sonars and G > S > P Sys GNSS positioning

The paragraph presents data from static and kinematic tests to evaluate GNSS receivers' geolocation capabilities. Tab. 32 displays real-time static Single Point Positioning data for Deeper Smart Sonar CHIRP+ (Deeper GNSS CHIRP+), Deeper Smart Sonar Pro+ 2 (Deeper GNSS Pro+ 2), and G > S > P Sys. All three devices were observed for 8 hours (28,800 seconds). Δ denotes the mean GNSS positioning errors in East (ΔE), North (ΔN), and Up (ΔU) relative to FATA. The Standard Deviation (SD) for GNSS positioning in East (SDE), North (SDN), and Up (SDU) for the receivers is also provided.

Tab. 32 - Real-time static SPP results of Deeper Smart Sonar CHIRP+, Deeper Smart Sonar Pro+ 2, and G > S > P Sys.

Device	Positioning	Obs. time [s]	ΔE [m]	ΔN [m]	ΔU [m]	SDE [m]	SDN [m]	SDU [m]	THU [m]
Deeper GNSS CHIRP+	SPP	28,800	0.761	2.621	ND	0.624	0.877	ND	2.150
Deeper GNSS Pro+ 2	SPP	28,800	1.706	3.537	ND	0.980	0.674	ND	2.401
G > S > P Sys	SPP	28,800	0.570	2.484	2.018	0.199	0.194	0.659	0.487

Fig. 33 simplifies the graphical assessment by displaying the real-time static horizontal SPP accuracy ($\Delta 2D$) of the G > S > P Sys over a 1 hour (3600 seconds) observation period.

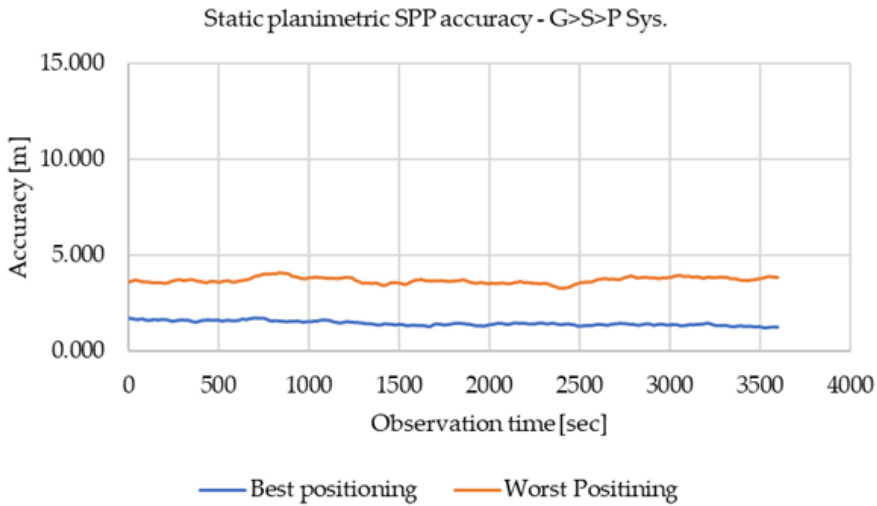


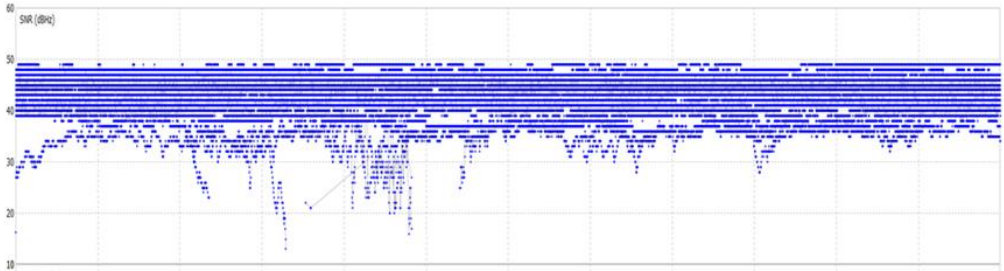
Fig. 33 – Accuracy levels (best and worst) in real-time static horizontal SPP for the G > S > P Sys over a 3600 second duration.

The best positioning observed during the 8 hour period is indicated in blue, while the worst positioning is shown in orange. The accuracy calculation is based on the following formula:

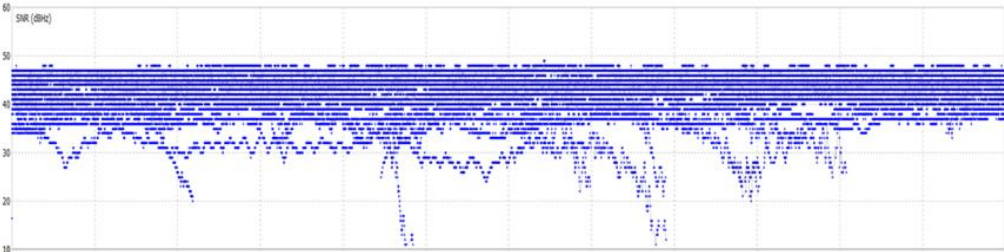
$$\Delta 2D = \sqrt{\Delta E^2 + \Delta N^2} \quad (70)$$

Figs. A12 and A13 in the Annexes compare the real-time static horizontal SPP accuracy of Deeper Smart Sonar CHIRP+ and Deeper Smart Sonar Pro+ 2.

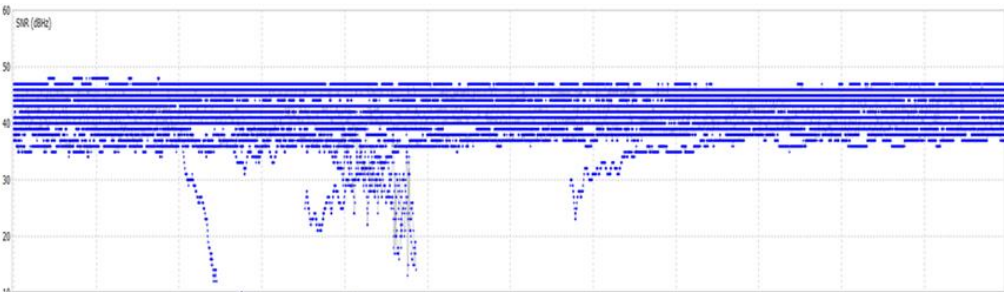
Fig. 34 displays the Signal-to-Noise Ratio (SNR) for the G > S > P Sys, where a higher SNR indicates improved measurement quality. These images present the SNR for L1 and L2 frequencies, correlating with the best and worst positions shown in Fig. 33 (over a 3600 second period). Additionally, Fig. A14 in the Annexes shows the SNR values for the Huawei P30 Pro (for L1 and L5 frequencies) for further comparison.



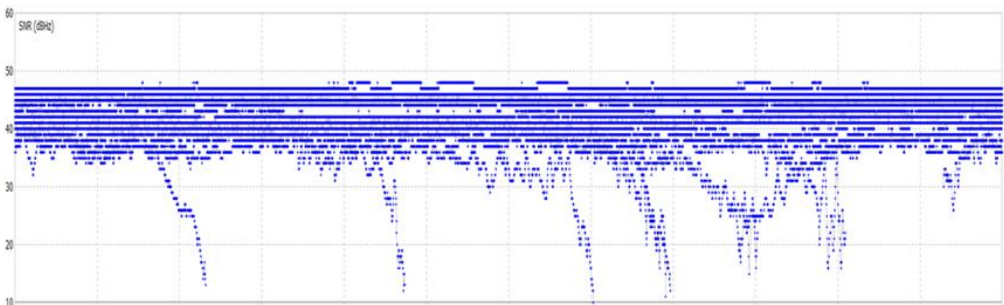
(a)



(b)



(c)



(d)

Fig. 34 – $G > S > P$ Sys SNR values: (a) best L1; (b) worst L1; (c) best L2; (d) worst L2.

Tab. 33 displays the G > S > P Sys's GNSS static positioning data, post-processed in both static and PPP modes. The Δ and SD values are derived from observations lasting 5 minutes (300 seconds), 15 minutes (900 seconds), 30 minutes (1800 seconds), and 1 hour (3600 seconds), from eight samples gathered over an 8 hour observation period.

Tab. 33 - Performances of the G > S > P Sys: static positioning and static PPP.

Device	Positioning	Obs. time [s]	ΔE [m]	ΔN [m]	ΔU [m]	SDE [m]	SDN [m]	SDU [m]	THU [m]
G > S > P Sys	Static	300	0.006	0.001	0.031	0.002	0.002	0.004	0.005
		900	0.006	0.001	0.030	0.002	0.002	0.005	0.005
		1800	0.006	0.001	0.031	0.002	0.001	0.006	0.004
		3600	0.006	0.001	0.031	0.001	0.001	0.006	0.003
	PPP	300	0.632	0.667	0.249	0.906	0.474	1.107	2.220
		900	0.712	0.639	0.074	0.317	0.134	0.320	0.778
		1800	0.765	0.636	0.043	0.143	0.058	0.148	0.352
		3600	0.750	0.646	0.026	0.022	0.010	0.033	0.053

Fig. 35 simplifies interpretation with a diagram illustrating the G > S > P Sys's accuracy evolution in static planimetric post-processed positioning over 3600 seconds. Data post-processed in static positioning is shown in grey, while data in PPP is in yellow. Additionally, Fig. A15 in the Annexes provides a diagram of 3D positioning accuracy.

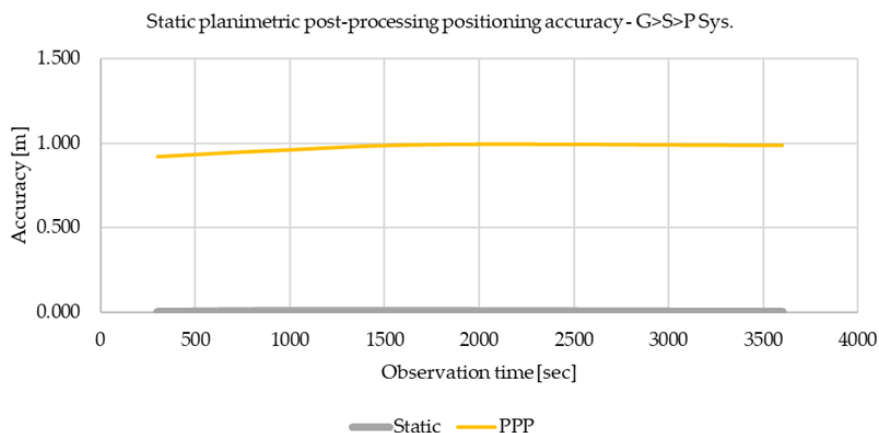


Fig. 35 – Accuracy of the G > S > P Sys in static planimetric post-processed positioning: static (grey); PPP (yellow).

Tabs. 34 and 35 present GNSS kinematic positioning test data for the Deeper Smart Sonar CHIRP+, Deeper Smart Sonar Pro+ 2, and the G > S > P Sys. Tab. 34 details sea test data, while Tab. 35 covers pool test data. For the Deeper Smart Sonars (CHIRP+ and Pro+ 2), sea test SPP data are included. The G > S > P Sys’s SPP, PPP kinematic, and PPK data from both sea and pool tests are reported. The μ 2D and μ 3D values indicate the mean distance of surveyed points from the travelled trajectory in horizontal and 3D, with SD2D and SD3D being their respective standard deviations.

Tab. 34 - Results of the Deeper Smart Sonar CHIRP+, Deeper Smart Sonar Pro+ 2, and G > S > P Sys in GNSS kinematic horizontal positioning during the sea test.

Path length [m]	Device	Positioning	μ 2D [m]	SD2D [m]	THU [m]
~11.50 linear	Deeper GNSS CHIRP+	SPP	2.007	1.911	4.682
	Deeper GNSS Pro+ 2	SPP	0.700	0.482	1.180
	G > S > P Sys	SPP	1.034	0.095	0.232
		PPP kinematic	0.640	0.092	0.226
		PPK	0.043	0.031	0.075

Tab. 35 - Results of the G > S > P Sys in GNSS kinematic positioning during the pool test.

Path length [m]	Device	Positioning	μ 2D [m]	SD2D [m]	μ 3D [m]	SD3D [m]	THU [m]
~26.84 rectangular	G > S > P Sys	SPP	0.438	0.390	0.524	0.350	0.956
		PPP kinematic	0.417	0.309	0.465	0.290	0.757
		PPK	0.037	0.040	0.061	0.060	0.098

Fig. 36 aids in assessing the dispersion of points surveyed in the pool test by comparing the G > S > P Sys's positioning data with the actual travelled trajectory, displayed in green. Specifically, Figs. 36a and 36d illustrate the SPP data in horizontal and 3D views, respectively. Figs. 36b and 36e depict the PPP kinematic positioning data in both horizontal and 3D formats, and Figs. 36c and 36f demonstrate the PPK positioning data in the same views. Additionally, Fig. A16 in the Annexes presents the dispersion of points surveyed in the sea test.

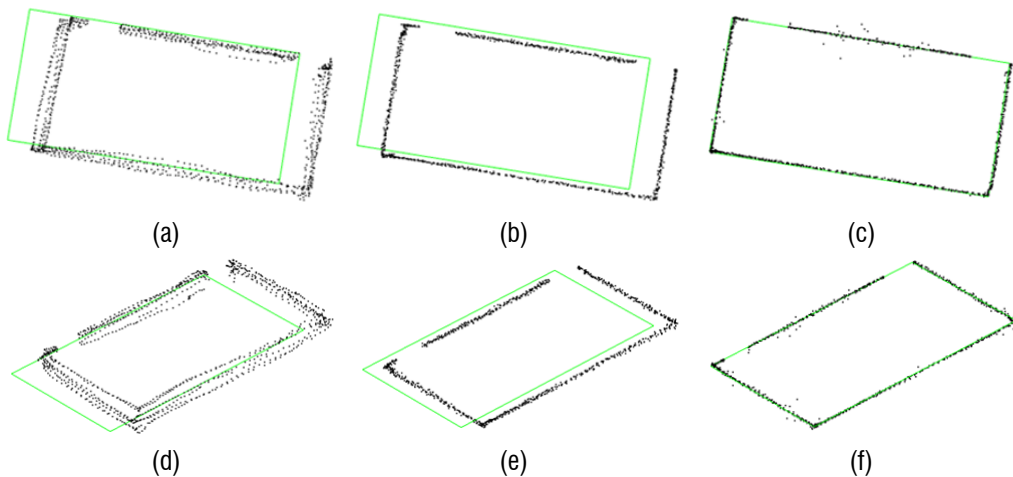


Fig. 36 – Results of G > S > P Sys's GNSS kinematic positioning in the pool test includes: (a) horizontal SPP; (b) horizontal PPP kinematic; (c) horizontal PPK; (d) 3D SPP; (e) 3D PPP kinematic; (f) 3D PPK positioning.

4.4.2. Sonars depth measurement results and bathymetric 3D modelling

The paragraph presents data assessing sonars performances in depth measurement and 3D modelling methods. Tab. 36 displays data evaluating the Deeper

Smart Sonars CHIRP+ and Pro+ 2 for depth measurement accuracy and precision. Measurements were taken at depths of 0.9 m and 1.52 m in both fresh and sea water (salinity 37.8‰). ΔV indicates the difference between the mean of 3700 measured depth samples and the actual depth, while SDV denotes the standard deviation of these measurements.

Tab. 36 - Results of depth measurement for Deeper Smart Sonars.

Device	Real depth [m]	Water	ΔV [m]	SDV [m]	TVU [m]
Deeper Smart Sonar CHIRP+	0.9	Fresh	0.02	0.00	0.00
		Salt ~ 37.8‰	0.02	0.02	0.04
	1.52	Fresh	0.01	0.00	0.00
		Salt ~ 37.8‰	0.01	0.11	0.21
Deeper Smart Sonar Pro+ 2	0.9	Fresh	0.03	0.00	0.00
		Salt ~ 37.8‰	0.02	0.02	0.04
	1.52	Fresh	0.02	0.00	0.01
		Salt ~ 37.8‰	0.04	0.06	0.12

To assess the quality of the 3D models produced, Cloud-To-Mesh (C2M) distance comparisons were conducted using CloudCompare, as shown in Tab. 37. For seabed, comparisons were made between the FCR, OK, and IDW 3D models, with 40% of points selected for final validation. In the case study of the pool, the 3D model generated by the proposed method was compared with a model reconstructed by traditional survey methods. Additionally, for the swimming pool, C2M analysis was applied to both the entire structure and the bottom only. In Tab. 37, μ_{3D} represents the mean C2M distance, and SD_{3D} is the corresponding standard deviation.

Tab. 37 – Mean and standard deviation of C2M distances for seabed and pool models.

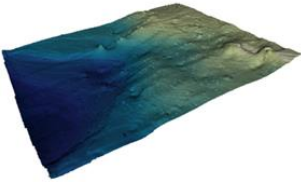
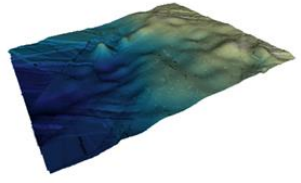
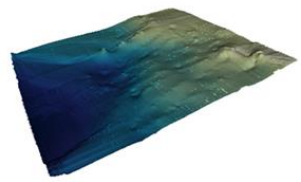
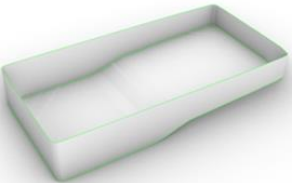

Model	Example images	Interpolation method	μ_{3D} [m]	SD _{3D} [m]
3D model FCR – natural surface		Forest-based Classification and Regression	0.0020	0.0323
3D model OK – natural surface		Ordinary Kriging	0.0043	0.0283
3D model IDW – natural surface		IDW	0.0059	0.0317
3D model pool – artificial structure		Linear interpolation	0.0124	0.0245
3D model bottom pool – artificial structure		Linear interpolation	0.0002	0.0140

Fig. 37 displays vertical sections of three seabed 3D models to evaluate interpolation and 3D modelling methods. Validation points are marked with black squares. The FCR model's section is in blue, OK's in orange, and IDW's in red. Fig. 37a presents all three sections together, while Figs. 37b and 37c offer disaggregated data for easier comparison between models (FCR vs. IDW in Fig. 37b and FCR vs. OK in Fig. 37c).

Additionally, Fig. A17 in the Annexes provides histograms of the analysis conducted on the pool.

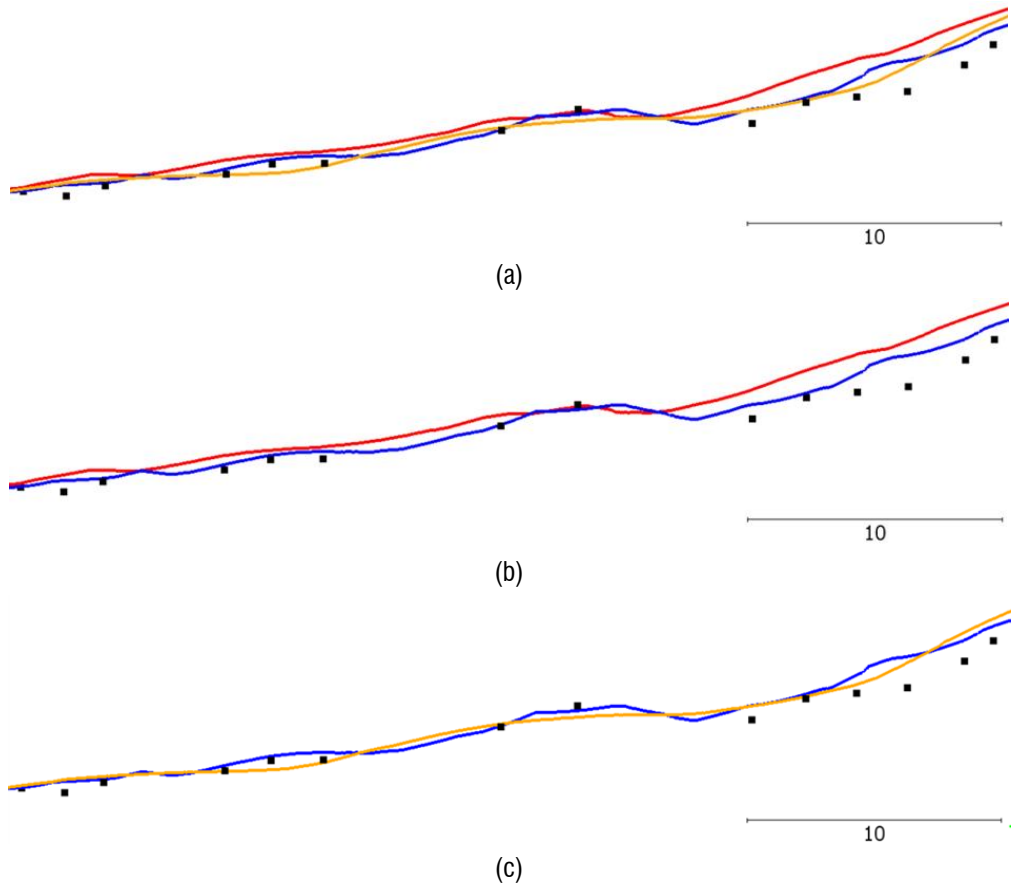


Fig. 37 – Longitudinal vertical sections of 3D models with validation points shown as black squares: (a) FCR model (blue) - OK model (orange) - IDW model (red); (b) FCR model (blue) - IDW model (red); (c) FCR model (blue) - OK model (orange).

4.5. Evaluations and discussions of the third part of the research project

Comparing the TVU values in Tab. 36 (best at 0.00 m and worst at 0.21 m) with the IHO TVU standards (International Hydrographic Organization, 2020) shown in Tab. 38, the Deeper Smart Sonars' depth measurements fall between the Exclusive and Special Orders.

The geolocation of devices in static tests shows that the $G > S > P$ Sys outperformed the Deeper Smart Sonars in Single Point Positioning, as indicated in Tab. 32

and Figs 33, A12 and A13. In post-processing, as shown in Tab. 33, Figs. 35, and A15, static processing yielded better results compared to PPP static.

Dynamic test analysis shows the THU values for Deeper Smart Sonars, as listed in Tab. 34 (1.180 and 4.682 m), align between the Special Order and Order 1 when compared to reference THU standards in Tab. 38 (International Hydrographic Organization, 2020). For the G > S > P Sys, as indicated in Tabs. 34 and 35 and Fig. 36, THU values in all positioning types (SPP, PPP kinematic and PPK) meet the Exclusive Order criteria, with the highest value being 0.956 m. The point dispersion for the G > S > P Sys in SPP, as shown in Fig. A16, was less than that of the Deeper Smart Sonars. Additionally, Figs. 34 and A14 reveal that the SNR of the G > S > P Sys consistently surpasses the internal GNSS receiver of the Huawei P30 Pro.

Reviewing the THU and TVU values of the Deeper Smart Sonars, it appears that these systems' sensors show uncertainty values ranging from Order 1 in the worst case to Special Order in the best case. Conversely, the G > S > P Sys's uncertainty values range from Special Order in the worst case to Exclusive Order in the best case.

Tab. 38 – Bathymetry IHO standards for safety of navigation hydrographic surveys (data source: International Hydrographic Organization, 2020).

Criteria	Order 2	Order 1 (a/b)	Special order	Exclusive order
THU	20 m + 10% of depth	5 m + 5% of depth	2 m	1 m
TVU	a = 1.0 m b = 0.023	a = 0.5 m b = 0.013	a = 0.25 m b = 0.0075	a = 0.15 m b = 0.0075
$\sqrt{a^2 + (b \cdot d)^2}$ (71)				

Where, in TVU calculations, “a” represents the constant portion of uncertainty, “b” is a coefficient for the depth-dependent portion of uncertainty, and “d” denotes the depth.

The μ 2D values of the Deeper Smart Sonar’s internal GNSS receivers, as shown in Tab. 34 (2.007 and 0.700 m), surpassed the accuracy levels estimated by Bandini *et al.* (2018), aligning more closely with Bogoyavlensky *et al.* (2020). While Giambastiani *et al.* (2020) described the Deeper Smart Sonar’s GNSS receiver as “highly

accurate”, it is more accurately characterized as having good accuracy. The ΔV values in Tab. 36 (ranging from 0.01 to 0.04 m) indicate better shallow water depth measurement accuracy than Kellerer-Pirklbauer *et al.* (2021) estimated, aligning more with Bandini *et al.* (2018). These variances might stem from different measurement methods and advancements in the studied systems’ sensors. The $\mu 2D$ values of the $G > S > P$ Sys in PPK, shown in Tabs. 34 and 35 (0.043 and 0.037 m), demonstrate its greater accuracy compared to the method in Bandini *et al.* (2018) and its independence from UAV usage. Compared to Bandini *et al.* (2023), the $G > S > P$ Sys offers excellent real-time geolocation in SPP, meeting the THU Exclusive Order standards. Using smartphones as sensors provided advantages in system prototyping, operation, and microchip conservation during the semiconductor crisis. Its lightweight nature also allows for UAV and USV deployment (Pepe, Alfio and Costantino, 2022). However, a system based on smartphones has inherent weaknesses, such as susceptibility to malfunctions due to varying smartphone models and the impact of OS and app updates over time.

Regarding 3D modelling of natural surfaces, analysis of C2M values in Tab. 37 indicates that the FCR 3D model achieved the best $\mu 3D$ value, with only marginal differences in SD3D values. For the 3D modelling of artificial structures, both the $G > S > P$ Sys and the proposed 3D modelling pipeline demonstrated the capability to achieve centimetre-level accuracy and precision.

The analysis of Machine Learning interpolation is notably insightful. By examining the bathymetric grids in Fig. 28 and the 3D models in Fig. 29, it’s apparent that the FCR grid maintained the overall structure of the IDW grid while attempting to adjust values based on sonar points used for training. As demonstrated in Fig. 37c, this approach resulted in the FCR 3D model section being numerically similar to the OK model section.

To provide a comprehensive perspective, a comparison was conducted between the proposed spatio-temporal PPK synchronization method and an alternative time-only PPK synchronization method. In the time-only approach, sonar time is synchronized in post-processing with the GPS Time from the File PPK, converting times to Coordi-

nated Universal Time (UTC). This method doesn't involve intermediate steps like electronic and spatial synchronization but introduces inherent errors due to aligning two different time systems (sonar and GPS clocks) and limits synchronization to the nearest second. The outcomes of this method showed a μ 2D of 0.308 m, a SD2D of 0.130 m, and a THU of 0.318 m, which are inferior to the results from the spatio-temporal PPK synchronization but still align with the Exclusive Order THU standards.

CHAPTER 5. GNSS-AIDED PHOTOGRAMMETRY VIA VIDEO BY SMARTPHONE AND LOW-COST SENSORS SYSTEMS

In chapter 3, it was observed how the release of the mobile devices (smartphone and tablet) equipped with depth sensors on the consumer market generated an interesting line of research based on the use of the depth sensors for the production of point clouds and creation of 3D mesh models of reality in a rapid and expeditive mode. Despite the great potential application of depth sensors, the second research conducted showed problems in the point clouds generated by these sensors (e.g. deformation and surface splitting) due to INS drift problems. These problems, for example, limit the use of these sensors systems for scanning large objects and large scenarios. Furthermore, it can be noted that depth sensors for mobile devices are only available for certain devices with a high price, and this limits the diffusion of expeditious scanning methods via smartphones and tablets. On the other hand, studies on smartphones and tablets depth sensors show a strong interest in the scientific and professional community around the low-cost expeditive scanning systems and methods. Based on these observations, in the fourth part of the research project, the GNSS-aided terrestrial photogrammetry were explored. In fact, as will be seen in the literature review paragraph 5.1, the GNSS-aided terrestrial photogrammetry allows the production of point clouds automatically scaled and georeferenced in expeditive mode and without the use of Ground Control Points (GCPs) in the photogrammetric elaboration, for a subsequently application in 3D mesh modelling. Furthermore, the GNSS-aided terrestrial photogrammetry, if implemented on smartphones (partially or fully) by choosing the correct method, could be a valid alternative to mobile devices depth sensors scanning as it could preserve a very similar user experience, improve some critical aspects of point clouds produced by depth sensors and it could be more cost-effective and applicable also on smartphones and tablets without depth sensors (so cheaper).

5.1. Literature review of the fourth part of the research project

Regarding the other works related to the topics of the GNSS-aided terrestrial photogrammetry; Forlani *et al.* (2014) tested a system consisting of a digital camera and a Global Positioning System (GPS) receiver, with the camera mounted on a pole together with the GPS antenna. The authors performed several tests in urban scenarios (several buildings, a car parking and a city block) and found an accuracy in the range of 3-8 cm.

Jaud *et al.* (2020) experimented a system consisting of a high-precision Real-Time Kinematic (RTK) GNSS receiver mechanically aligned via a frame to a camera. In particular, the authors experimented with two cameras in their system, an reflex camera and a smartphone camera. Using this system, Jaud *et al.* (2020) surveyed a coastal cliff and obtained a mean error of 0.3 cm and a standard deviation of 4.7 cm with the reflex camera and a mean error of 0.2 cm and a standard deviation of 3.8 cm with the smartphone camera.

Tungol *et al.* (2021) tested the possibility of using photogrammetry assisted by the GNSS receiver integrated in smartphones to create appropriately scaled 3D models to estimate the fragmentation size distribution in mining. The authors, in order to overcome the problem of low accuracy of the smartphone GNSS receiver, proposed increasing the number of geotagged images to statistically reduce the scaling error of the 3D model.

Barazzetti, Previtali and Roncoroni (2022) studied the use of videos captured with 360° cameras assisted by the GNSS receiver integrated in the smartphone. The authors used the approximate trajectory recorded by the GNSS smartphone receiver to obtain the initial external orientation parameters of the video frames in order to reduce the number of combinations during the image matching phase and georeference the photogrammetric project. To compensate for the lack of reliable measurements, the authors integrated surveyed GNSS points with a more accurate external GNSS receiver to increase the overall georeferencing accuracy of the project.

Eker *et al.* (2022), inspired by the UAV systems that integrate differential GNSS receivers, realised a system for terrestrial photogrammetry assisted by the GNSS posi-

tioning in Post-Processed Kinematic (PPK) mode. With their system, the authors surveyed a historical windmill.

Toriya *et al.* (2022), applied the photogrammetry assisted by the GNSS receiver integrated in smartphones to measure the fragmentation size distribution in a real mining site, a quarry.

Morelli *et al.* (2022) tested a system consisting of a low-cost GNSS receiver and an action camera. The GNSS antenna was mounted on top of a geodetic pole and the action camera was mounted on the same pole via a short arm. The authors proposed a calibration method for calculating the lever arm between the antenna phase centre and the centre of projection of the camera. In addition, Morelli *et al.* (2022) tested two operative surveying pipelines, static and kinematic, and experimented the use of photos or video frames georeferenced.

Eker (2023), in a following paper dedicated to the comparison of a handheld mobile laser scanning and PPK-aided terrestrial photogrammetry, was able to determine the surface deformation of a section of forest road.

Previtali *et al.* (2023) tested a GNSS-aided photogrammetry system consisting of a 360° action camera and a high-precision GNSS receiver mounted together on a geodetic pole. In the application of the system, Previtali *et al.* (2023) proposed three operational approaches for data acquisition called: static, stop-and-go and kinematic; and subsequently in photogrammetric processing the authors used geotagged images (photos and video frames) in combination with appropriately decomposed video in frames. In the survey of the courtyard of the Politecnico di Milano (Lecco Campus), the authors obtained an mean discrepancy between the static approach and a reference point cloud of 2.7 cm for vertical surfaces (e.g. building façades) and 3.5 cm for the courtyard horizontal paving.

5.2. Aims of the fourth part of the research project

Analysing the literature, it can be observed that among the various GNSS-aided photogrammetry methods used by the various authors, the operative approaches proposed by Previtali *et al.* (2023), being mainly based on video acquisition, are closest to the user experience of depth sensors systems for smartphones and tablets.

Furthermore, as reported in Morelli *et al.* (2022) and Previtali *et al.* (2023), in contrast to UAV applications, the scientific research devoted little attention to research concerning GNSS-aided photogrammetry in terrestrial applications.

Based on these observations, the specific aims of the fourth research will concern:

1. the study of GNSS-aided photogrammetry via video acquisition implemented by smartphones and low-cost sensors systems (in this case it would be possible to call it also “GNSS-aided videogrammetry”) in order to increase the knowledge of the performance of these methodologies in the production of point clouds and 3D mesh models;
2. the application of GNSS-aided terrestrial photogrammetry in two challenging case studies to test the method under real field conditions;
3. the qualitative and quantitative comparison between GNSS-aided terrestrial photogrammetry by smartphone and mobile devices depth sensors scanning, to highlight performance and limitations.

5.3. Materials and methods of the fourth part of the research project

5.3.1. Cameras, devices and apps

The devices used in the experimentation were the Huawei P30 Pro, the SimpleRTK2B and the Insta360 X3 (Arashi Vision Inc., Shenzhen, China).

The Huawei P30 Pro smartphone was used as a device for managing apps and capturing photos and videos. Photos and videos were captured with the integrated rear camera with a 1/1.7” 40 MP CMOS sensor, F1.6 aperture and 27 mm equivalent focal length (35 mm). The other technical specifications of the Huawei P30 Pro were listed in the Tab. 17. and in paragraph 4.3.2.1.

The SimpleRTK2B, with the same settings and hardware configuration described in the paragraph 4.3.2.1, was used as smartphone external GNSS receiver for the Huawei P30 Pro. The SimpleRTK2B was used to geolocalise the other devices in Network Real-Time Kinematic (NRTK) GNSS mode and to record the raw GNSS data for subsequent post-processing. The technical specifications of the SimpleRTK2B are shown in the Tab. 25.

Insta360 X3 is a 360° action camera with 1/2” 48 MP CMOS sensors, F1.9 aperture, 6.7 mm equivalent focal length (35 mm) and 6-axis gyroscope. In the experimentation, the Insta360 X3 was used to implement GNSS-aided photogrammetry approaches that required spherical photos and videos. Tab.39 shows the main technical features of the camera.

Tab. 39 – Main technical features of the Insta360 X3

Device	Insta360 X3
Image	
Digital camera [MP]	48
Sensor size [“]	1/2
Aperture size	F 1.9
Equivalent focal length (35mm) [mm]	6.7
Inertial sensors	6 axis gyroscope
Weight [g]	180
Dimensions [mm]	46 × 114 × 33.1

Regarding the apps, SW Maps GIS & Data Collector and RTK camera (REDcatch GmbH - Pointcloud Engineering, Fulpmes, Austria) were used.

SW Maps was used (together with SimpleRTK2B) for NRTK GNSS positioning and GNSS raw data recording for post-processing.

RTK camera, allowing the connection of the smartphone to an external GNSS receiver (e.g. the SimpleRTK2B) and the connection to a network of permanent stations (e.g. HxGN SmartNet), enables the acquisition of automatically georeferenced photos in NRTK GNSS and the recording of the route travelled. In the research, the app was

used to automatically geotag, via the SimpleRTK2B, photos acquired with the built-in camera of the smartphone.

Finally, in line with chapter 3, depth sensor scans were performed with the iOS LiDAR scanner of the iPad 2021 Pro and the 3D Scanner App™. The iOS LiDAR was chosen because it has the best resolution and is currently the most studied of the depth sensors for mobile devices.

5.3.2. The GNSS-aided photogrammetry via videos and geotagged images

The observation at the base of the three practical approaches to GNSS-aided photogrammetry proposed in Previtali *et al.* (2023), consists in the possibility of merging data from videos of the surveyed element with some geotagged images (photos and/or video frames) of the element itself to automatically produce a scaled and georeferenced point cloud without the use of GCPs. Specifically, the videos, captured and subsequently decomposed into video frames (to be introduced in the photogrammetric process), provide the necessary data for the production of the point cloud in terms of form, while the geolocalised images, “dragging” the video frames during the images alignment process, provide the data to scale and georeference the entire point cloud.

The point cloud production process is performed via digital photogrammetric approach using Structure from Motion and Multi-View Stereo (SfM-MVS) algorithms in software that supports the use of georeferenced images. The point clouds produced can subsequently be transformed into 3D mesh models. The photogrammetry software Agisoft Metashape Professional 1.7.6 (Agisoft LLC, St. Petersburg, Russia) was used to produce the point clouds and 3D mesh models.

Three approaches to GNSS-aided photogrammetry were investigated in the experimentation; these approaches differed from each other in terms of the method of geolocalisation of the images, the type of images and the type of sensors systems used. According to the classification of Previtali *et al.* (2023), the first and second approaches correspond to static approaches while the third approach is kinematic. The differences with other systems and approaches proposed in the literature will be discussed in the paragraph devoted to evaluations and discussions (paragraph 5.5).

In the first approach, the sensors system consists of the Huawei P30 Pro, the built-in rear camera of the smartphone and the SimpleRTK2B. Videos and geotagged images are captured with the camera of the Huawei P30 Pro. The images consist of photographs automatically geotagged in NRTK GNSS via the RTK camera app. The data merging between the video frames (derived from the videos) and the geotagged photographs is performed automatically in the photogrammetry software. In the three approaches described, the decomposition of videos into video frames is performed in the Open Source software VLC media player 3.0.18 Vetinari (VideoLAN). Fig. 38 shows the pipeline of the first approach.

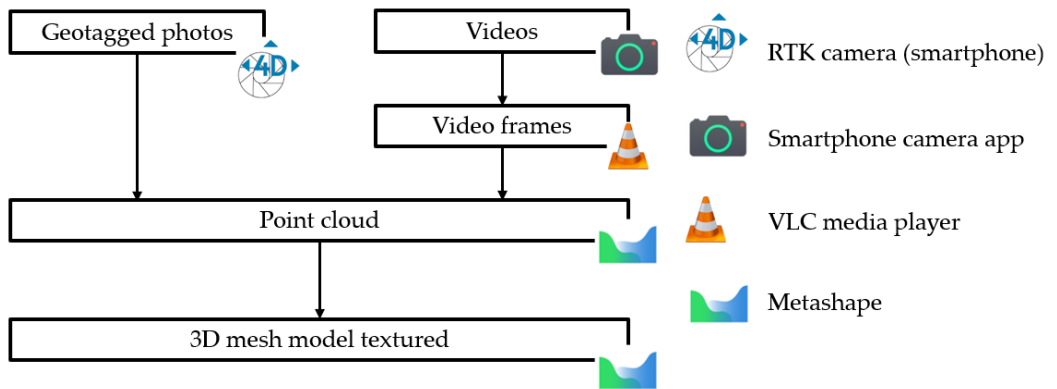


Fig. 38 – Pipeline of the first approach to GNSS-aided photogrammetry via videos and geotagged photos (smartphone).

In the second approach, the sensors system consists of the Huawei P30 Pro, the Insta360 X3 and the SimpleRTK2B. The images to be geolocalised consist of photographs; the videos and photographs are acquired in spherical format with the Insta360 X3, and in the photogrammetric process they are used in equirectangular format (Herban *et al.*, 2022; Pepe *et al.*, 2022). To geolocalise the photos, the positions occupied by the Insta360 X3 during the images acquisition phase are simultaneously surveyed in NRTK GNSS mode via the SW Maps app. Subsequently, the geolocation data and photos are associated in the photogrammetry software according to the acquisition sequence, thus the geotagged spherical photos are created in Metashape. Finally, photogrammetric processing is performed, where video frames (derived from

the acquired videos) and geolocalised photos are merged to produce the point cloud. Fig. 39 shows the pipeline of the second approach.

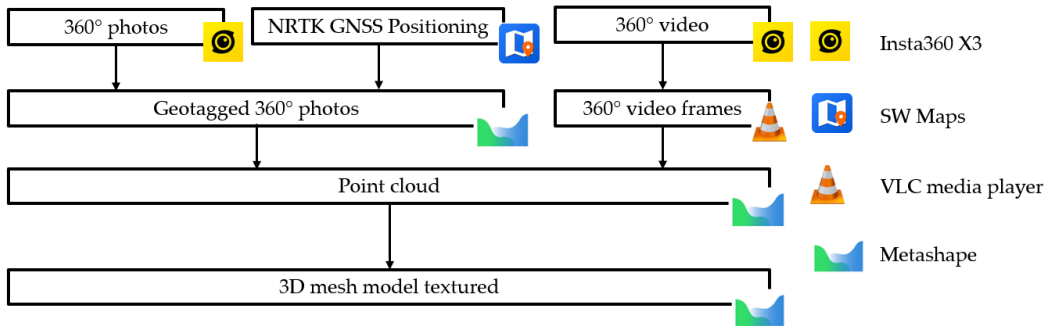


Fig. 39 – Pipeline of the second approach to GNSS-aided photogrammetry via videos and geotagged photos (360° action camera).

In the third approach, the sensors system consists (as in the second approach) of the Huawei P30 Pro, the Insta360 X3 and the SimpleRTK2B. But differently to the second approach, the images to be georeferenced consist of the video frames extracted from the spherical videos used for the survey (if there are multiple videos, it is not necessary to georeference all the videos, but only the videos chosen to georeference the point cloud).

The principle at the basis of georeferencing video frames is to iteratively estimate the optimised trajectory travelled by the 360° action camera, based on the GNSS trajectory recorded during the survey and post-processed. The operation is based on the use of the Iterative Closest Point (ICP) algorithm, that among its many applications is also used for motion and location estimation in the fields of robot navigation and autonomous driving (Martínez *et al.*, 2006; Almeida and Santos, 2013). Introduced by Chen and Medioni (1992) and Besl and McKay (1992), the ICP algorithm iteratively solves the problem of optimal geometric alignment between two three-dimensional models (e.g. two sets of structured points) by searching the translations and rotations that minimise a certain error metric, the algorithm provides an initial rough alignment (Rusinkiewicz and Levoy, 2001). In the Point-to-Point version of the algorithm, the

objective function of the ICP is expressed by the equation (Holz *et al.*, 2015; Balazadegan Sarvrood, Hosseinyalamdary and Gao, 2016):

$$\min_{R, T} \sum_{a_i} \|(Ra_i + T - b_i)\|^2 \quad (72)$$

where, T is the translation vector, R is the rotation matrix, a_i is the i-th point of the first set of points to be aligned with b_i , which represents the i-th point of the second set of points, to form matching pairs of points.

From an applicative point of view, for the georeferencing of the video frames, an initial photogrammetric alignment of the video frames is performed to determine the camera poses. The camera poses are then iteratively re-aligned with the GNSS trajectory acquired during the survey and post-processed. In accordance with the use of the ICP algorithm, the re-alignment first is performed in roughly mode and then optimised via ICP to arrive at the best possible alignment. In the application of the algorithm, the camera poses represent the set of points to be aligned and the post-processed GNSS trajectory represents the set of reference points. At the end of the alignment process, the camera poses are re-associated with the video frames and the photogrammetric process to generate the point cloud is performed.

Regarding the GNSS trajectory, in this experimentation, the raw GNSS data were collected with the SW Maps app and post-processed in PPK mode in RTKLIB, the continuous GNSS trajectory was generated in ArcGIS PRO and the point set was produced in CloudCompare (resolution: 1 mm). The ICP alignments were also performed in CloudCompare. Fig. 40 shows the pipeline of the third approach.

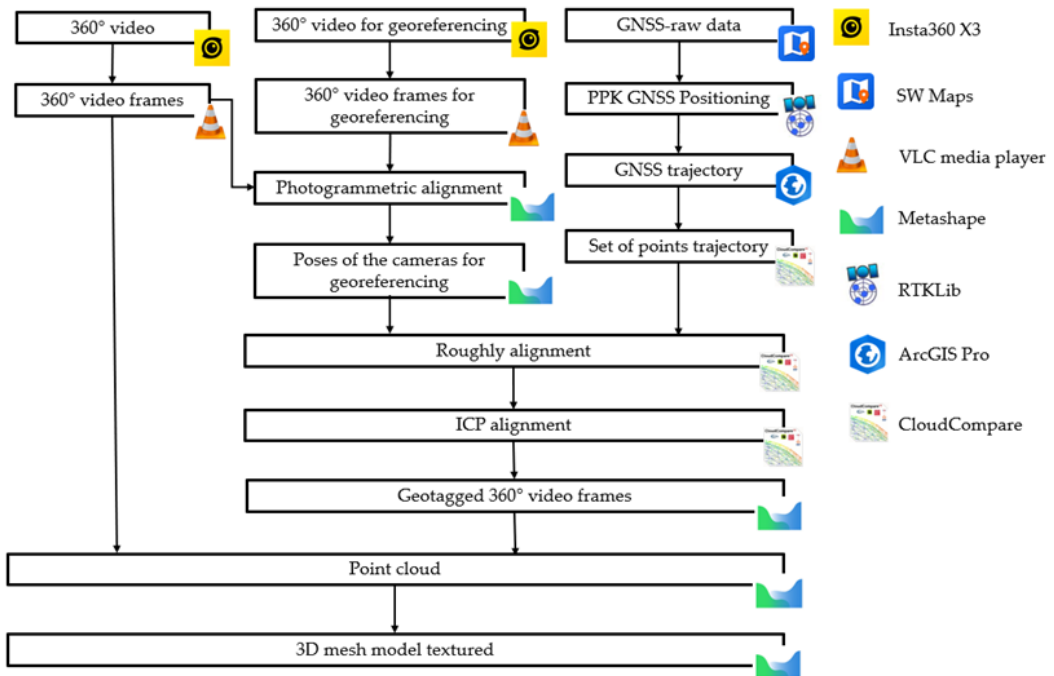


Fig. 40 – Pipeline of the third approach to GNSS-aided photogrammetry via georeferenced videos (360° action camera).

5.3.3. Fourth research methodology

The fourth research consisted of five phases: survey, point clouds generation, point clouds analysis, 3D mesh model textured production, 3D mesh model textured analysis.

In the first phase, a preliminary test was conducted to estimate the quality of the NRTK GNSS positioning of the SimpleRTK2B, subsequently some significant objects and architectural structures were surveyed in order to obtain the datasets for the subsequent research phases. The elements surveyed in the tests and case studies were: an ornamental garden boulder, the cavea of an amphitheatre, the three façades of a historical building used as a hospital and the two arcades of a bridge. The surveys of the boulder and cavea were performed in controlled conditions and were used to construct datasets for the evaluation and comparison of the systems, methods and approaches investigated. The surveys of the hospital and the bridge, on the other hand, concern two interesting case studies where the purpose was to experiment the GNSS-

aided photogrammetry in the field. In particular, the purpose of the boulder survey was to compare GNSS-aided photogrammetry and iOS LiDAR in the reconstruction of small to medium sized elements, elements where, as noted in chapter 3, the iOS LiDAR should not experience any problems in scanning (surface splitting, deformations etc.) The purpose of the cavea survey was to compare the different approaches of GNSS-aided photogrammetry and iOS LiDAR in surveying a medium to large sized structure, so that possible scanning errors of the iOS LiDAR could be highlighted. Furthermore, the enveloping and extended shape of the cavea provided a good test for evaluating GNSS-aided photogrammetry approaches based on the 360° action camera. Concerning the survey of the historical building used as a hospital (first case study), the site where the structure is located was characterised (at the time of the survey) by the massive presence of trees that in some areas reduced to occlude the view of parts of the façades. The aim of the survey was to study the GNSS-aided photogrammetry in a particularly challenging situation, where the presence of trees was a disturbance for both GNSS positioning and photogrammetric reconstruction. In addition, another disturbance for the operator was the passing cars. Finally, the survey of the bridge arcades (second case study) aimed to reconstruct both the north-east (N-E) and south-west (S-W) façades of the bridge (characterised by their respective frontal arches) and the intrados of the vaults. In particular, below the vaults, the GNSS signal is absent, this allowed to experiment the possibility of reconstructing the structure of the interior spaces by merging georeferenced photos acquired outside the structure with videos whose function is the survey of both the exterior and interior structure and the connection between the georeferenced photos of the exterior with the interior and exterior video frames.

In general, the data acquired in the tests (photos, videos, GNSS NRTK positionings and GNSS raw data) were primarily those useful for investigating and evaluating approaches to GNSS-aided photogrammetry via video: first, second and third. In order to perform comparisons with mobile devices equipped with depth sensors, scans were performed with the iOS LiDAR of the iPad 2021 Pro in high resolution (1 cm) and low resolution (~1.5 cm). Furthermore, in order to be able to evaluate the differ-

ences if only photos and not videos were used, photos were acquired following photogrammetric rules. This allowed video frames to be replaced by photos in approaches first and second. These approaches were called “fourth approach” and “fifth approach” respectively. More details are given in paragraph 5.3.4 (and specific tables) on dataset construction.

In order to couple the electronic devices during the survey phases, based on the previous research of Jaud *et al.* (2020), two prototype mechanical frames were constructed to planimetrically align the GNSS antenna with the cameras (integrated smartphone camera or 360° action camera) during the acquisition of georeferenced images. To enable field positioning, the frames were mounted on a photographic tripod (of course, the verticality of the frames must be ensured during the acquisition of geotagged images). Fig. 41a shows the frame for smartphone and Fig. 42b the frame used for the 360° action camera, the frames are adaptable to fit different devices, lightweight and transportable so they can be taken on travel. For the offset correction between cameras and GNSS antenna, previously equation (29) was used and applied, according to Jaud *et al.* (2020), as follows (definition of terms is given in section 1.4.):

$$\begin{bmatrix} X_o \\ Y_o \\ Z_o \end{bmatrix} = \begin{bmatrix} X_{GNSS} \\ Y_{GNSS} \\ Z_{GNSS} \end{bmatrix} - \begin{bmatrix} 0 \\ 0 \\ Z_{offset} \end{bmatrix} \quad (73)$$

The proper correction of the offsets was also verified experimentally during the first tests under controlled conditions.



(a)



(b)

Fig. 41 – Frames for devices alignment: (a) frame to couple the integrated rear camera of the smartphone with the GNSS antenna; (b) frame to couple the 360° action camera with the GNSS antenna.

In the second phase, point clouds of the surveyed objects and structures were produced. The point clouds derived from images and videos were generated through digital photogrammetric modelling using an SfM-MVS approach. As reported in Bianco, Ciocca and Marelli (2018) and Pepe, Alfio and Costantino (2022), a classic SfM-MVS pipeline consists synthetically of the following steps.

Structure from Motion

I. Correspondences search.

- **Feature extraction:** for each image, key points (points of interest with certain features) of the scene are identified, the key points are described by local image features.
- **Feature matching:** through key points, partially overlapping images representing parts of the same scene are selected.
- **Geometric verification:** a geometric verification is performed on the potentially overlapping images pairs.

Principal products: Scene Graph, a graph where images are the nodes and geometrically verified images pairs are joined by arcs.

II. Iterative incremental reconstruction.

- **Initialisation:** the common points of an images pair (selected accurately in a dense area of the Scene Graph and geometrically verified) are used to initialise the point cloud reconstruction process and establish the pose (position and rotations) of the camera pair.
- **Image registration:** new images are registered to the model by estimating the poses of the cameras; this is done by using the correspondence between the key points of the image to be registered and the points of the model corresponding to the key points of the previously registered images. The three-dimensional coordinates and three-axis rotations of the cameras are defined by solving a Perspective-n-Point (PnP) problem.
- **Triangulation:** through triangulation, the three-dimensional position in the model of the new common points observed in the new images registered to the model and at least one previously registered image is established.
- **Bundle adjustment:** through this operation, the SfM solution is optimised by improving the point cloud structure and camera poses.

Principal products: camera pose estimation for each image and sparse point cloud.

Multi-View Stereo

In this step, starting from the group of calibrated images showing the same scene, whose cameras poses and calibration parameters were estimated, the MVS algorithms estimate the depth maps of each image and reconstruct the dense point cloud (Campbell *et al.*, 2008; Gao *et al.*, 2023).

Principal products: dense point cloud.

An SfM-MVS pipeline can be implemented using various algorithms (in some cases non-public in the case of professional software), so please refer to the previously mentioned authors for a more extensive and specialised description of the implementation methods.

Regarding iOS LiDAR, the iPad 2021 Pro produced the point clouds directly into the scanning app used for the survey.

The point clouds produced were subsequently post-processed in order to have, in the following processing and analysis, a less noise, cleaner and more focused data on the elements of interest. The operation was performed through an initial rough segmentation to exclude other elements in the scene (e.g. trees, cars, parts of private residences, etc.), then a colour filter was applied, mainly for the removal of parts of the sky, and a Statistical Outlier Removal (S.O.R.) filter for noise reduction. The S.O.R. filter computes the mean distance of a point from its neighbours and then discards all points that are at a distance greater than the mean distance plus the standard deviation multiplied by a number n . The equation at the basis of the S.O.R. filter is as follows (*SOR filter - CloudCompareWiki*, accessed: 21 October 2023):

$$D = d + n \cdot SD \quad (74)$$

where, D is the exclusion distance, d is the mean distance, n is a multiplicative number of the standard deviation and SD is the standard deviation. Finally, the point clouds were subjected to a final fine segmentation to exclude the remaining clusters of points extraneous to the surveyed elements.

In the third phase, first a visual analysis was conducted (by appropriately sectioning the point clouds) to detect the macro problems of the point clouds, and then the point clouds were compared with reference point clouds, created using established and reliable methods, to derive metrics capable of describing the quality of the products.

In the fourth phase, the post-processed point clouds of the three approaches to GNSS-aided photogrammetry via video investigated (first, second and third) were transformed into 3D mesh models textured. On a theoretical level, what was written in the paragraph 4.3.1 on 3D mesh models reconstruction is also applicable here (Pois-

son surface reconstruction method). The 3D mesh models were subsequently refined by correcting non-manifold edges, self-intersections, high-fold edges, spikes, small components, small tunnels, small holes, smoothing the surface, uniformizing the dimensions of triangles and filling the larger holes (where this was required) (Costantino *et al.*, 2021). Subsequently, textures were applied to the refined mesh model, producing the final 3D mesh models textured.

Finally, in the fifth phase, in order to evaluate the quality of the mesh products, the 3D models were compared with reference point clouds.

5.3.4. Tests and case studies

This paragraph contains details on the construction of the datasets. Tests and case studies were conducted in Italy and Romania. GNSS positioning in Italy was performed using the HxGN SmartNet CORS network, while GNSS positioning in Romania was performed using the SYSCAD RTK CORS network (SC SysCAD Solutions SRL, Clinceni, Romania).

5.3.4.1. Datasets of tests under controlled conditions

The datasets of the tests conducted under controlled conditions consist of the NRTK GNSS positioning evaluation test of the SimpleRTK2B, the surveys of the ornamental garden boulder and the surveys of the amphitheatre cavea.

The NRTK GNSS positioning evaluation test was conducted to preliminarily estimate the potential of the SimpleRTK2B in this type of geolocation. In line with previously performed static GNSS positioning tests, the test was executed under open sky conditions on the roof of the Politecnico di Bari, headquarters of Taranto, Italy. Also in this case, the Helical antenna of the SimpleRTK2B was placed on FATA, the old vertex of a permanent GNSS network. Based on these conditions, a dataset consisting of fourteen NRTK GNSS positions of the SimpleRTK2B was constructed. Tab. 40 shows the composition of the dataset.

Tab. 40 – NRTK GNSS positioning dataset composition.

Device	Positioning	Data sample (no.)	Main data
SimpleRTK2B	NRTK	14	Latitude, longitude, ellipsoid height

Regarding the surveys, the ornamental boulder was the first test performed. The boulder is located inside the Politecnico di Bari, Taranto (Italy), and has a maximum height of approximately 1.35 m and a maximum width of approximately 1.84 m. An image of the ornamental garden boulder is shown in Fig. 42a. Considering the size and the non “enveloping” shape of the boulder, it was decided to survey the boulder with the first approach, the fourth approach and with the iOS LiDAR in high and low resolution. The dataset produced is shown in Tab. 41, the dataset (as well as the following ones) contains the data on: method, positioning, number of geotagged images (photos or video frames depending on the approach), number of video frames (or photos in the case of the fourth and fifth approaches), resolution, total survey time (sum of image and video acquisition time) and number of point clouds produced. The reference point cloud, used for the comparative analyses, was produced by digital photogrammetry from photos acquired with a digital camera Nikon D3300 and scaled using Control Scale Bars.

In the next tables “G-a P” stands for “GNSS-aided Photogrammetry”, “LiDAR” (High resolution and Low resolution) will instead refer to the iOS LiDAR scanner of the iPad 2021 Pro.

Tab. 41 – Ornamental garden boulder survey dataset composition.

Object	Method	Positioning	Geotagged images (no.)	Video frames or photos (no.)	Resolution	Total survey time	Points cloud (no.)
Garden boulder	G-a P – approach 1°	NRTK	10	121	1080p	00:06:51	809,064
	G-a P – approach 4°	NRTK	10	44	16 MP	00:07:39	4,798,140
	LiDAR high resolution	INS	/	/	1 cm	~ 00:01:00	35,992
	LiDAR low resolution	INS	/	/	~1.5 cm	~ 00:01:00	34,239

The second test concerned the survey of an amphitheatre cavea. The cavea is located inside the Politecnico di Bari, Taranto (Italy), has a length (summing the three sections) of about 45.71 m, a depth of about 2.12 m and a height of about 1.46 m. Fig. 42b shows an image of the cavea. Considering the shape of the structure and the aim of the test, the cavea was surveyed with iOS LiDAR in high and low resolution and with GNSS-aided photogrammetry approaches: first, second, third, fourth and fifth. The dataset composition is shown in Tab. 42. In this case, the reference point cloud for the final comparison was produced by digital photogrammetry from photos acquired with a UAV DJI Mavic Mini 3 Pro, scaled and georeferenced using GCPs acquired with the GNSS receiver Geomax Zenith 25 Pro, Total Station Leica TS11 and Control Scale Bars.

Both test sites are located in a circular area with a radius of no more than approximately 70 m from TARA (the nearest HxGN SmartNet CORS).

Tab. 42 – Amphitheatre cavea dataset composition.

Object	Method	Positioning	Geotagged images (no.)	Video frames or photos (no.)	Resolution	Total survey time	Points cloud (no.)
Cavea	G-a P - approach 1°	NRTK	75	233	1080p	00:19:34	8,099,176
	G-a P - approach 2°	NRTK	14	61	5.7k	00:27:21	604,767
	G-a P - approach 3°	PPK	67	61	5.7k	00:03:16	500,170
	G-a P - approach 4°	NRTK	75	84	16 MP	00:25:30	14,270,140
	G-a P - approach 5°	NRTK	14	37	72 MP	00:37:25	1,947,121
	LiDAR high resolution	INS	/	/	1 cm	~00:03:00	1,336,541
	LiDAR low resolution	INS	/	/	~1.5 cm	~00:03:00	1,140,656



(a)



(b)

Fig. 42 – Objects surveyed in tests under controlled conditions: (a) ornamental garden boulder; (b) amphitheatre cavea.

5.3.4.2. Datasets of case studies

For the field applications of GNSS-aided Photogrammetry, two particular case studies were chosen.

In the first case study, the three façades facing the street of a historic building that mainly hosts the University Clinic of Obstetrics and Gynaecology Bega were surveyed. The clinic is located in Timișoara, Romania (ϕ : 45° 44' 39.45" N; λ : 21° 13' 45.66" E) and is situated approximately 8.52 km from TIMI, the nearest SYSCAD RTK CORS (the coordinates of TIMI are given in the Annexes, Tab. A4). The total length of the three façades (summed together) is approximately 153.320 m with a maximum height of approximately 17.375 m. As can be seen in Figs. 43a and 43c, the façades are in some places partially (if not totally) covered by trees, which also constitute an interference for the GNSS signal. Based on the conformation of the site, the second approach was chosen. This approach allowed the acquisition of geolocalised photos only in areas where the quality of NRTK positioning was fixed. Using the Insta360 X3, on the other hand, allowed the fast and easy acquisition of a 360° video, which, due to the spherical Field of View (FoV or Angle of View), was able to survey the façades for their entire height in a single acquisition phase and to “bypass” (even if only partially) the obstructions constituted by the trees, through the subsequent fusion of the video frames into the final photogrammetric model. In addition, the survey was performed at the roadside and the use of spherical video allowed the operator to work more safely by being able to pay more attention to oncoming cars. The dataset pro-

duced is shown in Tab. 43. The reference point cloud was produced by TLS survey using the Z+F IMAGER® 5010C, Total Station Leica TCRP 1205+ and Control Points.

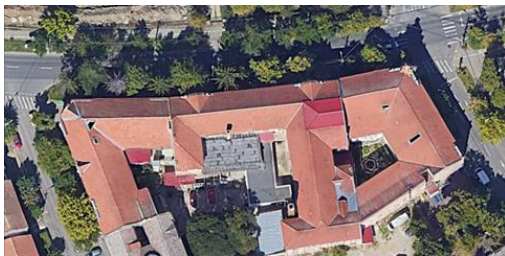
Tab. 43 – Historical building (clinic) dataset composition.

Object	Method	Posi- tioning	Geotagged images (no.)	Video frames or photos (no.)	Resolu- tion	Total survey time	Points cloud (no.)
Histori- cal building (clinic)	G-a P - approach 2°	NRTK	12	207	5.7k	00:14:41	9,655,110

In the second case study, two arcades were surveyed (the rest were inaccessible) of a bridge (Figs. 43b and 43d) located in Bari, Italy (ϕ : 41° 05' 42.56" N; λ : 16° 57' 24.94" E). The arcades have a length of approximately 10.00 m, a width between approximately 5.90 - 5.93 m and a height between approximately 3.72 - 3.76 m (these values vary depending on the debris accumulated at the sides and the level of the mud deposited at the bottom). The structure is about 18.90 km from COAN, the nearest HxGN SmartNet CORS (the coordinates of COAN are given in the Annexes, Tab. A4). Considering the aim of the case study, the second approach was chosen to conduct the survey. Using the second approach, georeferenced photos were acquired only in significant areas outside the structure, while the 360° action camera was the best and most natural solution for capturing video both outside and inside completely “enveloping” structures such as the bridge vaults. The data produced during the survey are shown in Tab. 44; in this case study the quality of the final products was verified by comparison with the point clouds of the frontal arches of the N-E and S-W façades produced by photogrammetric survey with a UAV DJI Mavic 2 Pro, GNSS receiver Leica Viva GS12 and GCPs.

Tab. 44 – Bridge arcades dataset composition.

Object	Method	Positioning	Geotagged images (no.)	Video frames or photos (no.)	Resolution	Total survey time	Points cloud (no.)
Bridge arcades	G-a P - approach 2°	NRTK	15	278	5.7k	00:24:00	7,289,484



(a)



(b)



(c)



(d)

Fig. 43 – Structures surveyed in the case studies in field: (a) historical building used as a clinic; (b) bridge; (c) detail of the road facing the main façade of the historical building; (d) detail of the frontal arches of the N-E façade of the bridge.

5.3.5. Technical notes on point clouds production and 3D mesh modelling

This paragraph provides some technical notes on the processing performed in the applications for producing the point clouds and the 3D mesh models.

The implementation of the SfM-MVS pipeline was performed in Metashape, the processing blocks Align Photos and Build Dense Cloud were used to produce the point

clouds. In Align Photos the Accuracy was set to “High” and in Build Dense Cloud the Quality was set to “High”.

The post-processing phase of the dense point clouds was performed in CloudCompare software using the following tools and edit operations. The raw segmentation was performed via Cross Section; the colour filter was implemented via Colors and Convert to Scalar field; the SOR Filter was applied via the specific tool and finally the fine segmentation was performed via Segment.

After this phase, the post-processed point clouds were transformed into 3D mesh models in Metashape using the Build Mesh processing block. In Build Mesh, the Face Count was set to “High”.

The mesh models were refined using Geomagic Wrap 2021 software (3D Systems, Rock Hill, South Carolina, USA) (Costantino *et al.*, 2021). The correction of non-manifold edges, self-intersections, high-fold edges, spikes, small components, small tunnels and small holes was done via Mesh Doctor, the surface smoothing and uniformizing the triangle dimensions were done via QuickSmooth and the filling of the larger holes via Fill All.

The refined 3D mesh models were finally textured in Metashape via the Build Texture block.

A synthetic pipeline of the steps performed is shown in Fig.44.

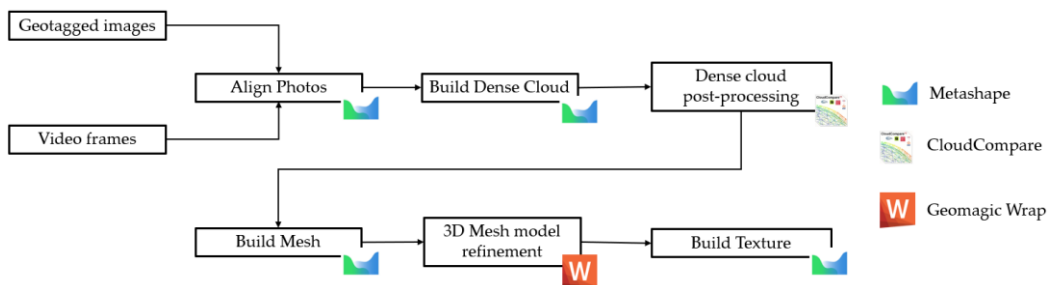


Fig. 44 – Synthetic pipeline of the production of point clouds and 3D mesh models textured

5.4. Results of the fourth part of the research project

This paragraph reports the results obtained in the tests conducted under controlled conditions and in the two case studies. Point clouds and 3D mesh models were analysed and compared in CloudCompare by sections extraction, comparison between point clouds Cloud-To-Cloud (C2C) and comparison between reference point clouds and 3D mesh models Cloud-To-Mesh (C2M). The results will be commented on in the next paragraph 5.5 devoted to evaluations and discussions.

5.4.1. Tests under controlled conditions

Below are shown the results of tests performed under controlled conditions at the Politecnico di Bari, Taranto, Italy.

Tab. 45 shows the results obtained by SimpleRTK2B in the NRTK GNSS positioning on FATA (known coordinate point). In accordance with the previous chapters, ΔE , ΔN and ΔU represent the mean GNSS positioning errors in the components East, North and Up (respectively). The standard deviation (SD) is denoted by SDE (East component), SDN (North component) and SDU (Up component).

Tab. 45 – Performances in NRTK GNSS positioning of SimpleRTK2B.

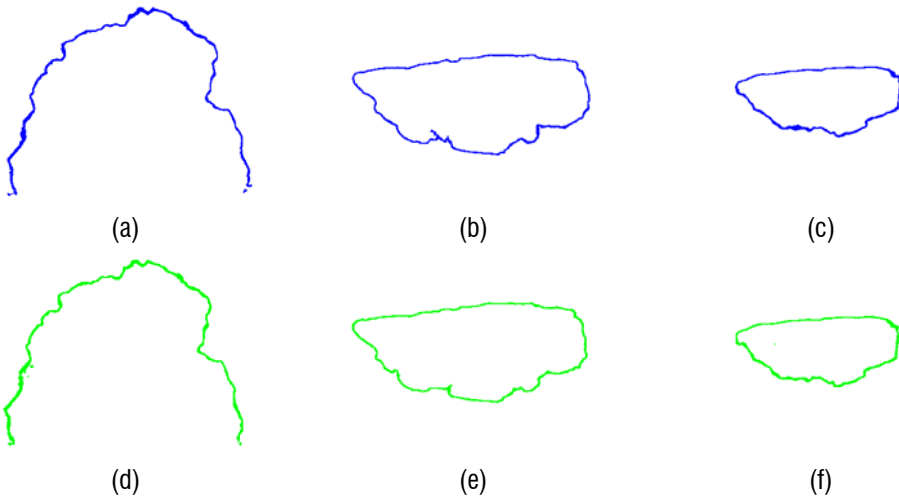
Device	Positioning	Data sample (no.)	ΔE [m]	ΔN [m]	ΔU [m]	SDE [m]	SDN [m]	SDU [m]
SimpleRTK2B	NRTK	14	0.017	0.007	0.035	0.001	0.001	0.002

Figs. 45, 46 and 47 and Tab. 46 are dedicated to presenting the results obtained in the survey and point clouds creation of the ornamental garden boulder. In particular, Fig. 45 shows the point cloud obtained using the first approach and the section planes (D-D in Fig. 45a, E-E and F-F in Fig. 45b) created to study the point clouds generated with the different approaches and sensors by sections analysis.



Fig. 45 – Point cloud of the ornamental garden boulder produced by the first approach: (a) plan section D-D, (b) plan sections E-E and F-F.

In Fig. 46, the sections obtained from the point clouds were collected. More specifically: Figs. 46a, 46b and 46c show (in blue) the sections D-D, E-E and F-F (respectively) of the point cloud obtained with the first approach; Figs. 46d, 46e and 46f show (in green) the sections D-D, E-E and F-F (respectively) of the point cloud of the fourth approach; Figs. 46g, 46h and 46i show (in magenta) the sections D-D, E-E and F-F (respectively) of the point cloud of the iOS LiDAR in high resolution; finally, Figs. 46j, 46k and 46l show (in orange) the D-D, E-E and F-F sections (respectively) of the iOS LiDAR point cloud in low resolution.



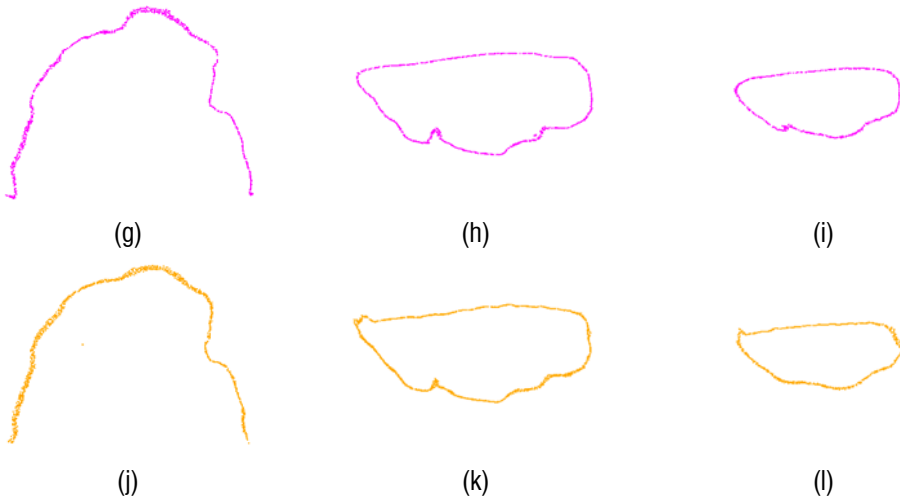


Fig. 46 – Collection of point cloud sections of the ornamental boulder from gardens: (a) section D-D first approach; (b) section E-E first approach; (c) section F-F first approach; (d) section D-D fourth approach; (e) section E-E fourth approach; (f) section F-F fourth approach; (g) section D-D iOS LiDAR high resolution; (h) section E-E iOS LiDAR high resolution; (i) section F-F iOS LiDAR high resolution; (j) section D-D iOS LiDAR low resolution; (k) section E-E iOS LiDAR low resolution; (l) section F-F iOS LiDAR low resolution.

Fig. 47 shows the histograms of the C2C analysis performed for the comparison between the boulder point cloud and the reference point cloud. Fig. 47a shows the C2C analysis of the point cloud created by the first approach, Fig. 47b shows the C2C analysis of the point cloud of the fourth approach, Fig. 47c shows the C2C analysis of the point cloud of the iOS LiDAR in high resolution and Fig. 47d shows the C2C analysis of the point cloud of the iOS LiDAR in low resolution. Finally, Tab. 46 shows the numerical results of the C2C comparison, μ_{3D} represents the mean C2C distance and SD_{3D} represents the C2C standard deviation.

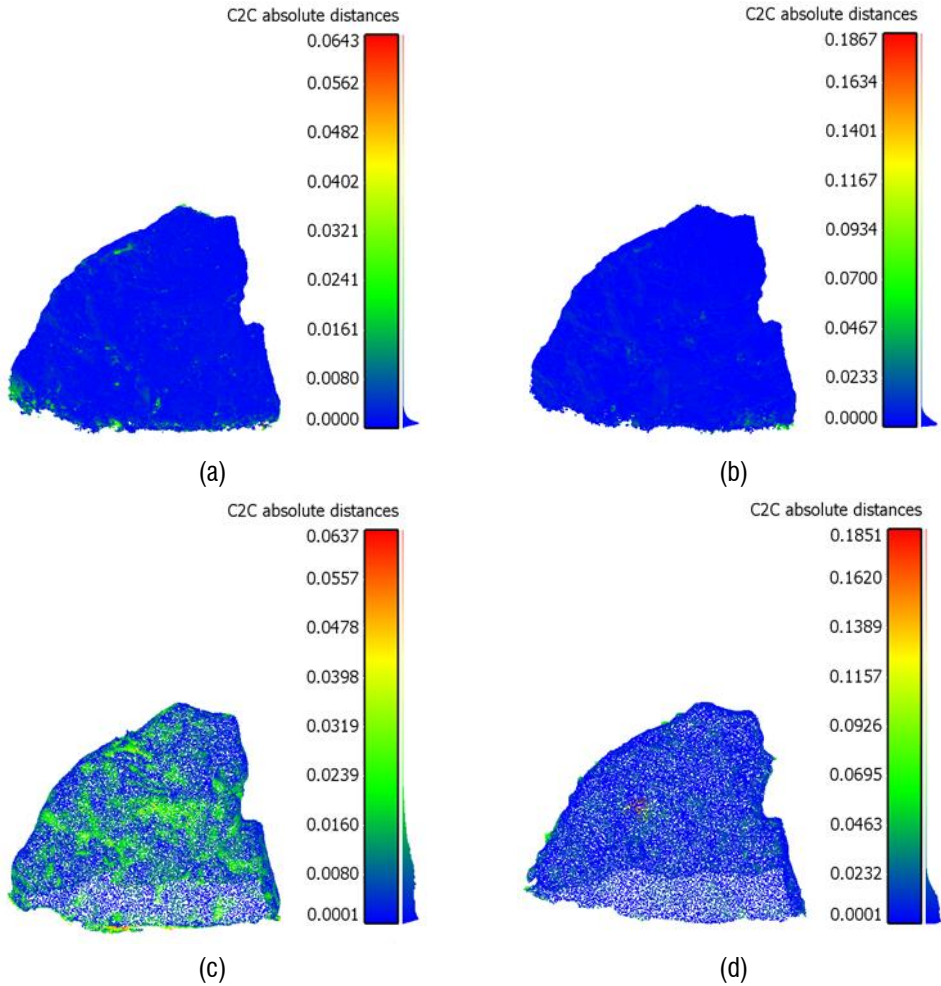


Fig. 47 – C2C histograms of point clouds of the ornamental garden boulder: (a) first approach; (b) fourth approach; (c) iOS LiDAR high resolution; (d) iOS LiDAR low resolution.

Tab. 46 – Mean distance and standard deviation of the C2C analysis performed on the point clouds of the ornamental garden boulder.

Object	Method	μ 3D [m]	SD3D [m]
Garden boulder	G-a P – approach 1°	0.0019	0.0022
	G-a P – approach 4°	0.0038	0.0036
	LiDAR high resolution	0.0087	0.0066
	LiDAR low resolution	0.0112	0.0123

Figs 48, 49, 50, 51 and Tabs. 47 and 48 show the results of the point clouds production of the amphitheatre cavea. Fig. 48 shows the point cloud obtained using the first approach and the section planes G-G, H-H and I-I of the point cloud.

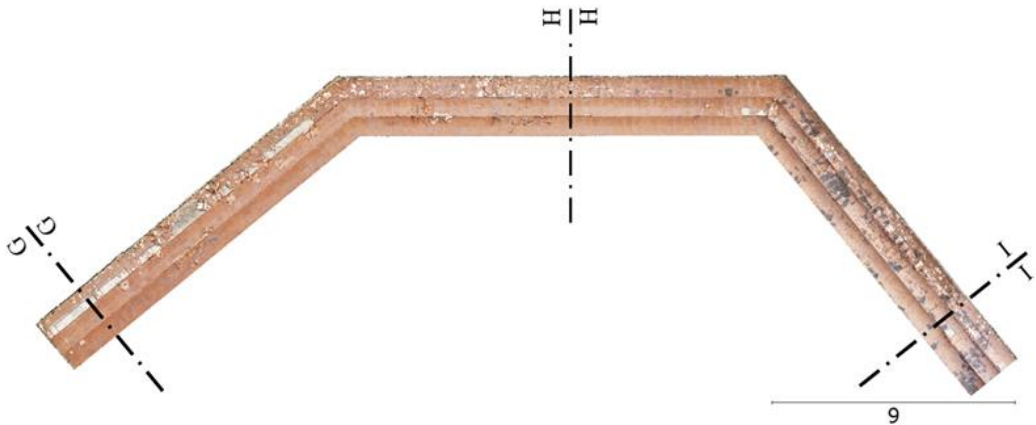
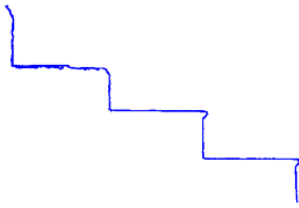
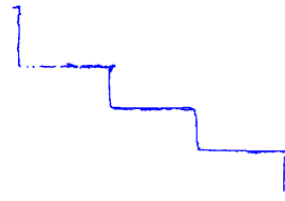


Fig. 48 – Point cloud and planes sections G-G, H-H and I-I of the amphitheatre cavea produced by the first approach.

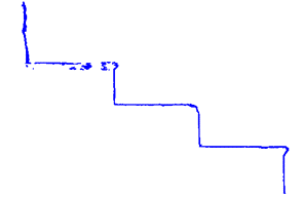
Fig. 49 shows the sections of the various point clouds of the cavea. Figs. 49a, 49b and 49c show (in blue) respectively the G-G, H-H and I-I sections of the point cloud of the cavea generated with the first approach; Figs. 49d, 49e and 49f show (in black) respectively the G-G, H-H and I-I sections of the point cloud of the second approach; Figs. 49g, 49h and 49i show (in brown) respectively the G-G, H-H and I-I sections of the point cloud of the third approach; Figs. 49j, 49k and 49l show (in green) respectively the G-G, H-H and I-I sections of the point cloud of the fourth approach; Figs. 49m, 49n and 49o show (in cyan) respectively the G-G, H-H and I-I sections of the cavea point cloud of the fifth approach; Figs. 49p, 49q and 49r show (in magenta) respectively the G-G, H-H and I-I sections of the cavea point cloud generated with the iOS LiDAR in high resolution; Figs. 49s, 49t and 49u show (in orange) respectively the G-G, H-H and I-I sections of the point cloud of the iOS LiDAR in low resolution.



(a)



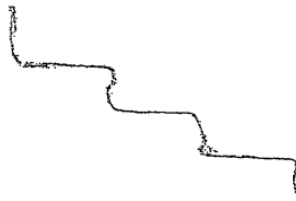
(b)



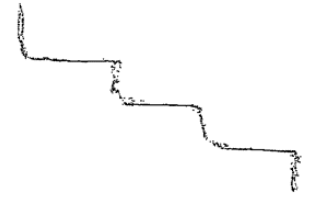
(c)



(d)



(e)



(f)



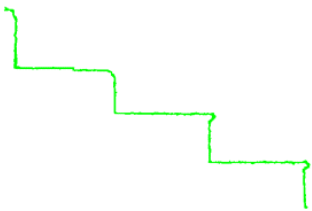
(g)



(h)



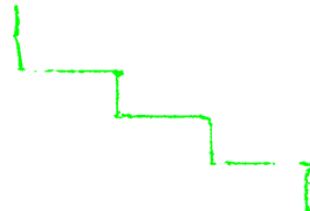
(i)



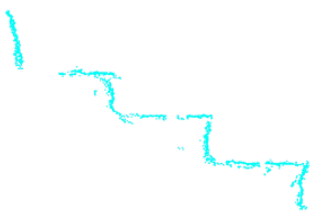
(j)



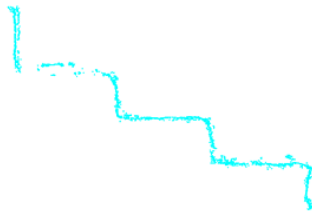
(k)



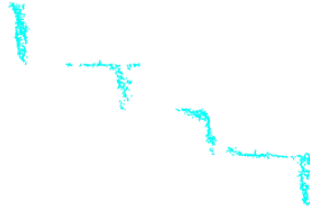
(l)



(m)



(n)



(o)

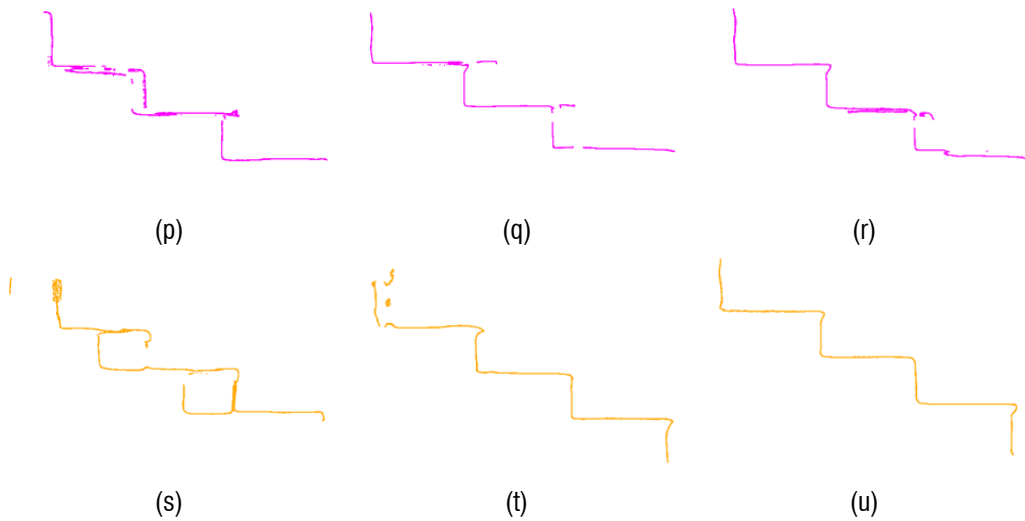


Fig. 49 – Collection of point cloud sections of the amphitheatre cavea: (a) section G-G first approach; (b) section H-H first approach; (c) section I-I first approach; (d) section G-G second approach; (e) section H-H second approach; (f) section I-I second approach; (g) section G-G third approach; (h) section H-H third approach; (i) section I-I third approach; (j) section G-G fourth approach; (k) section H-H fourth approach; (l) section I-I fourth approach; (m) section G-G fifth approach; (n) section H-H fifth approach; (o) section I-I fifth approach; (p) section G-G iOS LiDAR high resolution; (q) section H-H iOS LiDAR high resolution; (r) section I-I iOS LiDAR high resolution; (s) section G-G iOS LiDAR low resolution; (t) section H-H iOS LiDAR low resolution; (u) section I-I iOS LiDAR low resolution.

In order to evaluate the performance of GNSS-aided photogrammetry in point cloud georeferencing, the histograms of C2C analyses performed between the point clouds of the cavea georeferenced using geolocalised images and the point cloud chosen as reference georeferenced in NRTK by GCPs are shown in Fig. 50. In particular, Fig. 50a shows the point cloud georeferenced with the first approach, Fig. 50b shows the point cloud of the second approach, Fig. 50c shows the point cloud of the third approach, Fig. 50d shows the C2C analysis of the point cloud of the fourth approach and Fig. 50e shows the C2C analysis of the point cloud georeferenced with the fifth approach. Tab. 47 shows the respective numerical values of the mean distances ($\mu 3D$) and standard deviations ($SD3D$) of the C2C analyses performed.

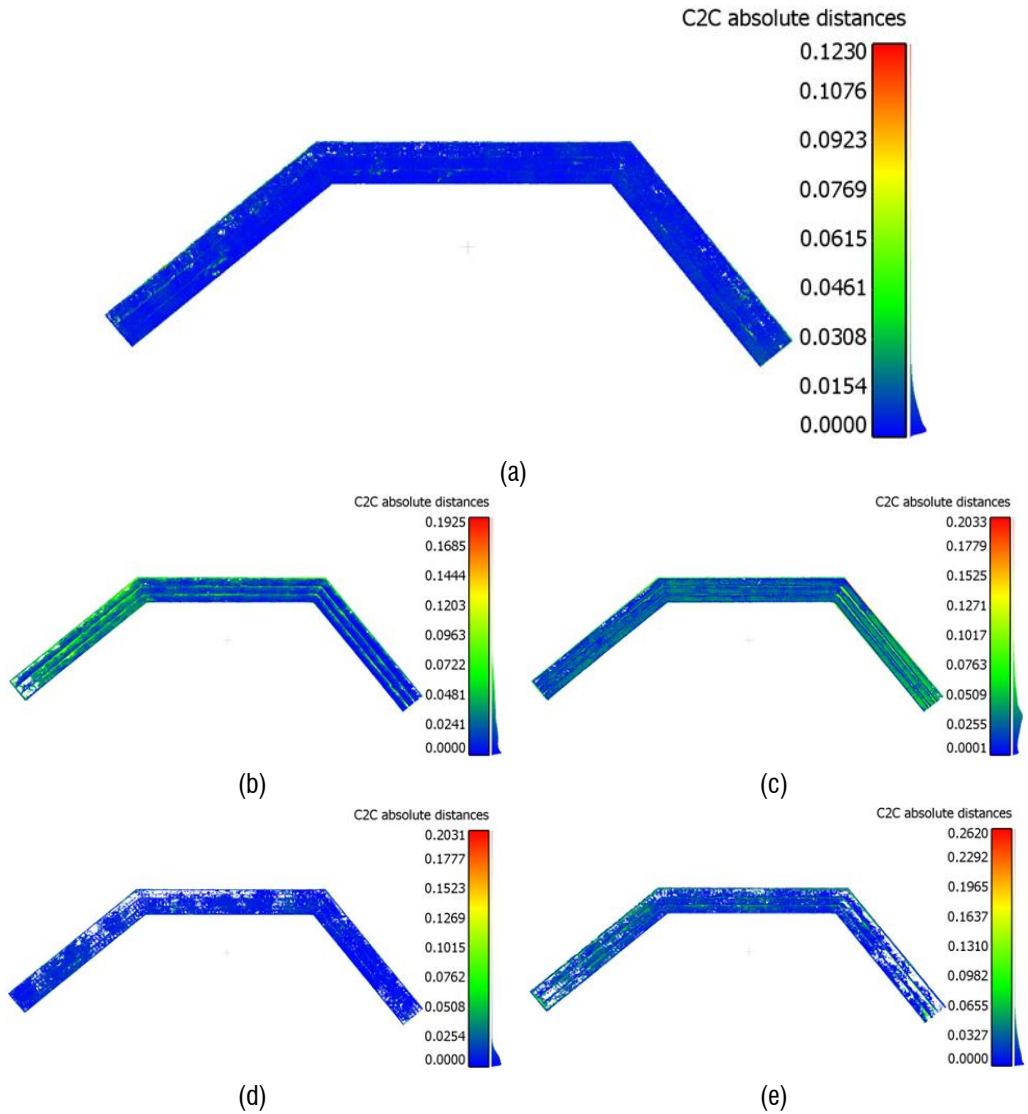
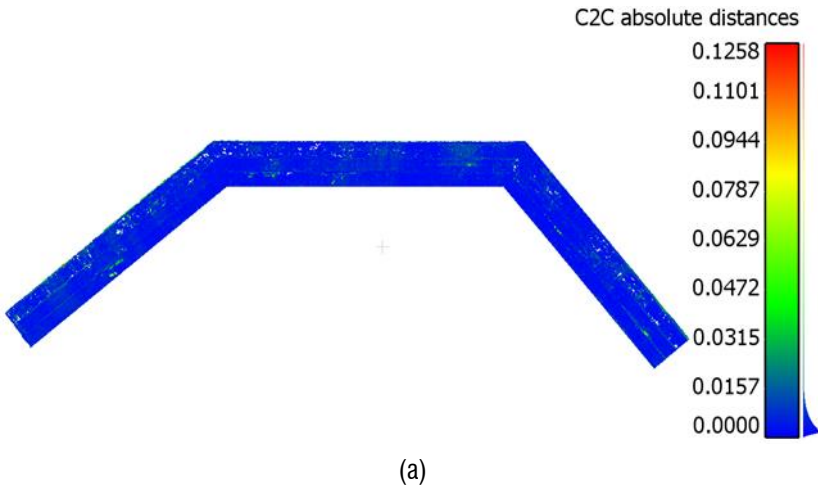


Fig. 50 – C2C histograms for point cloud georeferencing analysis of the amphitheatre cavea: (a) first approach; (b) second approach; (c) third approach (d) fourth approach; (e) fifth approach.

Tab. 47 – Mean distance and standard deviation of C2C analysis to evaluate the automatic georeferencing of point clouds of the amphitheatre cavea.

Object	Method	μ 3D – georeferencing [m]	SD3D – georeferencing [m]
Cavea	G-a P - approach 1°	0.0089	0.0073
	G-a P - approach 2°	0.0314	0.0232
	G-a P - approach 3°	0.0404	0.0284
	G-a P - approach 4°	0.0094	0.0071
	G-a P - approach 5°	0.0243	0.0205

Fig. 51 and Tab. 48 show the results of the C2C comparative analysis between the point clouds of the cavea and the reference UAV point cloud for the evaluation of the dimensional correctness of the point clouds. Fig. 51a shows the point cloud generated with the first approach, Fig. 51b shows the point cloud of the second approach, Fig. 51c shows the point cloud of the third approach, Fig. 51d shows the point cloud of the fourth approach, Fig. 51e shows the point cloud reconstructed with the fifth approach, Fig. 51f shows the point cloud of the iOS LiDAR in high resolution and Fig. 51g shows the point cloud analysis of the iOS LiDAR in low resolution. Tab. 48 shows the respective numerical values of the mean distances (μ 3D) and standard deviations (SD3D) of the C2C comparisons.



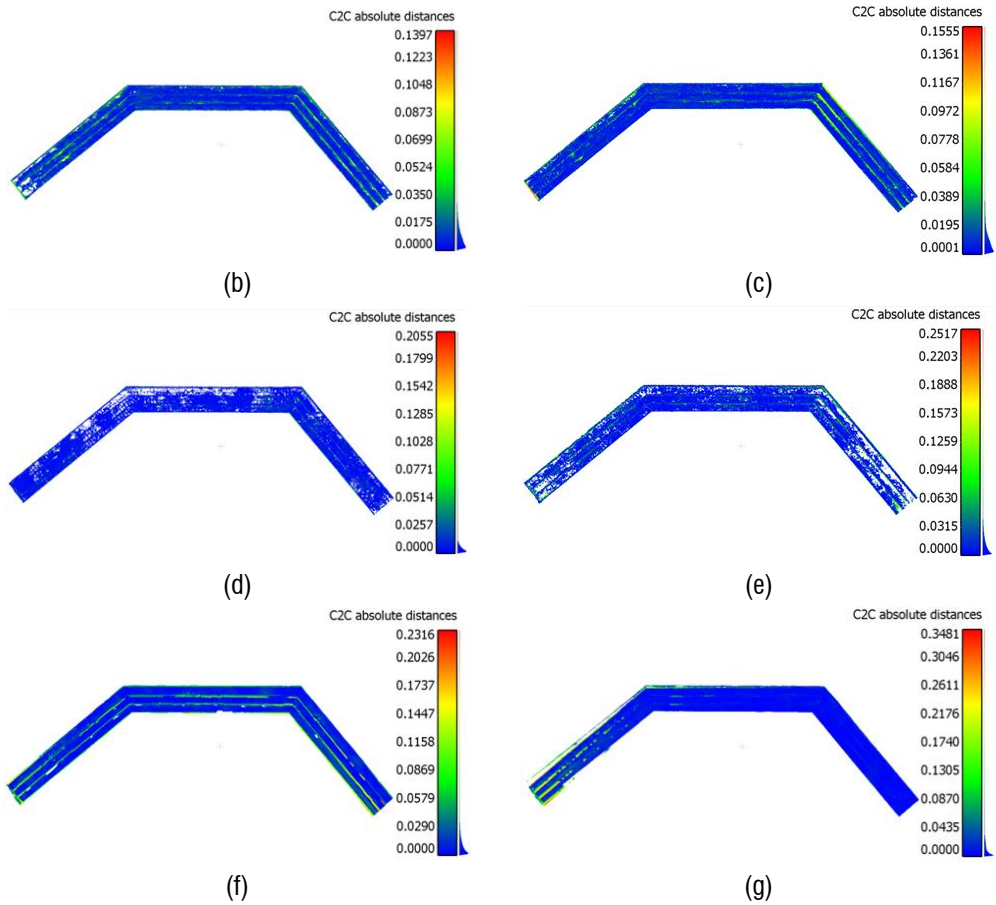
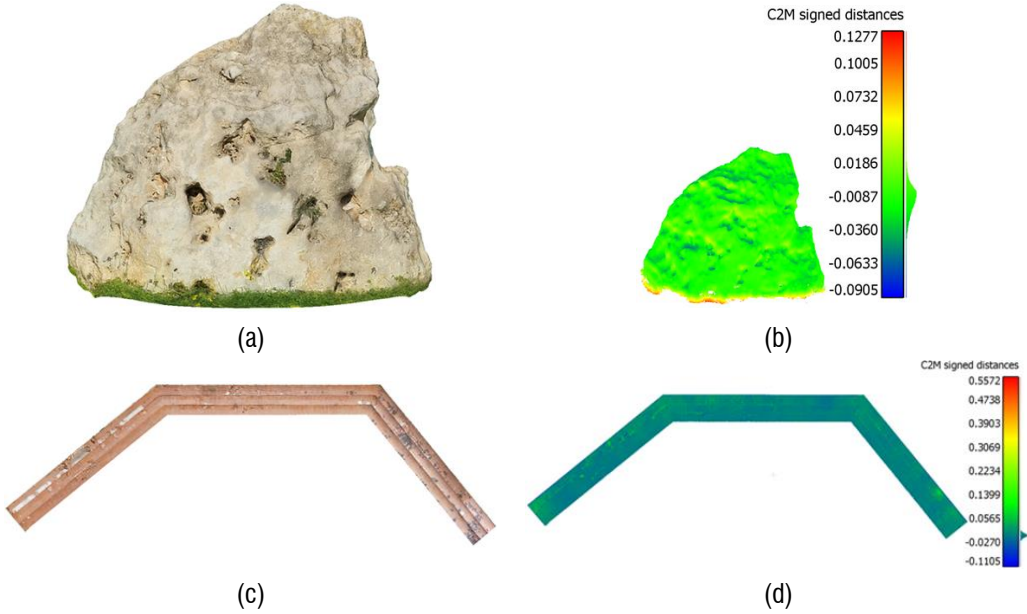


Fig. 51 – C2C histograms for the dimensional comparison of point clouds of the amphitheatre cavea: (a) first approach; (b) second approach; (c) third approach; (d) fourth approach; (e) fifth approach; (f) iOS LiDAR high resolution; (g) iOS LiDAR low resolution.

Tab. 48 – Mean distance and standard deviation of the C2C dimensional comparison performed on the point clouds of the amphitheatre cavea.

Object	Method	$\mu 3D$ [m]	SD3D [m]
Cavea	G-a P - approach 1°	0.0062	0.0059
	G-a P - approach 2°	0.0128	0.0126
	G-a P - approach 3°	0.0165	0.0193
	G-a P - approach 4°	0.0056	0.0056
	G-a P - approach 5°	0.0171	0.0175
	LiDAR high resolution	0.0267	0.0323
	LiDAR low resolution	0.0301	0.0462

Finally, Fig. 52 and Tab. 49 show the 3D mesh models textured and the results of the C2M comparative analysis between the reference point clouds and the 3D mesh models, for the evaluation of the dimensional correctness of the 3D models. Fig. 52a shows the 3D mesh model textured of the ornamental garden boulder generated with the first approach, Fig. 52b shows the C2M histogram of the boulder referred to the first approach, Fig. 52c shows the 3D mesh model textured of the cavea created with the first approach, Fig. 52d shows the C2M histogram of the cavea referred to the first approach, Fig. 52e shows the cavea 3D mesh model textured generated with the second approach, Fig. 52f shows the C2M histogram of the cavea referring to the second approach, Fig. 52g shows the cavea 3D mesh model textured generated with the third approach and Fig. 52h shows the C2M histogram of the cavea referring to the third approach. Tab. 49 shows the numerical values of the mean distances (μ_{3D}) and standard deviations (SD_{3D}) of the C2M comparison.



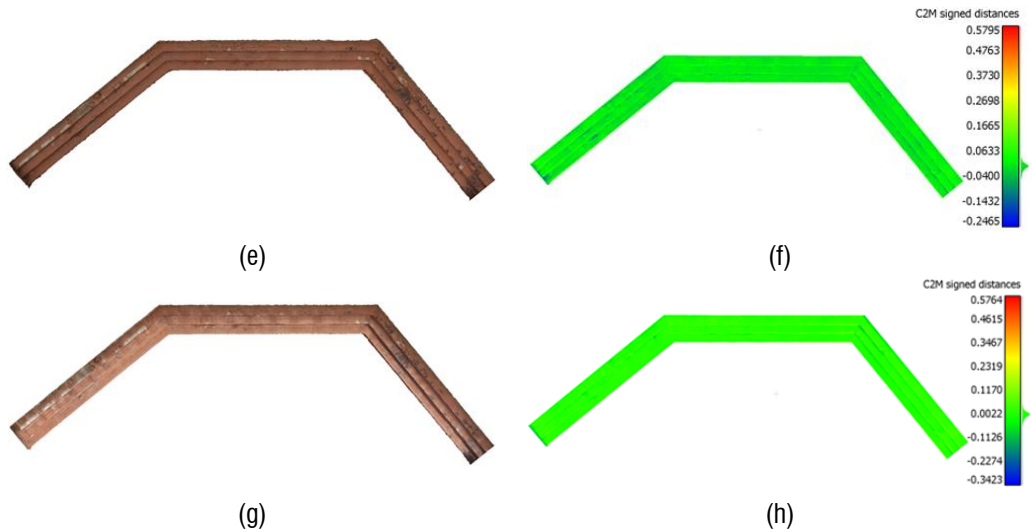


Fig. 52 – 3D mesh models textured and C2M histograms of the ornamental garden boulder and the amphitheatre cavea: (a) mesh model of the boulder first approach; (b) C2M histogram of the boulder first approach; (c) mesh model of the cavea first approach; (d) C2M histogram of the cavea first approach; (e) mesh model of the cavea second approach; (f) C2M histogram of the cavea second approach; (g) mesh model of the cavea third approach; (h) C2M histogram of the cavea third approach.

Tab. 49 – Mean distance and standard deviation of the C2M comparison performed on the 3D mesh models of the ornamental garden boulder and the amphitheatre cavea.

Object	Method	μ_{3D} [m]	SD _{3D} [m]
Garden boulder	G-a P - approach 1°	0.0078	0.0187
	G-a P - approach 1°	0.0003	0.0111
Cavea	G-a P - approach 2°	0.0024	0.0260
	G-a P - approach 3°	0.0054	0.0334

5.4.2. Case studies in field conditions

This paragraph reports the results of the case studies conducted in the field. Fig. 53 and Tab. 50 show the results obtained from surveying the three façades of the historical building (clinic) surveyed in the first case study (second approach). Fig. 53a illustrates the coloured point cloud produced, while Fig. 53b shows the histogram of the C2C comparative analysis between the point cloud produced and the reference point cloud generated by the TLS survey. Tab. 50 shows the numerical results of the

mean distance C2C ($\mu3D$) and the standard deviation ($SD3D$) obtained from the analysis.

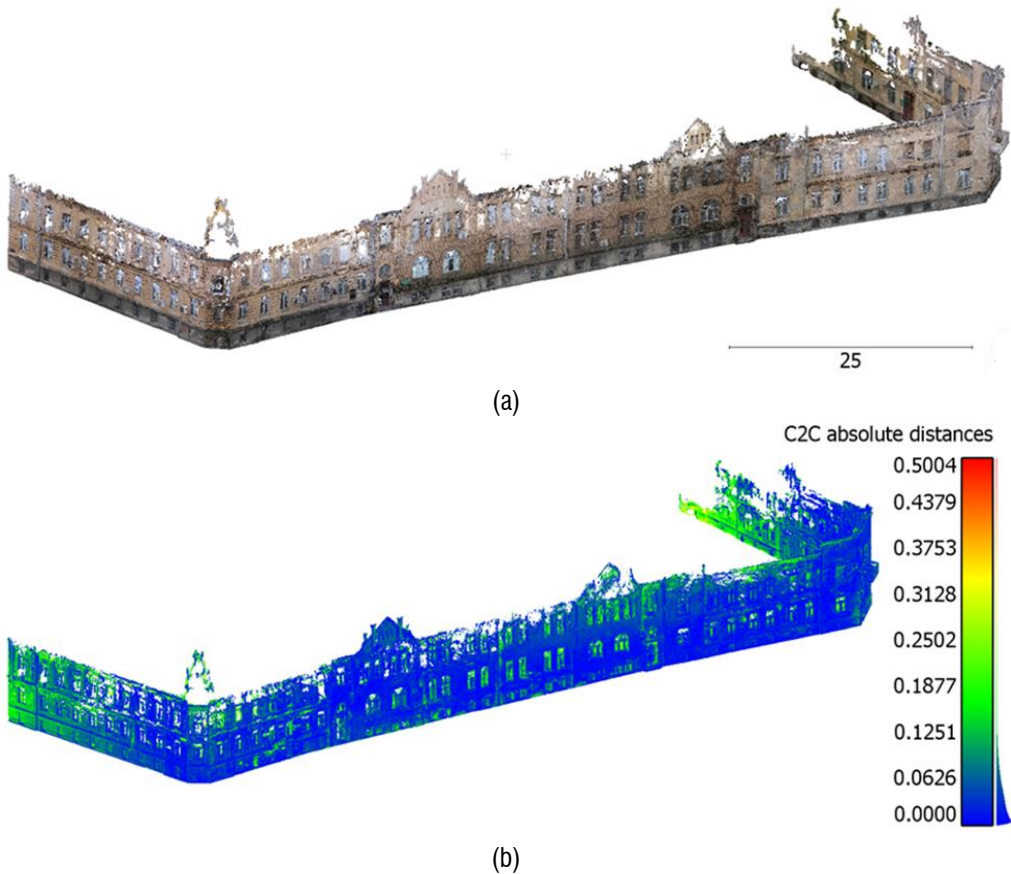


Fig. 53 – Point cloud produced by the survey of the historical building (clinic) surveyed in the first case study with the second approach: (a) coloured point cloud; (b) C2C histogram.

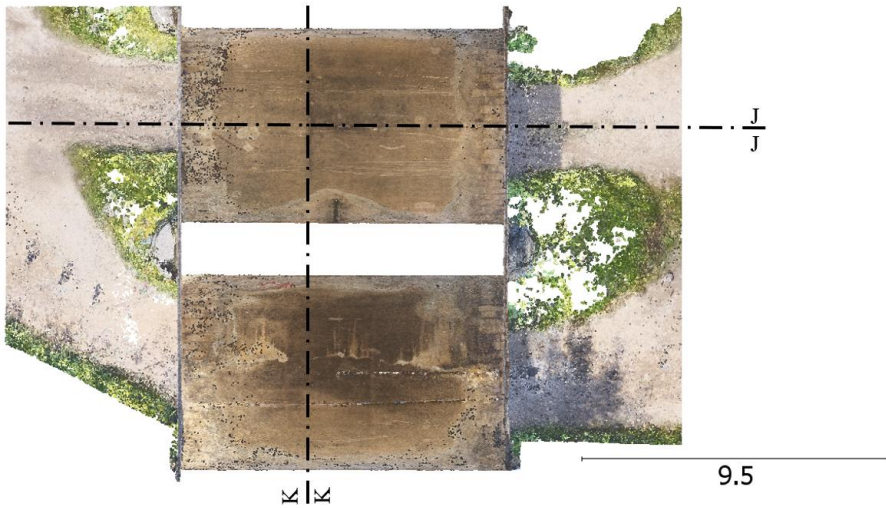
Tab. 50 – Mean distance and standard deviation of the C2C comparative analysis performed on the point cloud of the historical building (clinic) surveyed in the first case study.

Object	Method	$\mu3D$ [m]	$SD3D$ [m]
Historical building (clinic)	G-a P - approach 2°	0.0493	0.0454

Fig. 54 and Tab. 51 show the results obtained in the bridge arcades survey conducted in the second case study (second approach). In particular, Fig. 54a shows an overview of the coloured point cloud produced, Fig. 54b, c and d show the extracted J-J and K-K sections for a visual evaluation of the results obtained, Fig. 54e shows the C2C histogram referring to the frontal arcs of the N-E façade and Fig. 54f shows the C2C histogram of the frontal arcs of the S-W façade. Tab. 51 shows the results of the mean distance C2C ($\mu 3D$) and standard deviation ($SD3D$) obtained from the analysis of the frontal arches of the N-E and S-W facades.



(a)



(b)

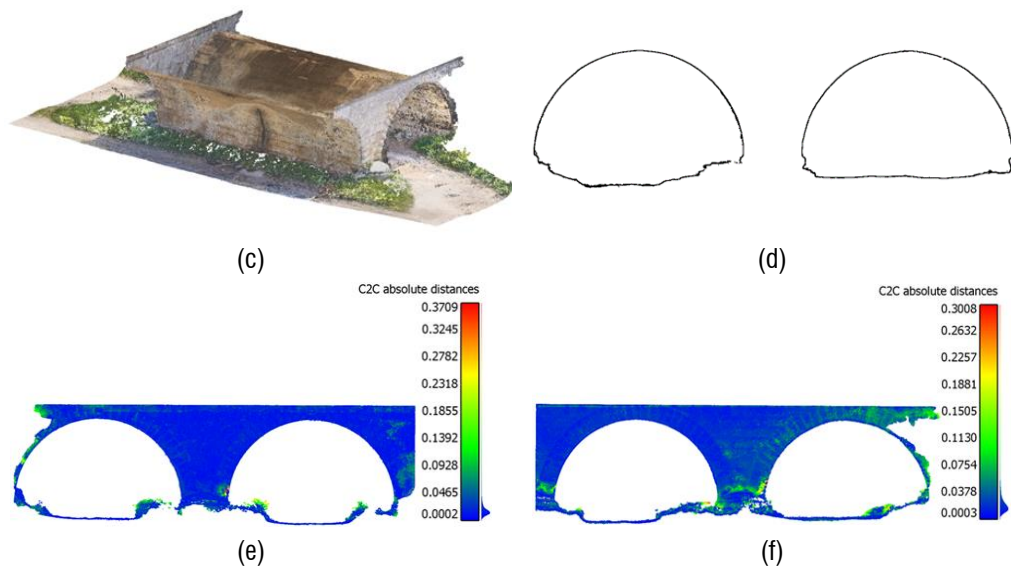


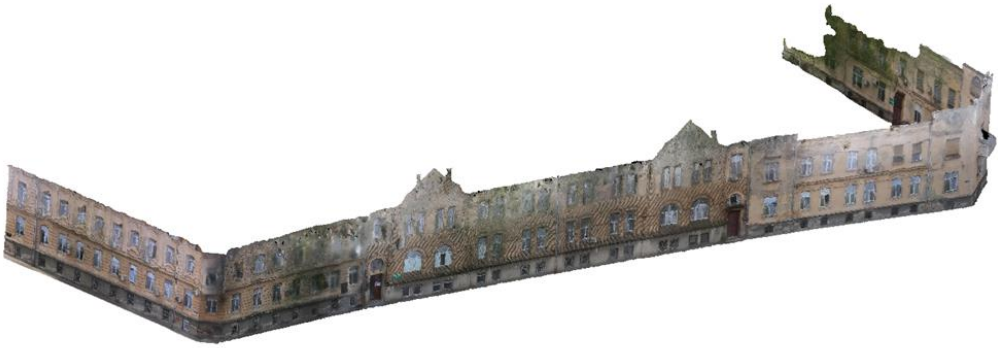
Fig. 54 – Point cloud produced by the survey of the bridge arcades in the second case study with the second approach: (a) coloured point cloud; (b) indication of the J-J and K-K section planes; (c) J-J section of a bridge vault; (d) K-K section of the two bridge vaults; (e) C2C histogram of the frontal arches of the N-E façade; (f) C2C histogram of the frontal arches of the S-W façade.

Tab. 51 – Mean distance and standard deviation of the C2C comparative analysis performed on the point clouds of the frontal arches of the N-E and S-W facades in the second case study.

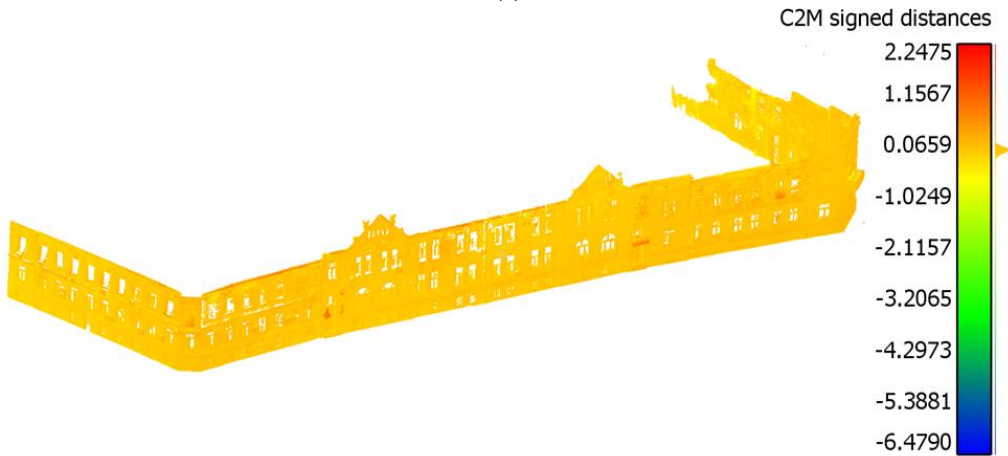
Object	Method	μ 3D [m]	SD3D [m]
Front arch façade N-E	G-a P - approach 2°	0.0222	0.0198
Front arch façade S-W		0.0262	0.0211

Finally, Fig.55 and Tab. 52 show the 3D mesh models textured of the three façades of the historic building (clinic), the bridge arcades and the results of the C2M comparative analysis between the reference point clouds and the 3D mesh models. In particular, Fig. 55a shows the 3D mesh model textured of the three façades of the historic building (clinic), Fig. 55b shows the C2M histogram of the historic building (clinic), Fig. 55c shows the 3D mesh model textured of the bridge arches, Fig. 55d shows the C2M histogram referring to the frontal arches of the N-E façade and Fig. 55e shows the C2M histogram of the frontal arches of the S-W façade. Tab. 52 shows the nu-

merical values of the C2M analyses, mean distance C2M (μ_{3D}) and standard deviation (SD3D).



(a)



(b)

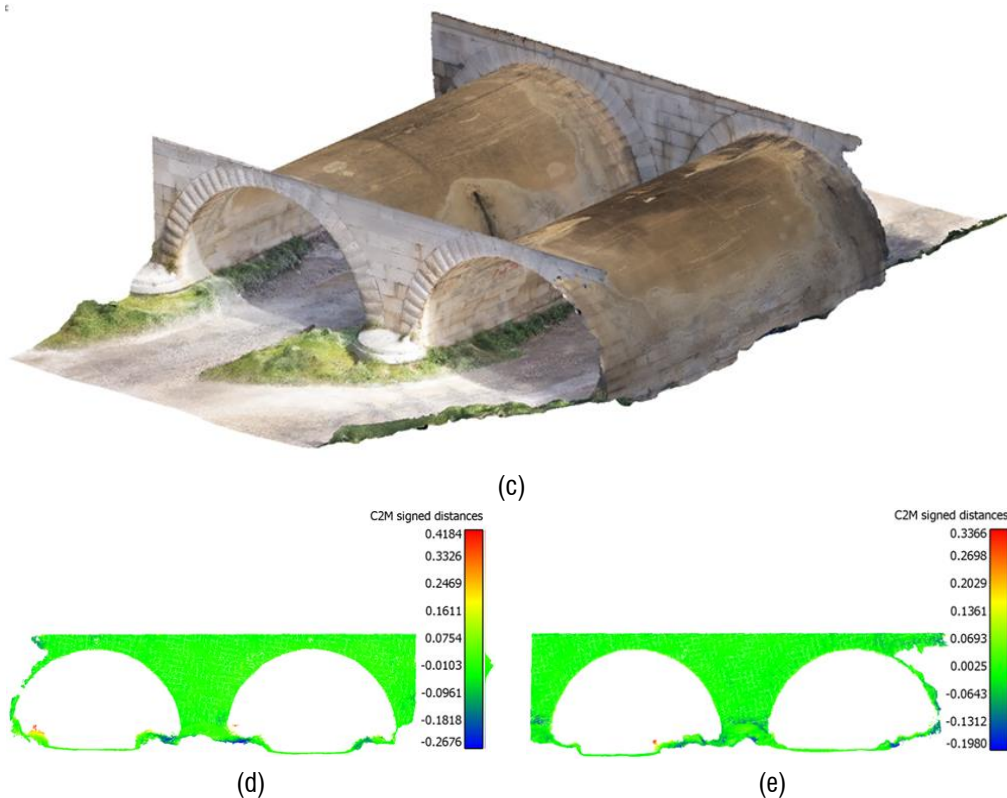


Fig. 55 – 3D mesh models textured and C2M histograms of the historical building (clinic) and the bridge arcades: (a) 3D model of the historical building (clinic); (b) C2M histogram of the historical building (clinic); (c) 3D model of the bridge arcades; (d) C2M histogram of the frontal arches of the N-E façade; (e) C2M histogram of the frontal arches of the S-W façade.

Tab. 52 – Mean distance and standard deviation of the C2M comparison performed on the 3D mesh models of the historical building (first case study) and the frontal arches of the N-E and S-W façades (second case study).

Object	Method	μ_{3D} [m]	SD _{3D} [m]
Historical building (clinic)		0.0161	0.0968
Front arch façade N-E	G-a P - approach 2°	0.0075	0.0475
Front arch façade S-W		0.0135	0.0307

5.5. Evaluations and discussions of the fourth part of the research project

Comparing the values of the C2C and C2M analyses in Tabs. 47, 48 and 49 and Figs. 50, 51 and 52, it can be seen that, between the first, second and third approaches to GNSS-aided photogrammetry via video, the best performance was achieved by the first approach. From the analysis of the point cloud sections in Fig. 49, it can be seen that the use of the 360° action camera produced slightly noisier point clouds affected by deformations at the corners, which can be assumed to have affected the C2C and C2M results. Furthermore, considering the values for point cloud numerosity in Tab. 42, it can be seen that the first approach produced more point clouds than the second and third approaches.

Analysing the values in Tabs. 41, 42, 46, 47 and 48 and in Figs. 47, 50 and 51, it can be seen that, when comparing the fourth approach with the first and the fifth approach with the second, the fourth and fifth approaches achieve larger point clouds and comparable C2C values by using fewer photos than video frames, but at the expense of a longer survey time despite the smaller number of images acquired.

With regard to the comparison with other approaches and systems proposed in the literature, in the first approach proposed in this research, compared to the static approach of Previtali *et al.* (2023), the use of the smartphone camera and the RTK Camera app allowed, in the pipeline, to automatically produce geotagged smartphone photos. With regard to the third approach presented, in order to avoid the time synchronisation problems reported in Morelli *et al.* (2022) and Previtali *et al.* (2023) in kinematic approaches with videos, in this experimentation it was decided to use a method of georeferencing the video frames based on the geometry and features of the path executed. This resulted in similar C2C and C2M values between the third and second approaches (Tabs. 47, 48 and 49 and Figs. 50, 51 and 52). However, further studies will have to be conducted on the third approach in order to assess how different geometries, path features and greater extent of survey may affect the final performance of the approach. In addition, the mechanical frame for the third approach will need to be improved with the addition of a stabiliser to ensure planimetric alignment between the GNSS antenna and the 360° action camera during continuous motion.

Analysing the results of the first and second case study, it can be seen that the C2C values (Tabs. 50 and 51 and Figs. 53 and 54) are consistent with the values obtained in Previtali *et al.* (2023), the slightly worse values in the first case study can be attributed to disturbances due to tree canopies. Observing the point cloud, mesh model and textures of the first case study (Figs. 53 and 55), it can be seen that the presence of the tree canopies produced some noise in the point cloud, which subsequently turned into shape errors in the mesh model and noise in the texture. Furthermore, due to the low number of input point clouds in some areas, the mesh construction process did not produce the mesh surface in some places. For example, comparing Figs. 53 and 55, it can be seen that the elevation structure on the roof of the building, on the edge between the North and North-East façades, did not produce a mesh surface due to the low number of input point clouds in that area.

Regarding the second case study, from the experience conducted, in agreement with e.g. Barazzetti *et al.* (2019) and Previtali, Cantini and Barazzetti (2023), it can be deduced that it is possible to create a connection between the exterior and interior of a structure by spherical images. In addition, however, the application of GNSS-aided photogrammetry via video allowed for an automatically georeferenced and scaled final model. In the case study under consideration, as there were wide passages between the exterior and interior of the structure, no particular problems were encountered in the processing phase, however, it must be pointed out that more complex connections (e.g. narrow doors between rooms) might require specific survey design to ensure the connection between exterior and interior. Furthermore, from the point of view of the correctness of the surveyed geometry, the “vaulted” structure, with no angles, performed well when surveyed with a 360° action camera.

Finally, by comparing the C2C values in Tabs. 46 and 48 and Figs. 47 and 51 of the three approaches to GNSS-aided photogrammetry via video with those obtained from iOS LiDAR, it can be seen that in the tests performed, GNSS-aided photogrammetry showed better performance in surveying both small-medium and medium-large objects. Furthermore, it can be seen in Fig. 49 that some medium to large object surfaces scanned by iOS LiDAR exhibit the surface splitting problem previously observed in

the chapter 3. Some problems in the creation of point clouds due to errors in video frames and images alignment and geolocation also occurred in the application of GNSS-aided photogrammetry. But working with raw data, the problems that occurred could be solved during photogrammetric processing by, for example, re-aligning the images with different parameters or disabling them. When using the GNSS-aided photogrammetry, therefore, it is always advisable to provide some redundancy in the acquisition of videos and photos.

CONCLUSIONS

For your knowledge, coherently with the previous chapters, some parts of the materials reported here were previously published in:

Pepe, M., Costantino, D., **Vozza, G.** and Alfio, V.S. (2021) '**Comparison of Two Approaches to GNSS Positioning Using Code Pseudoranges Generated by Smartphone Device**', Applied Sciences, 11(11), p. 4787. Available at: <https://doi.org/10.3390/app11114787>.

Costantino, D., **Vozza, G.**, Pepe, M. and Alfio, V.S. (2022) '**Smartphone LiDAR Technologies for Surveying and Reality Modelling in Urban Scenarios: Evaluation Methods, Performance and Challenges**', Applied System Innovation, 5(4), p. 63. Available at: <https://doi.org/10.3390/asi5040063>.

Vozza, G., Costantino, D., Pepe, M. and Alfio, V.S. (2023) '**Smart Sensors System Based on Smartphones and Methodology for 3D Modelling in Shallow Water Scenarios**', Applied System Innovation, 6(1), p. 28. Available at: <https://doi.org/10.3390/asi6010028>.

The thesis work's research project examined sensors on mobile devices (smartphones and tablets) and low-cost external sensor systems. It aimed to cost-efficiently gather and produce geospatial data in terrestrial and aquatic environments. The project was divided into four distinct parts (researches/experimentations). The first research presented a statistical method to evaluate smartphone GNSS positioning accuracy using pseudorange measurements, focusing on two methods: DGNS and SPP. The study found that SPP performs better for longer observation periods, while DGNS is more effective short-term. The results suggest smartphone GNSS could be used in citizen science projects, like environmental and heritage monitoring, where its accuracy meets project needs. However, for this research project's specific applications (discussed in chapters 4 and 5), smartphone GNSS

was deemed inadequate, leading to the preference for a low-cost external GNSS receiver for smartphones.

The second research evaluated and compared depth sensors on iOS (LiDAR scanners) and Android (ToF cameras) devices through four case studies. Mathematical descriptors were used to quantify anomalies in depth sensor point clouds, aiding in the understanding and simplification of visual analysis. This method also identifies potential scan issues without needing additional reference scans.

Smartphone and tablet depth sensors are effective for scanning urban objects and environments. Their advantages include portability, ease of use, always available scanning, quick model sharing, fast scanning, and on site scan review and rescanning capabilities. Issues include surface splitting, loss of surface planarity, and INS drift. Additionally, depth sensors are currently limited to a few high-end devices due to market demand, technology availability, and manufacturer decisions. These sensors are best suited for scanning small to medium-sized objects and scenarios that match human movement and account for drift problems.

In the third study, low-cost external sensors, used with smartphones, gathered bathymetric data, leading to a novel method for 3D modeling of underwater environments. This research focused on four main areas:

1. testing the performance of Deeper Smart Sonars CHIRP+ and Pro+ 2 in shallow water;
2. developing a system to sync Deeper Smart Sonars with an external GNSS receiver via smartphone for enhanced real-time and post-processing geolocation;
3. testing a mapping method using machine learning;
4. implementing a pipeline for 3D modeling of natural surface and artificial underwater structures.

The findings suggest Deeper Smart Sonars are effective for regular seabed surveys in natural aquatic settings, relevant for scientific fields like biology, geology, and climatology. For detailed surveys of artificial structures, complex natural environments near coasts, or data fusion across aquatic and terrestrial areas, using

the G > S > P Sys with space-time PPK synchronization is recommended for improved bathymetric data geolocation and 3D modeling.

The ML-based mapping method showed results comparable or superior to traditional interpolation methods, with the advantage of being more automatic. Future research will explore varying surface morphologies and scenarios for further data.

The 3D modeling pipeline demonstrated flexibility, easy implementation, and centimetre-level accuracy. Using MeshLab and Rhino 7 allows for various modeling algorithms based on project objectives, while CloudCompare facilitates geometric data analysis. This approach paves the way for easier data fusion using different techniques (like photogrammetry, LiDAR) and in diverse environments in future research.

In the fourth research, two sensors systems and three approaches to GNSS-aided photogrammetry via video were studied.

The main topics explored in the fourth experimentation were:

1. testing of GNSS-aided photogrammetry via video implemented by smartphones and low-cost sensors;
2. investigate the use of GNSS-aided photogrammetry in cases where the GNSS signal may be disturbed (first case study) or not available for the entire survey area (second case study);
3. experimentation of a method for georeferencing videos (third approach) that was not based on time but on the geometry and features of the path executed;
4. comparison between GNSS-aided photogrammetry by smartphone and the mobile devices depth sensors scanning methods.

Based on the tests conducted on the three approaches, it can be stated that the built-in camera of the smartphone performs better than the 360° action camera and would therefore be preferred in all those cases where it can be used. On the other hand, case studies show that for some specific surveys, the 360° action camera is the best (if not the only) choice. Furthermore, the 360° action camera, by not requiring the operator to pay particular attention to the object to be surveyed, increases the ease of

surveying in the field as the operator is mainly required to follow a certain path. Both types of camera therefore have pros and cons that must be properly evaluated at the survey planning stage in order to choose the most appropriate camera.

Regarding the mode of GNSS data acquisition, the case studies show that continuous acquisition of GNSS data is not always the best strategy and in some cases it is better to geolocate images only at specific points where the quality of GNSS positioning is guaranteed. Based on this, it is therefore considered that the three approaches studied, instead of being considered alternatives to each other, should all be considered equally valid according to the survey to be performed.

Concerning the comparison between GNSS-aided photogrammetry by smartphone and depth sensors for mobile devices, in terms of performances, GNSS-aided photogrammetry performed better in tests than the iOS LiDAR scanner of the iPad 2021 Pro. GNSS-aided photogrammetry cannot perform indoor surveys without a connection to external data, but it can be applied for surveys of both small to medium-sized objects and large scenarios. The GNSS-aided photogrammetry has no real-time feedback on the status of the survey, that means that using the first approach the operator must have some basic knowledge on how to execute a photogrammetric survey, on the other hand if using a 360° action camera the operator must not pay special attention to the object to be surveyed. Finally, the GNSS-aided photogrammetry by allowing more control in post-processing on the raw data acquired during the survey makes it possible to perform some corrections on the acquired data, and this aspect is very important to ensure good final products.

Considering the overall results obtained in the research project and the experiments conducted, it can be seen that the critical aspect of using smartphones and tablets for geomatic purposes consists mainly in the sensor system dedicated to positioning the devices in the various applications. In the cases studied, based on the requirements of the systems to be implemented and the desired applications, the problem was solved with an external GNSS receiver for smartphones, which currently seems to be the most rational and cost-effective solution to solve the problem of smartphone positioning. Nevertheless, this does not exclude the existence of other types of

solutions to be explored in future research, also based on the expected technological evolution of mobile devices in an evolving market.

ACKNOWLEDGEMENTS

Besides the Professors mentioned on the cover, gratitude is also extended to engineers Vincenzo Saverio Alfio and Paul-Cristian Zdrenghea, as well as the reviewers of the thesis.

REFERENCES

About GLONASS. Available at: https://glonass-iac.ru/en/about_glonass/ (Accessed: 20 October 2023).

Alcaras, E., Carnevale, L. and Parente, C. (2020) 'Interpolating single-beam data for sea bottom GIS modelling', *Int. J. Emerg. Trends Eng. Res*, 8, pp. 591–597.

Alfio, V.S., Costantino, D., Pepe, M. and Restuccia Garofalo, A. (2022) 'A Geomatics Approach in Scan to FEM Process Applied to Cultural Heritage Structure: The Case Study of the "Colossus of Barletta"', *Remote Sensing*, 14(3), p. 664. Available at: <https://doi.org/10.3390/rs14030664>.

Alkan, R.M., Ozulu, I.M. and İlçi, V. (2017) 'Performance evaluation of Single Baseline and Network RTK GNSS', *MyCoordinates, December*, pp. 11–15.

Almeida, J. and Santos, V.M. (2013) 'Real time egomotion of a nonholonomic vehicle using LIDAR measurements', *Journal of Field Robotics*, 30(1), pp. 129–141. Available at: <https://doi.org/10.1002/rob.21441>.

Alvarez, L.V., Moreno, H.A., Segales, A.R., Pham, T.G., Pillar-Little, E.A. and Chilson, P.B. (2018) 'Merging unmanned aerial systems (UAS) imagery and echo soundings with an adaptive sampling technique for bathymetric surveys', *Remote Sensing*, 10(9), p. 1362.

Andrachuk, M., Marschke, M., Hings, C. and Armitage, D. (2019) 'Smartphone technologies supporting community-based environmental monitoring and implementation: a systematic scoping review', *Biological Conservation*, 237, pp. 430–442. Available at: <https://doi.org/10.1016/j.biocon.2019.07.026>.

Avtar, R., Aggarwal, R., Kharrazi, A., Kumar, P. and Kurniawan, T.A. (2019) 'Utilizing geospatial information to implement SDGs and monitor their Progress', *Environmental Monitoring and Assessment*, 192(1), p. 35. Available at: <https://doi.org/10.1007/s10661-019-7996-9>.

Balazadegan Sarvrood, Y., Hosseinyalamdary, S. and Gao, Y. (2016) 'Visual-LiDAR Odometry Aided by Reduced IMU', *ISPRS International Journal of Geo-Information*, 5(1), p. 3. Available at: <https://doi.org/10.3390/ijgi5010003>.

Bandini, F., Kooij, L., Mortensen, B.K., Caspersen, M.B., Thomsen, L.G., Olesen, D. and Bauer-Gottwein, P. (2023) 'Mapping inland water bathymetry with Ground Penetrating Radar (GPR) on board Unmanned Aerial Systems (UASs)', *Journal of Hydrology*, 616, p. 128789. Available at: <https://doi.org/10.1016/j.jhydrol.2022.128789>.

Bandini, F., Olesen, D., Jakobsen, J., Kittel, C.M.M., Wang, S., Garcia, M. and Bauer-Gottwein, P. (2018) 'Technical note: Bathymetry observations of inland water bodies using a tethered single-beam sonar controlled by an unmanned aerial vehicle', *Hydrology and Earth System Sciences*, 22(8), pp. 4165–4181. Available at: <https://doi.org/10.5194/hess-22-4165-2018>.

Banville, S. 'CSRS-PPP Version 3: Tutorial'. Surveyor General Branch, Natural Resources Canada. Available at: https://webapp.geod.nrcan.gc.ca/geod/tools-outils/sample_doc_filesV3/NRCan%20CSRS-PPP-v3_Tutorial%20EN.pdf (Accessed: 21 December 2020).

Barai, A. and Dey, L. (2017) 'Outlier detection and removal algorithm in k-means and hierarchical clustering', *World Journal of Computer Application and Technology*, 5(2), pp. 24–29. Available at: <https://doi.org/10.13189/wjcat.2017.050202>.

Barazzetti, L., Previtali, M. and Roncoroni, F. (2022) '3D MODELING WITH 5K 360° VIDEOS', *International Archives of the Photogrammetry, Remote Sensing and Spatial Information Sciences*, 46(2), pp. 65–71.

Barazzetti, L., Previtali, M., Roncoroni, F. and Valente, R. (2019) 'CONNECTING INSIDE AND OUTSIDE THROUGH 360° IMAGERY FOR CLOSE-RANGE PHOTOGRAMMETRY', *The International Archives of the Photogrammetry, Remote Sensing and Spatial Information Sciences*, XLII-2-W9, pp. 87–92. Available at: <https://doi.org/10.5194/isprs-archives-XLII-2-W9-87-2019>.

BeiDou Navigation Satellite System (China). Available at: <https://novatel.com/an-introduction-to-gnss/gnss-constellations/beidou> (Accessed: 20 October 2023).

Besl, P.J. and McKay, N.D. (1992) 'Method for registration of 3-D shapes', in *Sensor Fusion IV: Control Paradigms and Data Structures*. *Sensor Fusion IV: Control Paradigms and Data Structures*, SPIE, pp. 586–606. Available at: <https://doi.org/10.1117/12.57955>.

Bianco, S., Ciocca, G. and Marelli, D. (2018) 'Evaluating the Performance of Structure from Motion Pipelines', *Journal of Imaging*, 4(8), p. 98. Available at: <https://doi.org/10.3390/jimaging4080098>.

Bio, A., Gonçalves, J.A., Magalhães, A., Pinheiro, J. and Bastos, L. (2022) 'Combining Low-Cost Sonar and High-Precision Global Navigation Satellite System for Shallow Water Bathymetry', *Estuaries and Coasts*, 45(4), pp. 1000–1011. Available at: <https://doi.org/10.1007/s12237-020-00703-6>.

Blewitt, G. (1997) 'Basics of the GPS technique: observation equations', *Geodetic applications of GPS*, 1, p. 46.

Bogoyavlensky, V., Bogoyavlensky, I., Nikonov, R. and Kishankov, A. (2020) 'Complex of Geophysical Studies of the Seyakha Catastrophic Gas Blowout Crater on the Yamal Peninsula, Russian Arctic', *Geosciences*, 10(6), p. 215.

Bookhahn, M., Brechtel, A., Lorenz, T., Voit, F. and Neumann, F. (2021) 'SparePartAssist—a mobile app to identify spare parts based on 3D sensor data. An interim balance.', *3D NordOst 2021* [Preprint]. Available at: https://www.researchgate.net/profile/Frank-Neumann-6/publication/356810684_SparePartAssist_-_a_mobile_app_to_identify_spare_parts_based_on_3D_sensor_data_An_interim_balance/links/61ae1d73092e735ae2e77109/SparePartAssist-a-mobile-app-to-identify-spare-parts-based-on-3D-sensor-data-An-interim-balance.pdf (Accessed: 20 October 2023).

Breiman, L. (2001) 'Random Forests', *Machine Learning*, 45(1), pp. 5–32. Available at: <https://doi.org/10.1023/A:1010933404324>.

Broere, S., van Emmerik, T., González Fernández, D., Luxemburg, W., de Schipper, M., Cózar Cabañas, A. and van de Giesen, N. (2021) 'Towards Underwater Macroplastic Monitoring Using Echo Sounding'.

Campbell, N.D.F., Vogiatzis, G., Hernández, C. and Cipolla, R. (2008) 'Using Multiple Hypotheses to Improve Depth-Maps for Multi-View Stereo', in D. Forsyth, P. Torr, and A. Zisserman (eds) *Computer Vision – ECCV 2008*. Berlin, Heidelberg: Springer (Lecture Notes in Computer Science), pp. 766–779. Available at: https://doi.org/10.1007/978-3-540-88682-2_58.

Canada, N.R. (2013) *data*. Natural Resources Canada. Available at: <https://natural-resources.canada.ca/maps-tools-and-publications/geodetic-reference-systems/data/10923> (Accessed: 24 October 2023).

Cardellicchio, N., Annicchiarico, C., Di Leo, A., Giandomenico, S. and Spada, L. (2016) 'The Mar Piccolo of Taranto: an interesting marine ecosystem for the environmental problems studies', *Environmental Science and Pollution Research*, 23(13), pp. 12495–12501. Available at: <https://doi.org/10.1007/s11356-015-4924-6>.

Charbon, E., Fishburn, M., Walker, R., Henderson, R.K. and Niclass, C. (2013) 'SPAD-Based Sensors', in F. Remondino and D. Stoppa (eds) *TOF Range-Imaging Cameras*. Berlin, Heidelberg: Springer, pp. 11–38. Available at: https://doi.org/10.1007/978-3-642-27523-4_2.

Chen, Y. and Medioni, G. (1992) 'Object modelling by registration of multiple range images', *Image and Vision Computing*, 10(3), pp. 145–155. Available at: [https://doi.org/10.1016/0262-8856\(92\)90066-C](https://doi.org/10.1016/0262-8856(92)90066-C).

Cignoni, P., Callieri, M., Corsini, M., Dellepiane, M., Ganovelli, F. and Ranzuglia, G. (2008) 'Meshlab: an open-source mesh processing tool.', in *Eurographics Italian chapter conference*. Salerno, Italy, pp. 129–136.

Costantino, D., Pepe, M. and Angelini, M.G. (2021) 'EVALUATION OF REFLECTANCE FOR BUILDING MATERIALS CLASSIFICATION WITH TERRESTRIAL LASER SCANNER RADIATION', *Acta Polytechnica*, 61(1), pp. 174–198. Available at: <https://doi.org/10.14311/AP.2021.61.0174>.

Costantino, D., Vozza, G., Alfio, V.S. and Pepe, M. (2021) 'Strategies for 3D Modelling of Buildings from Airborne Laser Scanner and Photogrammetric Data Based on Free-Form and Model-Driven Methods: The Case Study of the Old Town Centre of Bordeaux (France)', *Applied Sciences*, 11(22), p. 10993. Available at: <https://doi.org/10.3390/app112210993>.

Dabove, P., Di Pietra, V., Hatem, S. and Piras, M. (2019) 'GNSS Positioning using Android Smartphone.', in *GISTAM*, pp. 135–142. Available at: <https://doi.org/10.5220/0007764801350142>.

Dabove, P., Di Pietra, V. and Piras, M. (2020) 'GNSS Positioning Using Mobile Devices with the Android Operating System', *ISPRS International Journal of Geo-Information*, 9(4), p. 220. Available at: <https://doi.org/10.3390/ijgi9040220>.

Das, S., Ganguly, K., Mitran, T. and Chakraborty, S.D. (2022) 'Applications of Geospatial and Information Technologies Toward Achieving Sustainable Development Goals', in V.P. Singh, S. Yadav, K.K. Yadav, G.A. Corzo Perez, F. Muñoz-Arriola, and R.N. Yadava (eds) *Application of Remote Sensing and GIS in Natural Resources and Built Infrastructure Management*. Cham: Springer International Publishing (Water Science and Technology Library), pp. 1–27. Available at: https://doi.org/10.1007/978-3-031-14096-9_1.

Di Leo, A., Annicchiarico, C., Cardellicchio, N., Giandomenico, S., Conversano, M., Castellano, G., Basile, F., Martinelli, W., Scortichini, G. and Spada, L. (2014) 'Monitoring of PCDD/Fs and dioxin-like PCBs and seasonal variations in mussels from the Mar Grande and the Mar Piccolo of Taranto (Ionian Sea, Southern Italy)', *Environmental Science and Pollution Research*, 21(23), pp. 13196–13207. Available at: <https://doi.org/10.1007/s11356-014-2495-6>.

Diakit , A.A. and Zlatanova, S. (2016) 'FIRST EXPERIMENTS WITH THE TANGO TABLET FOR INDOOR SCANNING.', *ISPRS Annals of Photogrammetry, Remote Sensing & Spatial Information Sciences*, 3(4).

Dorsey, A.J., Marquis, W.A., Fyfe, P.M., Kaplan, E.D. and Wiederholt, L.F. (2006) 'GPS System Segments', in E.D. Kaplan and C.J. Hegarty (eds) *Understanding GPS - Principles and Applications*. 2nd edn. Norwood: Artech House, pp. 67–112.

Durrant-Whyte, H. and Bailey, T. (2006) 'Simultaneous localization and mapping: part I', *IEEE Robotics Automation Magazine*, 13(2), pp. 99–110. Available at: <https://doi.org/10.1109/MRA.2006.1638022>.

Eissfeller, B. and Won, J.-H. (2017) 'Receiver Architecture', in P.J.G. Teunissen and O. Montenbruck (eds) *Springer Handbook of Global Navigation Satellite Systems*. Cham: Springer International Publishing (Springer Handbooks), pp. 365–400. Available at: https://doi.org/10.1007/978-3-319-42928-1_13.

Eker, R. (2023) 'Comparative use of PPK-integrated close-range terrestrial photogrammetry and a handheld mobile laser scanner in the measurement of forest road surface deformation', *Measurement*, 206, p. 112322. Available at: <https://doi.org/10.1016/j.measurement.2022.112322>.

Eker, R., Elvanoglu, N., Ucar, Z., Bilici, E. and Aydin, A. (2022) '3D modelling of a historic windmill: PPK-aided terrestrial photogrammetry vs smartphone app', *The International Archives of the Photogrammetry, Remote Sensing and Spatial Information Sciences*, 43, pp. 787–792.

Elmezayen, A. and El-Rabbany, A. (2019) 'Precise point positioning using world's first dual-frequency GPS/GALILEO smartphone', *Sensors*, 19(11), p. 2593. Available at: <https://doi.org/10.3390/s19112593>.

Engelhard, N., Endres, F., Hess, J., Sturm, J. and Burgard, W. (2011) 'Real-time 3D visual SLAM with a hand-held RGB-D camera', in *Proc. of the RGB-D Workshop on 3D Perception in Robotics at the European Robotics Forum, Vasteras, Sweden*, pp. 1–15.

European GNSS Agency (2017) 'White Paper on Using GNSS Raw Measurements on Android Devices'. European GNSS Agency. Available at: <https://www.gsa.europa.eu/newsroom/news/available-now-white-paper-using-gnss-raw-measurements-android-devices>.

Fangi, G. (2018) 'Some Metric Documentation of Cultural Heritage in Poland by Spherical Photogrammetry', in R. Cefalo, J.B. Zieliński, and M. Barbarella (eds) *New Advanced GNSS and 3D Spatial Techniques*. Cham: Springer International Publishing (Lecture Notes in Geoinformation and Cartography), pp. 189–203. Available at: https://doi.org/10.1007/978-3-319-56218-6_15.

Fangi, G. and Nardinocchi, C. (2013) 'Photogrammetric Processing of Spherical Panoramas', *The Photogrammetric Record*, 28(143), pp. 293–311. Available at: <https://doi.org/10.1111/phor.12031>.

Farella, E.M., Torresani, A. and Remondino, F. (2019) 'SPARSE POINT CLOUD FILTERING BASED ON COVARIANCE FEATURES', *The International Archives of the Photogrammetry, Remote Sensing and Spatial Information Sciences*, XLII-2/W15, pp. 465–472. Available at: <https://doi.org/10.5194/isprs-archives-XLII-2-W15-465-2019>.

Ferreira, I.O., Rodrigues, D.D., Santos, G.R. dos and Rosa, L.M.F. (2017) 'IN BATHYMETRIC SURFACES: IDW OR KRIGING?', *Boletim de Ciências Geodésicas*, 23, pp. 493–508. Available at: <https://doi.org/10.1590/S1982-21702017000300033>.

Forlani, G., Pinto, L., Roncella, R. and Pagliari, D. (2014) 'Terrestrial photogrammetry without ground control points', *Earth Science Informatics*, 7(2), pp. 71–81. Available at: <https://doi.org/10.1007/s12145-013-0127-1>.

Förstner, W. and Wrobel, B.P. (2016) *Photogrammetric Computer Vision*. Cham: Springer International Publishing (Geometry and Computing). Available at: <https://doi.org/10.1007/978-3-319-11550-4>.

Galeandro, A., Abate, G., Capra, A. and Costantino, D. (2005) 'Installazione e controllo della nuova stazione GPS permanente di Taranto', in. *IX conferenza ASITA*, pp. 1125–1127.

Galileo (European Union). Available at: <https://novatel.com/an-introduction-to-gnss/gnss-constellations/galileo> (Accessed: 20 October 2023).

Gao, R., Xu, J., Chen, Y. and Cho, K. (2023) 'Heterogeneous Feature Fusion Module Based on CNN and Transformer for Multiview Stereo Reconstruction', *Mathematics*, 11(1), p. 112. Available at: <https://doi.org/10.3390/math11010112>.

Giambastiani, Y., Giusti, R., Cecchi, S., Palomba, F., Manetti, F., Romanelli, S. and Bottai, L. (2020) 'Volume estimation of lakes and reservoirs based on aquatic drone surveys: The case study of Tuscany, Italy', *Journal of Water and Land Development*, no. 46. Available at: <https://doi.org/10.24425/jwld.2020.134200>.

Gioia, C. and Borio, D. (2020) 'Android positioning: from stand-alone to cooperative approaches', *Applied Geomatics*, pp. 1–22. Available at: <https://doi.org/10.1007/s12518-020-00333-4>.

Girardeau-Montaut, D. (2016) 'CloudCompare', *France: EDF R&D Telecom ParisTech* [Preprint].

GLONASS (Global Navigation Satellite System), *Russia*. Available at: <https://novatel.com/an-introduction-to-gnss/gnss-constellations/glonass> (Accessed: 20 October 2023).

Gogoi, N., Minetto, A., Linty, N. and Dovis, F. (2019) 'A controlled-environment quality assessment of android GNSS raw measurements', *Electronics*, 8(1), p. 5. Available at: <https://doi.org/10.3390/electronics8010005>.

Gollob, C., Ritter, T., Kraßnitzer, R., Tockner, A. and Nothdurft, A. (2021) 'Measurement of Forest Inventory Parameters with Apple iPad Pro and Integrated LiDAR Technology', *Remote Sensing*, 13(16), p. 3129. Available at: <https://doi.org/10.3390/rs13163129>.

GPS (Global Positioning System), United States. Available at: <https://novatel.com/an-introduction-to-gnss/gnss-constellations/gps> (Accessed: 20 October 2023).

GPS.gov: Space Segment. Available at: <https://www.gps.gov/systems/gps/space/> (Accessed: 20 October 2023).

Granshaw, S.I. (2020) 'Photogrammetric terminology: fourth edition', *The Photogrammetric Record*, 35(170), pp. 143–288. Available at: <https://doi.org/10.1111/phor.12314>.

Guo, L., Wang, F., Sang, J., Lin, X., Gong, X. and Zhang, W. (2020) 'Characteristics analysis of raw multi-GNSS measurement from Xiaomi Mi 8 and positioning performance improvement with L5/E5 frequency in an urban environment', *Remote Sensing*, 12(4), p. 744. Available at: <https://doi.org/10.3390/rs12040744>.

Gyongy, I., Dutton, N.A.W. and Henderson, R.K. (2022) 'Direct Time-of-Flight Single-Photon Imaging', *IEEE Transactions on Electron Devices*, 69(6), pp. 2794–2805. Available at: <https://doi.org/10.1109/TED.2021.3131430>.

Hackel, T., Wegner, J.D. and Schindler, K. (2016) 'Contour Detection in Unstructured 3D Point Clouds', in: *Proceedings of the IEEE Conference on Computer Vision and Pattern Recognition*, pp. 1610–1618. Available at: https://www.cv-foundation.org/openaccess/content_cvpr_2016/html/Hackel_Contour_Detection_in_CVPR_2016_paper.html (Accessed: 24 May 2022).

Hansard, M., Lee, S., Choi, O. and Horaud, R.P. (2012) *Time-of-Flight Cameras: Principles, Methods and Applications*. Springer Science & Business Media.

Hassan, A.T. and Fritsch, D. (2019) 'Integration of Laser Scanning and Photogrammetry in 3D/4D Cultural Heritage Preservation—A Review', *International Journal of Applied*, 9(4), p. 16.

Hauschild, A. (2017) 'Basic Observation Equations', in P.J.G. Teunissen and O. Montenbruck (eds) *Springer Handbook of Global Navigation Satellite Systems*. Cham: Springer International Publishing (Springer Handbooks), pp. 561–582. Available at: https://doi.org/10.1007/978-3-319-42928-1_19.

Hein, G.W. (2020) 'Status, perspectives and trends of satellite navigation', *Satellite Navigation*, 1(1), p. 22. Available at: <https://doi.org/10.1186/s43020-020-00023-x>.

Helminen, J., Linnansaari, T., Bruce, M., Dolson-Edge, R. and Curry, R.A. (2019) 'Accuracy and Precision of Low-Cost Echosounder and Automated Data Processing Software for Habitat Mapping in a Large River', *Diversity*, 11(7), p. 116. Available at: <https://doi.org/10.3390/d11070116>.

Herban, S., Costantino, D., Alfio, V.S. and Pepe, M. (2022) 'Use of Low-Cost Spherical Cameras for the Digitisation of Cultural Heritage Structures into 3D Point Clouds', *Journal of Imaging*, 8(1), p. 13. Available at: <https://doi.org/10.3390/jimaging8010013>.

Hoaglin, D.C., Iglewicz, B. and Tukey, J.W. (1986) 'Performance of some resistant rules for outlier labeling', *Journal of the American Statistical Association*, 81(396), pp. 991–999. Available at: <https://doi.org/10.1080/01621459.1986.10478363>.

Hofmann-Wellenhof, B., Lichtenegger, H. and Waskle, E. (2007) *GNSS – Global Navigation Satellite Systems: GPS, GLONASS, Galileo, and more*. Springer Science & Business Media.

Holz, D., Ichim, A.E., Tombari, F., Rusu, R.B. and Behnke, S. (2015) 'Registration with the Point Cloud Library: A Modular Framework for Aligning in 3-D', *IEEE Robotics & Automation Magazine*, 22(4), pp. 110–124. Available at: <https://doi.org/10.1109/MRA.2015.2432331>.

Horand, R., Hansard, M., Evangelidis, G. and Ménier, C. (2016) 'An overview of depth cameras and range scanners based on time-of-flight technologies', *Machine Vision and Applications*, 27(7), pp. 1005–1020. Available at: <https://doi.org/10.1007/s00138-016-0784-4>.

Hyypä, J., Virtanen, J.-P., Jaakkola, A., Yu, X., Hyypä, H. and Liang, X. (2018) 'Feasibility of Google Tango and Kinect for Crowdsourcing Forestry Information', *Forests*, 9(1), p. 6. Available at: <https://doi.org/10.3390/f9010006>.

International Hydrographic Organization (2011) *Manual on Hydrography*. Publication C-13, 1st ed. Monte Carlo, Monaco: International Hydrographic Bureau.

International Hydrographic Organization (2020) *IHO Standards for Hydrographic Surveys*. Special Publication No. 44, 6th ed. Monte Carlo, Monaco: International Hydrographic Organization.

Jaud, M., Bertin, S., Beauverger, M., Augereau, E. and Delacourt, C. (2020) 'RTK GNSS-Assisted Terrestrial SfM Photogrammetry without GCP: Application to Coastal Morphodynamics Monitoring', *Remote Sensing*, 12(11), p. 1889. Available at: <https://doi.org/10.3390/rs12111889>.

Jivthesh, M.R., Gaushik, M.R., Shibu, N.B.S., Raj, D. and Rao, S.N. (2022) 'A Comprehensive Survey of Web and Mobile Apps for Fishermen', in S. Sharma, S.-L. Peng, J. Agrawal, R.K. Shukla, and D.-N. Le (eds) *Data, Engineering and Applications*. Singapore: Springer Nature (Lecture Notes in Electrical Engineering), pp. 199–211. Available at: https://doi.org/10.1007/978-981-19-4687-5_15.

Jolliffe, I. (1990) 'Principal component analysis: A beginner's guide - I. Introduction and application', *Weather*, 45, pp. 375–382. Available at: <https://doi.org/10.1002/j.1477-8696.1990.tb05558.x>.

Jones, E.J.W.; (1999) *Marine Geophysics*. Hoboken, NJ, USA: John Wiley & Sons Inc.

Kannan, K.S., Manoj, K. and Arumugam, S. (2015) 'Labeling methods for identifying outliers', *International Journal of Statistics and Systems*, 10(2), pp. 231–238.

Kazhdan, M., Bolitho, M. and Hoppe, H. (2006) 'Poisson surface reconstruction', in *Proceedings of the fourth Eurographics symposium on Geometry processing*.

Kazhdan, M. and Hoppe, H. (2013) 'Screened poisson surface reconstruction', *ACM Transactions on Graphics (ToG)*, 32(3), pp. 1–13.

Kellerer-Pirklbauer, A., Avian, M., Benn, D.I., Bernsteiner, F., Krisch, P. and Ziesler, C. (2021) 'Buoyant calving and ice-contact lake evolution at Pasterze Glacier (Austria) in the period 1998–2019', *The Cryosphere*, 15(3), pp. 1237–1258.

Kelly, J. and Sukhatme, G.S. (2011) 'Visual-Inertial Sensor Fusion: Localization, Mapping and Sensor-to-Sensor Self-calibration', *The International Journal of Robotics Research*, 30(1), pp. 56–79. Available at: <https://doi.org/10.1177/0278364910382802>.

Koutalakis, P. and Zaimes, G.N. (2022) 'River Flow Measurements Utilizing UAV-Based Surface Velocimetry and Bathymetry Coupled with Sonar', *Hydrology*, 9(8), p. 148. Available at: <https://doi.org/10.3390/hydrology9080148>.

Koutsoudis, A., Ioannakis, G., Arnaoutoglou, F., Kiourt, C. and Chamzas, C. (2020) *3D Reconstruction Challenges Using Structure-From-Motion, Applying Innovative Technologies in Heritage Science*. IGI Global. Available at: <https://doi.org/10.4018/978-1-7998-2871-6.ch007>.

Kuperman, W.A. and Roux, P. (2014) 'Underwater Acoustics', in T.D. Rossing (ed.) *Springer Handbook of Acoustics*. New York, NY: Springer (Springer Handbooks), pp. 157–212. Available at: https://doi.org/10.1007/978-1-4939-0755-7_5.

Langley, R.B., Teunissen, P.J.G. and Montenbruck, O. (2017) 'Introduction to GNSS', in P.J.G. Teunissen and O. Montenbruck (eds) *Springer Handbook of Global Navigation Satellite Systems*. Cham: Springer International Publishing (Springer Handbooks), pp. 3–23. Available at: https://doi.org/10.1007/978-3-319-42928-1_1.

Li, G. and Geng, J. (2019) 'Characteristics of raw multi-GNSS measurement error from Google Android smart devices', *GPS Solutions*, 23(3), pp. 1–16. Available at: <https://doi.org/10.1007/s10291-019-0885-4>.

Li, L. (2014) 'Time-of-flight camera—An introduction', *Technical white paper* [Pre-print], (SLOA190B). Available at: <https://www.academia.edu/download/47210132/Time-of-Flight%20Camera%20-%20An%20Introduction.pdf> (Accessed: 20 October 2023).

Liu, W., Shi, X., Zhu, F., Tao, X. and Wang, F. (2019) 'Quality analysis of multi-GNSS raw observations and a velocity-aided positioning approach based on smartphones', *Advances in Space Research*, 63(8), pp. 2358–2377. Available at: <https://doi.org/10.1016/j.asr.2019.01.004>.

Luetzenburg, G., Kroon, A. and Bjørk, A.A. (2021) 'Evaluation of the Apple iPhone 12 Pro LiDAR for an Application in Geosciences', *Scientific Reports*, 11(1), p. 22221. Available at: <https://doi.org/10.1038/s41598-021-01763-9>.

Luhmann, T., Robson, S., Kyle, S. and Boehm, J. (2023) *Close-Range Photogrammetry and 3D Imaging*. Walter de Gruyter GmbH & Co KG.

Lurton, X. (2002) *An introduction to underwater acoustics: principles and applications*. Springer.

Martínez, J.L., González, J., Morales, J., Mandow, A. and García-Cerezo, A.J. (2006) 'Mobile robot motion estimation by 2D scan matching with genetic and iterative closest point algorithms', *Journal of Field Robotics*, 23(1), pp. 21–34. Available at: <https://doi.org/10.1002/rob.20104>.

Matheron, G. (1962) *Traité de géostatistique appliquée*. Editions Technip (14).

Medwin, H. (1975) 'Speed of sound in water: A simple equation for realistic parameters', *The Journal of the Acoustical Society of America*, 58(6), pp. 1318–1319. Available at: <https://doi.org/10.1121/1.380790>.

Medwin, H. and Clay, C.S. (1997) *Fundamentals of Acoustical Oceanography*. Academic Press.

Mehta, S., Patel, A. and Mehta, J. (2015) 'CCD or CMOS Image sensor for photography', *2015 International Conference on Communications and Signal Processing (ICCSP)*, pp. 0291–0294. Available at: <https://doi.org/10.1109/ICCSP.2015.7322890>.

Mikita, T., Balková, M., Bajer, A., Cibulka, M. and Patočka, Z. (2020) 'Comparison of Different Remote Sensing Methods for 3D Modeling of Small Rock Outcrops', *Sensors*, 20(6), p. 1663. Available at: <https://doi.org/10.3390/s20061663>.

Monteys, X., Harris, P., Caloca, S. and Cahalane, C. (2015) 'Spatial Prediction of Coastal Bathymetry Based on Multispectral Satellite Imagery and Multibeam Data', *Remote Sensing*, 7(10), pp. 13782–13806. Available at: <https://doi.org/10.3390/rs71013782>.

Moore, D.S., Notz, W.I. and Fligner, M.A. (2015) *The basic practice of statistics*. Macmillan Higher Education.

Morang, A., Larson, R. and Gorman, L. (1997) 'Monitoring the Coastal Environment; Part III: Geophysical and Research Methods', *Journal of Coastal Research*, 13(4), pp. 1064–1085.

Morelli, L., Menna, F., Vitti, A. and Remondino, F. (2022) 'Action Cams and Low-Cost Multi-Frequency Antennas for GnsS Assisted Photogrammetric Applications Without Ground Control Points', *The International Archives of the Photogrammetry, Remote Sensing and Spatial Information Sciences*, 48, pp. 171–176.

Nakamura, J. (2006) 'Basics of Image Sensors', in J. Nakamura (ed.) *Image Sensors and Signal Processing for Digital Still Cameras*. CRC Press - Taylor & Francis Group, pp. 53–93.

Odijk, D. (2017) 'Positioning Model', in P.J.G. Teunissen and O. Montenbruck (eds) *Springer Handbook of Global Navigation Satellite Systems*. Cham: Springer International Publishing (Springer Handbooks), pp. 605–638. Available at: https://doi.org/10.1007/978-3-319-42928-1_21.

Odijk, D. and Wanninger, L. (2017) 'Differential Positioning', in P.J.G. Teunissen and O. Montenbruck (eds) *Springer Handbook of Global Navigation Satellite Systems*. Cham: Springer International Publishing (Springer Handbooks), pp. 753–780. Available at: https://doi.org/10.1007/978-3-319-42928-1_26.

Padmanabhan, P., Zhang, C. and Charbon, E. (2019) 'Modeling and Analysis of a Direct Time-of-Flight Sensor Architecture for LiDAR Applications', *Sensors*, 19(24), p. 5464. Available at: <https://doi.org/10.3390/s19245464>.

Parente, C. and Vallario, A. (2019) 'Interpolation of Single Beam Echo Sounder Data for 3D Bathymetric Model', *International Journal of Advanced Computer Science and Applications*, 10(10). Available at: <https://doi.org/10.14569/IJACSA.2019.0101002>.

Pauly, M., Gross, M. and Kobbelt, L.P. (2002) 'Efficient simplification of point-sampled surfaces', in *IEEE Visualization, 2002. VIS 2002. IEEE Visualization, 2002. VIS 2002.*, pp. 163–170. Available at: <https://doi.org/10.1109/VISUAL.2002.1183771>.

Paziewski, J., Fortunato, M., Mazzoni, A. and Odolinski, R. (2021) 'An analysis of multi-GNSS observations tracked by recent Android smartphones and smartphone-only relative positioning results', *Measurement*, 175, p. 109162. Available at: <https://doi.org/10.1016/j.measurement.2021.109162>.

Pepe, M. (2018) 'CORS architecture and evaluation of positioning by low-cost GNSS receiver', *Geodesy and Cartography*, 44(2), pp. 36–44. Available at: <https://doi.org/10.3846/gac.2018.1255>.

Pepe, M., Alfio, V.S. and Costantino, D. (2022) 'UAV Platforms and the SfM-MVS Approach in the 3D Surveys and Modelling: A Review in the Cultural Heritage Field', *Applied Sciences*, 12(24), p. 12886. Available at: <https://doi.org/10.3390/app122412886>.

Pepe, M., Alfio, V.S., Costantino, D. and Herban, S. (2022) 'Rapid and Accurate Production of 3D Point Cloud via Latest-Generation Sensors in the Field of Cultural Heritage: A Comparison between SLAM and Spherical Videogrammetry', *Heritage*, 5(3), pp. 1910–1928. Available at: <https://doi.org/10.3390/heritage5030099>.

Pereira, G.W., Valente, D.S.M., Queiroz, D.M. de, Coelho, A.L. de F., Costa, M.M. and Grift, T. (2022) 'Smart-Map: An Open-Source QGIS Plugin for Digital Mapping Using Machine Learning Techniques and Ordinary Kriging', *Agronomy*, 12(6), p. 1350. Available at: <https://doi.org/10.3390/agronomy12061350>.

Pereira, G.W., Valente, D.S.M., de Queiroz, D.M., Santos, N.T. and Fernandes-Filho, E.I. (2022) 'Soil mapping for precision agriculture using support vector machines combined with inverse distance weighting', *Precision Agriculture*, 23(4), pp. 1189–1204. Available at: <https://doi.org/10.1007/s11119-022-09880-9>.

Piatti, D., Remondino, F. and Stoppa, D. (2013) 'State-of-the-Art of TOF Range-Imaging Sensors', in F. Remondino and D. Stoppa (eds) *TOF Range-Imaging Cameras*. Berlin, Heidelberg: Springer, pp. 1–9. Available at: https://doi.org/10.1007/978-3-642-27523-4_1.

Posa, D. and De Iaco, S. (2009) *Geostatistica: teoria e applicazioni*. Giappichelli.

Previtali, M., Barazzetti, L., Roncoroni, F., Cao, Y. and Scaioni, M. (2023) '360° IMAGE ORIENTATION AND RECONSTRUCTION WITH CAMERA POSITIONS CONSTRAINED BY GNSS MEASUREMENTS', *The International Archives of the Photogrammetry, Remote Sensing and Spatial Information Sciences*, XLVIII-1-W1-2023, pp. 411–416. Available at: <https://doi.org/10.5194/isprs-archives-XLVIII-1-W1-2023-411-2023>.

Previtali, M., Cantini, L. and Barazzetti, L. (2023) 'COMBINED 360° VIDEO AND UAV RECONSTRUCTION OF SMALL-TOWN HISTORIC CITY CENTERS', *The International Archives of the Photogrammetry, Remote Sensing and Spatial Information Sciences*, XLVIII-M-2-2023, pp. 1233–1240. Available at: <https://doi.org/10.5194/isprs-archives-XLVIII-M-2-2023-1233-2023>.

RadhaKrishna, M.V.V., Govindh, M.V. and Veni, P.K. (2021) 'A Review on Image Processing Sensor', *Journal of Physics: Conference Series*, 1714(1), p. 012055. Available at: <https://doi.org/10.1088/1742-6596/1714/1/012055>.

Realini, E., Caldera, S., Pertusini, L. and Sampietro, D. (2017) 'Precise GNSS positioning using smart devices', *Sensors*, 17(10), p. 2434. Available at: <https://doi.org/10.3390/s17102434>.

Riquelme, A., Tomás, R., Cano, M., Pastor, J.L. and Jordá-Bordehore, L. (2021) 'Extraction of discontinuity sets of rocky slopes using iPhone-12 derived 3DPC and comparison to TLS and SfM datasets', *IOP Conference Series: Earth and Environmental Science*, 833(1), p. 012056. Available at: <https://doi.org/10.1088/1755-1315/833/1/012056>.

Rizos, C. (2017) 'Surveying', in P.J.G. Teunissen and O. Montenbruck (eds) *Springer Handbook of Global Navigation Satellite Systems*. Cham: Springer International Publishing (Springer Handbooks), pp. 1011–1037. Available at: https://doi.org/10.1007/978-3-319-42928-1_35.

Robustelli, U., Paziewski, J. and Pugliano, G. (2021) 'Observation Quality Assessment and Performance of GNSS Standalone Positioning with Code Pseudoranges of Dual-Frequency Android Smartphones', *Sensors*, 21(6), p. 2125. Available at: <https://doi.org/10.3390/s21062125>.

Romano, J. (2015) 'People-centred post-2015 review & accountability with transparency and citizen participation at its core'.

RTKLIB: An Open Source Program Package for GNSS Positioning. Available at: <https://rtklib.com/> (Accessed: 22 October 2023).

Rtklibexplorer. *Release RTKLIB: demo5 b34f.1 · rtklibexplorer/RTKLIB, GitHub*. Available at: <https://github.com/rtklibexplorer/RTKLIB/releases/tag/b34f> (Accessed: 8 January 2023a).

Rtklibexplorer. *rtklibexplorer (rtklibexplorer) / Repositories · GitHub*. Available at: <https://github.com/rtklibexplorer?tab=repositories> (Accessed: 8 January 2023b).

Ruffell, A., Lally, A. and Rocke, B. (2021) 'Dronar—Geoforensic Search Sonar from a Drone', *Forensic Sciences*, 1(3), pp. 202–212. Available at: <https://doi.org/10.3390/forensicsci1030018>.

Rusinkiewicz, S. and Levoy, M. (2001) 'Efficient variants of the ICP algorithm', in *Proceedings Third International Conference on 3-D Digital Imaging and Modeling. Proceedings Third International Conference on 3-D Digital Imaging and Modeling*, pp. 145–152. Available at: <https://doi.org/10.1109/IM.2001.924423>.

Ryabinin, V., Barbière, J., Haugan, P., Kullenberg, G., Smith, N., McLean, C., Troisi, A., Fischer, A., Aricò, S., Aarup, T., Pissierssens, P., Visbeck, M., Enevoldsen, H.O. and Rigaud, J. (2019) 'The UN Decade of Ocean Science for Sustainable Development', *Frontiers in Marine Science*, 6. Available at: <https://www.frontiersin.org/article/10.3389/fmars.2019.00470> (Accessed: 22 February 2022).

Sanjou, M., Kato, K., Aizawa, W. and Okamoto, T. (2022) 'Development of drone-type float for surface-velocity measurement in rivers', *Environmental Fluid Mechanics*, 22(4), pp. 955–969. Available at: <https://doi.org/10.1007/s10652-022-09874-1>.

Schindler, K. and Förstner, W. (2014) 'Photogrammetry', in K. Ikeuchi (ed.) *Computer Vision: A Reference Guide*. Boston, MA: Springer US, pp. 597–599. Available at: https://doi.org/10.1007/978-0-387-31439-6_139.

Scott, G. and Rajabifard, A. (2017) 'Sustainable development and geospatial information: a strategic framework for integrating a global policy agenda into national geospatial capabilities', *Geo-spatial Information Science*, 20(2), pp. 59–76. Available at: <https://doi.org/10.1080/10095020.2017.1325594>.

Semler, Q., Mangin, L., Moussaoui, A. and Semin, E. (2019) 'DEVELOPMENT OF A LOW-COST CENTIMETRIC GNSS POSITIONING SOLUTION FOR ANDROID APPLICATIONS.', *International Archives of the Photogrammetry, Remote Sensing & Spatial Information Sciences* [Preprint].

Shapiro, S.S. and Wilk, M.B. (1965) 'An analysis of variance test for normality (complete samples)', *Biometrika*, 52(3/4), pp. 591–611. Available at: <https://doi.org/10.2307/2333709>.

Shen, N., Chen, L., Liu, J., Wang, L., Tao, T., Wu, D. and Chen, R. (2019) 'A Review of Global Navigation Satellite System (GNSS)-Based Dynamic Monitoring Technologies for Structural Health Monitoring', *Remote Sensing*, 11(9), p. 1001. Available at: <https://doi.org/10.3390/rs11091001>.

SOR filter - *CloudCompareWiki*. Available at: https://www.cloudcompare.org/doc/wiki/index.php/SOR_filter (Accessed: 21 October 2023).

Spreafico, A., Chiabrando, F., Losè, L.T. and Tonolo, F.G. (2021) 'The Ipad Pro Built-In LIDAR Sensor: 3d Rapid Mapping Tests and Quality Assessment', *The International Archives of Photogrammetry, Remote Sensing and Spatial Information Sciences*, 43, pp. 63–69. Available at: <https://doi.org/10.5194/isprs-archives-XLIII-B1-2021-63-2021>.

Stock, K. and Guesgen, H. (2016) 'Chapter 10 - Geospatial Reasoning With Open Data', in R. Layton and P.A. Watters (eds) *Automating Open Source Intelligence*. Boston: Syngress, pp. 171–204. Available at: <https://doi.org/10.1016/B978-0-12-802916-9.00010-5>.

System. Available at: <http://en.beidou.gov.cn/SYSTEMS/System/> (Accessed: 20 October 2023).

System | *European GNSS Service Centre*. Available at: <https://www.gsc-europa.eu/galileo/system> (Accessed: 20 October 2023).

Takasu, T. (2013) 'RTKLIB ver. 2.4. 2 Manual', *RTKLIB: An Open Source Program Package for GNSS Positioning*, pp. 29–49.

Takasu, T. and Yasuda, A. (2009) 'Development of the low-cost RTK-GPS receiver with an open source program package RTKLIB', in *International symposium on GPS/GNSS*. International Convention Center Jeju Korea.

Tannant, D.D. (2015) 'Review of photogrammetry-based techniques for characterization and hazard assessment of rock faces', *International Journal of Georesources and Environment-IJGE (formerly Int'l J of Geohazards and Environment)*, 1(2), pp. 76–87.

Tavani, S., Billi, A., Corradetti, A., Mercuri, M., Bosman, A., Cuffaro, M., Seers, T. and Carminati, E. (2022) 'Smartphone assisted fieldwork: Towards the digital transition of geoscience fieldwork using LiDAR-equipped iPhones', *Earth-Science Reviews*, 227, p. 103969. Available at: <https://doi.org/10.1016/j.earscirev.2022.103969>.

Tétreault, P., Kouba, J., Héroux, P. and Legree, P. (2005) 'CSRS-PPP: an internet service for GPS user access to the Canadian Spatial Reference Frame', *Geomatica*, 59(1), pp. 17–28. Available at: <https://doi.org/10.5623/geomat-2005-0004>.

Teunissen, P. (2006) 'The Lambda Method for the GNSS Compass', *Artificial Satellites*, 41(3), pp. 89–103. Available at: <https://doi.org/10.2478/v10018-007-0009-1>.

Tomaščík, J., Saloň, Š., Tunák, D., Chudý, F. and Kardoš, M. (2017) 'Tango in forests – An initial experience of the use of the new Google technology in connection with forest inventory tasks', *Computers and Electronics in Agriculture*, 141, pp. 109–117. Available at: <https://doi.org/10.1016/j.compag.2017.07.015>.

Tonion, F., Pirotti, F., Faina, G. and Paltrinieri, D. (2020) 'A MACHINE LEARNING APPROACH TO MULTISPECTRAL SATELLITE DERIVED BATHYMETRY', *ISPRS Annals of the Photogrammetry, Remote Sensing and Spatial Information Sciences*, V-3–2020, pp. 565–570. Available at: <https://doi.org/10.5194/isprs-annals-V-3-2020-565-2020>.

Toriya, H., Tungol, Z.P.L., Ikeda, H., Owada, N., Jang, H.D., Adachi, T., Kitahara, I. and Kawamura, Y. (2022) 'Fragmentation Size Distribution Measurement by GNSS-Aided Photogrammetry at Real Mine Site', *Mining*, 2(3), pp. 438–448. Available at: <https://doi.org/10.3390/mining2030023>.

Toyoda, K. (2006) 'Digital Still Cameras at a Glance', in J. Nakamura (ed.) *Image Sensors and Signal Processing for Digital Still Cameras*. CRC Press - Taylor & Francis Group, pp. 1–19.

Tsoukalos, D., Drosos, V. and Tsohis, D.K. (2021) 'Attempting to reconstruct a 3D indoor space scene with a mobile device using ARCore', in *2021 12th International Conference on Information, Intelligence, Systems Applications (IISA)*. *2021 12th International Conference on Information, Intelligence, Systems Applications (IISA)*, pp. 1–6. Available at: <https://doi.org/10.1109/IISA52424.2021.9555529>.

Tukey, J.W. (1977) *Exploratory data analysis*. Reading, Mass.

Tungol, Z.P.L., Toriya, H., Owada, N., Kitahara, I., Inagaki, F., Saadat, M., Jang, H.D. and Kawamura, Y. (2021) 'Model Scaling in Smartphone GNSS-Aided Photogrammetry for Fragmentation Size Distribution Estimation', *Minerals*, 11(12), p. 1301. Available at: <https://doi.org/10.3390/min11121301>.

United Nations (2012) 'The Future We Want'.

United Nations (2015) 'Transforming our World: The 2030 Agenda for Sustainable Development'.

Vogt, M., Rips, A. and Emmelmann, C. (2021) 'Comparison of iPad Pro®'s LiDAR and TrueDepth Capabilities with an Industrial 3D Scanning Solution', *Technologies*, 9(2), p. 25. Available at: <https://doi.org/10.3390/technologies9020025>.

Wanninger, L. and Heßelbarth, A. (2020) 'GNSS code and carrier phase observations of a Huawei P30 smartphone: Quality assessment and centimeter-accurate positioning', *GPS Solutions*, 24(2), pp. 1–9. Available at: <https://doi.org/10.1007/s10291-020-00978-z>.

Wells, D., Beck, N., Delikaraoglou, D., Kleusberg, A., Krakiwsky, E.J., Lachapelle, G., Langley, R.B., Nakiboglu, M., Schwarz, K.-P., Tranquilla, J.M. and Vanicek, P. (1986) *Guide to GPS Positioning*. Fredericton, New Brunswick, Canada: Department of Geodesy and Geomatics Engineering Lecture Note No. 58, University of New Brunswick.

What is geospatial data? | IBM. Available at: <https://www.ibm.com/topics/geospatial-data> (Accessed: 20 October 2023).

Wübbena, T., Darugna, F., Ito, A. and Wübbena, J. (2018) *Geo++'s Experiments on Android GNSS Raw Data*.

Yadav, J. and Sharma, M. (2013) 'A Review of K-mean Algorithm', *International journal of engineering trends and technology*, 4(7), pp. 2972–2976.

Yilmaz, H.M., Yakar, M. and Yildiz, F. (2008) 'Digital photogrammetry in obtaining of 3D model data of irregular small objects', *The International Archives of the Photogrammetry, Remote Sensing and Spatial Information Sciences*, 37, pp. 125–130.

Zhang, K., Jiao, W., Wang, L., Li, Z., Li, J. and Zhou, K. (2019) 'Smart-RTK: Multi-GNSS kinematic positioning approach on android smart devices with Doppler-smoothed-code filter and constant acceleration model', *Advances in Space Research*, 64(9), pp. 1662–1674. Available at: <https://doi.org/10.1016/j.asr.2019.07.043>.

Zhang, L., Jin, Y., Lin, L., Li, J. and Du, Y. (2009) 'The comparison of CCD and CMOS image sensors', in *2008 International Conference on Optical Instruments and Technology: Advanced Sensor Technologies and Applications. 2008 International Conference on Optical Instruments and Technology: Advanced Sensor Technologies and Applications*, SPIE, pp. 231–235. Available at: <https://doi.org/10.1117/12.806221>.

Zhang, X., Tao, X., Zhu, F., Shi, X. and Wang, F. (2018) 'Quality assessment of GNSS observations from an Android N smartphone and positioning performance analysis using time-differenced filtering approach', *Gps Solutions*, 22(3), pp. 1–11. Available at: <https://doi.org/10.1007/s10291-018-0736-8>.

ANNEXES



For your knowledge, coherently with the previous chapters, the materials reported here were previously published in:

Pepe, M., Costantino, D., **Vozza, G.** and Alfio, V.S. (2021) '**Comparison of Two Approaches to GNSS Positioning Using Code Pseudoranges Generated by Smartphone Device**', Applied Sciences, 11(11), p. 4787. Available at: <https://doi.org/10.3390/app11114787>.

Costantino, D., **Vozza, G.**, Pepe, M. and Alfio, V.S. (2022) '**Smartphone LiDAR Technologies for Surveying and Reality Modelling in Urban Scenarios: Evaluation Methods, Performance and Challenges**', Applied System Innovation, 5(4), p. 63. Available at: <https://doi.org/10.3390/asi5040063>.

Vozza, G., Costantino, D., Pepe, M. and Alfio, V.S. (2023) '**Smart Sensors System Based on Smartphones and Methodology for 3D Modelling in Shallow Water Scenarios**', Applied System Innovation, 6(1), p. 28. Available at: <https://doi.org/10.3390/asi6010028>.

Tab. A1 – Oppo Reno4 z 5G and Huawei P20 Lite key features.

Device	Oppo Reno4 z 5G	Huawei P20 Lite
Image		
Chipset	Dimensity 800 MediaTek MT6873	Huawei HiSilicon Ki-rin 659
RAM [GB]	8	4
Original operative system	Android 10 ColorOS 7.2	Android 8.0 Emotion UI 8.0 Oreo
GNSS constellation	GPS, GLONASS, BeiDou, Galileo, QZSS	GPS, GLONASS
Frequency	L1/L5	L1
Observations	Code, carrier-phase	Code, carrier-phase
Weight [g]	184	145
Dimensions [mm]	163.8 × 75.5 × 8.1	148.6 × 71.2 × 7.4

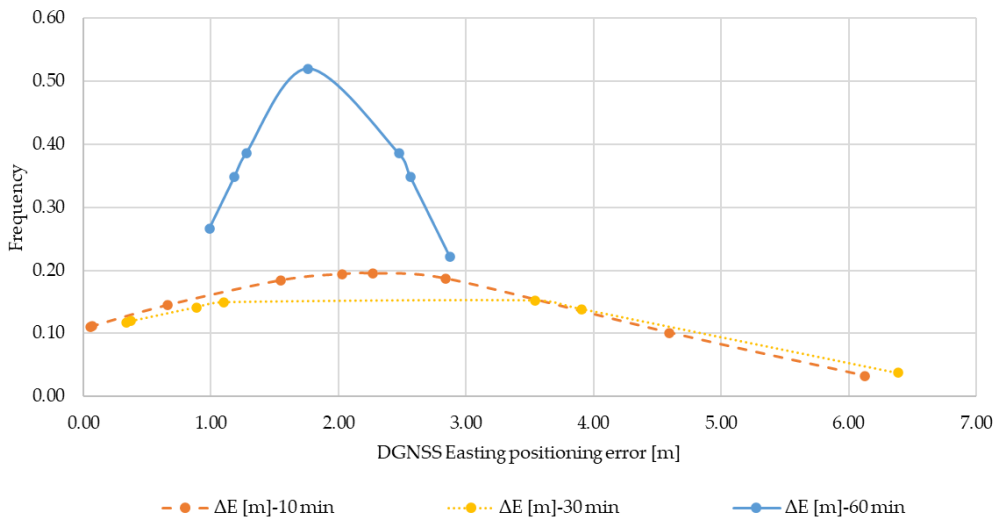


Fig. A1 - Normal distribution DGNSS - ΔE.

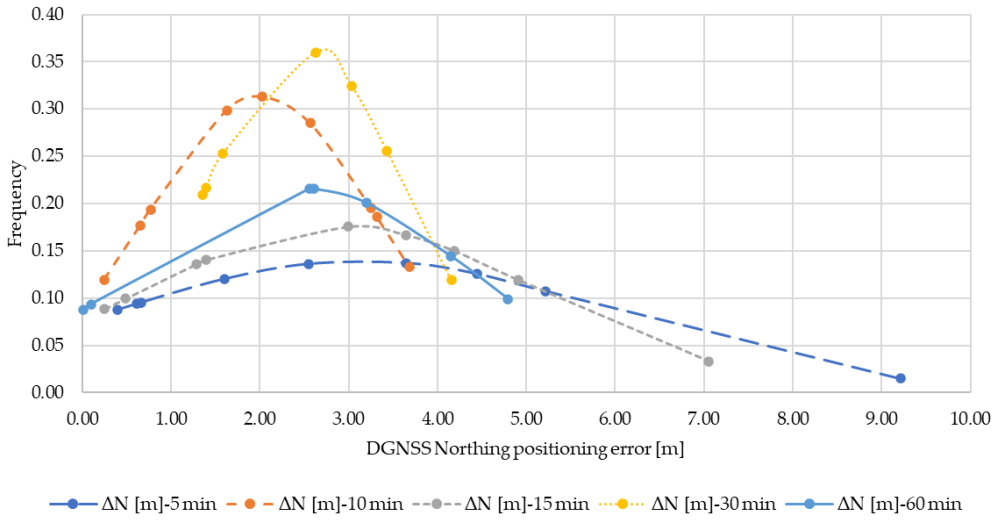


Fig. A2 - Normal distribution DGNSS - ΔN.

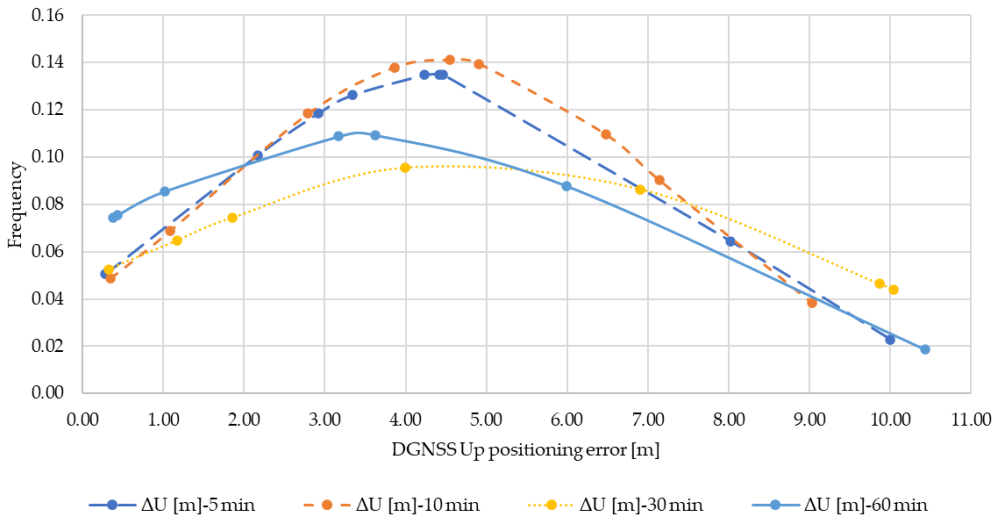


Fig. A3 - Normal distribution DGNSS - ΔU.

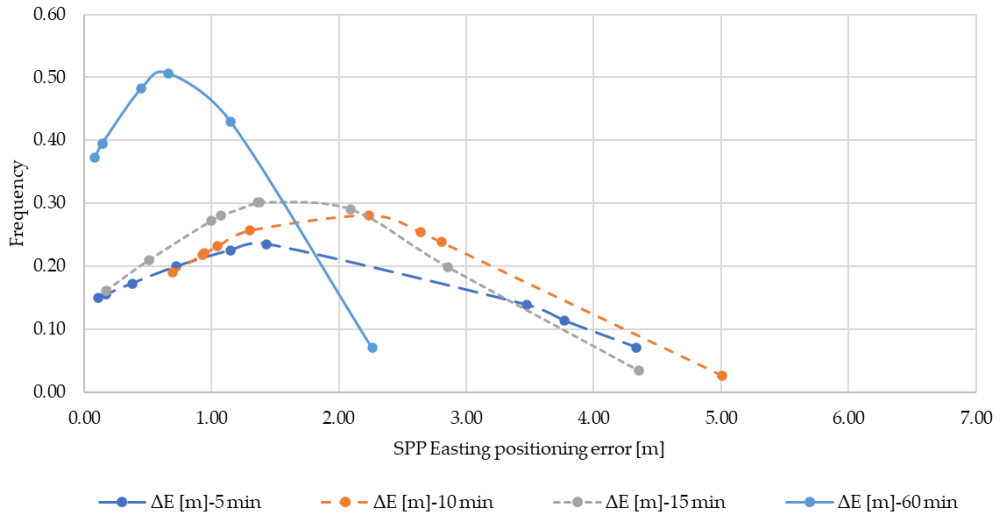


Fig. A4 - Normal distribution SPP - ΔE.

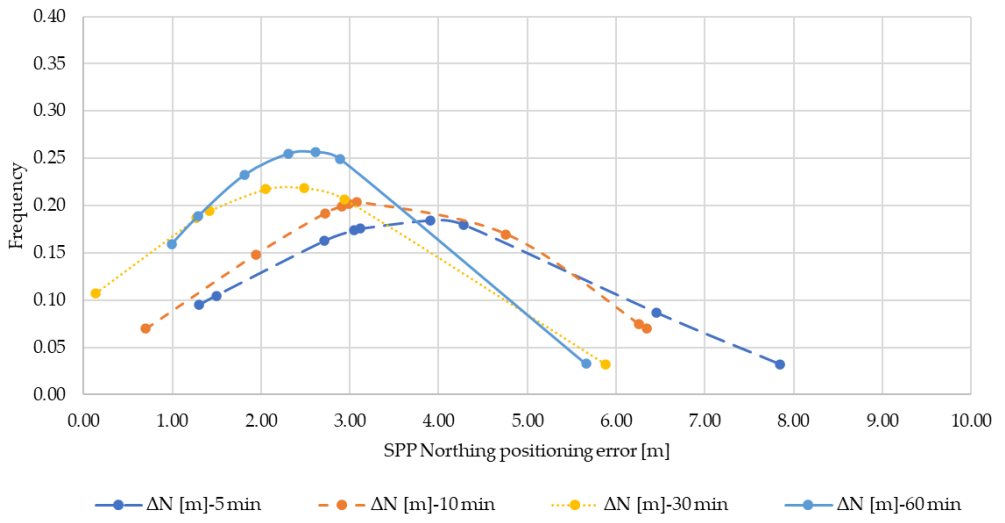


Fig. A5 - Normal distribution SPP - ΔN.

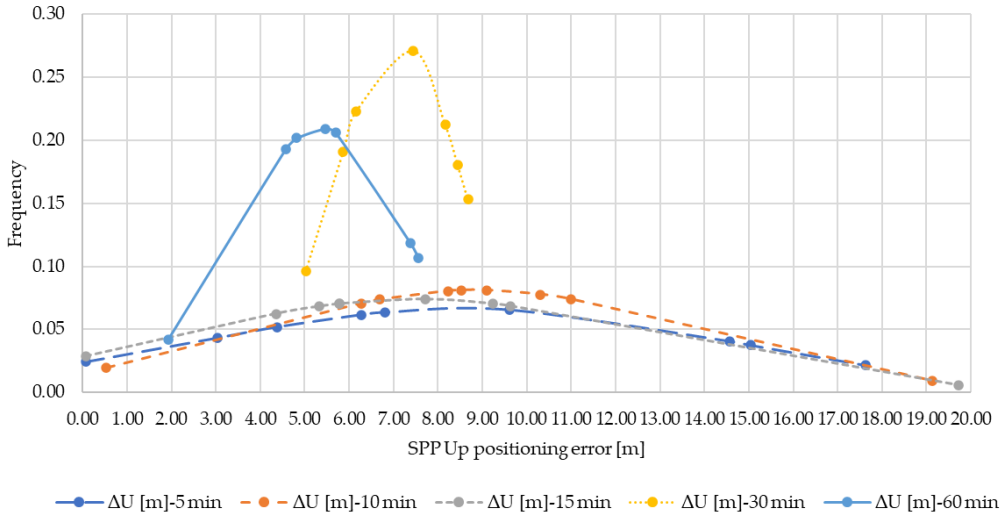
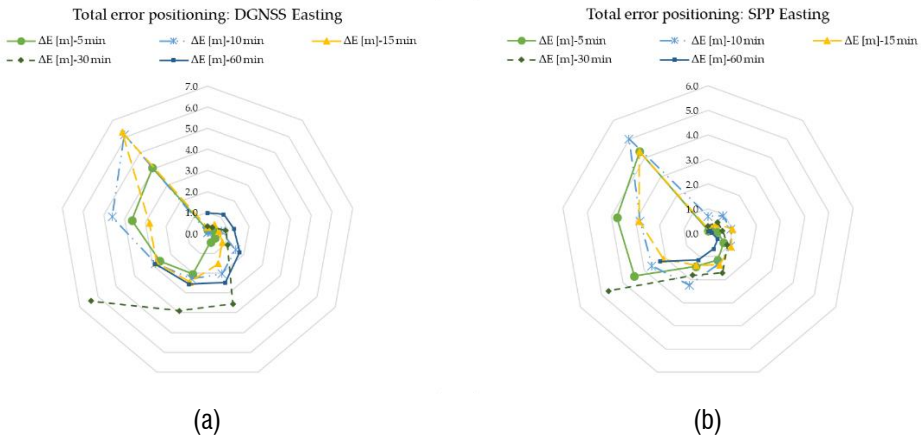
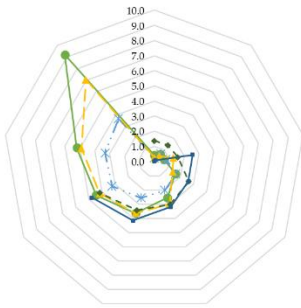


Fig. A6 - Normal distribution SPP - ΔU .

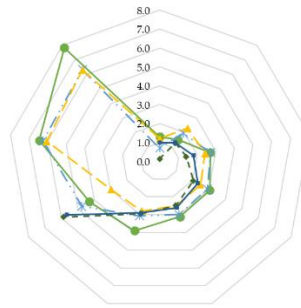


Total error positioning: DGNSS Northing



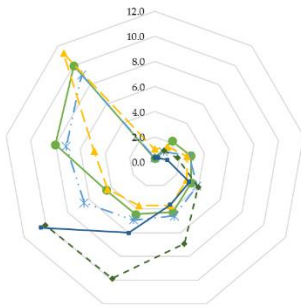
(c)

Total error positioning: SPP Northing



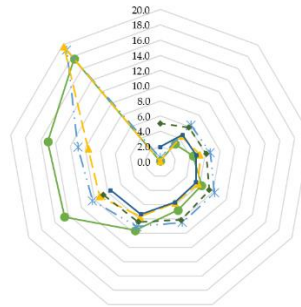
(d)

Total error positioning: DGNSS Up



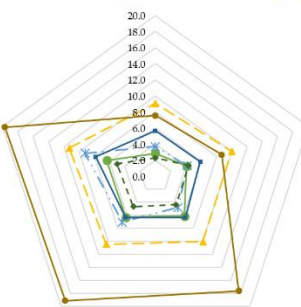
(e)

Total error positioning: SPP Up



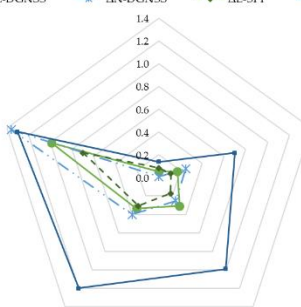
(f)

Max error positioning: DGNSS vs. SPP



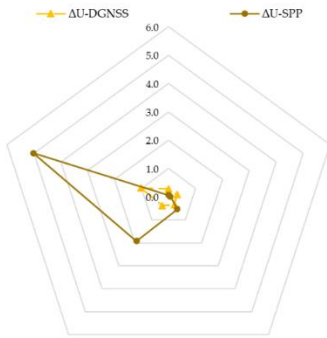
(g)

Minimum error positioning: DGNSS vs. SPP



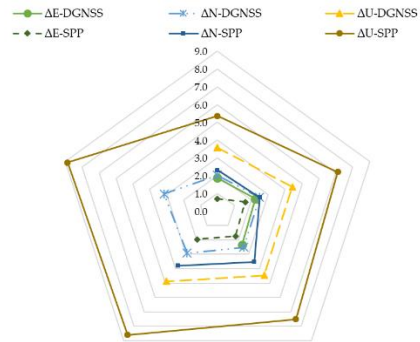
(h)

Minimum error positioning Up: DGNSS vs. SPP



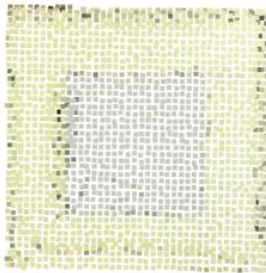
(i)

Mean error positioning: DGNSS vs. SPP



(j)

Fig. A7 – Evaluation of positioning errors for ΔE , ΔN , ΔU : (a) DGNSS positioning error ΔE ; (b) SPP error ΔE ; (c) DGNSS positioning error ΔN ; (d) SPP error ΔN ; (e) DGNSS positioning error ΔU ; (f) SPP error ΔU ; (g) max error positioning DGNSS - SPP; (h) minimum horizontal error positioning errors DGNSS - SPP; (i) minimum error positioning up DGNSS - SPP; (j) mean error positioning DGNSS – SPP.



(a)



(b)



(c)

Fig. A8 – Point cloud of building materials examples: (a) raw cement plaster; (b) white lime plaster; (c) coloured lime plaster.

Tab. A2 – Surface variation values of the point clouds of the 10 building materials samples.

Sample material	Scan distance: 0.5 m			Scan Distance: 1.5 m		
	SV_λ	SV_λ	SV_λ	SV_λ	SV_λ	SV_λ
	1 cm	1.5 cm	2 cm	1 cm	1.5 cm	2 cm
Smooth cement plaster	0.0020	0.0041	0.0082	0.0016	0.0041	0.0060
Raw cement plaster	0.0024	0.0037	0.0056	0.0016	0.0019	0.0036
White lime plaster	0.0021	0.0022	0.0037	0.0005	0.0013	0.0017
Coloured lime plaster	0.0009	0.0026	0.0021	0.0004	0.0010	0.0008
Tetrafluoroethylene (TFE)	0.0013	0.0034	0.0004	0.0001	0.0001	0.0003
Methacrylate (PMMA)	0.0012	0.0010	0.0003	0.0002	0.0002	0.0003
High-density polyethylene (HDPE)	0.0003	0.0001	0.0001	0.0001	0.0001	0.0002
Frosted glass	0.0004	0.0001	0.0001	0.0002	0.0001	0.0001
Steel	No data	No data	0.1672	0.0005	0.0003	0.0051
Brass	0.0021	0.1455	0.1000	0.0003	0.0007	0.0142

Tab. A3 – Planarity values of the point clouds of the 10 building materials samples.

Sample material	Scan distance: 0.5 m			Scan Distance: 1.5 m		
	P_λ	P_λ	P_λ	P_λ	P_λ	P_λ
	1 cm	1.5 cm	2 cm	1 cm	1.5 cm	2 cm
Smooth cement plaster	0.70	0.53	0.73	0.66	0.52	0.67
Raw cement plaster	0.70	0.54	0.71	0.65	0.53	0.68
White lime plaster	0.69	0.53	0.74	0.67	0.52	0.78
Coloured lime plaster	0.71	0.53	0.80	0.67	0.52	0.84
Tetrafluoroethylene (TFE)	0.67	0.50	0.72	0.65	0.52	0.70
Methacrylate (PMMA)	0.66	0.51	0.63	0.65	0.48	0.73
High-density polyethylene (HDPE)	0.67	0.51	0.76	0.66	0.51	0.75
Frosted glass	0.70	0.54	0.82	0.67	0.52	0.79
Steel	No data	No data	-	0.67	0.52	0.66
Brass	0.63	-	-	0.63	0.53	-

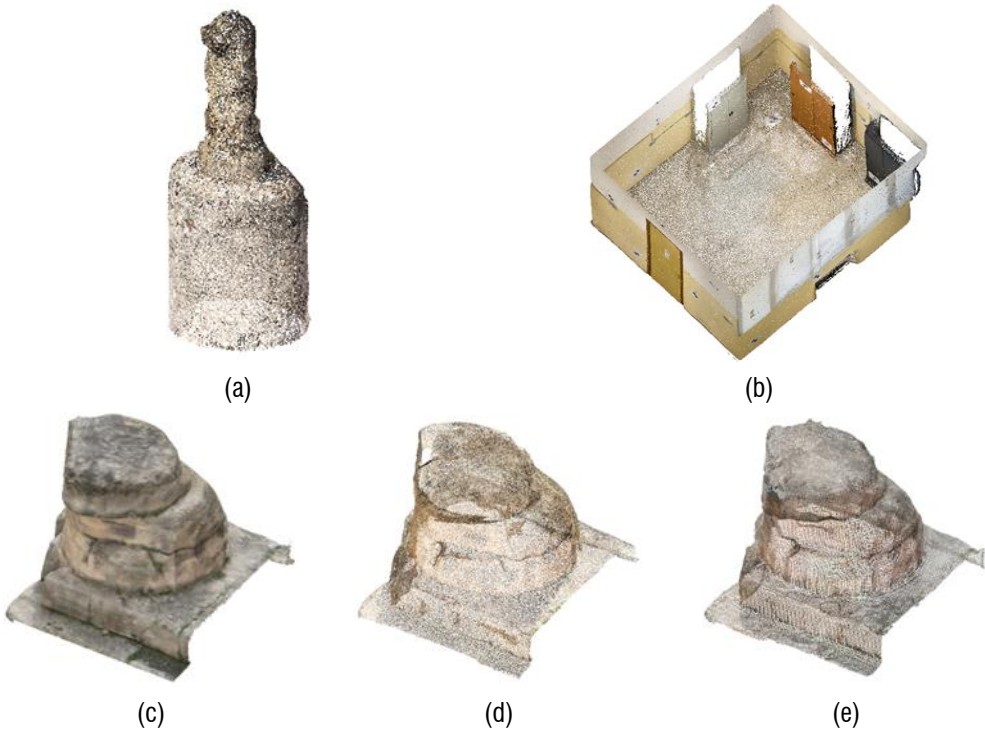


Fig. A9 – Point clouds examples of the second, third and fourth case studies: (a) statue - 1.5 cm resolution, (b) laboratory room - 1 cm resolution, (c) remains of a Doric column – 1 cm resolution; (d) remains of a Doric column - 1.5 cm resolution; (e) remains of a Doric column - 2 cm resolution.

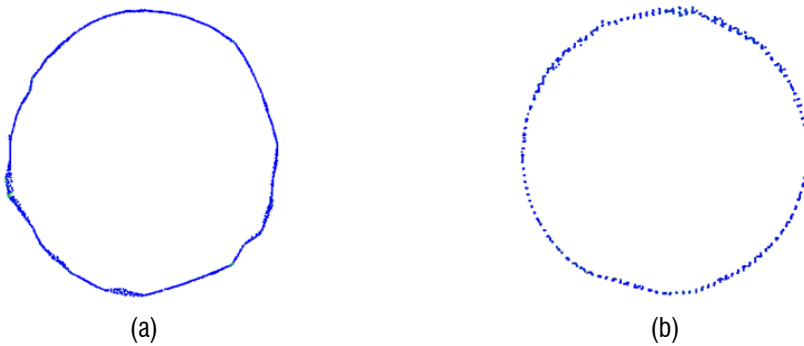


Fig. A10 - Sections of the stem of the statue, the scalar field refers to the surface variation value: (a) scan distance 2 m – 1.5 cm resolution; (b) scan distance 2 m - 2 cm resolution.

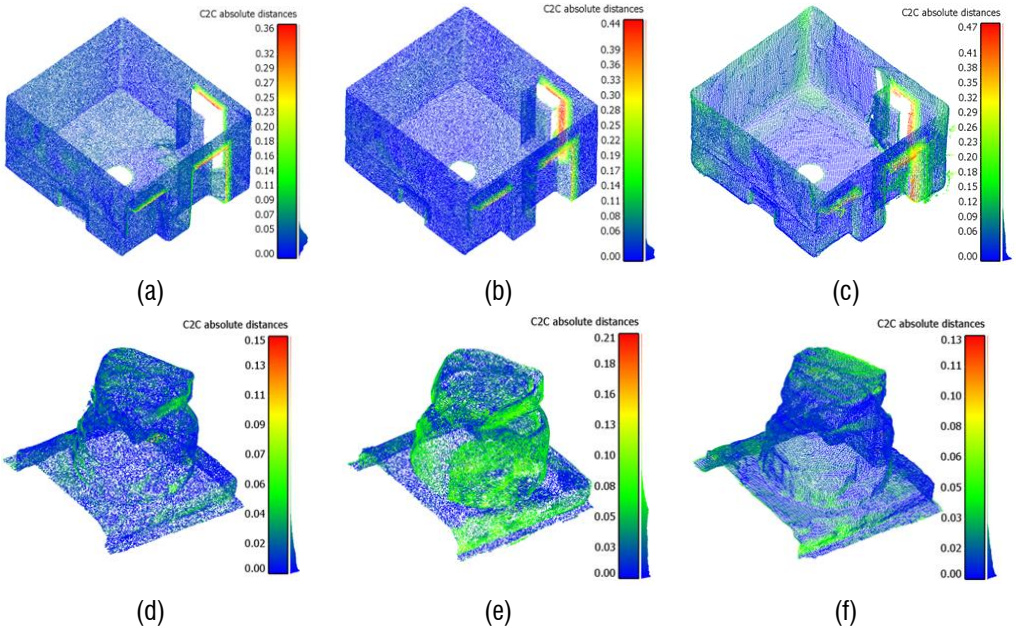


Fig. A11 - C2C histograms mobile devices depth sensors - reference point clouds: (a) laboratory room - 1 cm resolution; (b) laboratory room - 1.5 cm resolution; (c) laboratory room - 2 cm resolution; (d) Doric column remains - 1 cm resolution (d); (e) Doric column remains - 1.5 cm resolution; (f) Doric column remains - 2 cm resolution.

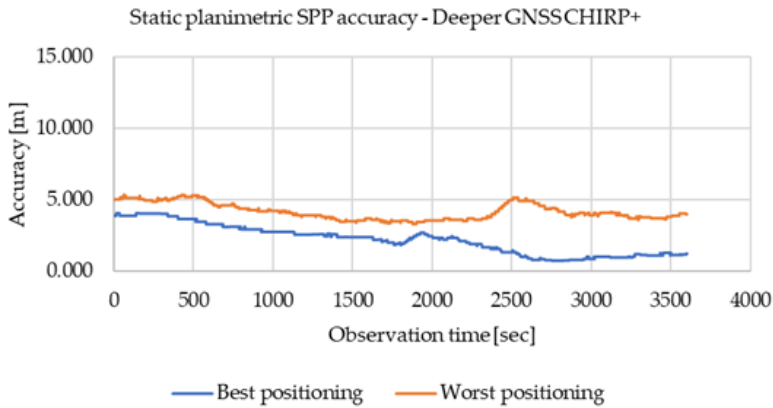


Fig. A12 - Accuracy levels (best and worst) in real-time static horizontal SPP for the Deeper Smart Sonar CHIRP+ during 3600 s.

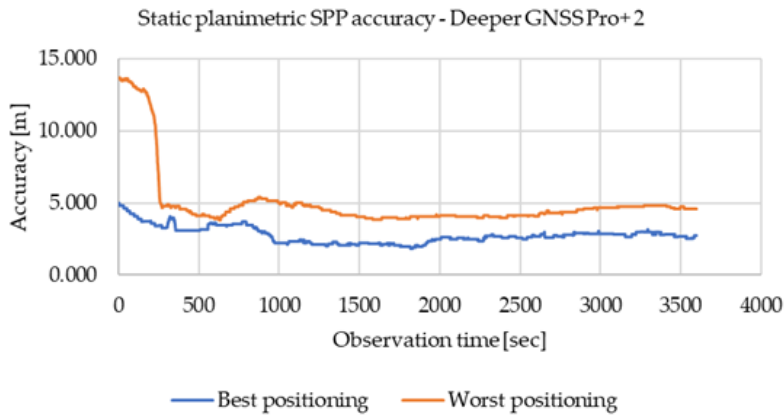
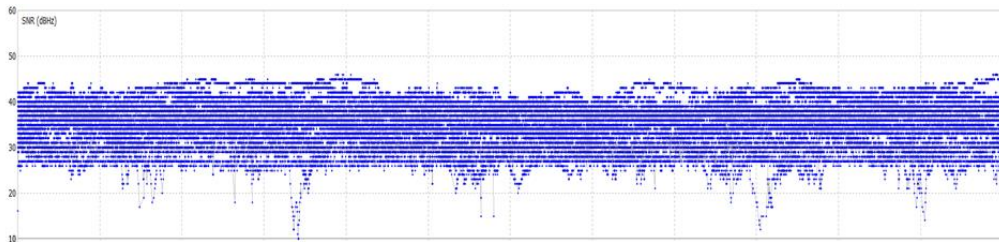
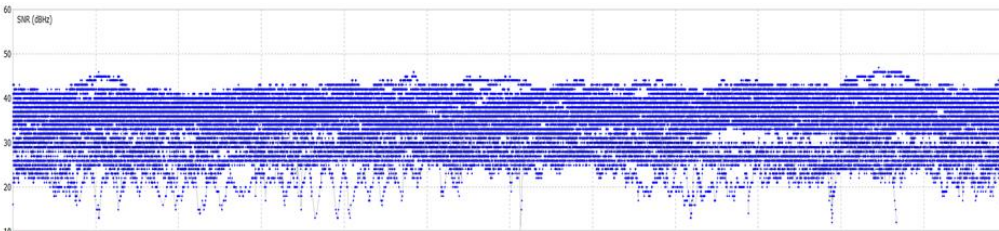


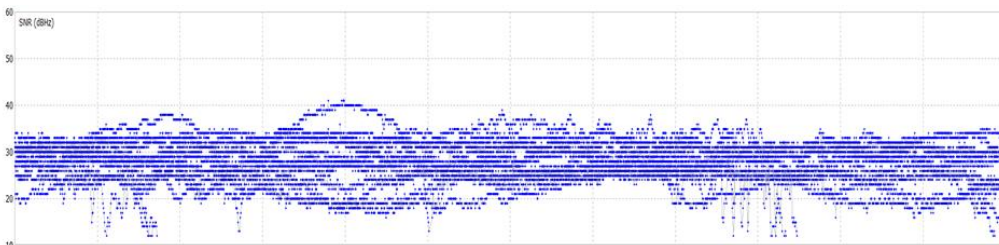
Fig. A13 - Accuracy levels (best and worst) in real-time static horizontal SPP for the Deeper Smart Sonar Pro+ 2 during 3600 s.



(a)



(b)



(c)

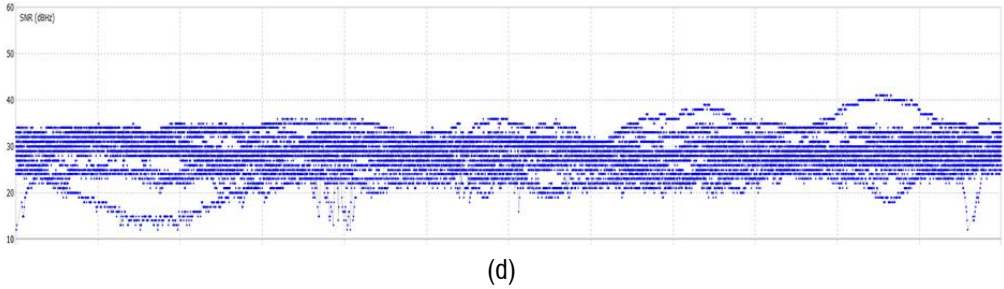


Fig. A14 - Huawei P30 Pro SNR values: (a) best for L1; (b) worst for L1; (c) best for L5; (d) worst for L5.

Fig. A15 displays a diagram illustrating the accuracy evolution in 3D static post-processing positioning of the G > S > P Sys over 3600 seconds. The diagram marks data post-processed in static mode in grey, and data post-processed in PPP mode in yellow. The accuracy calculation employed the following formula:

$$\Delta 3D = \sqrt{\Delta E^2 + \Delta N^2 + \Delta U^2} \quad (A1)$$

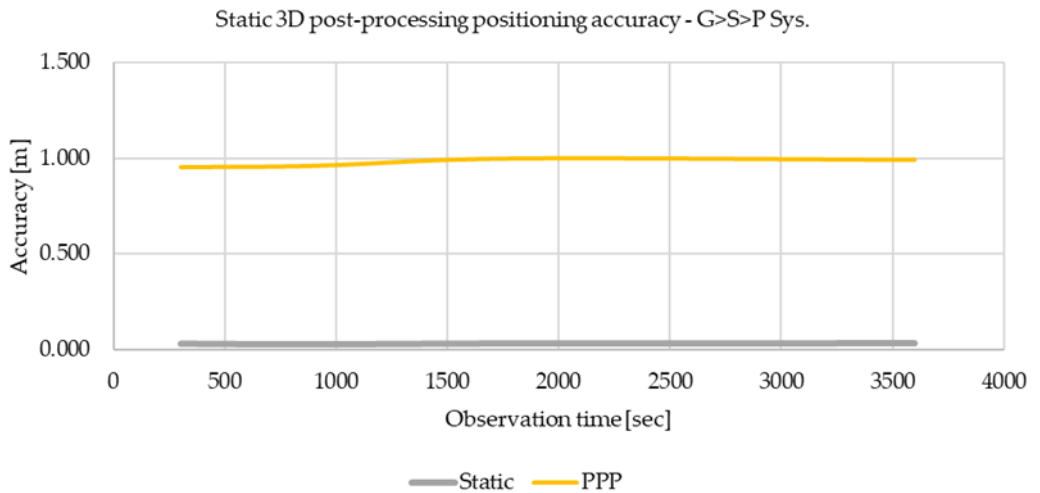


Fig. A15 - Accuracy of the G > S > P Sys in static 3D post-processed positioning: static (grey); PPP (yellow).

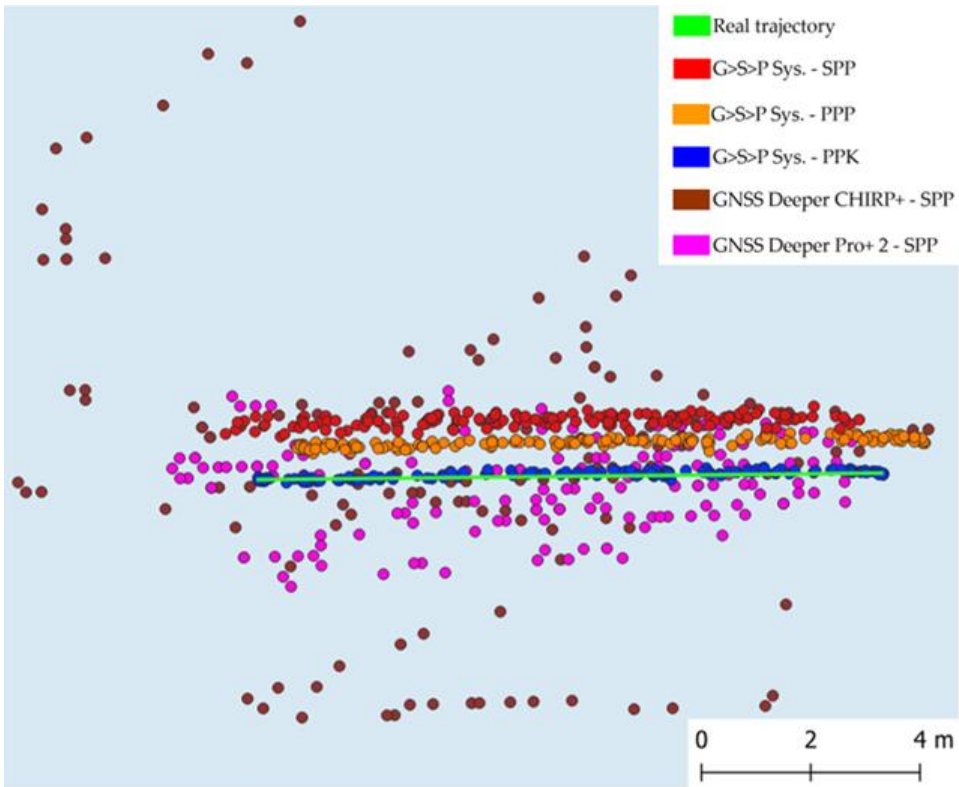
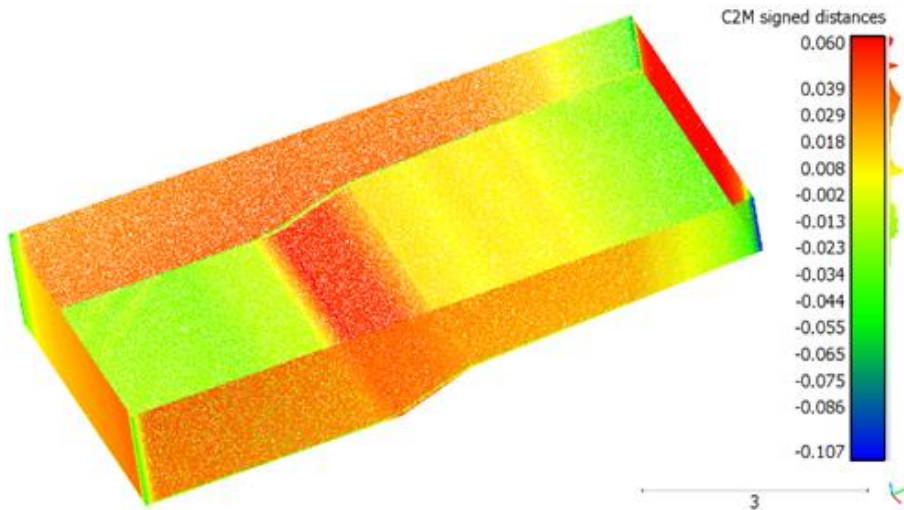
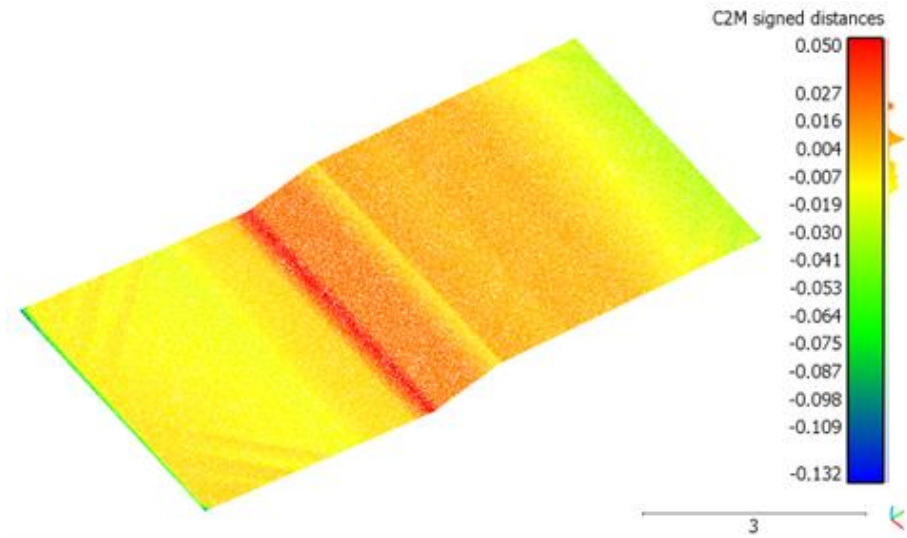


Fig. A16 - Comparison of the positioning accuracy of the G > S > P Sys and Deeper Smart Sonars against the actual sea test trajectory.



(a)



(b)

Fig. A17 - C2M analysis results: (a) the pool; (b) the pool bottom.

Tab. A4 – Location of AVTR, COAN, FATA, TARA and TIMI stations

Station	Latitude	Longitude	Height
AVTR	40° 20' 30.4324" N	17° 43' 56.9979" E	104.227 m
COAN	40° 58' 06.6952" N	17° 06' 25.5737" E	257.773 m
FATA	40° 31' 35.6679" N	17° 16' 59.5887" E	126.839 m
TARA	40° 31' 35.6068" N	17° 17' 00.4990" E	126.575 m
TIMI	45° 41' 10.0090" N	21° 18' 02.1587" E	139.835 m

CURRICULUM VITAE



Personal information

Name	Gabriele Vozza
Place and date of birth	Taranto(TA), 01 March 1986
Address	Via Umbria n.192, 74121, Taranto (TA), Italy
Phone	+39 3283539727
E-mail	gabriele.vozza@poliba.it
Nationality	Italian

Education

Currently

Polytechnic University of Bari

Ph.D. student in Risk and Environmental, Territorial and Building Development, 35° cycle.

26 September 2017

Polytechnic University of Bari

Master's Degree in Environmental and Territorial Engineering

17 April 2014

Polytechnic University of Bari

Bachelor's Degree in Civil Engineering

Scientific production

Vozza, G., Costantino, D., Pepe, M. and Alfio, V.S. (2023) 'Smart Sensors System Based on Smartphones and Methodology for 3D Modelling in Shallow Water Scenarios', *Applied System Innovation*, 6(1), p. 28. Available at: <https://doi.org/10.3390/asi6010028>.

Pepe, M., Costantino, D., Barnaba, G., Alfio, V.S. and Vozza, G. (2022) 'Building 3D City model from painting: the case study of Old Town of Taranto, Italy', in 2022 IMEKO TC-4 International Conference on Metrology for Archaeology and Cultural Heritage, *MetroArchaeo 2022*. International Measurement Confederation (IMEKO), pp. 186–190. Available at: <https://ricerca.unich.it/handle/11564/802712>.

Costantino, D., Pepe, M., Alfio, V.S., Vozza, G. and Occhinegro, M. (2022) 'Building 3D CityGML Model and Digital Management of a Vernacular Architecture', *International Review of Civil Engineering (IRECE)*, 13(3). Available at: <https://doi.org/10.15866/irece.v13i3.21242>.

Costantino, D., Vozza, G., Pepe, M. and Alfio, V.S. (2022) 'Smartphone LiDAR Technologies for Surveying and Reality Modelling in Urban Scenarios: Evaluation Methods, Performance and Challenges', *Applied System Innovation*, 5(4), p. 63. Available at: <https://doi.org/10.3390/asi5040063>.

Costantino, D., Vozza, G., Alfio, V.S. and Pepe, M. (2021) 'Strategies for 3D Modelling of Buildings from Airborne Laser Scanner and Photogrammetric Data Based on Free-Form and Model-Driven Methods: The Case Study of the Old Town Centre of Bordeaux (France)', *Applied Sciences*, 11(22), p. 10993. Available at: <https://doi.org/10.3390/app112210993>.

Pepe, M., Costantino, D., Alfio, V.S., Vozza, G. and Cartellino, E. (2021) 'A Novel Method Based on Deep Learning, GIS and Geomatics Software for Building a 3D City Model from VHR Satellite Stereo Imagery', *ISPRS International Journal of Geo-Information*, 10(10), p. 697. Available at: <https://doi.org/10.3390/ijgi10100697>.

Pepe, M., Costantino, D., Vozza, G. and Alfio, V.S. (2021) 'Comparison of Two Approaches to GNSS Positioning Using Code Pseudoranges Generated by Smartphone Device', *Applied Sciences*, 11(11), p. 4787. Available at: <https://doi.org/10.3390/app11114787>.

Costantino, D., Angelini, M.G. and Vozza, G. (2015) 'The engineering and assembly of a low cost UAV', in *2015 IEEE Metrology for Aerospace (MetroAeroSpace)*. 2015 IEEE Metrology for Aerospace (MetroAeroSpace), pp. 351–355. Available at: <https://doi.org/10.1109/MetroAeroSpace.2015.7180681>.

Vozza, G. (2014) 'Progetto di un APR Low Cost', in *ASITA 2014. 18^a Conferenza Nazionale ASITA 2014, Firenze (Italia)*, pp. 1237–1244.
